U.PORTO

DOUTORAMENTO

BIOTECNOLOGIA MOLECULAR E CELULAR APLICADA ÀS CIÊNCIAS DA SAÚDE

A tissue engineering approach to fabricate a stomach-on-a-chip: a biomimetic device to decode the role of CD44v6 in gastric cancer

Daniel André Gonçalves Ferreira

D

2021

U.PORTO

Daniel André Gonçalves Ferreira

A tissue engineering approach to fabricate a stomach-on-a-chip: a biomimetic device to decode the role of CD44v6 in gastric cancer

Daniel André Gonçalves Ferreira

D.ICBAS 2021

SEDE ADMINISTRATIVA

INSTITUTO DE CIÊNCIAS BIOMÉDICAS ABEL SALAZAR

FACULDADE DE FARMÁCIA

DANIEL ANDRÉ GONÇALVES FERREIRA

A TISSUE ENGINEERING APPROACH TO FABRICATE A STOMACH-ON-A-CHIP: A BIOMIMETIC DEVICE TO DECODE THE ROLE OF CD44V6 IN GASTRIC CANCER

Tese de candidatura ao grau de Doutor em Biotecnologia Molecular e Celular Aplicada às Ciências da Saúde.
Programa Doutoral da Universidade do Porto (Instituto de Ciências Biomédicas Abel Salazar e Faculdade de Farmácia).

Orientador - Doutor Pedro Lopes Granja
Categoria - Investigador Principal
Afiliação - Instituto de Investigação e Inovação em Saúde (i3S), Instituto de Engenharia Biomédica (INEB)

Co-orientadora – Doutora Carla Isabel Gonçalves Oliveira
Categoria – Investigadora Principal, Professora Afiliada
Afiliação - Instituto de Investigação e Inovação em Saúde (i3S), Instituto de Patologia e Imunologia Molecular da Universidade do Porto (ipatimup), Departamento de Patologia da Faculdade de Medicina da Universidade do Porto (FMUP)

Co-orientador – Doutor João Pedro Estrela Rodrigues Conde
Categoria – Investigador Principal, Professor Associado
Afiliação – Departamento de Bioengenharia do Instituto Superior Técnico (IST), Instituto de Engenharia de Sistemas e Computadores – Microsistemas e Nanotecnologia (INESC MN).

“I try all things; I achieve what I can.”

Quote from Moby Dick | Herman Melville

HOSTING INSTITUTIONS

Instituto de Investigação e Inovação em Saúde (i3S), Universidade do Porto

Instituto de Engenharia Biomédica (INEB), Universidade do Porto

Instituto de Patologia e Imunologia Molecular da Universidade do Porto (Ipatimup)

Instituto de Engenharia de Sistemas e Computadores – Microsistemas e Nanotecnologia (INESC MN)

Technische Universität Wien (TU Wien), Universidade de Viena

FUNDING

This work was supported by:

Fundação para a Ciência e Tecnologia (FCT) and Doctoral Programme on Cellular and Molecular Biotechnology Applied to Health Sciences (BiotechHealth Programme; ref. PD/00016/2012) and by Programa Operacional Potencial Humano (POPH).

SkinChip project (PTDC/BBB-BIO/1889/2014).

Fundo Europeu de Desenvolvimento (FEDER) Regional funds through the COMPETE 2020 - Operacional Programme for Competitiveness and Internationalization (POCI), Portugal 2020, and by Portuguese funds through FCT/Ministério da Ciência, Tecnologia e Inovação in the framework of the projects "Institute for Research and Innovation in Health Sciences" (POCI-01-0145-FEDER-007274).

3DChroMe (POCI-01-0145-FEDER-30164).

Norte Portugal Regional Programme (NORTE 2020), under the PORTUGAL 2020 Partnership Agreement, through the European Regional Development Fund (ERDF) for projects NORTE-01-0145-FEDER-000029 and DOCnet (NORTE-01-0145-FEDER-000003).

European Structural and Investment funds through the Compete Programme (Grant #: LISBOA-01-0145-FEDER-016405).

National funds through FCT (SAICTPAC/0019/2015) via the research project POINT4PAC, and FCT funding through INESC MN (Unidade ID 5367).

Daniel A. Ferreira acknowledges FCT for the support through a FCT/BiotechHealth PhD Programme grant, ref. PD/BD/105976/2014.

ACKNOWLEDGEMENTS

Um projeto de doutoramento nunca é uma caminhada solitária. Foram muitas as dificuldades e os desafios, mas felizmente, foram também muitas as pessoas que caminharam ao meu lado. A todas elas deixo os meus mais sentidos agradecimentos.

As minhas primeiras palavras não podiam deixar de ser para o Pedro e para a Carla.

Pedro, muito obrigado por me teres recebido no teu grupo e por teres aceitado supervisionar um projeto tão complexo e desafiante. Acima de tudo, por me teres deixado seguir o caminho que escolhi, sem qualquer entrave. Nada disto teria sido possível sem o teu apoio e sem a tua preciosa ajuda e inspiração contagiante. Mesmo nos momentos mais difíceis, conseguiste sempre encontrar uma solução, com uma boa dose de calma e positivismo. Levo muita ciência comigo, mas nem só de ciência se fez o caminho. Contigo cresci também pessoalmente e aprendi a trabalhar de forma diferente os desafios. Por tudo isto, deixo-te os meus mais sentidos agradecimentos. Estou certo de que os nossos caminhos se cruzarão no futuro.

Carla, já lá vão 14 anos desde que nos cruzamos pela primeira vez nos corredores do Ipatimup. Será certamente difícil em tão curto espaço extravasar tudo o que já fizeste por mim. “Pegaste” em mim no início da caminhada e ensinaste-me a fazer ciência. Se hoje este projeto chega a bom Porto, é em boa parte pelo teu apoio constante e atenção ao detalhe. Estiveste sempre disponível, mesmo quando o tempo era escasso e pude sempre contar contigo e com o teu grupo para discutir a ciência deste projeto. Uma palavra de apreço especial por teres assumido a liderança a par do Pedro, na altura mais difícil e delicada do projeto. Fizeste o possível e o impossível e foste muito para lá do que alguma vez poderia pedir. Muito obrigado por fazeres parte desta caminhada.

João, muito obrigado pelo apoio, pelas discussões científicas e pela forma entusiasmante como “faz” ciência. Acima de tudo, obrigado por acreditar neste projeto tão desafiante. Não teria sido possível sem o seu precioso contributo. Foi um privilégio trabalhar no INESC-MN. Lá, encontrei uma segunda casa onde passei largas jornadas e encontrei uma equipa experiente e acolhedora que me ensinou a fazer microfluídica.

Peter, my heartfelt gratitude goes to you, for welcoming me at your lab. You gave me all the time and resources needed to make this project a reality. Above all else, you taught me

that complex problems often have a simple solution. Thank you for giving me the unique opportunity to work at your lab and learn the ins and outs of organ-on-a-chip technology.

Professores Mário Barbosa e Manuel Vilanova, na qualidade de diretores do programa doutoral BiotechHealth, durante o período em que decorreu este projeto, gostaria de lhes agradecer o apoio prestado e as excelentes discussões científicas durante os simpósios do programa doutoral. Não menos importante, gostaria de lhes agradecer a oportunidade que me concederam, ao aceitarem a minha candidatura ao programa doutoral BiotechHealth.

Cristina Barrias e Filipa Sousa, não poderia deixar de agradecer o vosso apoio. Este projeto chega agora à sua conclusão, em grande parte, porque na sua fase mais difícil, vocês permitiram que a chama se mantivesse acesa. Obrigado pelo vosso contributo e apoio.

A todos os membros dos grupos Biofabrication e Bioengineered 3D microenvironments, que partilharam comigo durante todos estes anos, a casa, os desafios, as frustrações, mas também as conquistas e as alegrias, partilhamos momentos profissionais, mas também momentos de lazer, o meu grande obrigado. Acolheram-me e fizeram-me sentir em casa desde o primeiro dia.

A todos os membros do grupo Expression Regulation in Cancer, deixo-vos o meu agradecimento pela partilha de conhecimento e pela discussão científica em torno deste projeto. Um obrigado especial à Carla Pereira e à Gabriela por serem parte integrante deste trabalho.

A todos os membros do grupo INESC Microsystems and Nanotechnologies com que me cruzei, obrigado pela partilha, ensinamentos e camaradagem. Convosco aprendi a “fazer” microfluídica, mas também tivemos oportunidade de partilhar alguns momentos de descontração. Obrigado também, por fazerem de Lisboa a minha segunda casa.

To all the Cell Chip Group members, thank you for welcoming me to the group, for your help and for sharing the cookies. It was truly an amazing environment to work in.

O percurso na ciência vai longo, e alguns nomes, embora não sejam agora presença diária e constante, continuam a fazer parte desta caminhada. Hugo, Renata, Joana, Patrícia, Sílvia, Rita, Mafalda, Agata, Erik, Fernando, Cristina, Pau, Nikos, Nita, Joana, Rui, Sérgia, Inês, Miguel, André, Diana, Pedro, Conceição, Filipa, Joana Gomes. Obrigado a todos por partilharem comigo parte do percurso.

Babi, tu mereces umas palavrinhas à parte. Por seres uma pessoa muito especial, por me teres recebido de forma tão carinhosa no Ipatimup, já lá vão 14 anos, mas acima de tudo porque continuas a ser a melhor amiga de sempre. Que tenhas sempre a mesma energia que te acompanhou até agora.

Because life is not always about work, I need to thank all the people that in one way or the other helped me take my mind away from work. Games are a part of my essence and to all my boardgame and wargame partners, I would like to extend my gratitude for sharing so many great moments, rolling dice and chatting away. Jorge, Pedro, Gonçalo, João, Vanessa thank you for all the good times. A special thank you word to Thomas, Georg and Christoph, for welcoming me to the gaming group in Austria and making my stay, an enjoyable one.

Aos parceiros de sempre e amigos para a vida, Rafael, Susana e Sofia, Beta, Bruno e pequenotes, Filipe, Karishma e Afonso, Clara, Tiago, André, Jessica, Mârcio, Nel, Nádia, Sara, Filipa, Eliel, Erica, Ana. Continuaremos a partilhar bons momentos! Vocês serão sempre parte essencial no meu percurso.

Termino os meus agradecimentos com algumas palavras dedicadas à minha família, a base sem a qual esta demanda não seria possível.

Aos meus avós, que infelizmente partiram cedo demais e não poderão partilhar este momento, agradeço todo o carinho e apoio que me deram ao longo de todos estes anos. Este trabalho é também um pouco vosso. Obrigado!

Ao meu irmão, o meu grande orgulho e o meu melhor exemplo. Por estar sempre presente todos estes anos, pelo apoio constante e pela ajuda preciosa que me deu neste projeto. Obrigado!!! Célia e Leonor, obrigado por me acompanharem, me aturarem, e por fazerem parte do meu dia a dia. Serão sempre parte essencial e especial da minha vida.

Ao Zeca, Marisol e Babi, por me terem recebido de braços abertos já lá vão uns aninhos. Não podia ter pedido melhor. Obrigado pelos bons momentos, pela cumplicidade e acima de tudo por me aturarem. Esta caminhada foi certamente mais fácil ao vosso lado.

Aos meus pais. que desde o início foram o meu pilar, me acompanharam, me motivaram, fizeram o possível e o impossível para que este caminhada fosse possível. Fica difícil expressar em palavras tudo aquilo que vos gostaria de dizer. Obrigado por serem o meu

melhor exemplo, o meu porto seguro e os meus melhores amigos. Muito obrigado por estarem sempre presentes!!!

Cheila e Clarinha, partilhamos estes últimos anos intensamente. Viveram ao meu lado as conquistas, os sucessos, as alegrias, mas também os longos dias de trabalho, as dificuldades e as frustrações. Não conseguiria imaginar a minha vida sem o vosso apoio. Tudo o que consegui, foi com a vossa ajuda e o vosso contributo. Ao longo deste tempo, foram a minha companhia, as minhas melhores amigas, as minhas confidentes, as minhas companheiras de passeios e aventuras e por vezes, foram também as minhas terapeutas. Agora e em perspetiva, penso que não há nada que não se resolva com um abraço ao fim do dia. Sou imensamente sortudo por vos ter na minha vida e espero poder retribuir todo o apoio que me deram. Obrigado por serem sempre a parte constante e boa da minha vida e por me aturarem ao longo destes anos todos. Esta conquista é tanto minha como vossa.

TABLE OF CONTENTS

ABSTRACT

Gastric cancer (GC) ranks worldwide, as one of the leading causes of cancer related deaths representing a major clinical concern. The lack of reliable biomarkers for early-stage diagnosis and the heterogeneous nature of the molecular alterations governing the disease, poses an extremely difficult challenge to overcome, as disease is often detected at a late stage, at a point when therapeutical options are severely limited. Understanding the fundamental molecular and cellular alterations leading to disease onset and progression is the key for better GC management. Patient derived histological specimens provide an accurate depiction of the disease in a biologically relevant context. However, they offer a time-stamped view of the disease. While they are a useful readout of the cellular and molecular alterations of GC and a fundamental tool for carcinoma detection and grading, they are of limited use to understand the causal alterations directing the initiation and development of the transformative process. Understanding the disease in a broader scope requires biological models that can mimic the disease in its entirety or its constituent parts. The work outlined in this thesis describes an integrative overview on the engineering principles of two *in vitro* cell culture platforms designed to study the molecular and cellular mechanisms leading to GC onset and progression.

The first part of this thesis was dedicated to unravelling the role of CD44 variants containing the exon v6 (CD44v6) in the context of GC, particularly its role in therapy response and implication in the transformative process guiding GC onset and progression. To study such task, two isogenic cell line models expressing *de novo* CD44v6 or the canonical form of CD44, termed CD44 standard (CD44s) were established. Despite no observed correlation between CD44v6 expression and development of cancer-related features, such as invasion, migration, cell adhesion, an interesting link was found between CD44v6 expression and increased resistance to cisplatin-mediated chemotherapy, possibly via a STAT3 and P38 mediated pathway. Interestingly, our work with co-culture experiments of CD44v6+ and CD44v6- cells showed that CD44v6+ cells could have some selective advantage when a heterogeneous gastric tumor was treated with cisplatin-based chemotherapy. This overgrowth of CD44v6+ cells after chemotherapy, may indicate that this cell population can get enriched in GC relapses that arise after chemotherapy. These results and our previous work showing that CD44v6 expression can be found in premalignant gastric lesions, show that CD44v6 is a good biomarker candidate for early-stage diagnostic of the disease as well as a potential therapeutic target.

Despite the obvious advantages of 2D cell culture systems as study models, the field of GC research can greatly benefit from the development of biomimetic models representing

the gastric mucosa. 3D cell culture platforms represent a merge of tissue engineering concepts with those of conventional monolayered cell culture, standing at a middle-ground between 2D and *in vivo* animal models. However, mimicking *in vitro* the complex multicellular microenvironment of the gastric epithelium is an extremely challenging task that requires a revised approach to currently existing methodologies.

The second part of the thesis concerns the development of a novel method for the fabrication of elastomeric organ-on-a-chip devices with integrated mechanical microactuators and the prototyping of a proof-of-principle stomach-on-a-chip device. The fabrication method described is a significant improvement to current soft lithography-based methodologies, allowing the fabrication of a complex multilayered device in a matter of hours and for a fraction of the cost. Devices produced were tested for biocompatibility and ability to operate without delamination under prolonged exposure to cell culture conditions. In addition, the designed microactuator was shown to elicit mechanical stretching of the cell culture substrate in a physiologically relevant range. A prototype stomach-on-a-chip was then designed using the developed fabrication method. The stomach-on-a-chip combined in a single platform the three innermost layers of the gastric mucosa, namely the epithelial barrier, the basement membrane and an analogue of the lamina propria, consisting of a bioinspired collagen type I hydrogel mesh, embedded with gastric fibroblasts. The combination of tissue-like microarchitecture and dynamic conditions provided by fluid flow and mechanical stretching, to emulate the intra-luminal stomach flow and the peristaltic movements respectively, compose a biomimetic device capable of eliciting a physiologically relevant molecular and cellular response of the gastric mucosa analogue. Cells within the device evidenced secondary differentiation traits common to the native gastric tissue, but otherwise lost, in monolayer cultures, as well as recovery, to the extent tested, of partial gastric function.

Collectively the body of work presented in this thesis offers a significant contribution to the field of GC research. We have described the establishment of two isogenic gastric cancer cell line models. Despite their simple nature, they proved to be a useful tool to tackle the role played by the CD44v6 variant in GC and helped in identifying this molecule as a putative therapeutic target for cisplatin resistant tumors. Furthermore, we have engineered a fast alternative methodology to soft lithography, for the fabrication of organ-on-a-chip devices and devised a biomimetic model of the gastric mucosa. The engineered platform highlights the importance of addressing the dynamic native microenvironment to potentiate a tissue-level response and could be an interesting tool to dissect the molecular pathways involved in GC.

RESUMO

O cancro gástrico (CG) é uma das causas mais comuns de morte relacionada com cancro, representando um grave problema clínico a nível mundial. A inexistência de biomarcadores fiáveis para o diagnóstico precoce e a heterogeneidade molecular das alterações que governam a doença, representam um desafio árduo que dificulta o seu tratamento. O diagnóstico de CG é muitas vezes feito de forma tardia, numa altura em que as opções terapêuticas são limitadas. Nesse sentido, entender os princípios moleculares e celulares básicos que estão na origem do processo transformativo que leva ao início e progressão da doença é fundamental. Espécimes histológicos de pacientes são uma ferramenta nuclear no estudo do CG, permitindo o estudo da doença num contexto biológico relevante, sendo ferramentas essências para a deteção e estratificação da doença. No entanto, esta ferramenta permite apenas uma visão de túnel, representativa do tumor na altura da sua colheita. Para ser possível uma visão mais abrangente dos processos moleculares que determinam o início e a progressão da doença, são necessários modelos de estudo diferentes que mimetizem parcialmente ou na sua totalidade os vários aspetos do CG. O trabalho descrito nesta tese, aborda os princípios de bioengenharia empregues para criar dois modelos distintos para estudar em detalhe, os aspetos moleculares e celulares do CG.

A primeira parte desta tese, foi dedicada a elucidar o papel de variantes da CD44, contendo o exão v6 (CD44v6), em particular o seu papel no processo transformativo que leva ao CG, bem como a influência destas isoformas na resposta à terapia. Para tal, criamos duas linhas isogénicas que expressam *de novo* as formas CD44v6 ou a forma canónica da CD44 (CD44 standard - CD44s). Apesar de não se ter observado uma correlação entre a expressão de CD44v6 e o desenvolvimento de características típicas do cancro, como invasão e proliferação aumentadas ou diminuição de adesão celular, foi possível observar causalidade entre a expressão de CD44v6 e uma resistência aumentada a quimioterapia por cisplatina. Concomitantemente, em co-culturas de células CD44v6+ com células CD44v6-, observamos um enriquecimento das células CD44v6+ após tratamento com cisplatina. Esta observação parece indicar que num contexto *in vivo*, a população de células CD44v6+ pode aumentar consideravelmente após terapia com cisplatina. Estes resultados, em conjunto com a nossa anterior observação de que isoformas CD44v6 são expressas em lesões pré-malignas, sugere o CD44v6 como um potencial biomarcador para diagnóstico precoce, mas também um potencial alvo terapêutico em recidivas de tumores após tratamento com cisplatina.

Apesar das vantagens obvias de sistemas de cultura celular em 2D, como os descritos na primeira parte desta tese, o ramo de estudo dedicado ao cancro gástrico, beneficiaria imenso do desenvolvimento de modelos biomiméticos que representem com precisão a mucosa gástrica. Modelos de cultura 3D representam uma fusão de conceitos de engenharia de tecidos, com técnicas de cultura 2D convencional, representado um compromisso entre os tradicionais sistemas 2D e os sistemas *in vivo* de experimentação animal. Não obstante, mimetizar o ambiente multicelular e complexo do epitélio gástrico, é um desafio difícil que obriga a repensar as atuais metodologias.

Na segunda parte desta tese, desenvolvemos um novo método de fabrico de dispositivos órgão-em-chip produzidos em silicone biocompatível, com microatuadores integrados. Adicionalmente, a tecnologia desenvolvida foi aplicada na criação de um protótipo que recria um estômago-em-chip. Os dispositivos produzidos foram testados quanto à sua biocompatibilidade e capacidade para operar sem delaminação em ambientes apropriados à cultura celular. Adicionalmente, demonstramos que o microatuador desenhado, foi capaz de reproduzir estímulos biomecânicos em regimes fisiologicamente relevantes. O protótipo de estômago-em-chip criado, combinou num só dispositivo a arquitetura das 3 camadas internas da mucosa gástrica, nomeadamente, a camada epitelial, a membrana basal e a lamina própria, esta última constituída por uma matriz extracelular biomimética de colagénio tipo I, com fibroblastos gástricos dispersos pela matriz. A reconstituição da micro-arquitetura da mucosa gástrica, pareada com as condições dinâmicas características do estômago, estabeleceram um dispositivo biomimético capaz de induzir uma resposta bio-relevante por parte do modelo criado. A mucosa gástrica representada pelo estômago-em-chip, evidenciou características de diferenciação que são comuns à mucosa gástrica nativa, mas que são comummente perdidas em monoculturas 2D.

Coletivamente, o trabalho apresentado nesta tese, representa um contributo significativo para o ramo de estudo do CG. Descrevemos a criação de um modelo isogénico de CG, que foi utilizado para estudar em detalhe a contribuição das isoformas CD44v6 no processo transformativo que leva ao CG, bem como na resistência a regimes terapêuticos, permitindo confirmar a CD44v6 como um potencial biomarcador para terapêutica. Adicionalmente, o método de fabrico de plataformas órgão-em-chip desenvolvido, permitiu criar com sucesso um estômago-em-chip capaz de mimetizar muitos dos aspetos do tecido nativo da mucosa gástrica. Esta ferramenta pode ser uma ferramenta muito interessante para dissecar as vias moleculares envolvidas no desenvolvimento do CG.

LIST OF ACRONYMS AND ABBREVIATIONS

5-FU – 5-fluorouracil

AMINE-PDMS LINKER - poly[dimethylsiloxane-co-(3-aminopropyl)methylsiloxane]

APC – allophycocyanin

APTES - (3-aminopropyl)triethoxysilane

APTMS - (3-aminopropyl)trimethoxysilane

BIS-AMINO SILANE - bis[3-(trimethoxysilyl)propyl]amine

BSA – bovine serum albumin

CAD – computer assisted design

CDH1 – gene encoding the protein E-cadherin

cDNA – complementary DNA

CSC – cancer stem cell

CA 19-9 – carbohydrate antigen 19-9

CAE – carcinoembryonic antigen

CD44s – canonical form of CD44

CD44v6 - CD44 isoforms resulting from alternative splicing and expressing the exon v6

DAPI - 2-(4-amidinophenyl)-1H-indole-6-carboxamidine

ECL – enhanced chemiluminescence

ECM – extracellular matrix

EMT - epithelial to mesenchymal transition

FACS – fluorescence activated cell-sorting

FBS – fetal bovine serum

G418 - geneticin

GC – gastric cancer

GI – gastrointestinal

HDGC – hereditary diffuse gastric cancer

HE - hematoxylin and eosin

HER2 – human epidermal growth factor receptor 2

H. pylori – helicobacter pylori

HCl – hydrocloric acid

IPA - isopropanol

iPSCs – induced pluripotent stem cells

JCRB – Japanese collection of research bioresources

MCS – multiple cloning site

MET - mesenchymal to epithelial transition

O_2 – oxygen

O.C.T. - optical cutting temperature compound

OS – overall survival

OU – organoid units

PB – presto blue

PBS – phosphates buffered saline

PDMS – polydimethylsiloxane

PEEK - poly(ether-ether-ketone)

PEN - penicillin

PET - polyethylene terephthalate

PLGA - poly(lactic-co-glycolic acid)

qRT-PCR – quantitative real time-PCR

RFUs - relative fluorescence units

SD – standard deviation

SDS – sodium dodecyl sulfate

SRB - sulforhodamine B

STREP - streptomycin

TBS – tris-buffered saline

TEER - transepithelial electric resistance

VEGFA – vascular endothelial growth factor A

WHO – World Health Organization

ZO-1 - zonula occludens-1

MOTIVATION FOR THIS WORK

Gastric disease represents a global health burden, with many clinically described ailments affecting the stomach in particular. The one imposing the most serious burden is gastric cancer, a disease for which there are no clinically relevant early-detection diagnostic tools. This results in late-stage curative solutions that entail high morbidity and lower overall patient survival. Finding new diagnostic and therapeutic avenues requires an intimate knowledge of the disease at molecular and cellular level. Identifying relevant biomarkers that can aid in the early diagnosis of the disease or act as potential therapy targets is of paramount importance. However, peering into the basic biology of disease initiation and progression, is limited by the ability of available models to replicate the complex nature of the disease they emulate. In this context, biomimetic tools can offer a practical and relevant contribution.

Tissue engineering has been for many years at the forefront of regenerative medicine, contributing for the establishment of many clinically relevant biomimetic solutions for wound healing and tissue recovery. In the past decades, the same principles guiding tissue engineering have been borrowed extensively by the field of cellular and molecular biology. The ultimate goal being, to develop bioinspired and biomimetic tissue and cell culture platforms, that aim to replicate *in vitro* the complex microarchitecture and dynamics of the living tissue in health and disease. Human derived cell culture models that replicate *in vitro* the intricacies of human physiology and disease are an invaluable tool to study predicaments such as gastric cancer. One such technology, termed organ-on-a-chip offers a low cost, fine-tunable solution to this problem and importantly, represents a physiologically relevant alternative to animal experimentation.

In the work outlined in this thesis, we aimed to address the following points:

Chapter II – Original publication 1

Develop an isogenic gastric cancer cell line model, expressing *de novo* CD44v6 or CD44s and use the newly engineered cell lines, to understand the role of CD44v6 in the transformative process leading to gastric cancer initiation and progression and whether CD44v6 plays a key role in resistance to cisplatin mediated chemotherapy resistance.

Chapter III – Original publication 2

Develop a fast and reliable method for the fabrication of complex, multilayered organ-on-a-chip devices capable of producing physiologically relevant biomechanical cues.

Chapter IV – Original publication 3

Using the technology developed and described under Chapter III, engineer a bioinspired organ-on-a-chip platform exhibiting *in vivo*-like function and representing the microarchitecture of the 3 innermost layers of the gastric mucosa.

THESIS OUTLINE AND STRUCTURE

This thesis is divided into 5 chapters organized as follows:

Chapter I introduces the reader to some general concepts relevant to the present work. The first section covers the gastric landscape, with a focus towards the stomach's cellular and molecular physiology, followed with a detailed overview on gastric cancer's epidemiology, etiology and classification. The section is closed with a look into gastric cancer biomarkers with a particular focus on CD44v6, an adhesion molecule that will be further explored later in this thesis.

The second section of the general introduction approaches keys aspects of replicating the human physiology *in vitro*, discourses over the many available methodologies to mimetize human tissue at a microscale, with a particular focus towards the end, on microfluidics and organs-on-a-chip, a technology that will be explored in further detail throughout chapters III and IV of this work.

The third and final section of the introduction, revolves around crucial aspects of transposing the complexity of the gastric mucosa into bioinspired *in vitro* models and elaborates on the state-of-the-art platforms currently in use or under development, to replicate the gastric environment.

Chapter II details the establishment of two isogenic gastric cancer cell lines expressing *de novo* the CD44v6 isoform or the canonical form, CD44s. This is followed by work aiming to elucidate whether CD44v6 holds a key role in the transformative process leading towards gastric cancer development and progression. We also address if CD44v6 plays a role in the modulation of therapy response, or if this molecule is a bystander effect of the transformative process, playing a secondary role in the process.

Chapters III and **IV**, concerns the development of a novel fabrication method for the production of elastomeric, multilayered, organ-on-a-chip devices with integrated mechanical actuators using a technique based on xurography. The devices fabricated are explored for their potential to hold a long-term culture of gastric epithelial cells under native physiological conditions. This is followed by the establishment of a proof-of-principle bioinspired stomach-on-a-chip platform with intra-luminal flow and peristaltic-like motion, emulating the gastric tissue microenvironment and function.

Chapter V presents the closing statements concerning the work produced within the scope of this thesis and provides the reader some highlights concerning future perspectives.

The **Appendix** provides detailed documentation pertaining to the patent application on the fabrication method described in Chapter III.

LIST OF MAIN OUTPUTS

PUBLICATIONS IN PEER-REVIEWED JOURNALS

Original publication 1

Ferreira D.A.*, Pereira C.*, Mendes N., Granja P.L., Almeida G.M., Oliveira C. Expression of CD44v6-containing isoforms influences cisplatin response in gastric cancer cells. Cancers (Basel). 2020; 12.

*These authors contributed equally to this work.

Original publication 2

Ferreira D.A., Rothbauer M., Conde J.P., Ertl P., Oliveira C., Granja P.L. A fast alternative to soft lithography for the fabrication of organ-on-a-chip elastomeric-based devices and microactuators. Adv Sci (Weinh). 2021; 8: 2003273.

Original publication 3

Ferreira D.A., Conde J.P., Rothbauer M., Ertl P., Granja P.L., Oliveira C. Bioinspired human stomach-on-a-chip with in-vivo like function and architecture. (In preparation)

COMPLEMENTARY PUBLICATIONS IN RELATED FIELDS

Lourenco B.N., Springer N.L., **Ferreira D.A.**, Oliveira C., Granja P.L., Fischbach C. CD44v6 increases gastric cancer malignant phenotype by modulating adipose stromal cell-mediated ECM remodeling. Integr Biol (Camb). 2018; 10: 145-158.

Kennedy P.J., Sousa F., **Ferreira D.A.**, Pereira C., Nestor M., Oliveira C., Granja P.L., Sarmento B. Fab-conjugated PLGA nanoparticles effectively target cancer cells expressing human CD44v6. Acta Biomater. 2018.

Kennedy P.J., Perreira I., **Ferreira D.**, Nestor M., Oliveira C., Granja P.L., Sarmento B. Impact of surfactants on the target recognition of Fab-conjugated PLGA nanoparticles. Eur J Pharm Biopharm. 2018; 127: 366-370.

POSTER PRESENTATIONS IN INTERNATIONAL CONFERENCES

Ferreira D.A., Almeida G., Reis I., Lourenço B., Santos T., Granja P.L., Oliveira C., "CD44v6 in gastric cancer, a marker of progression or a culprit?", 5th Advanced Summer School: Interrogations at the Biointerface – the nano/medicine interface, 29 of June – 3 of July 2016, Porto, Portugal

Ferreira D.A., Rothbauer M., Conde J.P., Ertl P., Oliveira C., Granja P.L., A Fast Alternative to Soft Lithography for the Fabrication of Organ-on-a-Chip Elastomeric-Based Devices and Microactuators, 1st Conference of the European Society for Biomaterials (ESB2021) together with 43rd Annual Congress of the Iberian Society of Biomechanics and Biomaterials (SIBB), September 5-9, 2021, Porto, Portugal

Ferreira D.A., Conde J.P., Ertl P., Oliveira C., Granja P.L., Fabrication of a human stomach-on-a-chip device displaying organ-like features, 25th Annual Meeting of the SPGH, November 18-19, 2021, Virtual Conference

PATENTS

Ferreira D.A., Ertl P., Oliveira C., Granja P.L., "Fabrication of microactuator and in-line degasser in organ-on-chips, devices and methods thereof", 2020, European Patent Application 20201000039961 (patent application submission).

CHAPTER I

GENERAL INTRODUCTION

1. The Digestive System

The digestive system is an open system whose main function is the uptake, processing of food and elimination of dietary byproducts. It can be subdivided into two main parts, the gastrointestinal tract and the accessory organs. The gastrointestinal (GI) tract encompasses the main functional organs of the digestive system, namely mouth, pharynx and esophagus, stomach, small and large intestine. These organs assume a main role in the digestive process, namely in the routing of food across its length and by mediating the mechanical and chemical dissociation of food and the absorption of nutritionally valuable molecules. The accessory organs coupled to the GI tract are the salivary glands, gallbladder, liver and pancreas. Despite not being part of the digestive tract, these organs play an important role in the digestion of foods.

The digestive system must breakdown complex macromolecules like proteins, fats and carbohydrates, that cannot be readily absorbed across the wall of the digestive tract, into smaller molecular subunits, such as amino-acids, glucose, fatty acids. The process of digestion is initiated at the mouth with chewing and partial chemical digestion by enzymes present in the saliva. The food is then transported by cyclical peristaltic motions to the stomach where churning and mixing of the food, ensures further mechanical dissociation of the food particles. The final breakdown of food is a chemical process known as hydrolysis, by which enzymes present in the stomach's lumen, breakdown the macromolecules into smaller molecules that can be absorbed by the body. The smaller molecules resulting from the chemical digestion, are transported across the cell membranes lining the small intestine into the blood and lymph capillaries.[1, 2]

1.1. The stomach

1.1.1. Anatomy of the stomach

The stomach is a J shaped intraperitoneal digestive organ that forms the first intra-abdominal part of the GI tract. The stomach connects to the esophagus, by the gastroesophageal junction, and on the opposite side, to the duodenum, the first portion of the small intestine, by the pyloric sphincter. Anatomically the stomach is sub-divided into 5 regions. The upper part is formed by the **cardia**, a small region surrounding the superior opening of the stomach and the **fundus**, a region of the stomach above and to the left of the cardia, that is usually filled with gas. The **body** represents the largest portion of the

stomach's anatomy and is the major region where food breakdown and mixing occurs. The lower portion of the stomach is sub-divided in two regions, the **pyloric antrum**, that communicates with the body, and the **pyloric canal** the region immediately before the duodenum.[1-3]

1.1.2. Histology of the stomach

The wall of the stomach has 4 layers. The 3 outermost layers are the **serosa**, a squamous epithelium of mesodermal origin and loose areolar connective tissue, the **muscularis externa** consisting of 3 layers of smooth muscle, an inner oblique layer, a middle circular layer and an outer longitudinal layer and the **submucosa**, consisting of a highly irrigated and innervated mesh of dense connective tissue.[4-6] The innermost layer is the **mucosa** which is further subdivided in 4 regions, the epithelium, the basement membrane, the lamina propria and the muscularis mucosae (Figure 1). The epithelial layer lines the surface of the stomach's lumen and is formed by a single-layered columnar epithelium consisting of surface mucus cells. Across the epithelium's surface and depending on the region, cardiac, fundic or pyloric mucosal glands can be found. The gastric glands are the bottom portion of tubular structures about 150 to 300 μm deep,[6] that protrude towards the lamina propria and muscularis mucosae. These tubular formations can be sub-divided in 3 regions, the pit, the isthmus and the gastric gland and are lined with several types of exocrine and endocrine gland cells, as well as undifferentiated adult stem cells. The latter can be found at the central region, the isthmus. As these cells differentiate into their specific lineage, they will travel upwards to the pit region forming new mucus neck cells with a turnover time of 3 to 5 days, while cells that form the gastric gland travel downward form the isthmus and have a turnover of approximately 1 year. Mucus neck cells populate the gastric pit region and, like surface mucus cells, secrete mucus, a gastro protective layer mainly constituted by glycoproteins, mucins and water, that under the acidic conditions of the stomach ensures a pH gradient that reaches a neutral pH at the region closest to the epithelium. The protective action of this layer is four-fold. It acts as a physical barrier between the gastric mucosa and the food inside the stomach's lumen, it protects the epithelium against enzymatic auto-digestion, assures the epithelium is kept at physiological pH in the acidic environment of the stomach lumen and acts as a first line of defense against food borne pathogens.[2, 7] Gastric glands contain a variety of exocrine and endocrine cells and their abundance varies with the type of gland. Chief cells secrete gastric lipase and pepsinogen, the inactive precursor of pepsin onto the lumen of the stomach while parietal cells produce intrinsic factor, which is essential for the absorption of Vitamin B12 as well as hydrochloric acid (HCl), that creates

an acidic environment responsible for converting pepsinogen to pepsin and starting the digestive process of dietary proteins. G cells are also present in the gastric gland, although restricted mainly to the pyloric antrum region. G cells play an enteroendocrine role, by producing and secreting gastrin directly into the circulatory system.[1, 2, 8] The epithelial lining of the mucosa is directly attached to the basement membrane. This anchoring substrate is a pliable sheet of extracellular matrix (ECM) composed mainly of laminins, collagen type IV, nidogens and proteoglycans.[9, 10] Further below in the mucosa structure, the lamina propria can be found. This is a loose connective tissue of complex composition, comprised mainly of fibrillar collagens and proteoglycans that also shares an expression of accessory molecules with the basement membrane, namely fibronectin and tenascin. The lamina propria provides structural support for the rich vasculature and lymphatics that permeate its mesh-like structure and is also a cell-rich environment, containing fibroblasts, macrophages, lymphocytes, plasma and mast cells. The large proportion of immune cells within the lamina propria, provides an effective second line defense against food borne pathogens that permeate the epithelial barrier.[11] Finally, the muscularis mucosae is formed by two layers of smooth muscle. a circular inner layer, which protrudes towards the lamina propria and an outer layer, arranged longitudinally.[1, 2, 5]

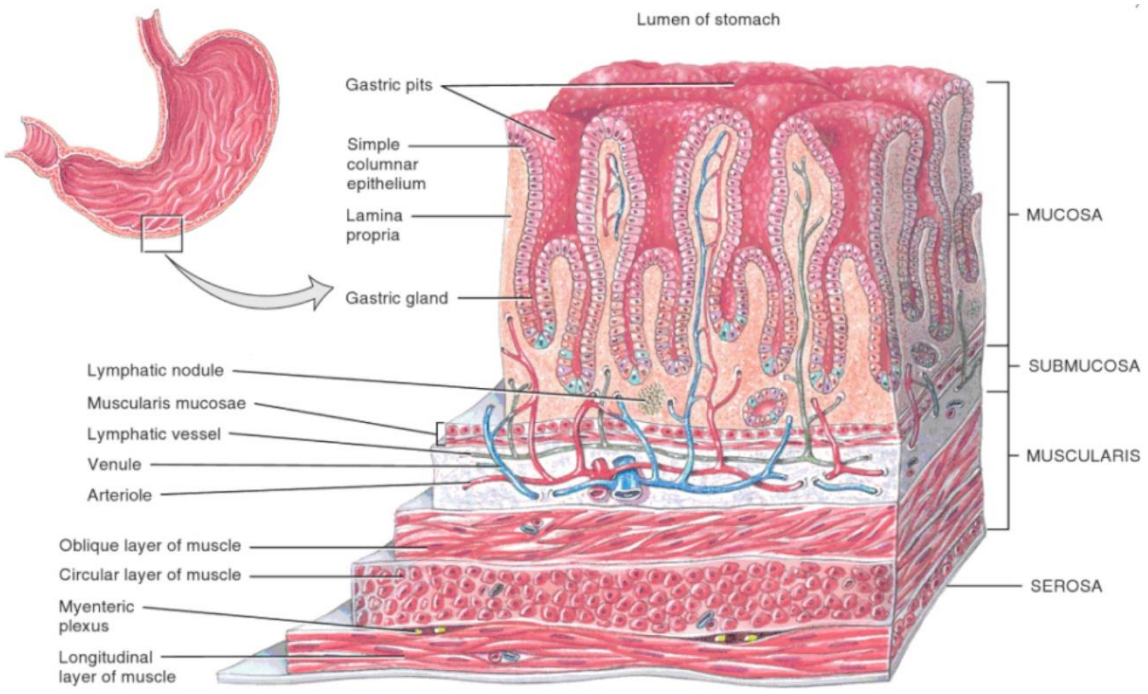

Figure 1. Schematic drawing depicting the 4 composite layers of the stomach wall. Adapted from [2]

1.2 The stomach in health and disease

The stomach plays a key function in human physiology, holding a central role in the digestive process. This organ mediates the initiation of the second phase of digestion and possesses unique immunology, biochemistry and microbiology. Every particle that is ingested, whether of nutritional value or not, must first negotiate the stomach. Unsurprisingly, the stomach is subjected to external insult on a regular basis, originating from food borne pathogens and chemicals. The particular physiology of the organ however, is well suited as a first line of defense, namely by the presence of a thick mucus layer and also by the highly acidic composition of the gastric digestive fluid.[12, 13]

When operating in a healthy state, the stomach function is under tight hormonal regulation that controls both motility and secretion. Motility is effected by way of mechanical distension and contraction, which ensures the churning motion that is required to breakdown dietary products and the ejection motion that permits the digested material to keep travelling along the GI tract. Secretion is regulated by the heterogeneous population of cells that compose the gastric epithelium. Surface mucus cells produce gastric mucus, while a variety of endocrine cells, present in the gastric gland produce and secrete to the stomach's lumen a complex acidic mixture known as gastric juice. Gastric juice is mainly composed by HCl, pepsin/pepsinogen, lipase and intrinsic factor and performs the double role of defense against pathogens and breakdown of macromolecules into micronutrients, in preparation for the absorption process across the intestinal epithelium.[12, 14] However, unlike the intestine, the absence of microvilosities in the stomach lining and the complex structure of the stomach mucosa, renders it virtually impermeable to absorption. Therefore, molecular absorption of nutrients across the gastric mucosa is of limited importance and mainly restricted to some lipid-soluble compounds, salts and water.[15, 16]

Given the preponderant role of the stomach in human physiology it is unsurprising that complications leading to impaired gastric function contribute to the development of gastric disease, that bear a high morbidity rate with concomitant loss in quality of life. This poses a serious economic burden to the health care system. Gastric disease can be classified in two different types, **functional**, where the function of the organ is compromised, but no apparent lesions can be detected, and **structural**, where impaired function is also accompanied with observable abnormalities. These conditions can in turn be of an acute or chronic nature. Despite this stratification, it is not uncommon to observe a tight interplay between differential diseased states, where one state eventually progresses to another in time. One such case can be observed in a chronic helicobacter pylori (*H. pylori*) infection, where gastric mucosa colonization with the bacteria can induce chronic gastritis, which in

turn can lead to the development of stomach adenocarcinoma.[12, 17] Gastric motility disorders are usually of a functional nature. Common examples are functional dyspepsia, gastroparesis and dumping syndrome.[18, 19] Structural disease includes but is not limited to, polyps, peptic ulceration and gastric cancer (GC). Although the scope of this publication is not an extensive review of gastric disease, it bears to pay additional attention to the latter, as gastric cancer remains one of the leading causes of cancer related death worldwide.

1.3. Gastric Cancer

1.3.1. Epidemiology of gastric cancer

Gastric cancer poses a serious global health and economic burden to the global healthcare system on account of the high morbidity and high mortality rate of the disease. Worldwide estimates for 2020, indicate that GC is the carcinoma with the 5th highest incidence rate, just below breast, lung, colorectal and prostate cancers, accounting for 1.089.103 new cases and the 4th leading cause of cancer related mortality, with 768.793 deaths reported.[20] Incidence and mortality, however, seem to be highly variable across regions, with the highest numbers reported in the Asian region, followed by Europe and Latin America and the Caribbean.[20]

1.3.2. Etiology of GC

GC onset is still an elusive and multifactorial process, and diagnosis of the disease is usually done at a later stage of disease progression, a factor that contributes to the high mortality rate of the disease. Several non-pathogenic environmental and behavioral factors have been described as contributing factors for the development of GC. Unsurprisingly, poor dietary habits have been linked with development of the disease, in particular a high consumption of red and processed meats and a high salt intake.[21, 22] Smoking has also been described as a potential risk factor for the development of cancer in the cardia region.[23] Despite the evidence, these studies are mainly of an epidemiological nature and while the link between environmental and behavioral factors is not disputed, molecular evidence of how these factors affect disease initiation and progression is still lacking. Currently, the undisputed risk factor for GC development, still remains the colonization of the stomach mucosa by H. pylori.[12, 17, 24] Colonization of the gastric mucosa *per se* does not seem to be the driving factor behind GC onset, as only a small proportion of H. pylori

infected individuals develop GC. Rather, the infection seems to be the facilitator in the development of an inflammatory process of the gastric mucosa, that can later-on progress towards chronic gastritis and eventually undergo malignant transformation towards GC.[25] It is not uncommon, by the time progression to a malignant phenotype occurs, that H. pylori infection may have been eradicated, or is no longer an active infection focus, suggesting that H. pylori is not the driver in the carcinogenesis process, but rather, has the capacity to influence the first stages of the disease. In fact it has been shown that H. pylori eradication before the onset of pre-malignant lesions can effectively decrease GC incidence.[26, 27] Despite the high numbers of new GC cases still reported, overall yearly progression has seen a decline on the incidence of GC, a fact that is likely linked to better therapeutic management of H. pylori infection and a steady decline in its prevalence across the world.[17, 28, 29]

Although the majority of GCs are of a sporadic nature (90%), approximately 10% of total reported GC cases, display familial clustering, with about 3% of the aforementioned cases having an inherited genetic susceptibility. This subtype of GC is referred as hereditary diffuse gastric cancer (HDGC).[30] HDGC is an autosomal dominant cancer syndrome largely caused by inactivating germline mutations in the E-cadherin gene (CDH1). Mutations in the α-catenin gene (CTNNA1) have also been reported in a small percentage of HDGC cases. [31-33] Despite considerable advances and specialization of endoscopic techniques for the surveillance of HDGC, prophylactic gastrectomy remains the best recommended course of action for *CDH1* pathogenic mutation carriers.[34]

1.3.3. GC classification and stratification

The vast majority of cancers of the stomach are adenocarcinomas (90-95%), i.e., cancers arising from the cells in the gastric gland of the stomach mucosa. Despite this seemingly unique identity, from a histopathological standpoint, GC is in fact a vastly heterogeneous disease. It is extremely challenging to categorize all the histopathological variations in one unified classification system. The task is further complicated by the fact that molecular and phenotypic variability not only encompasses intertumor heterogeneity, but also intratumor heterogeneity.[35] The large number of classification systems proposed up to date, is indeed a testament to the complex endeavor that is to classify GC into well-defined categorical groupings. The first classification attempt was proposed in 1956 by Laurén.[36] Despite its longevity, the Laurén classification is still widely accepted in clinical practice. Laurén classification proposed a stratification in 3 groups. The two main groups are **intestinal-type**

GC, that forms papillary or tubular structures where the lesion area resembles the intestinal mucosa and **diffuse-type GC**, a poorly differentiated cancer, characterized by poorly cohesive and infiltrating tumor cells that may display signet cell ring morphology. Diffuse-type GC has a more aggressive nature than intestinal-type GC, disseminating commonly through the peritoneum, contrary to the intestinal-type which disseminates through the blood stream to the liver. The diffuse-type of GC has therefore been identified as an independent poor prognostic factor.[36-38] Carcinomas not fitting the above-mentioned histopathological criteria are termed of **mixed** type. Many other classification systems have been attempted. In chronological order and succeeding the Laurén classification, Nakamura (1968) [39], Ming (1977) [40], Goseki (1992) [41], Carneiro (1995) [42], Solcia (2009) [43], Japanese Gastric Cancer Association (updated in 2011) [44], World Health Organization (WHO : updated in 2019) [37]. Although there is no unifying consensual system, the WHO classification, together with the Laurén system, are both widely accepted. The former classifies adenocarcinomas of the stomach as papillary and tubular adenocarcinomas (these relate with the intestinal-type as described by the Laurén classification), mucinous, poorly cohesive carcinoma (relating to the diffuse-type as described by the Laurén classification), mixed and a small percentage of rare histological variations. The WHO classification approach lacks the integration of prognostic, epidemiological or clinicopathological factors, however it does provide a unified histopathological approach to its classification, as it profiles the type of alterations according to histopathological patterns common across other segments of the GI tract.[35, 37]

1.3.4. Biomarkers for GC diagnosis and patient management

Accurate and early detection of GC is essential for effective diagnosis and management of patients. This task is somewhat complicated by the fact that during early stages, GC assumes a silent and mostly asymptomatic nature. Early symptomatology includes manifestations that are prevalent throughout normal life and indicative of minor health conditions such as gut pain, early satiety, weight loss, dysphagia, dyspepsia, vomiting and iron deficiency anaemia.[45] When manifesting isolated and sporadically, these symptoms are seldom indicative of a major complication, however, when two or more of these manifest simultaneously and in a persistent form over a period of several weeks, patients should be enrolled in a surveillance program and monitored by an expert. Current diagnostic methodology for GC includes endoscopic surveillance of the upper GI tract and complementary surgical biopsy of suspected lesion areas. However, unlike in Asian countries, where GC incidence has been historically higher, and a robust surveillance

program has been introduced with encouraging results [46], most western European countries with high GC incidence, have not implemented such a large-scale screening strategy. Diagnostic is often achieved at a later stage of disease progression, at a point where most patients have inoperable disease, or experience relapsed disease after curative surgery, a fact that severely limits the treatment options and contributes to lower survival rates in these countries. [47, 48] Despite notable advances in the understanding of the molecular processes that induce malignant transformation towards GC as well as better diagnosis and treatment regimens, a good methodology for early-stage GC detection is still severely lacking, particularly by the intrinsically invasive nature of the current standard endoscopic procedure. In search of alternative methods, biomarkers come up as an attractive solution for a perennial clinical problem. By definition, a biomarker is a biochemical or genetic molecular feature, found in tissues or body fluids, that can be measured accurately and reproducibly and is indicative of a normal or abnormal state of an organism or used to predict the likely outcome of such state.[49, 50] In a broader definition, biomarkers have also been classified as potential therapeutic targets. Although there is not a consensual unified definition for a biomarker, the many definitions provided in the literature, do overlap considerably.[49] Biomarkers could broadly be compartmentalized into four distinct sub-categories, **diagnostic**, **predictive**, **prognostic** and **therapeutic**. Those of **diagnostic** value, provide an interesting and largely non-invasive alternative to predict the possible development of a diseased state. **Predictive** biomarkers represent molecular signatures that can be used to assess the likely outcome or response to a given therapeutic approach. **Prognostic** biomarkers encompass all those markers that can aid in predicting the outcome of a disease. Finally **therapeutic** biomarkers are molecules that can be specifically targeted to aid in the resolution of a diseased state.[51, 52] Successfully identifying biomarkers that could consistently and accurately aid in the early detection of GC would allow a major breakthrough towards GC prevention and/or patient management. One of the major challenges to this goal, concerns the heterogeneous landscape of inter and intra-tumoral variability of the disease.

An increasing body of evidence has been mounting on potential biomarkers for GC management over the years. Despite the increasing number of likely candidates, only a few biomarkers are currently accepted and used as predictive, prognostic or therapeutic markers for GC in a clinical setting, namely, carcinoembryonic antigen (CAE), carbohydrate antigen 19-9 (CA 19-9), HER2 and VEGFA.[47, 53, 54] Serological markers, CAE and CA 19-9 however, are of limited use for diagnostic of GC, as significantly higher levels of these antigens were found in patients with advanced stages of the disease.[48] Likewise, HER2

and VEGFA, are well suited as prognostic factors and targets for therapeutic stratification but lack usefulness in early diagnostic.

1.3.4.1. Adhesion molecules as GC biomarkers

Adhesion molecules fit in the group of non-targetable prognostic markers of GC.[51] Despite not being good candidates as co-adjuvant targeting for conventional chemotherapy regimens, alterations in adhesion molecules have been extensively reported in GC and thus could be useful predictors for diagnostic and or patient stratification. Alterations in these molecules are generally associated with tumor dissemination and metastatic invasion, as epithelial to mesenchymal transition (EMT) and the inverse process, mesenchymal to epithelial transition (MET) are tightly balanced by the temporary loss of adhesion and subsequent regain of the function, to establish a metastatic niche.[55]

The quintessential adhesion molecule governing GC initiation and progression is E-cadherin. This is a calcium-dependent transmembrane glycoprotein, that mediates cell-cell adhesion, by partnering with α-catenin, β-catenin and p120 catenin at the cell surface in a complex protein assembly, termed adherens-junction.[56, 57] (Figure 2).

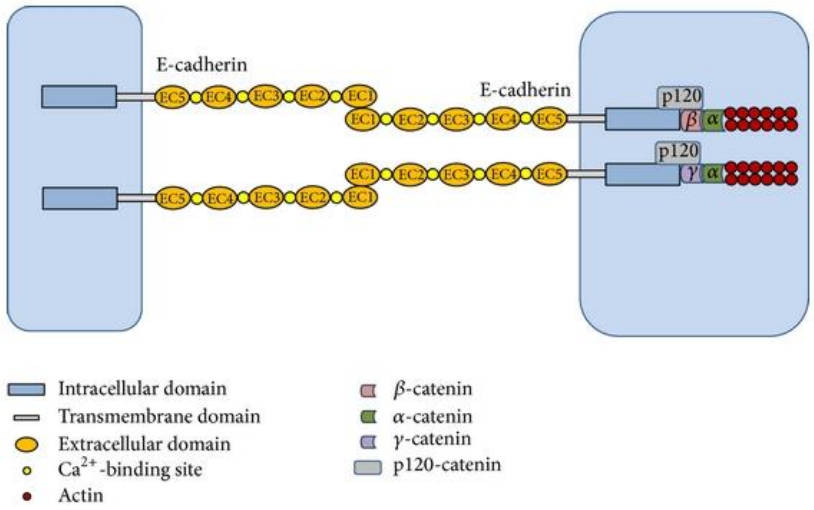

Figure 2. Adherens junction complex schematic, showing E-cadherin mediating strong cell-cell contact and adhesion, by indirectly linking the actin cytoskeleton of adjacent cells through its adherens-junction partners. Image adapted from [58]

As a major partner in the mediation of cell-cell adhesion, E-cadherin is classified as a tumor suppressor molecule. It is unsurprising thus, that loss of E-cadherin function is a key alteration in about 90% of GCs, and commonly associated with disease initiation and

progression as well as a poor prognosis factor.[51] Loss of E-cadherin function has been associated with both diffuse and intestinal types of GC, with similar prevalence of *CDH1* silencing alterations for both. Loss of function is also a well-established causative effect in HDGC, with about 45% of families reported, displaying germline mutations and deletions of E-cadherin (encoded by *CDH1*).[59] Aberrant E-cadherin expression has been associated with decreased tumor sensitivity to conventional GC therapies, suggesting a potential role for this molecule as a predictive biomarker of therapy response. [60-62] Concomitantly, loss of E-cadherin function has been shown to correlate with poorer prognosis and tumor stage and grade, regional lymph node involvement and depth of invasion, further strengthening the role of E-cadherin as a predictive biomarker for tumor invasion.[63] Interestingly, a recent report has shown that overexpression of CD44 isoforms containing exon V6 (CD44v6), another adhesion molecule, is observed in E-cadherin negative tumors in HDGC patients harboring *CDH1* germline mutations, suggesting that CD44v6 could be a potential biomarker for the detection of early invasive intramucosal carcinoma in these patients.[64]

1.3.4.2. CD44v6 as a potential marker of early-stage GC

The human CD44 gene (NG_008937) encodes a polymorphic group of proteins generated by alternative splicing. The coding sequence of the CD44 gene is divided into two distinct groups (Figure 3). One, comprises exons 1-5 and 16-20, that are spliced together to express the canonical form of the receptor, termed CD44 standard (CD44s). These exons form an N-terminal and a C-terminal structure that is mostly shared between all other isoforms. Exons 6-15 comprise the variable exons (corresponding respectively to v1-v10) that through a mechanism of alternative splicing can generate a myriad of different CD44 isoforms. Isoforms containing these variable exons, are termed CD44v.[65] Exon 6 (v1) containing isoforms are not expressed in humans, as the human coding sequence has a stop codon. Additional variation can be observed through an extensive post-translational modification

program, conveying very distinct patterns of glycosylation at the extracellular portion of the CD44 receptor.[66, 67]

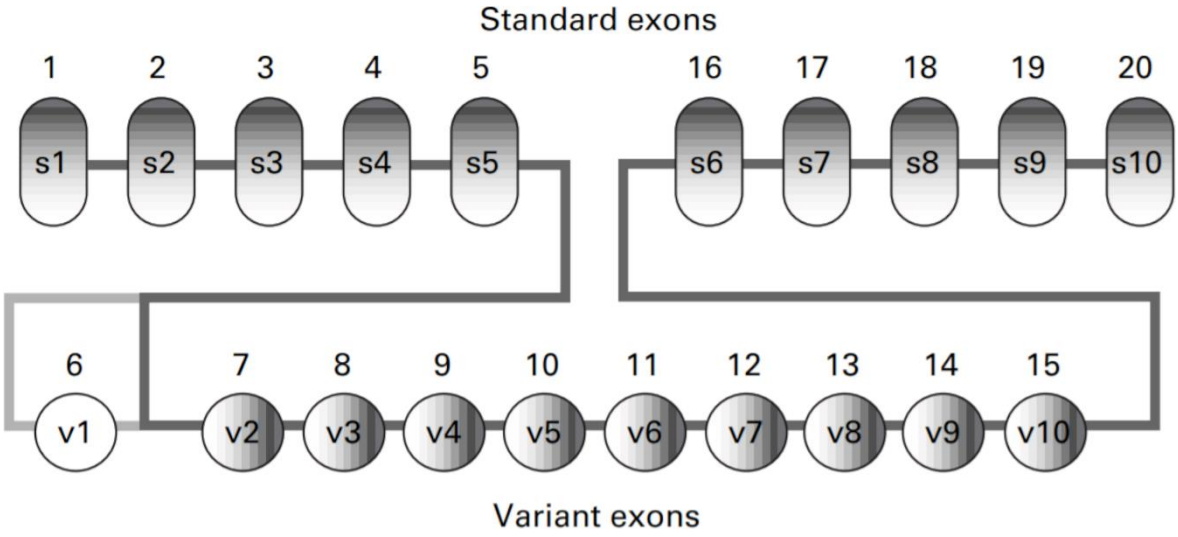

Figure 3. Schematic map of the CD44 gene, depicting the standard exons that constitute the canonical form of the CD44 receptor, and the variable exons (v1-v10), whose alternative splicing generates a number of different CD44 isoforms. Exon v1 (non-shaded) is not expressed in humans. Adapted from [65]

The canonical CD44s, is ubiquitously expressed at the cell surface of most vertebrates. This glycoprotein is an important cell adhesion and homing receptor, involved in a variety of cell-cell and cell-ECM interactions, cell migration and invasion and lymphocyte homing.[67-69] CD44 is the main receptor for hyaluronic acid, an integral component of the ECM, as well as the receptor for several other ECM molecules, such as osteopontin, laminin, fibronectin, collagen.[70-72] CD44 is also a co-receptor with a pivotal role in intracellular signaling, mediating key aspects of cellular behavior such as motility and cell survival.[68, 69, 73]

Unlike the canonical form, expression of CD44v variants is highly restricted to specific tissues. Evidence suggests that CD44v expression closely relates with tumor progression and the metastatic potential of some tumors.[74] Exclusive expression of some of these variants has been in fact reported in several tumors, such as GC,[64] pancreatic and breast,[75] lung,[76] colorectal,[77] among others. CD44v isoforms have also been pinpointed as putative cancer stem cell (CSC) markers and critical regulators of cancer stemness.[78, 79] One group of such variants, those containing exon 11 (CD44v6), has been widely studied and often associated with tumor progression. A first report was published in 1991 by Günthert U. and colleagues, where the authors demonstrated a causality between CD44v6

expression and metastatic potential in rat pancreatic and breast tumor cells, whereas non-metastasizing tumor cells and normal rat tissue lacked expression of CD44v6.[75] Subsequent reports have shown that inhibition of CD44v6 with antibodies or engineered peptides designed against the variable portion of exon v6, were able to limit tumor growth and limit angiogenesis and metastatic spread in pancreatic cells.[80, 81] These findings suggest a potential clinical interest in the role of CD44v6 as a putative therapeutic target in metastatic cancer. Concerning GC, Heider K. H. and colleagues reported in 1993, a work suggesting the use of CD44v6 variant expression as a potential diagnostic tool to differentiate between intestinal-type GC, positive for CD44v6 and diffuse-type GC, shown to be negative for CD44v6 expression.[82] Subsequently Cunha C. B. and colleagues studied in detail the splicing pattern of CD44v in pre-malignant lesions and gastric carcinomas and compared their expression to that found in normal gastric mucosa. An association was established between overexpression of CD44v6, with concomitant loss of CD44s, and disease progression, with the effect becoming more evident, as disease evolves from precursor lesions into advanced stage carcinoma. Furthermore, results also showed that CD44v6 overexpression was detected in E-Cadherin negative tumors from hereditary diffuse gastric cancer patients, harboring CDH1 mutations.[64] The same authors also reported a key role of the tumor microenvironment, particularly matrix stiffness as a driver of CD44v alternative splicing.[83] Recently, Kodama H. and colleagues demonstrated a relationship between the presence of CD44v6 positive CSCs at the invasive front with prognostic value in GC.[84] Taken together, these observations highlight the potential of CD44v6 as a putative biomarker for early stage diagnostic and stratification of GC, as well as a prognostic factor and a therapeutic molecular target. Part of the research effort has been devoted to the design and engineering of molecular probes that can specifically and accurately target CD44v6.[85-89] These molecular tools could play an essential role in future clinical applications as diagnostic tools or as targeting agents for therapeutic approaches. Our own efforts have led us to develop an *in vitro* isogenic cellular GC model, that expresses *de novo* CD44v6, in a work that will be further discussed later in this thesis.[90] The developed model was also used in a collaborative work to test the ability of poly(lactic-co-glycolic acid) (PLGA) based nanoparticles modified with polyethylene glycol (PEG) engrafted with a human Fab fragment that targets specifically human CD44v6. These nanoparticles were shown to selectively bind to cells expressing CD44v6 endogenously as well as exogenously, but not to non-expressing cells, or cells expressing exclusively the CD44s canonical form. [91, 92] The developed nanoparticles are a good candidate tool for early-stage *in vivo* diagnostic of GC, or as an anti-cancer targeting agent in CD44v6-positive stratified patients. Despite recent progress, there is currently no available technology being

translated into GC clinical practice, therefore this is an open field of investigation holding great promise.

2. Replicating in vitro the human physiology

Studying and understanding biological processes requires an intricate replication of the human body physiology. This is an extremely challenging endeavor and has been the subject of many research fields. From cellular biology to tissue engineering, the challenge is set to engineer increasingly complex biomimetic models. Despite the inherent difficulties of replicating the human physiology, particularly in an *in vitro* context, achieving biological mimicry is an essential aspect that must be tackled to ensure a greater robustness and relevance of generated data.

The longest standing approach to study human physiology, is perhaps the use of *in vivo* and *ex vivo* animal models, although the way animal models are used in the laboratory today, has dramatically evolved from the initial approach, which was merely observational and comparative with regards to human physiology . The apex of animal models' evolution is perhaps the establishment of the "humanized" model, *i.e.*, an animal model that closely mimics a particular aspect of the human normal or diseased physiology.[93] Despite their relevance, particularly in the early stages of drug development as surrogate models for drug toxicity, one undisputed fact still remains. Simply put, animal models have a limited ability to mimic the intricately complex processes of human physiology and disease initiation and progression. This fact may indeed offer an explanation as to why the translation success rate from animal models to clinical trials is so low, as the safety and efficacy data logged in animal models, fails to translate to a human clinical setting.[93-96] In fact, in a review by Hackam D. G. and Redelmeier D. A., the authors reported that only about one third of highly cited animal research reaches human clinical trials.[97] Furthermore, of those that reach human trials, only 8% successfully pass phase I clinical trials.[98] Concomitantly, there is an ever increasing pressure, due to ethical reasons, to find alternatives to animal experimentation, as evidenced by the recent EU ban (2013) on all animal experimentation for cosmetics purposes and a net worth investment of 238 million euros for the research of alternative models to animal experimentation.

Human derived *in vitro* models, despite their obvious lack of systemic output, are a clear alternative to animal modelling. The number of current in vitro systems is staggering and increasing in number and complexity every year. From the simple 2D cell culture model up to microfluidic organ-on-a-chip platforms[99, 100] and bioprinted cellular scaffolds[101-103], the

investment of resources in the development of new biological models that replicate human physiology is on the rise (Figure 4).

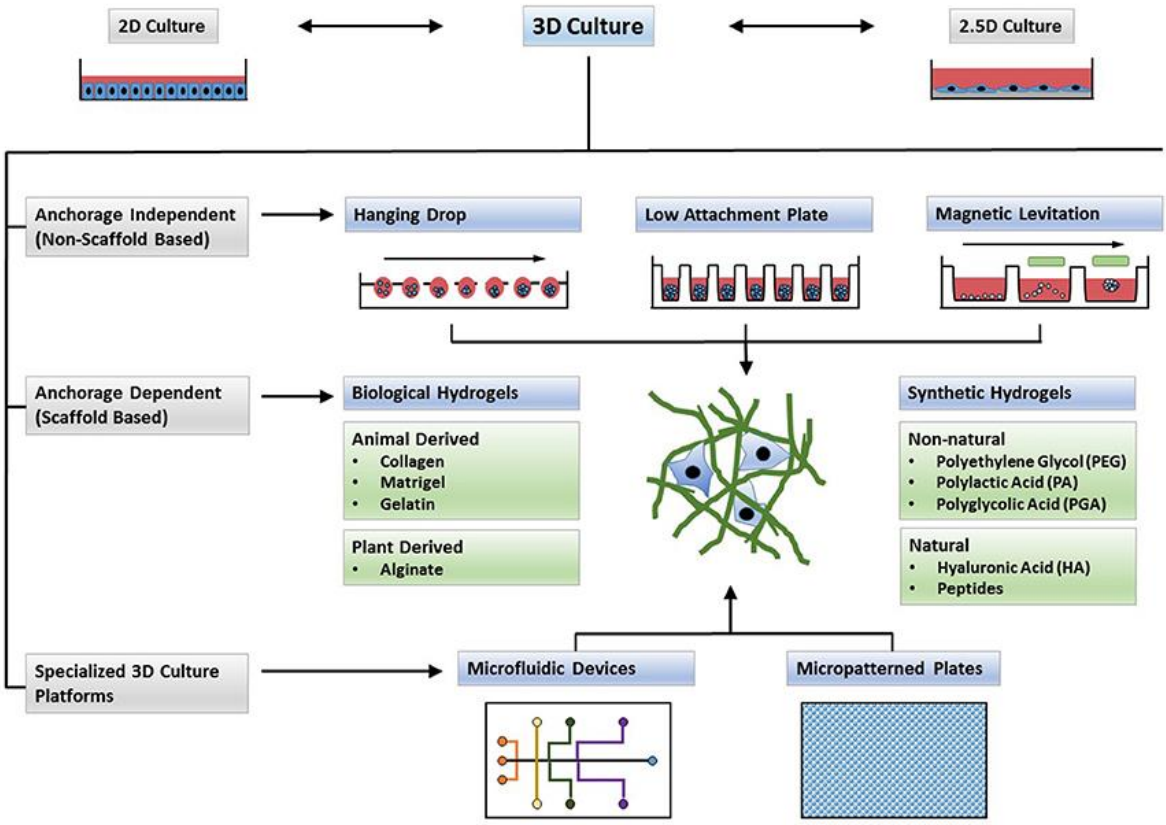

Figure 4. Types of *in vitro* models to study human physiology. 2D and 2,5D cultures are the simpler iteration of in vitro models, where cells are grown either on top of a flat surface, or over a thick hydrogel mesh. 3D culture systems, offer a much more complex system, where cells are grown in a 3D environment as aggregated biological structures usually in direct contact with ECM molecules. Microfluidic platforms offer an additional layer of complexity in which cells are not only under the constraints of a 3D architecture, but they are also under physiological dynamic conditions. .Adapted from [104]

At its fundamental core, 2D cell culture models are the simplest iteration of *in vitro* systems. Notwithstanding their apparently simple nature, 2D models, are undoubtedly the most common *in vitro* systems in use, across many life-sciences labs. The field of oncobiology in particular, has benefited greatly from these systems, as there are currently hundreds of well-established and well characterized human cancer cell lines.[105, 106] 2D culture models usually represent monoclonal populations cultivated as monolayers over a flat surface, usually a tissue-culture treated plastic, such as polystyrene or glass. A further evolution of 2D models, commonly referred in the literature as 2,5D models, is used to refer to systems where the cellular monolayer is cultivated over a thick biologically derived coating, usually an analogue of the native ECM.[104] 2D and 2,5D models present several advantages over

the *in vivo* alternative. Setup investment and maintenance cost is relatively low, their immortalized and monoclonal nature, allows unprecedented scalability and reproducibility, and extracting molecular and imaging data from these models is exceedingly simple. Importantly, there's a substantial body of literature accumulated over the years, that can be sourced for comparative purposes.[107, 108] There are however obvious gaps that 2D cell culture models cannot fill in. They are poor alternatives to replicating the complexity of the environment of a living organism and cells are usually cultivated in a semi-closed vessel, where nutrients from cell culture media are gradually depleted and cellular waste products and dead cells accumulate over time. Also, although many 2D culture models are of human origin, their lack of cellular heterogeneity, simpler microarchitecture, and lack of biomimetic ECM, means these systems also lack predictive power towards understanding human physiology, as heterotypic cell-cell and cell-ECM interactions are not recapitulated.[109]

Further up in complexity, are the 3D cell culture models. This broad designation encompasses in fact multiple methods and/or technologies that alone or combined in a complex system, aim to represent with a higher degree of fidelity, the architecture of the tissue or organ they mimic. (Figure 4).[110] In the native environment, cells interact with neighboring cells and ECM through mechanical and biochemical cues, as well as with cells that penetrate the ECM, via paracrine signaling. The intricate 3D communication network is the driving force behind tissue homeostasis and specificity, governing important cellular aspects such as proliferation, migration and apoptosis.[109, 111] Thus 3D models replicate to a higher extent the complex physiological cellular context that modulates the organizing principles of the living tissue.[112] Compared to 2D models where the lack of cell-cell and cell-ECM interactions suggests that critical signaling pathways may be lost, it is clear that 3D models bear a far more significant predictive value, and thus are a true alternative to bridge the gap between the 2D models and the animal models. 3D culture models can be divided broadly in 3 distinct categories. **Non-scaffold-based**, **scaffold-based** and **specialized 3D culture platforms** (Figure 4). **Non-scaffold-based** models are anchorage independent, i.e., systems where cells are cultured in a 3D environment but are not attached to an ECM analogue. Cells grown with non-scaffold-based methods, form spherical aggregates termed tissue spheroids or organoids.[113, 114] Notable examples of this methodology, are the hanging drop technique and the low adhesion plate. One of the main strengths of non-scaffold-based approaches is their scalability, as the techniques can be readily performed in a multi-well plate format. **Scaffold-based** models provide physical anchorage support, through a scaffold structure that can be of a biological or synthetic nature. Scaffold-based 3D cell cultures are cultivated on top or within an ECM analogue mesh, thus sensing a full array of biochemical and biomechanical cues that are not

replicated in non-scaffold-based approaches.[104] Notably, despite their seemingly unattractive appeal due to their non-human origin, synthetic and plant/algae-derived ECM analogues, present an interesting and versatile alternative to mammalian based ECM analogues. Their lack of endogenous anchoring molecules and human-derived extracellular molecules that are readily recognized by mammalian cells, means these systems can be used as a blank slate and tailored at will, to mimic specific tissue or tumor microenvironments.[115-117] One major caveat of scaffold-based platforms, particularly for industrial pre-clinical applications in cytotoxicity and pharmacokinetics testing for new drug development, is the laborious nature of the process. However, recent developments have seen the adaptation of additive manufacturing technology to automate the ECM analogue fabrication procedure by using 3D printing technology. Bioprinting or direct cell printing uses hardware and software based on conventional printing technology, such as inkjet-based printing,[118] extrusion-based deposition,[119] and laser-based writing.[102] Bioprinting allows unprecedented precision over the spatial placement of the cellular and the ECM components and does so in an automated fashion, thus bringing scaffold-based culture models one step closer to upscaled production and industrial application.[101, 119, 120] Finally **specialized 3D culture platforms** includes a collection of technologies that has gained traction in the past few years, aided in a large extent by the most current advances in microfabrication technology (Figure 4). One such example is surface patterning, a technology that is becoming a very relevant tool in biomedical research. Surface patterning is a technology used to modify the surface of inert biomaterials in a structured pattern. [121] Microcontact printing using soft lithography fabricated stencils and bioprinting are two technologies that permit the transference of biomolecules onto a surface in a prescribed pattern without degradation of the printed biomolecules. An interesting feature of the technology is the possibility of creating growth exclusion zones, by creating a patterned combination of cell-adhesive molecules and cell-repellent molecules and/or cell repellent microstructures.[122] Surface patterning can also be achieved on flexible silicone surfaces, presenting interesting applications for particular biomedical fields, such as skeletal or cardiac muscle tissue engineering. Undoubtedly the most impacting feature of this technology, is the automatized nature of the process, which can undoubtedly enable the development of high-throughput systems that could have a significant impact in drug screening and diagnostic testing. Microfluidic devices are another type of 3D cell culture platform that currently enjoy a lot of attention. This technology can be designed to operate as 3D cell culture devices but is not restricted to this application. Accordingly, the seminal work by Huh D. and colleagues, reported the development of a microfluidic platform capable of replicating organ-level function in an in *vitro* context.[123] These platforms have proven to

be a valuable asset in replicating the tissue microenvironment and thus it is important to discuss them in further detail.

2.1. Microfluidics

Microfluidics is the science of handling and controlling minute quantities of liquid, in the range of micro- or nanoliters within micro-sized structures that form a network of channels and chambers designed for fluid routing or as cell culture/reaction chambers. Microfluidics is a rapidly expanding, well established field of research, with a little over 40 years of existence.[124-126] This field of research, borrowed extensively from the concepts developed by the microelectronics and optoelectronics industry. Originally applied to the production of computer chips and micro/nano-sized sensors, this technology, has been gradually adapted to the fabrication of micro sized devices capable of reproducing key laboratory reactions/processes at a nano- or micro-scale, giving rise to the lab-on-a-chip concept.[124] Since its inception this technology has slowly permeated many aspects of biological assays. Devices designed for cell sorting, DNA sequencing, electrophoresis, 3D cell culture, are just a few examples of what can be achieved in a smaller scale.[127, 128] Despite being several decades in the making, microfluidics achieved central stage with the seminal works of Whitesides and colleagues, on rapid prototyping and soft lithography for the fabrication of microfluidic devices.[129, 130]

To understand how microfabrication techniques such as rapid prototyping came to play a relevant role in the field of life sciences, it is important to understand the development of soft lithography. Soft lithography is in fact, a collection of microfabrication techniques based on the use of elastomeric materials as stamps, to print, mold and micropattern suitable surfaces.[131, 132] The name thus originates from the soft nature of the materials used, usually organic materials and flexible polymers such as polydimethylsiloxane (PDMS). Soft lithography introduced the use of highly moldable materials that are easy to manipulate and revolutionized microfabrication techniques, by overcoming the limitations of conventional photolithography as the preferred method to reproduce surfaces. Fabrication of surfaces with customized topography, patterning of molecules relevant for biological applications or the ability to fabricate the complex network channels suitable for microfluidic applications, became a far easier endeavor after the introduction of soft lithography.[131] A second major breakthrough in the field, came just a few years into the development of soft lithography, from the realization that PDMS, the silicone elastomer that is today one of the most commonly used in microfluidic applications, could be used not only as a component for mold

and stamp production, but also as the primary material in the production of microfluidic devices, capable of sustaining normal cellular growth.[133-135] This observation would soon show the value of elastomeric microfluidic devices as bioreactors and cell culture platforms. PDMS is a cheap alternative for the microfabrication process, is biocompatible and optically transparent, making it ideal for direct morphological inspection of cells by microscopy. Finally, PDMS is also permeable to gases, a crucial aspect, as cells in culture are dependent on oxygen supply and microfluidic systems are generally self-contained closed systems.[136]

Microfluidic devices are proving to be a workhorse for current day scientists. Their small size makes them ideal to experimental scale-up and the fine control achievable over the experimental conditions, allows a more physiologically relevant spatial and kinetic control over the cell microenvironment, a factor for which macroscopic cell culture platforms offer no practical solution.[137-140]

2.1.1. Microfluidic devices as state-of-the art cell culture platforms

In vitro 2D cell culture requires a balance between functionality and the ability to maintain the cells alive in an artificial environment. Although an affordable and readily available method, it lacks in many aspects. Cells are generally cultured as a monolayer over plastic or glass surfaces and are, as a rule, subjected to static culture conditions, a reality far different from the dynamic and three-dimensional environment the cells experience *in vivo*.[109, 141] The limitations imposed by conventional *in vitro* cell culture methods, have spurred the interest for better and more physiologically relevant models. A great deal of effort has been spent in the development and research of culture models that better replicate the physiological environment, by providing chemical and physical cues to the cell culture on a 3D level.[83, 142-144] Unsurprisingly, the dynamic nature of microfluidic systems and the ability to control surface topography (both physically and chemically) during microfabrication, combined with cell culture techniques, paved the way for the creation of devices enabling precise control over cell function and shape in a dynamic 2D or 3D environment. Moreover, the microenvironment in which these cells are cultured, can more easily replicate the organ-specific mechanical and chemical gradient cues that these cells are subjected to in the native organ, as the small volumes and culture surface areas within these devices better replicate the physiological niches of the *in vivo* environment. From cell encapsulation[145] and cell trapping,[146] to gradient generators[147] or the study of heterotypic

cell to cell communication,[148] the possibilities are endless and only limited by current fabrication capabilities.

2.1.2. Organs-on-a-chip

Modelling human physiology *in vitro* is a formidable challenge. Both 2D cell culture models and experimental animal models lack predictive power, the first for its lack of biological functionality and the latter due to fundamental differences between animal and human physiology. Organ-on-a-chip are microfluidic platforms that aim to merge the best features of both, by combining the human origin of cell culture models and a tissue-specific 3D environment designed to recapitulate biochemical and physical cues of the cellular and extracellular microenvironment typical of the native organ. Despite the obvious name, organs-on-a-chip do not intend to reproduce a whole living organ, rather they aim to replicate a functional sub-unit of the organ they emulate (Figure 5). Therefore, design of organs-on-a-chip must be directed by the principle of recreating in a simplified manner the realistic model of the organ they emulate, paired with the functionality matching the intended application. Each organ-on-a-chip must replicate the particular biochemical and biomechanical cues characteristic of the emulated organ. Whether it's the 3D tissue architecture, fluid shear stress, active stretching of the culture substrate or any other type of biomimetic cue, the crucial aspects of the tissue being recreated, must be incorporated in order to elicit a tissue-level response from the system.

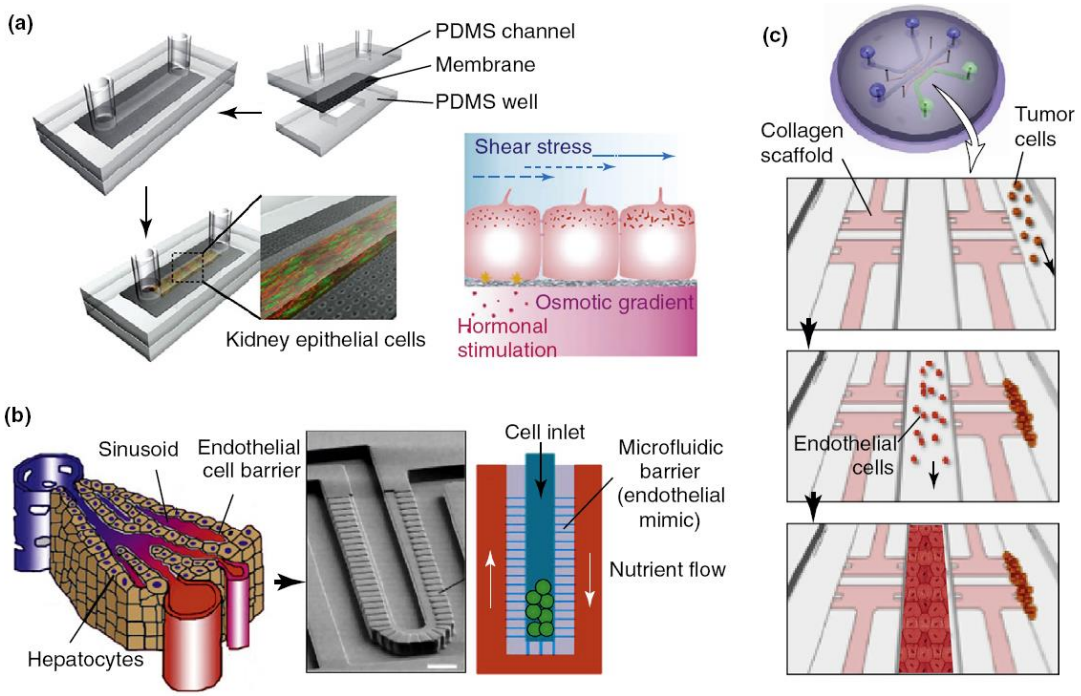

Figure 5. - Organ-on-chip technology. Devices developed to emulate functional units of the kidney (a), liver (b) and tumor microenvironment (c). While particular biochips emulate specific organ function, some are developed to study heterotypic cell to cell interaction, such as the biochip depicted on panel (c), a model to study the communication between endothelial and tumoral cells. Adapted from [99]

Microfabrication techniques offer a versatile and vast toolbox for the design of organ-on-a-chip platforms. Tissue-level function can be achieved in a cheap and effective way, even if fabrication of said devices, might be technically challenging. Epithelial barriers or epithelial-endothelial interfaces can be emulated by culturing cells on top of perforated membranes.[123, 149, 150] Biomechanical cues can be elicited by fabricating microactuators capable of stretching the cell culture substrate,[151-153] or micro-pillared structures that can apply cellular compression.[154] Electrical[155] and hydrodynamic[156] forces can also be harnessed to replicate *in vivo* like stimuli and multicellular patterns can be designed to study heterotypic cell-cell interaction.[157, 158] The possibility of controlling with a great degree of precision the pattern, intensity and duration of biomechanical cues within the devices, is perhaps the most distinctive feature of organ-on-a-chip devices and an invaluable contribution to elucidate how mechanotransduction influences cellular response at the tissue-level.

It is the deeper understanding of how cells behave in a tissue specific context that make these devices such valuable tools. They are not just overly complex 3D culture systems. They replicate the dynamic mechanical properties of the organ as well as its biological and biochemical function.[159]

3. Engineering the 3D microenvironment of the stomach mucosa

The human stomach is exposed daily to internal and external insults. Given its importance in human physiology, it is of no surprise that complications leading towards stomach disease often pose serious life-threatening consequences, and treatment is generally associated with high morbidity. Finding suitable models to study normal stomach function as well as disease has been a long-standing goal that has seen considerable efforts undertaken in the past decades, bring to fruition a myriad of models to study gastric physiology. Gastric models can be distinguished in two main broad categories, **acellular systems** and **cellular systems**.

Acellular systems offer some advantages over cellular based systems, as they are easily tunable and are prime candidates for point-of-care applications as they do not need concern over maintaining a running cell culture under physiological conditions. However, as they lack any of the biological components that make up the architecture of the living organ, their scope is limited towards the understanding of the fundamental processes that underlie the stomach's biology, and the deleterious events that lead to its disease. Rather, they are more suitable to tackle the biochemical and biomechanical aspects of digestion, namely in understanding the bioacessibility and interactions of nutrients, drugs and other dietary compounds.[160, 161] Acellular models are further subdivided in two groups, static and dynamic models. Static models are far more simple and cheaper iterations of the technology. They usually consist of a single reaction chamber and lack any physiological relevant biomechanical cues so they do not fully recapitulate many of the physiological aspects of digestion. Dynamic models are far more complex, albeit more expensive and more difficult to operate. They introduce dynamic cues in the system, such as simulated peristalsis and gastric ejection and allow injection of enzymes, drugs or other relevant biochemical cues in a time-dependent manner and pH monitoring and regulation.[161] Interestingly, microfluidic technology has been slowly permeating the field and many microfluidic devices are now available to tackle aspects of the digestive process in the GI tract.[162-164]

Cellular systems, incorporate not only biochemical and biomechanical aspects, but also a cellular component and are therefore well suited to study tissue-level response in an *in vitro* context. There are numerous cellular systems of the gastric microenvironment, ranging from 2D cell culture models to complex multicellular biomimetic systems.

Immortalized cell lines are ubiquitous and the staple of many research fields. However, gastric cell lines originating from normal healthy tissue have proven to be elusive and very difficult to isolate and immortalize. So far, two normal gastric cell lines have been reported, HFE-145[165] and GES-1[166], although both are unavailable commercially. The latter in particular, has not been made widely available and reports on the cell line are sparse, raising some concerns over its viability as a sustainable immortalized cell line model. Interestingly, a normal gastric fibroblastic cell line, NST-20 has also been reported.[115] Such a model of a stromal component derived from normal gastric tissue, could be an invaluable resource for future biomimetic multicellular models of the gastric mucosa, allowing the complex architecture of the stomach to be expanded from epithelial models, to models replicating the inner strata of the gastric mucosa. Immortalized cell lines representing the normal gastric epithelium, will definitely be a valuable asset for future research, as they mimic to a greater extent the physiology of the native tissue.

Gastric cancer cell lines, however, are an abundant resource and have been extensively characterized and explored.[167] There are currently dozens of reported human adenocarcinoma cell lines. Some of the most commonly reported are AGS,[168] Kato III,[169, 170] IPA220 (GP220),[171] GP202,[171] MKN45,[169] MKN74[169] and NCI-N87[170]. Despite their ancestry, some human gastric carcinoma cell lines share/retain some characteristics of the native normal tissue. Notably, NCI-N87 and MKN 74 have been suggested as good models to study gastric physiology *in vitro*, as they retain several key aspects of their epithelial ancestry, that are commonly lost in other human adenocarcinoma cell lines.[115, 167, 172, 173] Namely they exhibit correct expression and localization of E-cadherin and associated adherens junctions partners, α-catenin, β-catenin and p120 catenin, as well as tight junction protein ZO-1, occludin and respective tight junction partners. These two protein complexes are present at the basolateral surface of epithelial gastric cells and play a crucial role in cell-cell adhesion and paracellular trafficking respectively and are the key players in the formation of a tightly knit epithelial barrier exhibiting selective permeability, characteristic of the normal gastric epithelium. Notwithstanding their origin, these cell lines proved to be a valuable tool to study epithelial function and selective gastric permeability.[115, 174, 175] Immortalized carcinoma cell lines are commonly used as surrogate systems of normal human physiology not only to mimic the gastric environment[115] but also in many other in vitro human tissue models, such as lung,[123] intestine,[149], liver[176], among others.

Despite their usefulness, cell culture models lack many details of native tissue biology, such as, connective stromal tissue, vasculature and tissue microarchitecture. It is at this crossroads that the field of tissue engineering has offered a significant contribution. Tissue engineering is an interdisciplinary field that transposes engineering concepts to the

biological sciences, as the basis for the “bio-fabrication” of complex heterotypic structures that may replace or mimic the function of living organs. Although the term has been coined in the early 1980s and interspersed loosely in several publications, it was not until the seminal publication by Joseph Vacanti and Robert Langer in 1993, that tissue engineering became a discipline on its own.[177] Currently tissue engineering holds great promise in the areas of regenerative medicine and transplantation. With the advent of stem cell technology, tissue engineering is paving the way for the fabrication of miniaturized, *in vitro* artificial organs that replicate the function and metabolism of their living counterparts. The tissue engineering approach towards recreating a biomimetic gastric analogue has focused mainly on clinical applications towards regenerative medicine. A considerable effort has been expended in engineering an *in vivo* model for artificial organ transplantation, for those cases where total gastrectomy is the only viable option. The team of Joseph Vacanti has isolated heterotypic spheroid aggregates, termed organoid units (OU) from the stomach epithelium of 4-day-old Lewis rats. These multicellular bodies contained a core of mesenchymal cells surrounded by a polarized stomach epithelium. When seeded into a biocompatible scaffold and re-implanted into a syngeneic rat model or a pre-clinical animal model (Yorkshire swine), these organoids fused *in vivo* to form a biomimetic artificial stomach.[178-182] The series of works produced by the Vacanti team highlight the importance of reconstituting more than just the superficial epithelial layer of the stomach, to engineer a biomimetic gastric analogue that is capable of replicating native architecture and function. The same principles of tissue engineering are now being transposed to the field of cellular and molecular biology to generate meaningful *in vitro* 3D biomimetic analogues of the gastric mucosa. Recently, Lourenço B. N. and colleagues described a transwell-based *in vitro* system that goes beyond the superficial layer of the stomach epithelium, by reconstituting an inner stratum of the gastric mucosa. In this work the authors engineered a multilayered stomach analogue with MKN74 cells recreating the epithelial layer and a fibroblast-laden ECM that recapitulates both the cellular and dimensionality of the stomach’s lamina propria. Interestingly the authors showed that the model was able to reproduce key physiological features of the mucosa of the stomach and the fibroblastic population within the system was able to modulate the system’s permeability to FITC-dextran and nanoparticles.[115]

The power to harness *in vitro,* the culture and differentiation of primary cells and induced pluripotent stem cells (iPSCs) has catapulted spheroid- and organoid-based systems to the forefront of tissue-modelling research. For many years the goal of generating viable gastric primary cultures remained elusive, as these cells proved to be extremely difficult to isolate and maintain in a long-term culture, with only a few works reporting the successful establishment of *in vitro* primary gastric cells.[183-185] Concomitantly the lack of any relevant

gastric stem cell markers meant that recreating the complex heterotypic cellular environment of the gastric epithelium was very difficult and possibly resulting in models displaying limited cellular functionality. A cornerstone publication was reported in 2009 by the team of Hans Clevers, that helped shape the future of gastric organoid technology. In this publication, Barker and colleagues identified the Wnt target gene, Lgr5 as a gastric stem cell marker. Lineage tracing proved that Lrg5+ cells were multipotent, self-renewing stem cells involved in the long-term renewal of the gastric epithelium. Furthermore, the authors reported the establishment of long-lived mouse organoids resembling the mature pyloric epithelium.[186] A few years later, Katano and colleagues also reported a simpler method to isolate and expand gastric spheroids by culturing and expanding a gastric stem cell niche. The engineered gastrospheres were cultured in an air-liquid interface, within a collagen matrix and displayed a columnar epithelium morphology and a significant myofibroblast population on the outer lining, thus mimicking many aspects of the gastric mucosa architecture. The authors demonstrated that the gastrospheres exhibited a fully differentiated gastric surface mucous cell phenotype, with formation of microvilli, junctional complexes and glycogen secretory granules.[187] Notwithstanding the remarkable achievements of the previous works, a human derived model was still lacking from the primary gastric model repertoire. Recently, Boccellato and colleagues reported such a system.[188] The authors described the establishment of human-derived polarized epithelial monolayers resulting from antrum-derived gastric glands from surgery specimens. grown on a transient air-liquid interface, giving rise to “mucosoid cultures”. Although the system represents a purely epithelial population, without any other elements of the gastric mucosa, the model was able to reproduce the features of normal human gastric epithelium and thus can be a valuable tool to study human gastric physiology.

Tissue engineering principles have pushed forward the establishment of many biomimetic gastric models that are helping to elucidate the complex cross-talk between the molecular and cellular partners of the gastric mucosa. However, one important factor is still missing from all aforementioned models. They fail to recapitulate the dynamic nature of the gastric microenvironment. In vivo, cells are continually sensing its surroundings and that is particularly relevant for organs that are exposed to mechanical strain, such as in the stomach. In this context, organ-on-a-chip approaches can provide an additional layer of complexity. These devices excel not only as 3D cell culture vessels, but also at enabling the application of physiologically relevant biomechanical stimuli. A report on a proof of principle stomach-on-a-chip device incorporating luminal flow and peristaltic like motion has been described by Lee and colleagues.[189] The work describes the encapsulation and long-term culture of human derived organoids within a microfluidic chamber that is capable of

imparting cyclical stretching, thus mimicking the dynamics of the native stomach. Despite only reproducing the epithelial portion of the gastric mucosa, this model is a significant step towards elucidating the role of biomechanical cues on gastric cellular physiology.

There are presently a significant number of reported models emulating the stomach epithelium. The latest developments in 3D cell culture analogues present models that are closer than ever to a truly biomimetic gastric microenvironment. Standardization and scalability are now required for these systems to be the standard platforms for cytotoxicity and pharmacokinetics for new drug development. The successful translation of these platforms to the market, could possibly decrease the heavy dependence of the pharmaceutical industry on animal models.

References

[1] M. H. Ross,W. Pawlina, Histology : a text and atlas : with correlated cell and molecular biology, Wolters Kluwer, Philadelphia, **2020.**

[2] G. J. Tortora,B. Derrickson, Principles of anatomy & physiology, Wiley, Hoboken, NJ, **2012.**

[3] B. Sarmento, Concepts and Models for Drug Permeability Studies: Cell and Tissue based In vitro Culture Models, Elsevier Inc., **2015.**

[4] K. W., Cytology, Histology, and Microscopic Anatomy, Thieme, **2003.**

[5] A. L. Mescher, Junqueira's Basic Histology - Text & Atlas, McGraw-Hill Medical, **2016.**

[6] B. T. C. Sorenson R. L., Atlas of Human Histology: A Guide to Microscopic Structure of Cells, Tissues and Organs, University of Minnesota, **2008.**

[7] M. Phillipson, M. E. Johansson, J. Henriksnas, J. Petersson, S. J. Gendler, S. Sandler, A. E. Persson, G. C. Hansson,L. Holm, Am. J. Physiol. Gastrointest. Liver Physiol. **2008**, 295, G806.

[8] A. S. B. Pakurar, J. W., Digital Histology: An interactive CD atlas with Review text., Wiley, **2004.**

[9] A. Pozzi, P. D. Yurchenco,R. V. Iozzo, Matrix Biol. **2017**, 57-58, 1.

[10] R. Sekiguchi,K. M. Yamada, Curr. Top. Dev. Biol. **2018**, 130, 143.

[11] L. R. Johnson, Encyclopedia of gastroenterology, Academic Press, Amsterdam ; Boston, **2004.**

[12] R. H. Hunt, M. Camilleri, S. E. Crowe, E. M. El-Omar, J. G. Fox, E. J. Kuipers, P. Malfertheiner, K. E. McColl, D. M. Pritchard, M. Rugge, A. Sonnenberg, K. Sugano,J. Tack, Gut **2015**, 64, 1650.

[13] S. A. Sarker,K. Gyr, Gut **1992**, 33, 987.

[14] T. C. Martinsen, R. Fossmark,H. L. Waldum, Int. J. Mol. Sci. **2019**, 20,

[15] P. J. Kumar,M. L. Clark, Kumar & Clark's clinical medicine, Saunders Elsevier, Edinburgh, **2009.**

[16] H. J. E., Guyton and Hall textbook of medical physiology, Elsevier, **2011.**

[17] R. E. Sexton, M. N. Al Hallak, M. Diab,A. S. Azmi, Cancer Metastasis Rev. **2020**, 39, 1179.

[18] B. E. Lacy,K. Weiser, Dig. Dis. **2006**, 24, 228.

[19] W. E. Whitehead

[20] H. Sung, J. Ferlay, R. L. Siegel, M. Laversanne, I. Soerjomataram, A. Jemal,F. Bray, CA Cancer J. Clin. **2021**, 71, 209.

[21] A. Ferro, V. Rosato, M. Rota, A. R. Costa, S. Morais, C. Pelucchi, K. C. Johnson, J. Hu, D. Palli, M. Ferraroni, Z. F. Zhang, R. Bonzi, G. P. Yu, B. Peleteiro, L. Lopez-Carrillo, S. Tsugane, G. S. Hamada, A. Hidaka, D. Zaridze, D. Maximovitch, J. Vioque, E. M. Navarrete-Munoz, N. Aragones, V. Martin, R. U. Hernandez-Ramirez, P. Bertuccio, M. H. Ward, R. Malekzadeh, F. Pourfarzi, L. Mu, M. Lopez-Cervantes, R. Persiani, R. C. Kurtz, A. Lagiou, P. Lagiou, P. Boffetta, S. Boccia, E. Negri, M. C. Camargo, M. P. Curado, C. La Vecchia,N. Lunet, Int. J. Cancer **2020**, 147, 45.

[22] L. D'Elia, F. Galletti,P. Strazzullo, Cancer Treat. Res. **2014**, 159, 83.

[23] D. Praud, M. Rota, C. Pelucchi, P. Bertuccio, T. Rosso, C. Galeone, Z. F. Zhang, K. Matsuo, H. Ito, J. Hu, K. C. Johnson, G. P. Yu, D. Palli, M. Ferraroni, J. Muscat, N. Lunet, B. Peleteiro, R. Malekzadeh, W. Ye, H. Song, D. Zaridze, D. Maximovitch, N. Aragones, G. Castano-Vinyals, J. Vioque, E. M. Navarrete-Munoz, M. Pakseresht, F. Pourfarzi, A. Wolk, N. Orsini, A. Bellavia, N. Hakansson, L. Mu, R. Pastorino, R. C. Kurtz, M. H. Derakhshan, A. Lagiou, P. Lagiou, P. Boffetta, S. Boccia, E. Negri,C. La Vecchia, Eur. J. Cancer Prev. **2018**, 27, 124.

[24] J. Khatoon, R. P. Rai,K. N. Prasad, World. J. Gastrointest. Oncol. **2016**, 8, 147.

[25] M. Naumann,J. E. Crabtree, Trends Microbiol. **2004**, 12, 29.

[26] R. Mera, E. T. Fontham, L. E. Bravo, J. C. Bravo, M. B. Piazuelo, M. C. Camargo,P. Correa, Gut **2005**, 54, 1536.

[27] B. C. Wong, S. K. Lam, W. M. Wong, J. S. Chen, T. T. Zheng, R. E. Feng, K. C. Lai, W. H. Hu, S. T. Yuen, S. Y. Leung, D. Y. Fong, J. Ho, C. K. Ching, J. S. Chen,G. China Gastric Cancer Study, JAMA **2004**, 291, 187.

[28] M. Balakrishnan, R. George, A. Sharma,D. Y. Graham, Curr. Gastroenterol. Rep. **2017**, 19, 36.

[29] P. Rawla,A. Barsouk, Prz Gastroenterol **2019**, 14, 26.

[30] C. Oliveira, G. Suriano, P. Ferreira, P. Canedo, P. Kaurah, R. Mateus, A. Ferreira, A. C. Ferreira, M. J. Oliveira, C. Figueiredo, F. Carneiro, G. Keller, D. Huntsman, J. C. Machado,R. Seruca, Hered. Cancer Clin. Pract. **2004**, 2, 51.

[31] B. Shepard, L. Yoder,C. Holmes, ACG Case Rep J **2016**, 3, e179.

[32] S. Hansford, P. Kaurah, H. Li-Chang, M. Woo, J. Senz, H. Pinheiro, K. A. Schrader, D. F. Schaeffer, K. Shumansky, G. Zogopoulos, T. A. Santos, I. Claro, J. Carvalho, C. Nielsen, S. Padilla, A. Lum, A. Talhouk, K. Baker-Lange, S. Richardson, I. Lewis, N. M. Lindor, E. Pennell, A. MacMillan, B. Fernandez, G. Keller, H. Lynch, S. P. Shah, P. Guilford, S. Gallinger, G. Corso, F. Roviello, C. Caldas, C. Oliveira, P. D. Pharoah,D. G. Huntsman, JAMA Oncol **2015**, 1, 23.

[33] I. J. Majewski, I. Kluijt, A. Cats, T. S. Scerri, D. de Jong, R. J. Kluin, S. Hansford, F. B. Hogervorst, A. J. Bosma, I. Hofland, M. Winter, D. Huntsman, J. Jonkers, M. Bahlo,R. Bernards, J. Pathol. **2013**, 229, 621.

[34] V. R. Blair, M. McLeod, F. Carneiro, D. G. Coit, J. L. D'Addario, J. M. van Dieren, K. L. Harris, N. Hoogerbrugge, C. Oliveira, R. S. van der Post, J. Arnold, P. R. Benusiglio, T. M. Bisseling, A. Boussioutas, A. Cats, A. Charlton, K. E. C. Schreiber, J. L. Davis, M. D. Pietro, R. C. Fitzgerald, J. M. Ford, K. Gamet, I. Gullo, R. H. Hardwick, D. G. Huntsman, P. Kaurah, S. S. Kupfer, A. Latchford, P. F. Mansfield, T. Nakajima, S. Parry, J. Rossaak, H. Sugimura, M. Svrcek, M. Tischkowitz, T. Ushijima, H. Yamada, H. K. Yang, A. Claydon, J. Figueiredo, K. Paringatai, R. Seruca, N. Bougen-Zhukov, T. Brew, S. Busija, P. Carneiro, L. DeGregorio, H. Fisher, E. Gardner, T. D. Godwin, K. N. Holm, B. Humar, C. J.

Lintott, E. C. Monroe, M. D. Muller, E. Norero, Y. Nouri, J. Paredes, J. M. Sanches, E. Schulpen, A. S. Ribeiro, A. Sporle, J. Whitworth, L. Zhang, A. E. Reeve,P. Guilford, Lancet Oncol. **2020**, 21, e386.

[35] I. Gullo, F. Carneiro, C. Oliveira,G. M. Almeida, Pathobiology **2018**, 85, 50.

[36] P. Lauren, Acta Pathol. Microbiol. Scand. **1965**, 64, 31.

[37] I. D. Nagtegaal, R. D. Odze, D. Klimstra, V. Paradis, M. Rugge, P. Schirmacher, K. M. Washington, F. Carneiro, I. A. Cree,W. H. O. C. o. T. E. Board, Histopathology **2020**, 76, 182.

[38] M. Z. Qiu, M. Y. Cai, D. S. Zhang, Z. Q. Wang, D. S. Wang, Y. H. Li,R. H. Xu, J. Transl. Med. **2013**, 11, 58.

[39] K. Nakamura, H. Sugano,K. Takagi, Gan **1968**, 59, 251.

[40] S. C. Ming, Cancer **1977**, 39, 2475.

[41] N. Goseki, T. Takizawa,M. Koike, Gut **1992**, 33, 606.

[42] F. Carneiro, M. Seixas,M. Sobrinho-Simoes, Pathol. Res. Pract. **1995**, 191, 571.

[43] E. Solcia, C. Klersy, L. Mastracci, P. Alberizzi, M. E. Candusso, M. Diegoli, F. Tava, R. Riboni, R. Manca,O. Luinetti, Virchows Arch. **2009**, 455, 197.

[44] A. Japanese Gastric Cancer, Gastric Cancer **2011**, 14, 101.

[45] E. C. Smyth, M. Verheij, W. Allum, D. Cunningham, A. Cervantes, D. Arnold,E. G. Committee, Ann. Oncol. **2016**, 27, v38.

[46] M. Sasako, Ann Gastroenterol Surg **2020**, 4, 21.

[47] T. Matsuoka,M. Yashiro, World J. Gastroenterol. **2018**, 24, 2818.

[48] E. Van Cutsem, X. Sagaert, B. Topal, K. Haustermans,H. Prenen, Lancet **2016**, 388, 2654.

[49] K. Strimbu,J. A. Tavel, Curr. Opin. HIV AIDS **2010**, 5, 463.

[50] G. Biomarkers Definitions Working, Clin. Pharmacol. Ther. **2001**, 69, 89.

[51] C. Duraes, G. M. Almeida, R. Seruca, C. Oliveira,F. Carneiro, Virchows Arch. **2014**, 464, 367.

[52] C. N. Oldenhuis, S. F. Oosting, J. A. Gietema,E. G. de Vries, Eur. J. Cancer **2008**, 44, 946.

[53] M. Abbas, A. Faggian, D. N. Sintali, G. J. Khan, S. Naeem, M. Shi,C. Dingding, Biomed. Pharmacother. **2018**, 103, 1688.

[54] Y. J. Bang, E. Van Cutsem, A. Feyereislova, H. C. Chung, L. Shen, A. Sawaki, F. Lordick, A. Ohtsu, Y. Omuro, T. Satoh, G. Aprile, E. Kulikov, J. Hill, M. Lehle, J. Ruschoff, Y. K. Kang,G. A. T. I. To, Lancet **2010**, 376, 687.

[55] L. Huang, R. L. Wu,A. M. Xu, Am J Transl Res **2015**, 7, 2141.

[56] N. Pecina-Slaus, Cancer Cell Int. **2003**, 3, 17.

[57] F. van Roy,G. Berx, Cell. Mol. Life Sci. **2008**, 65, 3756.

[58] X. Liu,K. M. Chu, Biomed Res Int **2014**, 2014, 637308.

[59] G. Corso, J. Carvalho, D. Marrelli, C. Vindigni, B. Carvalho, R. Seruca, F. Roviello,C. Oliveira, J. Clin. Oncol. **2013**, 31, 868.

[60] P. Ferreira, M. J. Oliveira, E. Beraldi, A. R. Mateus, T. Nakajima, M. Gleave, J. Yokota, F. Carneiro, D. Huntsman, R. Seruca,G. Suriano, Exp. Cell Res. **2005**, 310, 99.

[61] H. W. Xin, J. H. Yang,D. M. Nguyen, Anticancer Res. **2013**, 33, 2401.

[62] S. E. Witta, R. M. Gemmill, F. R. Hirsch, C. D. Coldren, K. Hedman, L. Ravdel, B. Helfrich, R. Dziadziuszko, D. C. Chan, M. Sugita, Z. Chan, A. Baron, W. Franklin, H. A. Drabkin, L. Girard, A. F. Gazdar, J. D. Minna,P. A. Bunn, Jr., Cancer Res. **2006**, 66, 944.

[63] Z. Torabizadeh, A. Nosrati, S. N. Sajadi Saravi, J. Yazdani Charati,G. Janbabai, Int J Hematol Oncol Stem Cell Res **2017**, 11, 158.

[64] C. B. da Cunha, C. Oliveira, X. Wen, B. Gomes, S. Sousa, G. Suriano, M. Grellier, D. G. Huntsman, F. Carneiro, P. L. Granja,R. Seruca, Lab. Invest. **2010**, 90, 1604.

[65] S. Goodison, V. Urquidi,D. Tarin, Mol. Pathol. **1999**, 52, 189.

[66] L. A. Goldstein, D. F. Zhou, L. J. Picker, C. N. Minty, R. F. Bargatze, J. F. Ding,E. C. Butcher, Cell **1989**, 56, 1063.

[67] I. Stamenkovic, M. Amiot, J. M. Pesando,B. Seed, Cell **1989**, 56, 1057.

[68] H. Ponta, D. Wainwright,P. Herrlich, Int. J. Biochem. Cell Biol. **1998**, 30, 299.

[69] H. Ponta, L. Sherman,P. A. Herrlich, Nat. Rev. Mol. Cell Biol. **2003**, 4, 33.

[70] G. F. Weber, S. Ashkar, M. J. Glimcher,H. Cantor, Science **1996**, 271, 509.

[71] J. R. Knutson, J. Iida, G. B. Fields,J. B. McCarthy, Mol. Biol. Cell **1996**, 7, 383.

[72] A. Aruffo, I. Stamenkovic, M. Melnick, C. B. Underhill,B. Seed, Cell **1990**, 61, 1303.

[73] D. Naor, R. V. Sionov,D. Ish-Shalom, Adv. Cancer Res. **1997**, 71, 241.

[74] C. R. Mackay, H. J. Terpe, R. Stauder, W. L. Marston, H. Stark,U. Gunthert, J. Cell Biol. **1994**, 124, 71.

[75] U. Gunthert, M. Hofmann, W. Rudy, S. Reber, M. Zoller, I. Haussmann, S. Matzku, A. Wenzel, H. Ponta,P. Herrlich, Cell **1991**, 65, 13.

[76] S. Ochiai, Y. Nakanishi, K. Mizuno, S. Hashimoto, S. Inutsuka, M. Kawasaki, J. Yatsunami,N. Hara, Nihon Kyobu Shikkan Gakkai Zasshi **1997**, 35, 1179.

[77] D. C. Gotley, J. Fawcett, M. D. Walsh, J. A. Reeder, D. L. Simmons,T. M. Antalis, Br. J. Cancer **1996**, 74, 342.

[78] L. Wang, X. Zuo, K. Xie,D. Wei, Methods Mol. Biol. **2018**, 1692, 31.

[79] R. Thapa,G. D. Wilson, Stem Cells Int. **2016**, 2016, 2087204.

[80] S. Seiter, R. Arch, S. Reber, D. Komitowski, M. Hofmann, H. Ponta, P. Herrlich, S. Matzku,M. Zoller, J. Exp. Med. **1993**, 177, 443.

[81] A. Matzke-Ogi, K. Jannasch, M. Shatirishvili, B. Fuchs, S. Chiblak, J. Morton, B. Tawk, T. Lindner, O. Sansom, F. Alves, A. Warth, C. Schwager, W. Mier, J. Kleeff, H. Ponta, A. Abdollahi,V. Orian-Rousseau, Gastroenterology **2016**, 150, 513.

[82] K. H. Heider, J. Dammrich, P. Skroch-Angel, H. K. Muller-Hermelink, H. P. Vollmers, P. Herrlich,H. Ponta, Cancer Res. **1993**, 53, 4197.

[83] C. Branco da Cunha, D. D. Klumpers, S. T. Koshy, J. C. Weaver, O. Chaudhuri, R. Seruca, F. Carneiro, P. L. Granja,D. J. Mooney, Biomaterials **2016**, 98, 152.

[84] H. Kodama, S. Murata, M. Ishida, H. Yamamoto, T. Yamaguchi, S. Kaida, T. Miyake, K. Takebayashi, R. Kushima,M. Tani, Br. J. Cancer **2017**, 116, 186.

[85] L. Li, M. Schmitt, A. Matzke-Ogi, P. Wadhwani, V. Orian-Rousseau,P. A. Levkin, Adv Sci (Weinh) **2017**, 4, 1600202.

[86] S. Liang, C. Li, C. Zhang, Y. Chen, L. Xu, C. Bao, X. Wang, G. Liu, F. Zhang,D. Cui, Theranostics **2015**, 5, 970.

[87] Y. Chen, G. Lian, C. Liao, W. Wang, L. Zeng, C. Qian, K. Huang,X. Shuai, J. Gastroenterol. **2013**, 48, 809.

[88] D. Zhang, J. Huang, W. Li, Z. Zhang, M. Zhu, Y. Feng, Y. Zhao, Y. Li, S. Lu,S. He, Ann Transl Med **2020**, 8, 1442.

[89] Y. Wu, W. Wang, Y. Chen, K. Huang, X. Shuai, Q. Chen, X. Li,G. Lian, Int J Nanomedicine **2010**, 5, 129.

[90] C. Pereira, D. Ferreira, N. Mendes, P. L. Granja, G. M. Almeida,C. Oliveira, Cancers (Basel) **2020**, 12,

[91] P. J. Kennedy, F. Sousa, D. Ferreira, C. Pereira, M. Nestor, C. Oliveira, P. L. Granja,B. Sarmento, Acta Biomater. **2018**,

[92] P. J. Kennedy, I. Perreira, D. Ferreira, M. Nestor, C. Oliveira, P. L. Granja,B. Sarmento, Eur. J. Pharm. Biopharm. **2018**, 127, 366.

[93] A. C. Ericsson, M. J. Crim,C. L. Franklin, Mo. Med. **2013**, 110, 201.

[94] I. W. Mak, N. Evaniew,M. Ghert, Am J Transl Res **2014**, 6, 114.

[95] A. Knight, Altern Lab Anim **2007**, 35, 641.

[96] N. Cook, D. I. Jodrell,D. A. Tuveson, Drug Discov. Today **2012**, 17, 253.

[97] D. G. Hackam,D. A. Redelmeier, JAMA **2006**, 296, 1731.

[98]

[99] D. Huh, G. A. Hamilton,D. E. Ingber, Trends Cell Biol. **2011**, 21, 745.

[100] K. Ronaldson-Bouchard,G. Vunjak-Novakovic, Cell Stem Cell **2018**, 22, 310.

[101] I. T. Ozbolat,Y. Yu, IEEE Trans. Biomed. Eng. **2013**, 60, 691.

[102] J. A. Barron, P. Wu, H. D. Ladouceur,B. R. Ringeisen, Biomed. Microdevices **2004**, 6, 139.

[103] K. Jakab, A. Neagu, V. Mironov, R. R. Markwald,G. Forgacs, Proc. Natl. Acad. Sci. U. S. A. **2004**, 101, 2864.

[104] S. A. Langhans, Front. Pharmacol. **2018**, 9, 6.

[105] J. R. Masters, Nat. Rev. Mol. Cell Biol. **2000**, 1, 233.

[106] P. Mirabelli, L. Coppola,M. Salvatore, Cancers (Basel) **2019**, 11,

[107] M. W. Taylor, Viruses and Man: A History of Interactions, (Eds: M. W. Taylor), Springer International Publishing, Cham, 2014,

[108] a) C. O. Rodríguez-Hernández, S. Torres-García, C. Olvera-Sandoval, F. Y. Ramírez-Castillo, A. L. Muro, F. J. Avelar-González,A. Guerrero-Barrera, in Proc. **2014**; b) C. O. Rodríguez-Hernández, S. Torres-García, C. Olvera-Sandoval, F. Y. Ramírez-Castillo, A. L. Muro, F. J. Avelar-González,A. Guerrero-Barrera, presented at **2014**.

[109] F. Pampaloni, E. G. Reynaud,E. H. Stelzer, Nat. Rev. Mol. Cell Biol. **2007**, 8, 839.

[110] C. M. Magin, D. L. Alge,K. S. Anseth, Biomed. Mater. **2016**, 11, 022001.

[111] H. K. Kleinman, D. Philp,M. P. Hoffman, Curr. Opin. Biotechnol. **2003**, 14, 526.

[112] M. J. Bissell, D. C. Radisky, A. Rizki, V. M. Weaver,O. W. Petersen, Differentiation **2002**, 70, 537.

[113] B. Mayer, G. Klement, M. Kaneko, S. Man, S. Jothy, J. Rak,R. S. Kerbel, Gastroenterology **2001**, 121, 839.

[114] A. L. Bredenoord, H. Clevers,J. A. Knoblich, Science **2017**, 355,

[115] B. N. Lourenco, T. Dos Santos, C. Oliveira, C. C. Barrias,P. L. Granja, Acta Biomater. **2018**, 82, 68.

[116] F. R. Maia, A. H. Lourenco, P. L. Granja, R. M. Goncalves,C. C. Barrias, Macromol. Biosci. **2014**, 14, 759.

[117] U. S. K. Madduma-Bandarage,S. V. Madihally, J. Appl. Polym. Sci. **2021**, 138, 50376.

[118] T. Boland, T. Xu, B. Damon,X. Cui, Biotechnol. J. **2006**, 1, 910.

[119] V. Mironov, Expert Opin. Biol. Ther. **2003**, 3, 701.

[120] B. Derby, Science **2012**, 338, 921.

[121] J. S. Lee, R. T. Hill, A. Chilkoti,W. L. Murphy, Biomaterials Science (Fourth Edition), (Eds: W. R. Wagner, S. E. Sakiyama-Elbert, G. Zhang and M. J. Yaszemski), Academic Press, 2020,

[122] H. Jeon, S. Koo, W. M. Reese, P. Loskill, C. P. Grigoropoulos,K. E. Healy, Nat Mater **2015**, 14, 918.

[123] D. Huh, B. D. Matthews, A. Mammoto, M. Montoya-Zavala, H. Y. Hsin,D. E. Ingber, Science **2010**, 328, 1662.

[124] N. Convery,N. Gadegaard, Micro and Nano Engineering **2019**, 2, 76.

[125] G. M. Whitesides, Nature **2006**, 442, 368.

[126] S. C. Terry, J. H. Jerman,J. B. Angell, IEEE Transactions on Electron Devices **1979**, 26, 1880.

[127] P. A. Auroux, D. Iossifidis, D. R. Reyes,A. Manz, Anal. Chem. **2002**, 74, 2637.

[128] S. K. Sia,G. M. Whitesides, Electrophoresis **2003**, 24, 3563.

[129] D. C. Duffy, J. C. McDonald, O. J. Schueller,G. M. Whitesides, Anal. Chem. **1998**, 70, 4974.

[130] J. C. McDonald, D. C. Duffy, J. R. Anderson, D. T. Chiu, H. Wu, O. J. Schueller,G. M. Whitesides, Electrophoresis **2000**, 21, 27.

[131] G. M. Whitesides, E. Ostuni, S. Takayama, X. Jiang,D. E. Ingber, Annu. Rev. Biomed. Eng. **2001**, 3, 335.

[132] Y. N. Xia,G. M. Whitesides, Angewandte Chemie-International Edition **1998**, 37, 550.

[133] J. R. Anderson, D. T. Chiu, R. J. Jackman, O. Cherniavskaya, J. C. McDonald, H. Wu, S. H. Whitesides,G. M. Whitesides, Anal. Chem. **2000**, 72, 3158.

[134] D. T. Chiu, N. L. Jeon, S. Huang, R. S. Kane, C. J. Wargo, I. S. Choi, D. E. Ingber,G. M. Whitesides, Proc. Natl. Acad. Sci. U. S. A. **2000**, 97, 2408.

[135] E. Leclerc, Y. Sakai,T. Fujii, Biomed. Microdevices **2003**, 5, 109.

[136] S. G. Charati,S. A. Stern, Macromolecules **1998**, 31, 5529.

[137] C. Hansen,S. R. Quake, Curr. Opin. Struct. Biol. **2003**, 13, 538.

[138] I. E. Araci,P. Brisk, Curr. Opin. Biotechnol. **2014**, 25, 60.

[139] J. Melin,S. R. Quake, Annu. Rev. Biophys. Biomol. Struct. **2007**, 36, 213.

[140] E. W. Young,D. J. Beebe, Chem. Soc. Rev. **2010**, 39, 1036.

[141] E. R. Shamir,A. J. Ewald, Nature Reviews Molecular Cell Biology **2014**, 15, 647.

[142] R. Edmondson, J. J. Broglie, A. F. Adcock,L. J. Yang, Assay Drug Dev. Technol. **2014**, 12, 207.

[143] Y. K. Zhu, T. Umino, X. D. Liu, H. J. Wang, D. J. Romberger, J. R. Spurzem,S. I. Rennard, In Vitro Cellular & Developmental Biology-Animal **2001**, 37, 10.

[144] K. Kamei, Jala **2013**, 18, 469.

[145] L. Wu, P. Chen, Y. Dong, X. Feng,B. F. Liu, Biomed. Microdevices **2013**, 15, 553.

[146] J. T. S. Fernandes, S. Tenreiro, A. Gameiro, V. Chu, T. F. Outeiro,J. P. Conde, Lab on a Chip **2014**, 14, 3949.

[147] P. J. Hung, P. J. Lee, P. Sabounchi, R. Lin,L. P. Lee, Biotechnol. Bioeng. **2005**, 89, 1.

[148] J. T. Fernandes, O. Chutna, V. Chu, J. P. Conde,T. F. Outeiro, Front. Neurosci. **2016**, 10, 511.

[149] H. J. Kim, D. Huh, G. Hamilton,D. E. Ingber, Lab on a Chip **2012**, 12, 2165.

[150] D. A. Ferreira, M. Rothbauer, J. P. Conde, P. Ertl, C. Oliveira,P. L. Granja, Advanced Science n/a, 2003273.

[151] A. O. Stucki, J. D. Stucki, S. R. Hall, M. Felder, Y. Mermoud, R. A. Schmid, T. Geiser,O. T. Guenat, Lab Chip **2015**, 15, 1302.

[152] O. T. Guenat,F. Berthiaume, Biomicrofluidics **2018**, 12,

[153] E. Ergir, B. Bachmann, H. Redl, G. Forte,P. Ertl, Front. Physiol. **2018**, 9, 1417.

[154] S. H. Park, W. Y. Sim, B. H. Min, S. S. Yang, A. Khademhosseini,D. L. Kaplan, PLoS One **2012**, 7, e46689.

[155] S. S. Nunes, J. W. Miklas, J. Liu, R. Aschar-Sobbi, Y. Xiao, B. Zhang, J. Jiang, S. Masse, M. Gagliardi, A. Hsieh, N. Thavandiran, M. A. Laflamme, K. Nanthakumar, G. J. Gross, P. H. Backx, G. Keller,M. Radisic, Nat. Methods **2013**, 10, 781.

[156] M. L. Moya, Y. H. Hsu, A. P. Lee, C. C. Hughes,S. C. George, Tissue Eng Part C Methods **2013**, 19, 730.

[157] S. R. Khetani,S. N. Bhatia, Nat. Biotechnol. **2008**, 26, 120.

[158] C. H. Cho, J. Park, A. W. Tilles, F. Berthiaume, M. Toner,M. L. Yarmush, Biotechniques **2010**, 48, 47.

[159] C. Y. Chan, P.-H. Huang, F. Guo, X. Ding, V. Kapur, J. D. Mai, P. K. Yuen,T. J. Huang, Lab on a Chip **2013**, 13, 4697.

[160] R. Lucas-González, M. Viuda-Martos, J. A. Pérez-Alvarez,J. Fernández-López, Food Res. Int. **2018**, 107, 423.

[161] M. Xavier, I. A. Parente, P. M. Rodrigues, M. A. Cerqueira, L. Pastrana,C. Gonçalves, Trends Food Sci. Technol. **2021**, 109, 593.

[162] G. Cheng, S. J. Hao, X. Yu,S. Y. Zheng, Lab Chip **2015**, 15, 650.

[163] L. Li, O. Lieleg, S. Jang, K. Ribbeck,J. Han, Lab on a Chip **2012**, 12, 4071.

[164] N. Scheuble, A. Iles, R. C. R. Wootton, E. J. Windhab, P. Fischer,K. S. Elvira, Anal. Chem. **2017**, 89, 9116.

[165] C. R. A. Duane T. Smoot, Pamela Bames, Milton Brown, Suhas Phadnis, Ben Gold, Hassan Ashktorab, Gastroentererology **2000**, 118,

[166] Y. Ke, T. Ning,B. Wang, Zhonghua Zhong Liu Za Zhi **1994**, 16, 7.

[167] J. R. Basque, M. Chénard, P. Chailler,D. Ménard, J. Cell. Biochem. **2001**, 81, 241.

[168] S. C. Barranco, C. M. Townsend, Jr., C. Casartelli, B. G. Macik, N. L. Burger, W. R. Boerwinkle,W. K. Gourley, Cancer Res. **1983**, 43, 1703.

[169] T. Motoyama, H. Hojo,H. Watanabe, Acta Pathol. Jpn. **1986**, 36, 65.

[170] M. Sekiguchi, K. Sakakibara,G. Fujii, Jpn. J. Exp. Med. **1978**, 48, 61.

[171] F. Gärtner, L. David, R. Seruca, J. C. Machado,M. Sobrinho-Simões, Virchows Arch. **1996**, 428, 91.

[172] T. d. Santos, B. N. Lourenço, J. Coentro,P. L. Granja, Concepts and Models for Drug Permeability Studies, (Eds: B. Sarmento), Woodhead Publishing, Chippenham, UK, 2016, Ch. 3.2.

[173] M. Lemieux, F. Bouchard, P. Gosselin, J. Paquin,M. A. Mateescu, Biochem. Biophys. Res. Commun. **2011**, 412, 429.

[174] T. Oshima, H. Miwa,T. Joh, Am. J. Physiol. Cell Physiol. **2008**, 295, C800.

[175] K. Hashimoto, T. Oshima, T. Tomita, Y. Kim, T. Matsumoto, T. Joh,H. Miwa, Biochem. Biophys. Res. Commun. **2008**, 376, 154.

[176] L. D. Ma, Y. T. Wang, J. R. Wang, J. L. Wu, X. S. Meng, P. Hu, X. Mu, Q. L. Liang,G. A. Luo, Lab Chip **2018**, 18, 2547.

[177] R. Langer,J. P. Vacanti, Science **1993**, 260, 920.

[178] T. Grikscheit, A. Srinivasan,J. P. Vacanti, J. Pediatr. Surg. **2003**, 38, 1305.

[179] T. Maemura, M. Shin, O. Ishii, H. Mochizuki,J. P. Vacanti, ASAIO J. **2004**, 50, 468.

[180] T. Maemura, K. Ogawa, M. Shin, H. Mochizuki,J. P. Vacanti, Transplant. Proc. **2004**, 36, 1595.

[181] T. Maemura, M. Shin, M. Sato, H. Mochizuki,J. P. Vacanti, Transplantation **2003**, 76, 61.

[182] F. G. Sala, S. M. Kunisaki, E. R. Ochoa, J. Vacanti,T. C. Grikscheit, J. Surg. Res. **2009**, 156, 205.

[183] K. Matuoka, M. Tanaka, Y. Mitsui,S. I. Murota, Gastroenterology **1983**, 84, 498.

[184] A. Terano, K. J. Ivey, J. Stachura, S. Sekhon, H. Hosojima, W. N. McKenzie, Jr., W. J. Krause,J. H. Wyche, Gastroenterology **1982**, 83, 1280.

[185] K. Matsuda, C. Sakamoto, Y. Konda, O. Nakano, T. Matozaki, H. Nishisaki, T. Suzuki, T. Uchida, K. Wada, T. Fujimori, S. Maeda,M. Kasuga, J. Gastroenterol. **1996**, 31, 498.

[186] N. Barker, M. Huch, P. Kujala, M. van de Wetering, H. J. Snippert, J. H. van Es, T. Sato, D. E. Stange, H. Begthel, M. van den Born, E. Danenberg, S. van den Brink, J. Korving, A. Abo, P. J. Peters, N. Wright, R. Poulsom,H. Clevers, Cell Stem Cell **2010**, 6, 25.

[187] T. Katano, A. Ootani, T. Mizoshita, S. Tanida, H. Tsukamoto, K. Ozeki, M. Ebi, Y. Mori, H. Kataoka, T. Kamiya, S. Toda,T. Joh, Biochem. Biophys. Res. Commun. **2013**, 432, 558.

[188] F. Boccellato, S. Woelffling, A. Imai-Matsushima, G. Sanchez, C. Goosmann, M. Schmid, H. Berger, P. Morey, C. Denecke, J. Ordemann,T. F. Meyer, Gut **2019**, 68, 400.

CHAPTER II

Expression of CD44v6 containing isoforms influences cisplatin response in gastric cancer cells

Published in Cancers 2020, 12(4), 858

(DOI: 10.3390/cancers12040858)

Expression of CD44v6 containing isoforms influences cisplatin response in gastric cancer cells

***Daniel Ferreira*[1,2,3,4]*, *Carla Pereira*[1,2]*, *Nuno Mendes*[1,2], *Pedro Granja*[1,3,4], *Gabriela M Almeida*[1,2,5], *Carla Oliveira*[1,2,5]**

**These authors contributed equally to this work.*

[1] i3S – Instituto de Investigação e Inovação em Saúde, Universidade do Porto, Rua Alfredo Allen, 208, 4200-135 Porto, Portugal

[2] Ipatimup – Institute of Molecular Pathology and Immunology, Universidade do Porto, Rua Júlio Amaral de Carvalho 45, 4200-135 Porto, Portugal

[3] INEB – Instituto de Engenharia Biomédica, Universidade do Porto, Rua Alfredo Allen, 208, 4200-135 Porto, Portugal

[4] ICBAS – Instituto de Ciências Biomédicas Abel Salazar, Universidade do Porto, Rua Jorge de Viterbo Ferreira, 228, 4050-313 Porto, Portugal

[5] Department of Pathology, Faculty of Medicine, University of Porto, Alameda Prof. Hernâni Monteiro, 4200-319 Porto, Portugal

Keywords: Stomach cancer; chemotherapy; CD44 variants; apoptosis; cell population dynamics

ABSTRACT

CD44v6-containing isoforms are frequently de novo expressed in gastric cancer (GC). Whether CD44v6 has a central role in GC transformation and/or progression, whether it conditions response to therapy or whether it is only a bystander marker is still not known. Therefore, we aimed to clarify the role of CD44v6 in GC. We generated GC isogenic cell lines stably expressing CD44s or CD44v6 and tested them for different cancer hallmarks and response to cisplatin, and we further confirmed our findings in cells that endogenously express CD44v6. No correlation between overexpression of CD44v6 and the tested cancer hallmarks was observed, suggesting CD44v6 is not a driver of GC progression. Upon cisplatin treatment, CD44v6+ cells survive better and have lower apoptosis levels than CD44v6− cells, possibly due to concomitant activation of STAT3 and P38. In co-culture experiments, we discovered that CD44v6+ cells are involved in GC cell overgrowth after cisplatin treatment. In conclusion, we show that CD44v6 expression increases cell survival in response to cisplatin treatment in GC cells and that these cells override CD44v6-negative cells after cisplatin-treatment. This suggests that tumor expression of CD44v6-containing variants may condition the outcome of GC patients treated with chemotherapy.

Introduction

CD44 is a ubiquitous membrane receptor that was first described for its role as an organ-specific, lymphocyte homing, cell surface molecule [1]. It has since been associated with a large number of key cellular adhesion processes, such as homotypic and heterotypic cellular adhesion [2,3]. Additionally, CD44 mediates cell to extracellular matrix (ECM) adhesion, as shown by its function as the major receptor for hyaluronic acid, a major component of the ECM [4], and also by its ability to interact with fibronectin [5] and collagen [6]. CD44 has also been described as a co-receptor with a pivotal role in intracellular signaling, mediating key aspects of cellular behavior such as motility and cell survival [7–9].

The human CD44 gene (NG_008937) encodes a polymorphic group of transmembrane glycoproteins generated by alternative splicing. The standard CD44 isoform (CD44s) includes only the constitutive exons, while the variant isoforms (CD44v) contain one or more variable exons (in addition to the constitutive ones) [7,9–11].

Regarding gastric tissue, we have previously shown that CD44s is widely expressed in both normal and diseased gastric epithelial cells [12]. In contrast, CD44v6-containing isoforms are *de novo* expressed in stomach premalignant and malignant lesions and in ~70% of all gastric cancers [12], the third leading cause of cancer related mortality worldwide [13]. Aberrant expression of CD44v isoforms has been associated with several cancer-related features like invasion and metastization [10,14,15]. Moreover, CD44 and its CD44v isoforms are expressed as surface markers of cancer stem cells (CSCs), influencing key CSC-associated properties such as tumor initiation, self-renewal, metastasis and chemoresistance [10,16–18]. Indeed, increased expression of CD44 has been observed in trastuzumab resistant gastric [19] and breast [20] cancer cells, as well as in paclitaxel resistant ovarian cancer cells [21]. Likewise, expression of some CD44v has been associated with chemoresistance, like CD44v6 in pancreatic/prostate/colon cancer cells [22–24] and CD44v9 in gastric cancer cells [25]. Moreover, an association between increased CD44 or CD44v6 tumor expression and worse overall survival (OS) in gastric cancer (GC) patients has previously been reported [26–28]. In sum, much is known about the molecule CD44v6 (in general) and several studies suggest that it can have a function in GC. However, it is still not known whether the observed *de novo* expression of CD44v6 has a central role in the transformative process and/or progression of GC, if it conditions response to therapy or if it is only a bystander marker resulting from all or some of those events. Therefore, in the present work, we aimed to clarify the role of CD44v6 using both

an isogenic model of GC cells stably expressing CD44s or CD44v6, and GC cells that endogenously express CD44v6.

Materials and methods

1. *Cell lines and culture conditions*

Human GC cell lines MKN74 and MKN45 were purchased from the JCRB Cell Bank (Japanese Collection of Research Bioresources Cell Bank), and the non-commercial cell line GP202 cell line was established at Ipatimup [39]. All reagents were purchased from ThermoFisher Scientific (Waltham, MA, USA), unless otherwise stated. All cell lines were cultured in RPMI 1640 medium with 10% heat inactivated fetal bovine serum (FBS) (Biowest, Nuaillé, France). Cell lines were maintained at 37 °C and 5% CO_2 in a high humidity atmosphere and sub-cultured every 3 to 4 days. Cells were grown in the absence of antibiotics except for cell selection in MKN74 cells, where G418 was used. Cells were never continuously cultured for more than 4 months. Cell identification was confirmed by STR analysis and cells were confirmed to be free of mycoplasma contamination.

2. *Flow cytometry*

Flow cytometry was used to determine the expression of CD44 and/or CD44v6 in GC cell lines. All reagents were purchased from ThermoFisher Scientific (Waltham, MA, USA), unless stated otherwise. Cells were seeded in 6-well plates to a density of 5×10^5 cells/well and allowed to grow to approximately 90% confluency. Cells were then washed with phosphate buffered saline (PBS), versinized for 5 min and washed in ice-cold PBS-3%BSA (bovine serum albumin). Cells were then blocked in PBS-3%BSA for 30 min and incubated with the appropriate primary antibody: mouse monoclonal antibody against CD44 (clone 156-3C11; 1:100 dilution; 60 min incubation; Cell Signaling Technology (Beverly, MA, USA)) or mouse monoclonal antibody against CD44v6 (MA54; 1:100; 60 min). Cells were subsequently washed with PBS-3%BSA and incubated with a secondary antibody: anti-mouse Alexa Fluor 488 or anti-mouse Alexa Fluor 564 (1:500; 60 min). Fluorescence was analyzed using a FACS Calibur or an Accuri C6 cytometer (both from BD Biosciences, Franklin Lakes, NJ, USA). The mean fluorescence intensity was measured for at least 20,000 gated events per sample and data were analyzed using the software Flow Jo, version 10.

3. *RNA extraction and cDNA synthesis*

All reagents were purchased from ThermoFisher Scientific (Waltham, MA, USA), unless otherwise stated. RNA was isolated using the mIRVana™ extraction Kit by following the supplier recommended protocol. Extraction efficiency and quality was assessed using a NanoDrop ND-1000. First Strand cDNA synthesis was performed using SuperScript® II reverse transcriptase, random hexamer primers and 1 µg of template RNA, according to the manufacturers' protocol.

4. *Characterization of v6 containing transcripts in GP202 cell line*

To characterize the full spectrum of v6 containing transcripts present in the GP202 cell line, we used a set of primers that amplifies from exon 5 through to exon 20. Forward primers included one overlapping exon 5 (primer A, Table S1) and another overlapping exon v6 (primer B). A reverse orientation set of primers was designed to overlap exon v6 (primer D), exon boundary 17/18 (primer F), as well as two primers that amplify either the short tailed isoform variant, overlapping exon 19 (primer G) or the long tailed isoform variant, overlapping exon 20 (primer H). To identify the full length sequence of the v3–v10 transcript, we used a nested PCR approach to amplify the variable region of said transcript in the GP202 cell line. The first round of amplification included a forward primer overlapping exon 5 (primer A) and a reverse primer overlapping exon 20 (primer H). The second round of amplification was performed with a set of primers spanning the exon 5/exon v3 boundary (primer C, Table S1) and the exon 16/exon 17 boundary (primer E). The resulting amplicons were resolved on a 3% agarose gel. All bands were excised and DNA extracted using a band extraction kit (GE Healthcare, Chicago, IL, USA). Sequencing was achieved with a primer walking strategy, with each primer designed to correctly map each inter-exon region between exons 5 and 20. The primers used for this task were primers, A, B, D, F, G and H (Table S1). The sequence of this CD44v3–v10 (i.e., v6 containing) variant, endogenously expressed in the GP202 cell line, was then used to generate the isogenic cell model mentioned below.

5. *Generation of an isogenic cell line model of tumor CD44v6 status*

All reagents were from ThermoFisher Scientific (Waltham, MA, USA), unless otherwise stated. The sequences coding for CD44s (variant CD44-03-ENST00000263398) and CD44v6 (variant CD44-04-ENST00000415148; Ensembl release 68, July 2012) in a pCMV6-XL5 and pCMV6-AC backbone respectively, were purchased from OriGene. CD44s

was excised with EcoRI and SmaI and cloned directly into a pIRES-EGFP2 plasmid. CD44v6 was excised in two steps, first with EcoRI and XhoI and sub-cloned into a pIRES-EGFP2 plasmid with a custom made MCS constructed by Bordeira Carriço et al. [40] and subsequently cleaved with SacI and SalI and subcloned into a pIRES-EGFP2 plasmid. Restriction enzymes were all purchased from New England Biolabs (Ipswich, MA, USA). The correct sequence of each transcript was confirmed by Sanger sequencing. The pIRES-EGFP2 empty vector was used as the mock control. The MKN74 cell line, was transfected using Lipofectamine 2000 reagent with either the empty pIRES-EGFP2 vector (MKN74_Mock), the pIRES-EGFP2_CD44v6 (MKN74_CD44v6) or the pIRES-EGFP2_CD44s (MKN74_CD44s). Selective pressure to isolate stably expressing cells, was applied with 1 mg/mL of G418, 48 h after transfection. In order to obtain pure populations of CD44v6 and CD44s cells, magnetic bead sorting with the Magnetic Separation kit CELLection Pan Mouse IgG kit from Dynabeads® was performed, according to the manufacturers' instructions. Briefly, following transfection, cells were sorted according to the expression of CD44v6 or CD44s. After the first round of separation, cells were allowed to grow to confluence, and two more rounds of magnetic bead sorting performed. The efficiency of cell selection was assessed by flow cytometry, as described above. Correct expression and localization, of the desired CD44 isoform, at the cell membrane was determined by immunofluorescence, as described below.

6. *Immunofluorescence*

All immunofluorescence reagents were from ThermoFisher Scientific (Waltham, MA, USA), and all antibodies were from Cell Signaling Technology (Beverly, MA, USA) unless stated otherwise.

Cells were grown on glass coverslips for the desired amount of time under normal growth conditions or with specific treatments before being washed twice in PBS and fixed with 4% paraformaldehyde (Merck, Darmstadt, Germany) for 20 min. Post fixation, cells were washed with PBS, incubated 10 min with NH_4Cl, washed twice with PBS and incubated 5 min in PBS- 0.2%Triton X-100 for membrane permeabilization. Blocking was performed for 30 min with PBS-5% BSA. Coverslips were subsequently incubated with the desired primary antibodies. Detection of phosphorylated forms required methanol permeabilization for 10 min on ice prior to incubation with the primary antibody. Primary antibodies, diluted in PBS-5% BSA were: (i) mouse monoclonal antibodies–anti-CD44v6 (clone MA541; 1:100 dilution; 60 min incubation; ThermoFisher Scientific), anti-CD44 antibody (156-3C11; 1:100; 60 min), STAT3 antibody (124H6; 1:100); (ii) rabbit monoclonal antibodies–anti-P38 (D13E1; 1:100; ON incubation), anti-phospho-P38 (12F8; 1:100; ON), and phospho-STAT3 (D3A7; 1:100;

ON). Cells were then washed twice with PBS and incubated in the dark with secondary antibodies: Alexa Fluor 488 Donkey Anti-Mouse secondary antibody (1:500; 60 min; Life Technologies, (Carlsbad, CA, USA) or Alexa Fluor 594 anti-rabbit (1:500, 60 min; Life Technologies), after which a final PBS wash was performed. In all cases, the cell nuclei were stained using Vectashield mounting media with DAPI (Vector Laboratories, Burlingame, CA, USA). Cells were analyzed by fluorescence microscopy (Imager.Z1, AxioCam fluorescence microscope or Eclipse TE-2000, both from Zeiss, Gottingen, Germany) using AxioVision software (Rockville, MD, USA).

7. *Quantitative Real-Time Reverse Transcription PCR (qRT-PCR)*

Gene expression levels were assessed by real-time qRT-PCR. RNA Isolation and cDNA synthesis was performed as described above. Real time qRT-PCR was performed in duplicate with 200 ng of template cDNA on an ABI Prism 7000 Sequence Detection System, using probes specific for CD44v6 (exon span V5–V6, Hs.PT.58.45400024) and total CD44 (exon span V2–V3, Hs.PT.58.4880087) (both from iDT, Corallvile, IA, USA). The relative expression level of CD44v6 and total CD44 was determined by the comparative $2^{-\Delta\Delta C}{}_{T}$ method using the housekeeping gene GADPH (4352934E; ThermoFisher Scientific, Waltham, MA, USA), to normalize expression results between samples.

8. *Protein extraction and Western Blot*

Cells were cultured for the desired amount of time under normal growth conditions or with specific treatments before being washed twice with PBS and lysed with cold catenin lysis buffer [1% (*v/v*) Triton X-100, 1% (*v/v*) IGEPAL in PBS], supplemented with phosphatase (Sigma-Aldrich, Poole, UK) and protease (Roche, Basel, Switzerland) inhibitor cocktails. Total protein content of the samples was quantified by a modified Bradford Assay (Bio-Rad, Hercules, CA, USA). Thirty-five µg of total protein lysate were resolved by electrophoresis in a 7.5% or a 10% SDS polyacrylamide gel. The protein was transferred onto a Hybond nitrocellulose membrane (GE Healthcare, Chicago, IL, USA) and stained with Ponceau S solution (Sigma-Aldrich, Poole, UK) to confirm the efficacy of the transfer. Membrane blocking was performed by incubating membranes for 20 to 30 min with 5% non-fat milk diluted in 0.5% (*v/v*) PBS-Tween-20, or with 5% BSA diluted in 0.5% (*v/v*) TBS-Tween-20 or 5% non-fat milk diluted in 0.1% (*v/v*) TBS-Tween-20 (for the phosphorylated protein forms). Then, incubation of membranes with primary antibodies was performed overnight at 4 °C. Antibodies were all from Cell Signaling Technology (Beverly, MA, USA), unless stated otherwise. Primary antibodies used were: (i) mouse monoclonal antibody against

CD44v6 (MA54; 1:500; ThermoFisher Scientific, Waltham, MA, USA), CD44 (156-3C11; 1:1000); (ii) rabbit monoclonal antibodies against AKT (1:1000), EGFR (D38B1; 1:1000), p44/42 MAPK (Erk1/2) (1:1000), P38 MAPK (D13E1; 1:1000), STAT3 (124H6; 1:1000), phospho-AKT (Ser473) (D9E; 1:1000), phospho-EGFR (D7A5; 1:1000), phospho-p44/42 MAPK (Thr202/Tyr204), (1:1000), phospho-p38 MAPK (Thr180/Tyr182) (12F8; 1:1000), phospho-STAT3 (Tyr705) (D3A7; 1:1000). α-tubulin (1:10,000; Sigma-Aldrich, Poole, UK) or α-actin (1:1000; Santa Cruz Biotechnology, Dallas, TX, USA) were used as loading controls. Membranes were further incubated with horseradish peroxidase-conjugated secondary antibodies (GE Healthcare and Santa Cruz) and labelled protein specific signal was detected by ECL (GE Healthcare, Chicago, IL, USA). Bands were quantified with the Quantity One software (Bio-Rad, Hercules, CA, USA). Protein for Western blotting was extracted from at least three independent biological replicates.

9. *Cell Growth Assays*

The Sulforhodamine B (SRB) assay or Presto Blue (PB; ThermoFisher Scientific, Waltham, MA, USA), a resazurin-based assay, were used to assess cell growth. All reagents were purchased from Sigma-Aldrich (Poole, UK) unless otherwise stated. Cells were seeded in 96-well plates (2.5×10^3 per well) under normal conditions (5% CO2 humidified atmosphere at 37 °C) and allowed to adhere for 24 h. Cells were then allowed to grow for a further 48 h. At the required times: (i) for the SRB assay, cells were fixed in 10% trichloroacetic acid (TCA) for 1 h on ice, proteins stained with 4% SRB solution for 30 min, wells washed repeatedly with 1% acetic acid to remove the unbound dye, and the protein-bound stain was solubilized with 10 mM Tris solution. The SRB absorbance was measured at 560 nm and background corrected at 655 nm; (ii) for the PB assay, cells were incubated with PB solution (1×) for 45 min at 37 °C and fluorescence assessed (with an excitation wavelength of 560 nm and emission of 590 nm). Both absorbance and fluorescence were measured using a microplate reader (PowerWave HT Microplate Spectrophotometer; BioTek, Bad Friedrichshall, Germany). At least three independent experiments were performed, each measured in triplicate. The doubling time was calculated using the SRB assay as follows: Doubling Time = (0.301 × t)/(Log ODt/OD0), where ODt is the SRB absorbance at 48 h, OD0 is the SRB absorbance at an initial time and t is the time elapsed between the two (in this case, 48 h). Experiments to determine the IC50 for cisplatin were performed using the PB assay for all GC cell lines used (**Figure S3**): MKN74 IC50 ~ 3.6 μM; MKN45 IC50 ~ 6 μM and; GP202 IC50 ~ 17 μM. Cisplatin concentrations used in subsequent experiments were all performed within these ranges, depending on the assay.

The selection of 5-FU concentrations used was performed according to Nakamura et al. [41].

10. *Invasion and Slow Aggregation Assays*

Cell invasion assays were carried out using matrigel invasion chambers (BD Biosciences, Franklin Lakes, NJ, USA), according to manufacturer´s specifications. Briefly, prior to cell seeding, membranes were hydrated on both sides with complete culture medium for 1 h at 37 °C. Cells were seeded (1×10^5 per invasion chamber) and incubated for 24 h at 37 °C. Cells on the top portion of the filter were removed with a wet cotton swab. Invading cells, on the bottom portion of the membrane, were washed with PBS and fixed with ice cold methanol for 15 min. Each filter was detached from the plastic insert and mounted on a glass slide with mounting medium containing DAPI (Vector Laboratories, Burlingame, CA, USA). The total number of invading cells, from four independent biological replicates, was assessed by counting individual nuclei on a Zeiss Imager.Z1, AxioCam fluorescence microscope.

Slow aggregation assays, were performed by coating each well of a 96-well plate with 50 µL of a 6.7 mg/mL solution of bacto-agar in PBS. A total of 2×10^4 cells were plated per well in triplicate for each experimental condition. Aggregation was monitored under an inverted microscope and photographed at 0, 24 and 48 h post seeding with a Nikon Digital Camera. At least three independent biological replicates were performed.

11. *Wound Healing Assay*

Wound healing assays were performed by seeding 2.1×10^4 cells per condition in a culture insert µ-Dish (iBiDi, Martinsried Germany), according to manufacturers' specifications. Briefly, after detachment of the cell culture insert, cell migration was monitored with a Nikon Digital Camera every 6 h. The last time point recorded was at 32 h, as the gap between the two migrating regions was already closed. At least three biological replicates were performed.

12. *Tumor growth kinetics*

All procedures involving animals were performed in accordance with the European Guidelines for the Care and Use of Laboratory Animals, Directive 2010/63/UE and the National Regulation published in 2013 (Law number: 113/2013, from August 7th) and

approved by the national Ethics Committee from the Portuguese DGAV (ref. n° 013042/2017-05-08). The authors involved in these experiments have an accreditation for animal research given by the Portuguese National Authorities (Ministerial Directive 1005/92). NIH(S)II: nu/nu mice, a strain described by Azar et al. 1980 [42], were generated under Ipatimup/i3S supervision. MKN74_Mock and MKN74_CD44v6 cells (5×10^6) were subcutaneously injected bilaterally into the back of four 6–8 week old male nude mice. Animals' health was monitored daily. Tumor size was measured using external digital calipers, every 3 to 6 days, to assess tumor growth kinetics. Tumor volume was calculated using the following formula: length × width^2 × 0.5. The experiment was terminated and mice humanely euthanized by cervical dislocation preceded by anesthesia with isoflurane when individual tumor volumes reached ~1000 mm^3. Results are expressed as the average +/−SEM of three animals/tumors (each animal harbored one tumor from MKN74_Mock cells and one tumor from MKN74_CD44v6 cells).

13. *Assessment of cell survival upon drug treatments*

The effects of cisplatin and 5-FU (both from Sigma Aldrich, Poole, UK) on cell survival of the MKN74_Mock, MKN74_CD44v6 and MKN74_CD44s cells were evaluated by the PB assay, mentioned above. Briefly, cells were seeded in 96-well plates (2500 cells per well), allowed to adhere for 24 h and then incubated with cisplatin or 5-FU for 48 h. Cells were then processed for the PB assay, as described above. Cell survival for each drug treatment was calculated, as a percentage, in relation to the respective vehicle-treated control, for each cell line. At least three independent experiments were performed, each measured in triplicate.

14. *Assessment of cisplatin-induced apoptosis*

MKN74_Mock, MKN74_CD44v6 and MKN74_CD44s cells were seeded in 6-well plates (1.0×10^5 cells/ well), left to adhere for 24 h, and incubated with 10 µM of cisplatin for 24 and 48 h. Cisplatin-induced apoptosis was assayed by labelling cells with Annexin V-APC antibody (ImmunoTools, Friesoythe, Germany), according to the manufacturer's instructions. Briefly, cells were trypsinized, pelleted, washed with PBS, resuspended in Annexin V binding buffer (10 mM HEPES, pH 7.4; 140 mM NaCl; 2.5 mM $CaCl_2$) and incubated with Annexin V APC-conjugate for 15 min. Cells were then washed twice in PBS and resuspended in Annexin V binding buffer. Measurement of phosphatidylserine externalization was analyzed using an Accuri C6 flow cytometer and Accuri C6 software

(BD Biosciences, Franklin Lakes, NJ, USA), plotting at least 20,000 events per sample. Results represent the average of at least three independent experiments.

15. *CD44v6 expression inhibition by siRNA*

GP202 and MKN45 cells were transfected with siRNAs for CD44v6 using Lipofectamine® RNAiMax Transfection Reagent (ThermoFisher Scientific, Waltham, MA, USA), according to the manufacturers' instructions. Briefly, cells were seeded in 6-well plates (2×10^5 cells/well and 1.5×10^5 cells/well, respectively GP202 and MKN45 cell lines). After 24 h, lipid based conjugates were prepared by mixing 20 nM of non-targeting siRNA (negative control DS NC1; iDT, Leuven, Belgium), or human CD44v6 siRNA (Sense strand: 5'-GCGUCAGGUUCCAUAGGAAUCCUTT-3' and Antisense strand: 5'-AAAGGAUUCCUAUGGAACCUGACGCAG-3', custom made from iDT, Leuven, Belgium), to diluted Lipofectamine® RNAiMax Reagent in 1:1 ratio. The conjugates were incubated for 5 min at room temperature and added dropwise to the cells. Upon 48 h of incubation, protein extraction and Western blots were performed to evaluate the efficacy of CD44v6 silencing. In addition, in vitro cisplatin treatments (10 or 20 µM, for MKN45 and GP202 respectively) were carried out and apoptosis assessed (as described above).

16. *Assessment of percentage of CD44v6+ cells upon cisplatin incubation*

MKN74_Mock and MKN74_CD44v6 were mixed and seeded in 6-well plates with an initial density of 5×10^4 cells/well (50:50 proportion), allowed to grow for 24 h and incubated with 10 µM of cisplatin or vehicle (0.9% (*v/v*) NaCl) for 6 h (preliminary experiments indicated 6 h cisplatin incubation to be suitable for subsequent long-term experiments, as it induced a reasonable degree of apoptosis and cells were still able to recover/proliferate a few days after cisplatin incubation). Cells were then washed with PBS, growth medium was replaced with cisplatin-free media and co-cultures were maintained during 15 days. CD44v6 cell enrichment was assessed at several time points by flow cytometry using a CD44v6 conjugated antibody. Briefly, at each time point, cells were washed with PBS, versinized (ThermoFisher Scientific, Waltham, MA, USA) for 15 min, blocked in PBS-2% FBS for 30 min and incubated with CD44v6-APC conjugated antibody (2F10; 10 µL/106 cells; 30 min; R&D Systems, McKinley Place, MN, USA). Cells were subsequently washed with PBS-2% FBS and analysed by flow cytometry. Fluorescence was analyzed using a FACS Canto II (BD Biosciences, Franklin Lakes, NJ, USA). The mean fluorescence intensity was measured for at least 20,000 gated events per sample and data were analyzed using the software FlowJo, version 10.

17. *Statistical Analysis*

For statistical significance assessment, a Two-way ANOVA with Tukey's Post Hoc Test was performed. A p-value < 0.05 was considered significant and all analyses were performed using GraphPad Prism version 8.2.1 for Windows.

Results

1. CD44v6 overexpression is not a driver of GC development

In an attempt to clarify the role of CD44v6 overexpression in GC, we generated isogenic cell lines by stably expressing in a CD44-null MKN74 GC cell line (**Figure S1**), the following sequences: (i) a CD44v6-containing isoform highly expressed in GC cells (GP202 cell line, **Figure S2**) [12], from now on mentioned as MKN74_CD44v6 cells (**Figure 1A**); (ii) the CD44s isoform (MKN74_CD44s cells, **Figure 1A**), or; (iii) the empty plasmid (MKN74_Mock cells, **Figure 1A**). Characterization of the generated cells confirmed the expression of the intended transcripts at the transcript and protein levels, as well as its localization at the cell membrane (**Figure 1B–D**). Moreover, the CD44v6 expression levels, obtained here, are physiologically relevant since they are similar to those endogenously expressed in the GP202 cell line (data not shown).

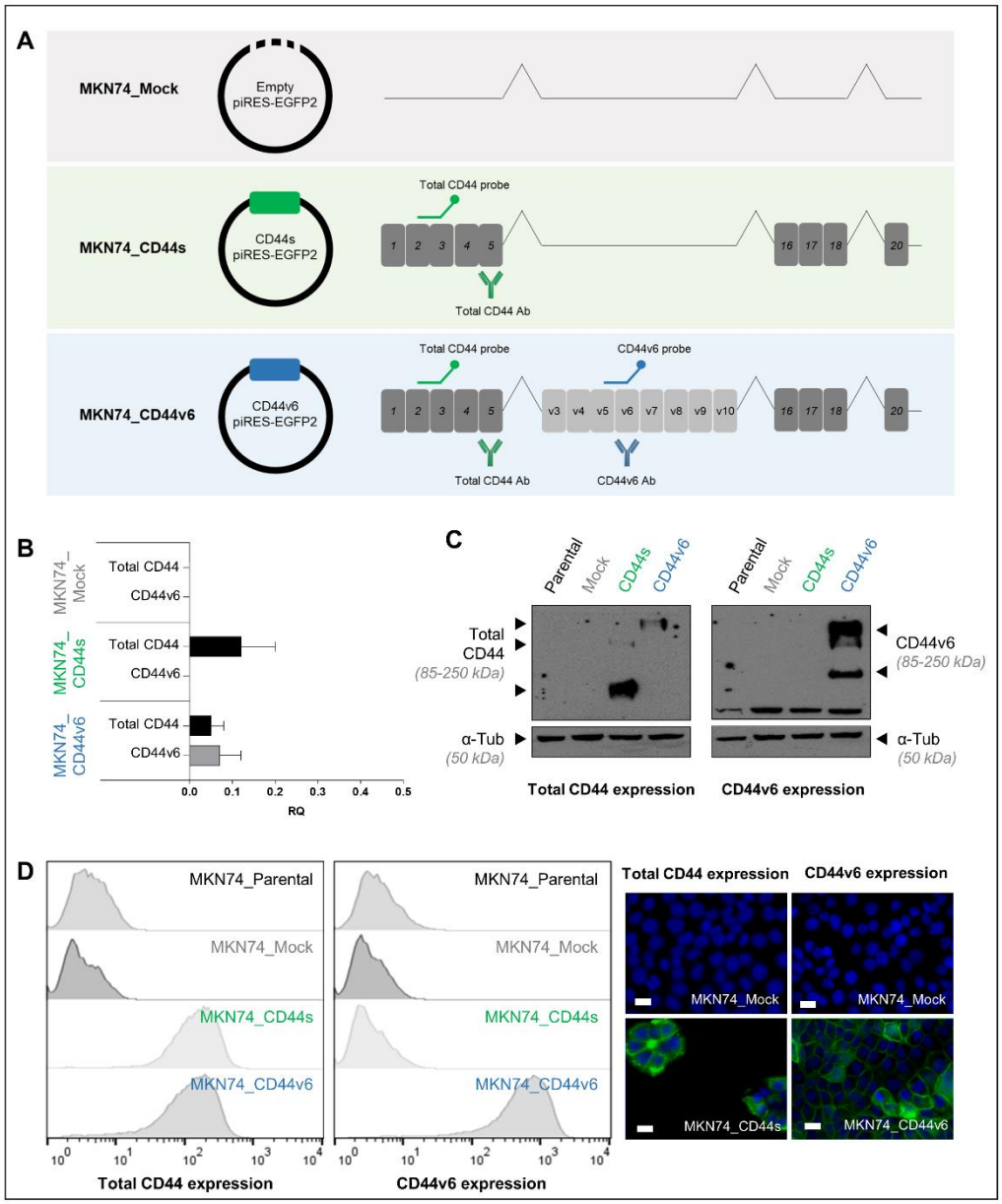

Figure 1. The generated MKN74 cells express the intended CD44 transcripts. (**A**) Transcripts transfected into the MKN74 (CD44v6 negative) gastric cancer (GC) cell line. The CD44 canonical form is the long cytoplasmic tail, exon 20 containing isoform (CD44-03 – ENST00000263398). The exon v6 containing transcript expresses the variable exons between v3-v10 (variant CD44-04 – ENST00000415148). Ensembl release 68, July 2012. It is highlighted where the probes and antibodies, used below, bind to the cDNA or protein, respectively; (**B**) Real time qRT-PCR representing the fold change expression of total CD44 and CD44v6 in transfected cells. Results are shown as average + SD and are representative of three independent experiments. The parental and MKN74_Mock transfected cells were used as negative controls; (**C**) Western Blot depicting total CD44 and CD44v6 protein levels in the generated MKN74 cells; (**D**) Expression was assessed at the post-translational level by immunofluorescence and flow cytometry against total CD44 and CD44v6. Nuclei are stained with DAPI (represented in blue) and white scale bars represent a distance of 20 µm.

These three isogenic cell lines were further characterized and no differences in growth rate, invasion, cell-cell aggregation or migration capacity were observed between them (**Figure 2A–D**). In addition, non-stimulated isogenic cell lines presented no differences regarding the expression of known CD44 interactors and downstream signaling partners (AKT, EGFR, ERK 1/2, P38 and STAT3) at the post-translational level (**Figure 2E, F**). In accordance with these results, tumor growth kinetics was also similar between MKN74_CD44v6 and MKN74_Mock cells (**Figure 2G**). The lack of an obvious correlation between overexpression of CD44v6 and the tested cancer hallmarks, suggests that CD44v6 is not a driver of GC progression.

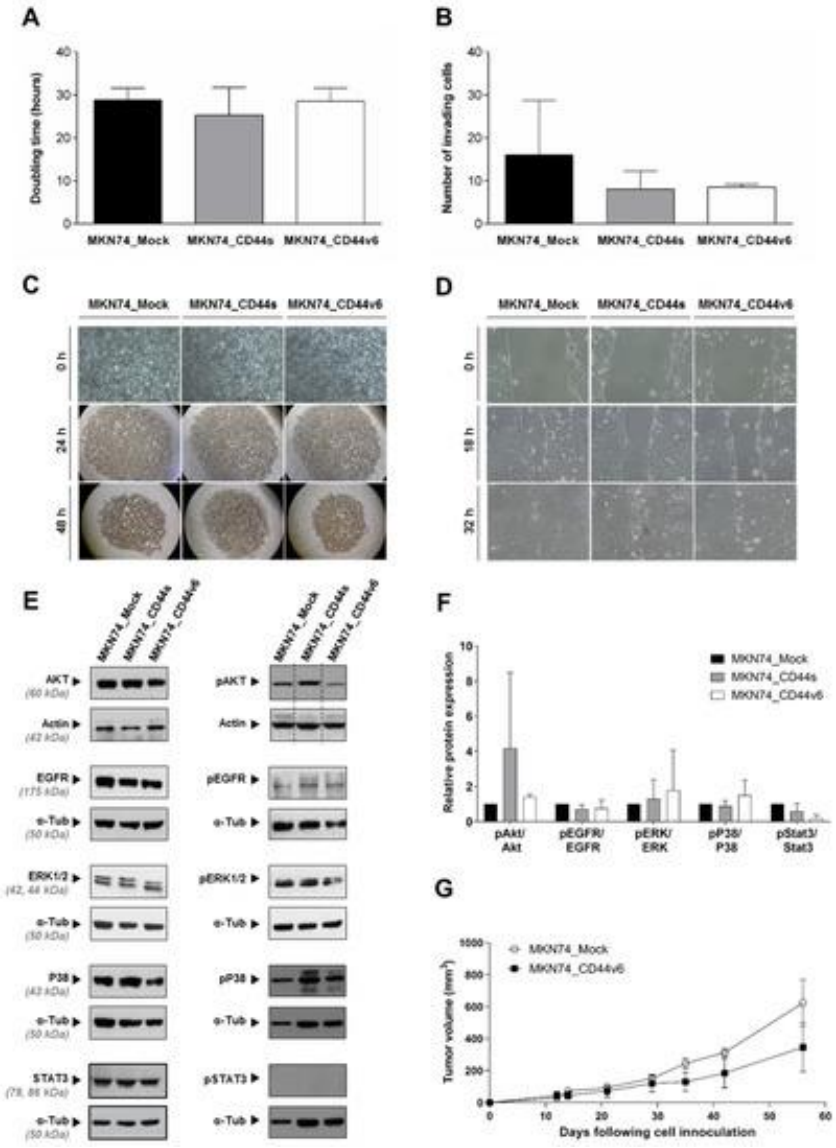

Figure 2. Functional characterization of the generated MKN74_Mock, MKN74_CD44s and MKN74_CD44v6 cells regarding: (**A**) Doubling time; (**B**) Invasion capacity; (**C**) Slow aggregation assay; (**D**) Migration capacity; (**E**) Protein expression of common CD44 interactors: AKT, EGFR, ERK 1/2, P38 and STAT3 and respective phosphorylated forms; (**F**) Relative protein quantification of pAKT, pEGFR, pERK 1/2, pP38 and pSTAT3 with respect to the respective total protein amount. All data are represented as average + SD and/or are representative of three independent experiments; (**G**) Tumor growth kinetics of MKN74_Mock and

MKN74_CD44v6 xenografts in nude mice, presented as average +/− SEM. No statistical differences were observed.

2. CD44v6 influences response to cisplatin treatment in GC cells

We then investigated whether CD44v6 influences response to conventional chemotherapeutic agents, namely cisplatin and 5-fluorouracil (5-FU), often included in the chemotherapy regimens provided to GC patients. We verified that MKN74_CD44v6 cells survive better to a clinically relevant cisplatin concentration (10 µM) (**Figure 3A**), compared to MKN74_Mock cells ($p < 0.05$), whereas no differential response was observed in response to 5-FU treatment (**Figure 3B**). Moreover, MKN74_CD44v6 cells also exhibited decreased apoptosis levels in response to cisplatin in comparison to both isogenic counterparts, $p < 0.001$ (**Figure 3C**). These results indicate that de novo expression of CD44v6 in GC cells allows tolerating cisplatin treatment.

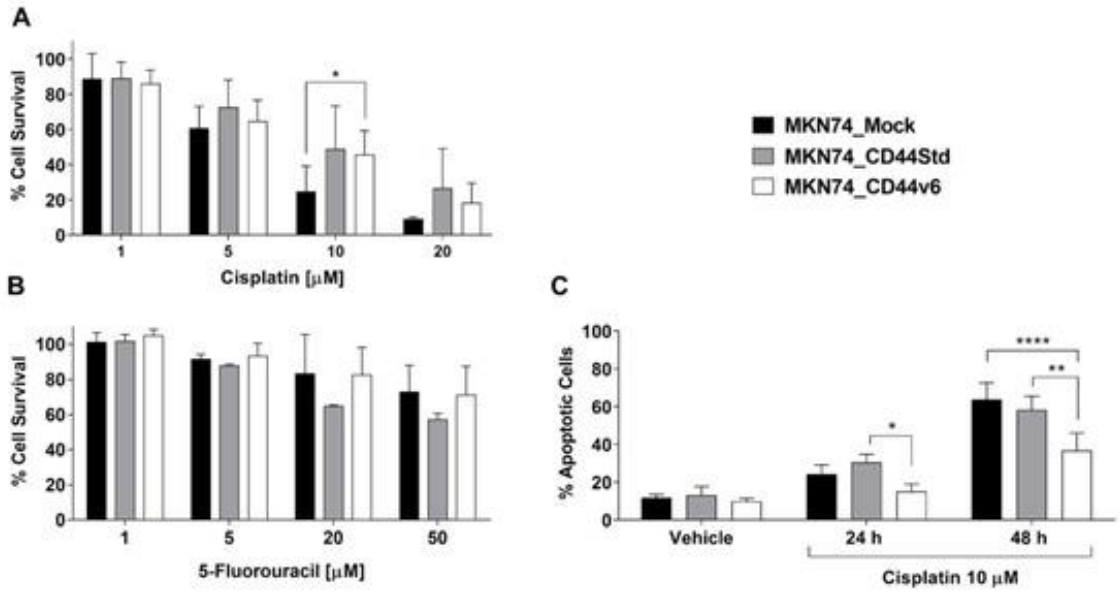

Figure 3. Assessing the response of the isogenic MKN74 cells to conventionally used chemotherapeutic agents: **(A)** Percentage cell survival upon incubation with cisplatin or **(B)** 5-FU for 48 h (compared to vehicle control) in MKN74 cells; **(C)** Percentage of apoptotic cells in MKN74 cells incubated with 10 µM cisplatin or vehicle (0.9% NaCl) for 48 h. Results are expressed as the average + SD of at least three independent experiments. Statistically significant results were determined by Two-way ANOVA with Tukey's multiple comparisons test (* $p < 0.05$; ** $p < 0.001$; **** $p < 0.0001$).

To confirm these results in a model that better mimics the natural context, we modeled the expression of CD44v6 in two non-edited GC cells that endogenously overexpress CD44v6 in all their cells (GP202 and MKN45; **Figure S1**) and treated them with cisplatin. Specific

siRNAs were used to inhibit CD44v6 expression, with 50% and 90% inhibition levels being obtained for MKN45 and GP202, respectively (**Figure 4A**). CD44v6 depleted cells displayed higher cisplatin-induced apoptosis levels when compared to siRNA scramble controls, $p < 0.001$ (**Figure 4B**), indicating that CD44v6 expression inhibition renders cancer cells more sensitive to the effects of this drug. Although the siRNAs we used in this experiment can efficiently inhibit the expression of CD44v6, our results could have been reinforced if an additional set of CD44v6 siRNAs had also been used. Nevertheless, taken together, these results consistently indicate that, in these GC controlled models, CD44v6 modulates response to cisplatin treatment.

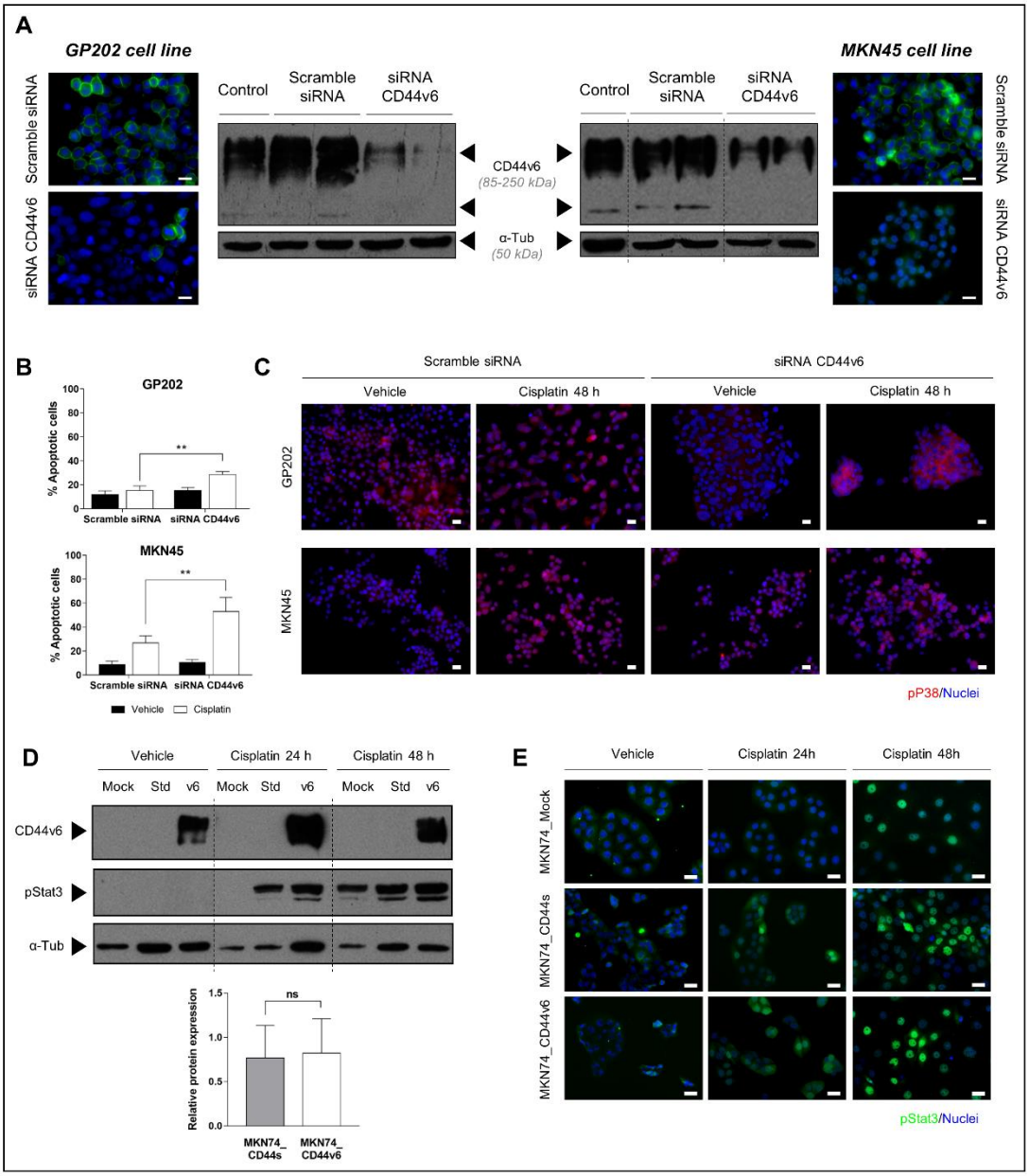

Figure 4. CD44v6-induced modulation to cisplatin response in GC cells is possibly mediated by pSTAT3 or pP38. (**A**) Immunofluorescence and Western blotting of CD44v6 in GP202 (left) and MKN45 (right) upon

incubation with CD44v6 specific siRNAs, compared with incubation with scramble siRNA. Expression inhibition levels were, on average, ~90% and ~50% for GP202 and MKN45, respectively, in two independent experiments for each cell line. CD44v6 is represented in green; (**B**) Percentage of apoptotic cells in GP202 and MKN45 cell lines in response to 48 h treatment with cisplatin (concentrations selected according to **Figure S3**) or vehicle, following a 24 h incubation with scramble or CD44v6 siRNAs. Results are expressed as the average + SD of at least three independent experiments. Statistically significant results were determined by Two-way ANOVA with Tukey's multiple comparisons test (* $p < 0.05$; ** $p < 0.001$; **** $p < 0.0001$); (**C**) Immunofluorescence of pP38 (seen in red) in GC cell lines treated with vehicle control or with cisplatin for 48 h (following a 24 h pre-incubation with scramble or CD44v6 siRNAs). Percentage of cells with nuclear pP38 expression is shown underneath the corresponding experimental conditions; **(D)** Western blotting of pSTAT3 in MKN74 isogenic cell lines in vehicle control and following 24 and 48 h with 10 μM cisplatin treatment. CD44v6 and pSTAT3 were run in the same gel against the same tubulin; **(E)** Immunofluorescence of pSTAT3 (seen in green) in vehicle and cisplatin treated cell lines. In all immunofluorescence images, nuclei are stained with DAPI (seen in blue) and white scale bars represent a distance of 50 μm.

3. CD44v6-induced modulation to cisplatin response in GC cells is likely mediated by pSTAT3 or pP38

Since activation of STAT3 or P38 signaling pathways have been described as mediators of survival in response to cisplatin, we evaluated the levels of pSTAT3 and/or pP38 in the MKN74 isogenic model and in the GC cells that endogenously overexpress CD44v6, GP202 and MKN45 (**Figure 4C–E**). Regarding the isogenic model, none of the three cell lines present the phosphorylated form of STAT3, pSTAT3, at basal level (**Figure 4D,E**; and previously observed in **Figure 2E**). However, following 24 h of cisplatin treatment, pSTAT3 levels increased in MKN74_CD44v6 overexpressing cells, but also in MKN74_CD44s cells, but not in Mock cells (**Figure 4D,E**). Only after 48 h following cisplatin treatment, all three cell lines presented high pSTAT3 levels. Although STAT3 activation, through phosphorylation, becomes a general survival response after 48 h of cisplatin treatment, CD44v6 cells seem to more rapidly induce and maintain STAT3 activation. Regarding P38, the activated form of this protein is already present in the parental MKN74 cell line and no changes were observed in the remaining conditions (**Figure S4 A,B**). We then used GP202 and MKN45 GC cell lines (that endogenously express CD44v6) to test STAT3 and P38 activation following cisplatin treatment in CD44v6 depleted cells. As pSTAT3 is constitutive in both cell lines, we could not use it as a readout of CD44v6 overexpression, nor of cisplatin treatment (**Figure S4C**). The CD44v6 expressing GP202 cells constitutively present pP38 (**Figure 4C**). Following cisplatin treatment, CD44v6 expressing cells show a small, although not statistically significant, increase in the activation of P38 (**Figure 4C**, upper left panel), without an evident difference in terms of cisplatin-induced apoptosis compared to vehicle control for this tested concentration (**Figure 4B**). However, upon CD44v6 depletion, pP38

expression is no longer observed in the nucleus of vehicle nor of cisplatin treated cells (**Figure 4C**, upper right panel), indicating that, in this cell line, nuclear pP38 expression is dependent on the presence of CD44v6. We can then hypothesize that the increased cisplatin sensitivity observed upon depletion of CD44v6 in GP202 cells, in **Figure 4B**, may be due to the loss of CD44v6 mediated pP38. MKN45 parental cells endogenously expressing CD44v6, also present P38 constitutively activated. Similarly to GP202, in the presence of CD44v6, there is only a small increase in P38 activation in response to cisplatin treatment (**Figure 4C**, lower left panel). However, contrary to GP202, in CD44v6 expressing MKN45 cells, there is a significant level of cisplatin-induced apoptosis, compared to vehicle (**Figure 4B**), which is probably related to the cisplatin concentrations used. Regarding P38 activation, while in GP202 cells this depends on the presence of CD44v6, in MKN45 cells P38 remains activated (and in the nucleus) of most cells upon CD44v6 depletion (**Figure 4C**, lower right panel). Interestingly, in MKN45 cells, CD44v6 also seems to be relevant for P38 activation, at least in the presence of cisplatin, since the percentage of cells with nuclear pP38 expression is significantly reduced when CD44v6 is depleted (**Figure 4C**, lower right panel). Nevertheless, in the presence of both CD44v6 and pP38, MKN45 cells cope better with cisplatin treatment than with only pP38. Overall, these results indicate that in the three GC cell lines, concomitant CD44v6 expression, STAT3 activation and P38 activation is associated with increased survival after cisplatin treatment.

4. CD44v6 expressing cells are involved in GC cell overgrowth after cisplatin treatment

As CD44v6-positive (CD44v6+) cells seem to survive better after cisplatin treatment than CD44v6-negative cells (CD44v6−), it is likely that the proportion of CD44v6+ and CD44v6− cells in heterogeneous tumors (often found in GC, as shown in [29]) influences response to chemotherapy. We set out to test this hypothesis in vitro, by mimicking the effects of chemotherapy on a CD44v6 heterogeneous tumor. For that, we co-cultured CD44v6+ and CD44v6− cells (in a 50:50 ratio), treated them with cisplatin and then allowed them to recover for 15 days, without drug treatment. We then analyzed the proportion of the two cell populations at intermediate time-points and at the end of the experiment by flow cytometry (**Figure 5A**). During recovery from cisplatin treatment, and from day 9 onwards, the CD44v6+ cell population constitutes more than 70–80% of the entire cell culture, $p < 0.0001$ (**Figure 5B**). These results indicate that CD44v6 is involved in GC cell overgrowth after cisplatin treatment. If formally demonstrated in patients, this may suggest that cancer relapses after platinum-based chemotherapy may also be enriched in CD44v6+ cells.

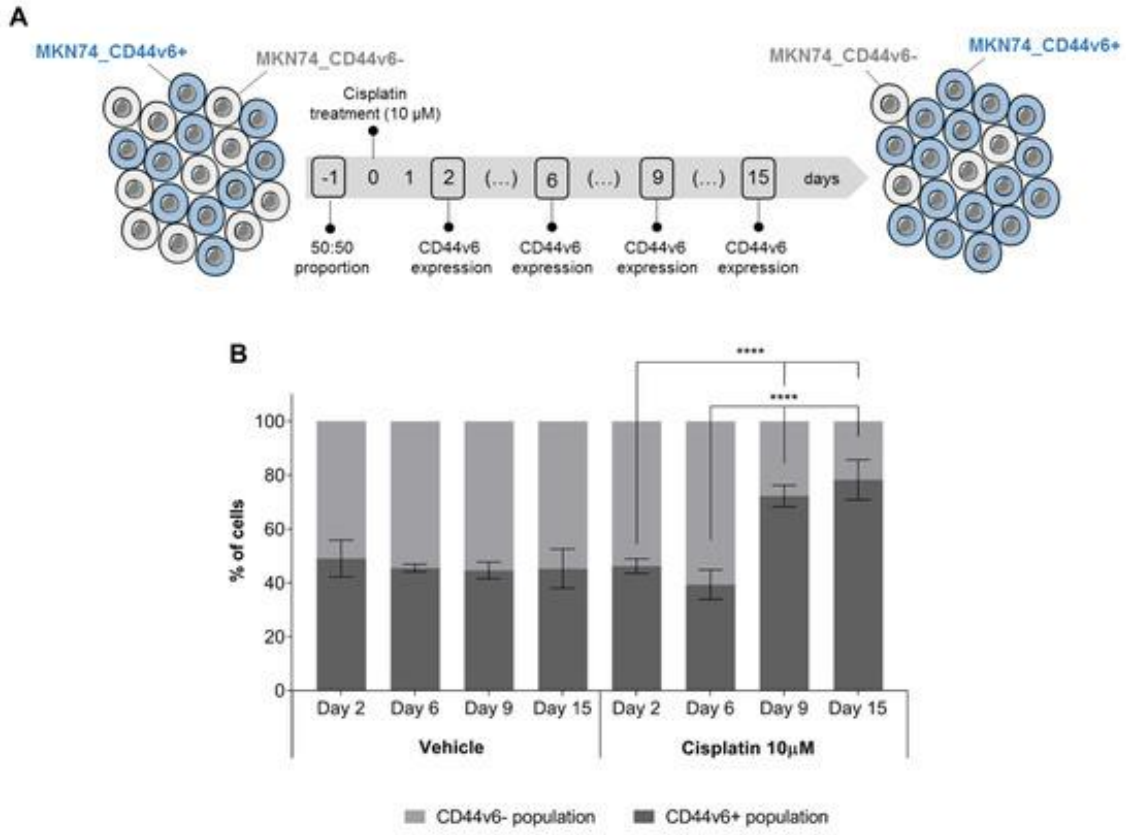

Figure 5. CD44v6+ expressing cells are involved in GC cell overgrowth after cisplatin treatment. (**A**) Scheme depicting the longitudinal assessment of CD44v6+ and CD44v6− population dynamics following cisplatin incubation, in a co-culture setting; (**B**) Percentage of CD44v6+ cells in co-cultures of CD44v6+ and CD44v6− MKN74 cells (MKN74_CD44v6 and MKN74_Mock cells, respectively) following a 6 h incubation with cisplatin (or vehicle control) and up to 15 days of recovery. At the end of the experiment > 80% of the cell culture is composed of CD44v6+ cells. The cisplatin concentration used is clinically relevant. Results expressed as the average +/− SD of at least three independent experiments. Statistically significant results were determined by Two-way ANOVA with Tukey's multiple comparisons test (**** $p < 0.0001$).

Discussion

Aiming to unveil the role of CD44v6 in GC, we generated an isogenic model of GC cells stably expressing CD44s or CD44v6. Expression of CD44v6 or CD44s induced no differences in terms of doubling-time, invasion, cell-adhesion, cell motility, and tumorigenic potential in vivo. These experiments were performed in a tumorigenic GC cell line, which is a limitation of our study regarding possible conclusions on the capacity of CD44v6 de novo expression to influence gastric tumor initiation. Nevertheless, this lack of an obvious correlation between overexpression of CD44v6 and the tested cancer hallmarks, together with our earlier report showing that CD44v6 was already overexpressed in pre-malignant

lesions [12] (most of which do not lead to cancer), suggests that CD44v6 is not a driver of GC progression.

Importantly, our data identify CD44v6 as a modulator of response to cisplatin treatment. Indeed, in the isogenic cell line model, overexpression of CD44v6 led to increased cell survival and decreased cisplatin-induced apoptosis. Likewise, downregulation of CD44v6-containing isoforms, in GC cell lines that endogenously express it, led to increased sensitivity to cisplatin-induced apoptosis. Similar results have been described in other cancer types [24,30], suggesting that expression of these variant isoforms could somehow mediate an escape mechanism to programmed cell death. In fact, expression of CD44v has been described to have a role in promoting chemoresistance through the upregulation of lyn kinase, via the Pi3K/AKT pathway in colon carcinoma cells [31] and CD44v6 in particular, was shown to block Fas mediated apoptosis [32]. The mechanism downstream of CD44v6, or cooperating with CD44v6, by which CD44v6 expressing cells have increased cisplatin survival is still unknown, however, our data show that in GC cells this may occur due to the concomitance of CD44v6 expression and activation of STAT3 or P38, depending on the cellular context. Indeed, high expression of activated STAT3 has been shown to contribute to cisplatin resistance in ovarian cancer [33]. Moreover, abrogation of STAT3 activity has been shown to circumvent cisplatin resistance in ovarian cancer cells [34], making it a promising target to reverse cisplatin resistance in ovarian and other cancer types [33,34,35]. It is therefore likely that the early activation of STAT3 we observed in response to cisplatin, in CD44-expressing cells, and mainly in CD44v6-expressing cells, is contributing to increase apoptosis resistance to this drug in the isogenic MKN74 cell line model. The mechanism by which CD44v6 is capable of modulating cisplatin response in GC cells seems to depend on the cellular context. In the two cell lines that endogenously express CD44v6 (MKN45 and GP202), it seems that activation of P38, which our data showed to be CD44v6 dependent in GP202 cells, is contributing to cisplatin resistance. Therefore, when we down-regulate the expression of CD44v6 in GP202 cells, P38 is no longer activated and cells become more sensitive to cisplatin. This is not surprising considering that inhibition of P38 has been shown to sensitize tumor cells to cisplatin-induced apoptosis [36]. In the MKN45 cells, where expression of pP38 is independent of CD44v6, it is not by losing pP38 that the CD44v6 depleted cells become more sensitive to cisplatin. This is probably due to another unexplored pathway. Nevertheless, what does become evident from our experiments is that both GP202 and MKN45 cells respond better to cisplatin treatment when they are expressing both CD44v6 and pP38. Indeed, the same can also be observed in the isogenic MKN74 cells that constitutively express pP38 (regardless of cisplatin treatment) but where the CD44v6 expressing cells cope better with cisplatin treatment. Regarding activation of STAT3, our data are less informative; however,

as STAT3 becomes or remains activated upon cisplatin treatment in all tested cell lines, we may hypothesize that it also contributes, in a context of CD44v6 expression and P38 activation, to promote survival of cancer cells when these are challenged by cisplatin. Indeed, a regulatory mechanism between STAT3 and P38 has been described in head and neck cancer, whereby STAT3 phosphorylation requires P38 [37]; however, additional experiments would be required to assess if this is also the case in GC cells. Importantly our study has some limitations since it only provides indications that activation of STAT3 and P38 may be implicated in CD44v6 mediated response to cisplatin. To confirm these findings, additional studies would have to be performed using, for instance, STAT3 inhibitors to see if in their presence MKN74_CD44v6 cells regain sensitivity to cisplatin, equal to that observed in the MKN74_Mock cells. Interestingly, our experiments using co-cultures of CD44v6+ and CD44v6− cells show that CD44v6+ cells could have some selective advantage when a heterogeneous gastric tumor is treated with cisplatin-based chemotherapy. This selective advantage of CD44v6+ cells was only observed following 9 days of incubation with cisplatin, and appeared to be a sudden increase when compared with the previous time-point tested (6 days). Nevertheless, and considering those results represent the balance between the cells that are dying and the cells that are proliferating in each of the CD44v6+ and CD44v6− cell populations, we believe this was indeed a gradual increase in CD44v6+ cells that took place between day 6 and day 9. However, from the previous results described herein, we can assume that the molecular changes, that ultimately gave rise to this result, started to occur much earlier during/shortly after the cisplatin treatment. This overgrowth of CD44v6+ cells after chemotherapy, may indicate that this cell population can get enriched in GC relapses that arise after chemotherapy. This is plausible as CD44/CD44v are considered CSC markers in several tumor types, including GC [16,17]. Further studies in patients' samples and supported by patients' clinical data are required to address this subject. If our findings are confirmed, strategies to specifically eliminate CD44v6+ cells could lead to decreased recurrence and improved patient survival. One possible strategy is the targeting of CD44v6 downstream effectors, as direct targeting of CD44v6 ought to be avoided due to the lethal skin toxicity side effects described in a Phase I clinical trial using a highly potent antimicrotubule agent coupled to a monoclonal antibody against CD44v6 [38]. Our data also shed light into GC molecular heterogeneity and its relation with therapy, by suggesting that the CD44v6+ population is responsible for tumor overgrowth and may potentially help drive recurrence following conventional chemotherapy, in tumors composed of CD44v6+ and CD44v6− cell populations. Indeed, considering that more than half of GC tumors possess some degree of heterogeneity regarding CD44v6 expression (with CD44v6+ and CD44v6− cell populations co-existing in

the same tumor) [29], this may have important consequences in terms of GC patients' clinical outcome.

Conclusions

In conclusion, we show that expression of CD44 isoforms containing exon v6 in the presence of activated STAT3 and P38, increase cell survival in response to cisplatin treatment in GC cells and that these cells override CD44v6-negative cells after cisplatin treatment. This suggests that tumor expression of CD44v6-containing variants may condition the outcome of GC patients treated with chemotherapy.

Funding

This work was supported by FEDER - Fundo Europeu de Desenvolvimento Regional funds through the COMPETE 2020 – Operacional Programme for Competitiveness and Internationalisation (POCI), Portugal 2020, and by Portuguese funds through FCT – Fundação para a Ciência e a Tecnologia/Ministério da Ciência, Tecnologia e Inovação in the framework of the project "Institute for Research and Innovation in Health Sciences" (POCI-01-0145-FEDER-007274). This work was also financed by the projects NORTE-01-0145-FEDER-000003 and NORTE-07-0124-FEDER-000029 - supported by Norte Portugal Regional Programme (NORTE 2020), under the PORTUGAL 2020 Partnership Agreement, through the European Regional Development Fund (ERDF) – project POCI-01-0145-FEDER-016390, funded by ERDF, POCI and FCT, and project PTDC/CTM-NAN/120958/2010, from FCT. CP was supported by the grant SFRH/BD/113031/2015 and DF by the grant PD/BD/105976/2014. GMA was supported by the Investigator FCT Program 2013 (IF/00615/2013), POPH - QREN Type 4.2, European Social Fund and Portuguese Ministry of Science and Technology (MCTES).

Acknowledgments

The authors acknowledge the support of the i3S Scientific Platforms "Advanced Light Microscopy", member of the PPBI (PPBI-POCI-01-0145-FEDER-022122), and "Translational Cytometry Unit". CP acknowledges the support of Faculty of Medicine from University of Porto, specifically by the Doctoral Programme in Biomedicine. DF acknowledges the support of the Institute for Biomedical Sciences Abel Salazar from the University of Porto, specifically by the Doctoral Programme on Cellular and Molecular Biotechnology Applied to Health Sciences (reference PD/00016/2012).

Author contributions

G.M.A. and C.O. conceived, designed and supervised the study; C.P., D.F., N.M., and G.M.A. acquired and analyzed the data; C.P., D.F., G.M.A. and C.O. interpreted the data; C.P., D.F., G.M.A. and C.O. drafted the manuscript; All authors critically revised the manuscript for important intellectual content; C.O. and P.L.G. obtained funding. All authors have read and agreed to the published version of the manuscript.

Conflicts of interest

The authors declare no conflict of interest.

References

1. Gallatin, W.M.; Weissman, I.L.; Butcher, E.C. A cell-surface molecule involved in organ-specific homing of lymphocytes. *Nature* **1983**, *304*, 30–34.
2. Koopman, G.; Vankooyk, Y.; Degraaff, M.; Meyer, C.J.L.M.; Figdor, C.G.; Pals, S.T. Triggering of the CD44 Antigen on Lymphocytes-T Promotes T-Cell Adhesion through the Lfa-1 Pathway. *J. Immunol.* **1990**, *145*, 3589–3593.
3. Shimizu, Y.; Vanseventer, G.A.; Siraganian, R.; Wahl, L.; Shaw, S. Dual Role of the CD44 Molecule in T-Cell Adhesion and Activation. *J. Immunol.* **1989**, *143*, 2457–2463.
4. Aruffo, A.; Stamenkovic, I.; Melnick, M.; Underhill, C.B.; Seed, B. CD44 Is the Principal Cell-Surface Receptor for Hyaluronate. *Cell* **1990**, *61*, 1303–1313.
5. Jalkanen, S.; Jalkanen, M. Lymphocyte CD44 Binds the Cooh-Terminal Heparin-Binding Domain of Fibronectin. *J. Cell Biol.* **1992**, *116*, 817–825.
6. Wayner, E.A.; Carter, W.G.; Piotrowicz, R.S.; Kunicki, T.J. The Function of Multiple Extracellular-Matrix Receptors in Mediating Cell-Adhesion to Extracellular-Matrix - Preparation of Monoclonal-Antibodies to the Fibronectin Receptor That Specifically Inhibit Cell-Adhesion to Fibronectin and React with Platelet Glycoproteins Ic-IIa. *J. Cell Biol.* **1988**, *107*, 1881–1891.
7. Ponta, H.; Sherman, L.; Herrlich, P.A. CD44: From adhesion molecules to signalling regulators. *Nat. Rev. Mol. Cell Biol.* **2003**, *4*, 33–45.
8. Naor, D.; Sionov, R.V.; Ish-Shalom, D. CD44: Structure, function, and association with the malignant process. *Adv. Cancer Res.* **1997**, *71*, 241–319.
9. Ponta, H.; Wainwright, D.; Herrlich, P. The CD44 protein family. *Int. J. Biochem. Cell Biol.* **1998**, *30*, 299–305.

10. Prochazka, L.; Tesarik, R.; Turanek, J. Regulation of alternative splicing of CD44 in cancer. *Cell. Signal.* **2014**, *26*, 2234–2239.

11. Ruiz, P.; Schwarzler, C.; Gunthert, U. CD44 Isoforms during Differentiation and Development. *Bioessays* **1995**, *17*, 17–24.

12. da Cunha, C.B.; Oliveira, C.; Wen, X.; Gomes, B.; Sousa, S.; Suriano, G.; Grellier, M.; Huntsman, D.G.; Carneiro, F.; Granja, P.L.; et al. De novo expression of CD44 variants in sporadic and hereditary gastric cancer. *Lab. Invest.* **2010**, *90*, 1604–1614.

13. Bray, F.; Ferlay, J.; Soerjomataram, I.; Siegel, R.L.; Torre, L.A.; Jemal, A. Global cancer statistics 2018: GLOBOCAN estimates of incidence and mortality worldwide for 36 cancers in 185 countries. *CA Cancer J. Clin.* **2018**, *68*, 394–424.

14. Naor, D.; Wallach-Dayan, S.B.; Zahalka, M.A.; Sionov, R.V. Involvement of CD44, a molecule with a thousand faces, in cancer dissemination. *Semin. Cancer Biol.* **2008**, *18*, 260–267.

15. Senbanjo, L.T.; Chellaiah, M.A. CD44: A Multifunctional Cell Surface Adhesion Receptor Is a Regulator of Progression and Metastasis of Cancer Cells. *Front. Cell Dev. Biol.* **2017**, *5*, 18.

16. Yan, Y.; Zuo, X.; Wei, D. Concise Review: Emerging Role of CD44 in Cancer Stem Cells: A Promising Biomarker and Therapeutic Target. *Stem Cells Transl. Med.* **2015**, *4*, 1033–1043.

17. Todaro, M.; Gaggianesi, M.; Catalano, V.; Benfante, A.; Iovino, F.; Biffoni, M.; Apuzzo, T.; Sperduti, I.; Volpe, S.; Cocorullo, G.; et al. CD44v6 is a marker of constitutive and reprogrammed cancer stem cells driving colon cancer metastasis. *Cell Stem Cell* **2014,** *14*, 342–356.

18. Zöller, M. CD44, Hyaluronan, the Hematopoietic Stem Cell, and Leukemia-Initiating Cells. *Front. Immunol.* **2015**, *6*, 235.

19. Yang, Z.; Guo, L.; Liu, D.; Sun, L.; Chen, H.; Deng, Q.; Liu, Y.; Yu, M.; Ma, Y.; Guo, N.; et al. Acquisition of resistance to trastuzumab in gastric cancer cells is associated with activation of IL-6/STAT3/Jagged-1/Notch positive feedback loop. *Oncotarget* **2015**, *6*, 5072–5087.

20. Boulbes, D.R.; Chauhan, G.B.; Jin, Q.; Bartholomeusz, C.; Esteva, F.J. CD44 expression contributes to trastuzumab resistance in HER2-positive breast cancer cells. *Breast Cancer Res. Treat.* **2015**, *151*, 501–513.

21. Gao, Y.; Foster, R.; Yang, X.; Feng, Y.; Shen, J.K.; Mankin, H.J.; Hornicek, F.J.; Amiji, M.M.; Duan, Z. Up-regulation of CD44 in the development of metastasis, recurrence and drug resistance of ovarian cancer. *Oncotarget* **2015**, *6*, 9313–9326.

22. Jung, T.; Gross, W.; Zöller, M. CD44v6 coordinates tumor matrix-triggered motility and apoptosis resistance. *J. Biol. Chem.* **2011**, *286*, 15862–15874.

23. Ni, J.; Cozzi, P.J.; Hao, J.L.; Beretov, J.; Chang, L.; Duan, W.; Shigdar, S.; Delprado, W.J.; Graham, P.H.; Bucci, J.; et al. CD44 variant 6 is associated with prostate cancer metastasis and chemo-/radioresistance. *Prostate* **2014**, *74*, 602–617.

24. Lv, L.; Liu, H.G.; Dong, S.Y.; Yang, F.; Wang, Q.X.; Guo, G.L.; Pan, Y.F.; Zhang, X.H. Upregulation of CD44v6 contributes to acquired chemoresistance via the modulation of autophagy in colon cancer SW480 cells. *Tumour Biol.* **2016**, *37*, 8811–8824.

25. Miyoshi, S.; Tsugawa, H.; Matsuzaki, J.; Hirata, K.; Mori, H.; Saya, H.; Kanai, T.; Suzuki, H. Inhibiting xCT Improves 5-Fluorouracil Resistance of Gastric Cancer Induced by CD44 Variant 9 Expression. *Anticancer Res.* **2018**, *38*, 6163–6170.

26. Chen, Y.; Fu, Z.; Xu, S.; Xu, Y.; Xu, P. The prognostic value of CD44 expression in gastric cancer: A meta-analysis. *Biomed. Pharmacother.* **2014**, *68*, 693–697.

27. Xie, J.W.; Chen, P.C.; Zheng, C.H.; Li, P.; Wang, J.B.; Lin, J.X.; Lu, J.; Chen, Q.Y.; Cao, L.L.; Lin, M.; et al. Evaluation of the prognostic value and functional roles of CD44v6 in gastric cancer. *J. Cancer Res. Clin. Oncol.* **2015**, *141*, 1809–1817.

28. Xu, Y.Y.; Guo, M.; Yang, L.Q.; Zhou, F.; Yu, C.; Wang, A.; Pang, T.H.; Wu, H.Y.; Zou, X.P.; Zhang, W.J.; et al. Regulation of CD44v6 expression in gastric carcinoma by the IL-6/STAT3 signaling pathway and its clinical significance. *Oncotarget* **2017**, *8*, 45848–45861.

29. Pereira, C.; Ferreira, D.; Lemos, C.; Martins, D.; Mendes, N.; Almeida, D.; Granja, P.; Carneiro, F.; Almeida, R.; Almeida, G.M.; et al. CD44v6 expression is a novel predictive marker of therapy response and poor prognosis in gastric cancer patients. *bioRxiv* **2018***,* 468934; doi: 10.1101/468934.

30. Mooney, K.L.; Choy, W.; Sidhu, S.; Pelargos, P.; Bui, T.T.; Voth, B.; Barnette, N.; Yang, I. The role of CD44 in glioblastoma multiforme. *J. Clin. Neurosci.* **2016**, *34*, 1–5.

31. Wang, J.L.; Su, W.Y.; Lin, Y.W.; Xiong, H.; Chen, Y.X.; Xu, J.; Fang, J.Y. CD44v6 overexpression related to metastasis and poor prognosis of colorectal cancer: A meta-analysis. *Oncotarget* **2017**, *8*, 12866–12876.

32. Bendardaf, R.; Lamlum, H.; Ristamäki, R.; Pyrhönen, S. CD44 variant 6 expression predicts response to treatment in advanced colorectal cancer. *Oncol. Rep.* **2004**, *11*, 41–45.

33. Wu, C.J.; Sundararajan, V.; Sheu, B.C.; Huang, R.Y.; Wei, L.H. Activation of STAT3 and STAT5 Signaling in Epithelial Ovarian Cancer Progression: Mechanism and Therapeutic Opportunity. *Cancers (Basel)* **2020**, *12*, 24.

34. Ji, T.; Gong, D.; Han, Z.; Wei, X.; Yan, Y.; Ye, F.; Ding, W.; Wang, J.; Xia, X.; Li, F.; et al. Abrogation of constitutive Stat3 activity circumvents cisplatin resistant ovarian cancer. *Cancer Lett.* **2013**, *341*, 231–239.

35. Sun, C.Y.; Nie, J.; Huang, J.P.; Zheng, G.J.; Feng, B. Targeting STAT3 inhibition to reverse cisplatin resistance. Biomed. *Pharmacother* **2019**, *117*, 109135.

36. Pereira, L.; Igea, A.; Canovas, B.; Dolado, I.; Nebreda, A.R. Inhibition of p38 MAPK sensitizes tumour cells to cisplatin-induced apoptosis mediated by reactive oxygen species and JNK. *EMBO Mol. Med.* **2013**, *5*, 1759–1774.

37. Riebe, C.; Pries, R.; Schroeder, K.N.; Wollenberg, B. Phosphorylation of STAT3 in head and neck cancer requires p38 MAPKinase, whereas phosphorylation of STAT1 occurs via a different signaling pathway. *Anticancer Res.* **2011**, *31*, 3819–3825.

38. Riechelmann, H.; Sauter, A.; Golze, W.; Hanft, G.; Schroen, C.; Hoermann, K.; Erhardt, T.; Gronau, S. Phase I trial with the CD44v6-targeting immunoconjugate bivatuzumab mertansine in head and neck squamous cell carcinoma. *Oral Oncol.* **2008**, *44*, 823–829.

39. Gärtner, F.; David, L.; Seruca, R.; Machado, J.C.; Sobrinho-Simões, M. Establishment and characterization of two cell lines derived from human diffuse gastric carcinomas xenografted in nude mice. *Virchows Arch.* **1996**, *428*, 91–98.

40. Bordeira-Carriço, R.; Ferreira, D.; Mateus, D.D.; Pinheiro, H.; Pêgo, A.P.; Santos, M.A.; Oliveira, C. Rescue of wild-type E-cadherin expression from nonsense-mutated cancer cells by a suppressor-tRNA. *Eur. J. Hum. Genet.* **2014**, *22*, 1085–1092.

41. Nakamura, A.; Nakajima, G.; Okuyama, R.; Kuramochi, H.; Kondoh, Y.; Kanemura, T.; Takechi, T.; Yamamoto, M.; Hayashi, K. Enhancement of 5-fluorouracil-induced cytotoxicity by leucovorin in 5-fluorouracil-resistant gastric cancer cells with upregulated expression of thymidylate synthase. *Gastric Cancer* **2014**, *17*, 188–195.

42. Azar, H.A.; Hansen, C.T.; Costa, J. N:NIH(S)-nu/nu mice with combined immunodeficiency: A new model for human tumour heterotransplantation. *J. Natl. Cancer Inst.* **1980**, *65*, 421–430.

SUPPORTING INFORMATION

(This section includes supporting materials for the original paper 1 - Expression of CD44v6 containing isoforms influences cisplatin response in gastric cancer cells)

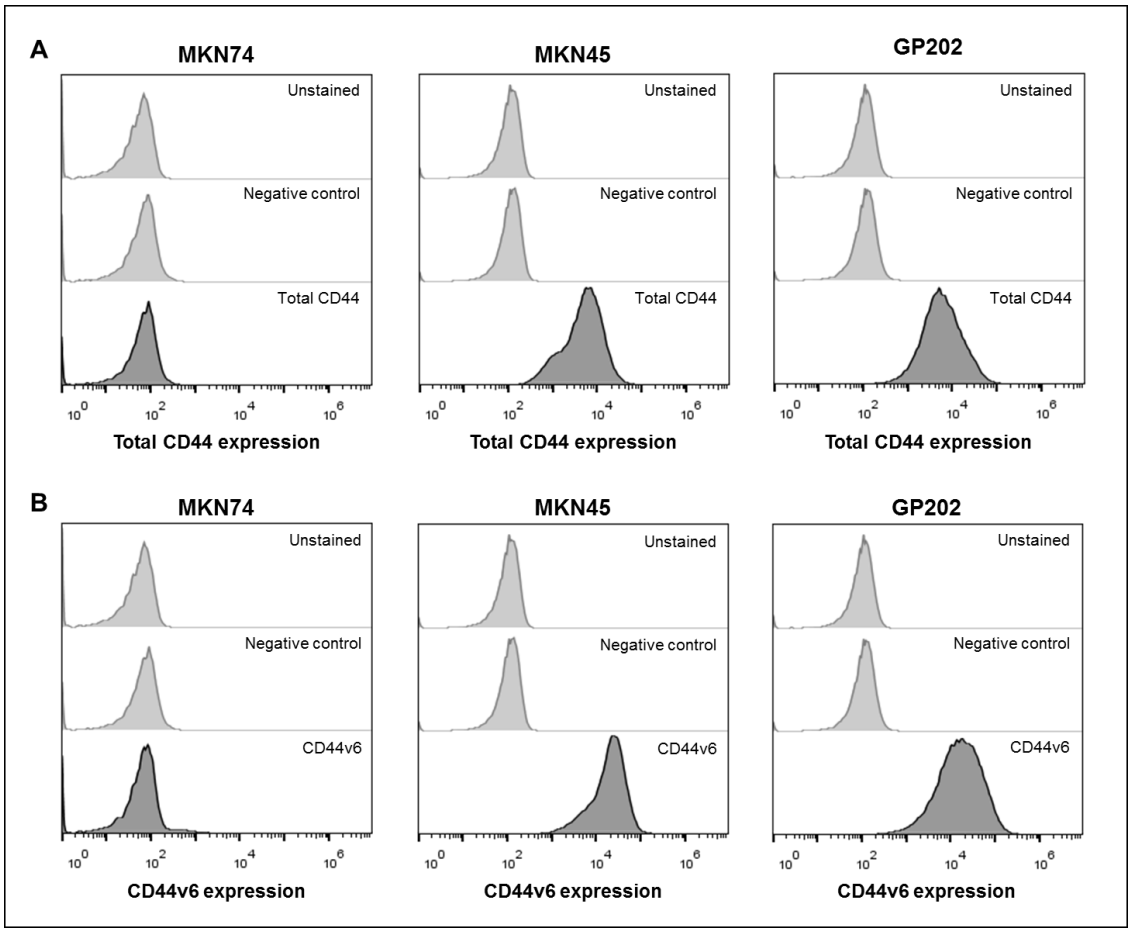

Figure S1. Confirmation that MKN74 cell line is CD44-null and does not express CD44, as determined by flow cytometry. **(*A*)** No expression of the standard version of total CD44 is detected in MKN74 cells (MKN45 and GP202 cells were used as a positive control for the expression of total CD44); **(*B*)** No expression of CD44v6 is detected in MKN74 cells (MKN45 and GP202 cells were used as a positive control for CD44v6 expression).

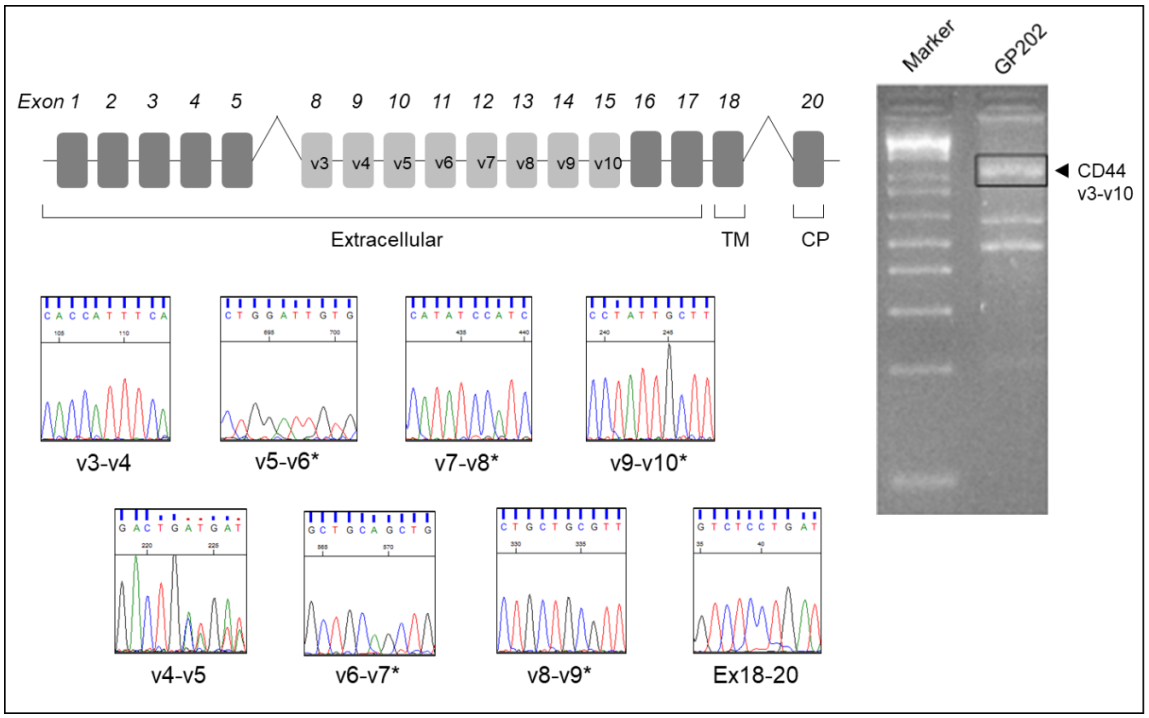

Figure S2. Identification of CD44v3-v10 variant endogenously expressed in the GP202 cell line. The band outlined in the gel represents the CD44v3-v10 transcript. Identity of the transcript was confirmed by Sanger sequencing. Each exon-exon junction in the boundary region was positively identified. It should be noted that the v4-v5 exon boundary displays a double reading frame after the Exonv5 start. One of the sequences has a CAG insertion identified using the mutation surveyor software. *These sequences were obtained with a reverse primer and are shown as the reverse complement of the forward strand.

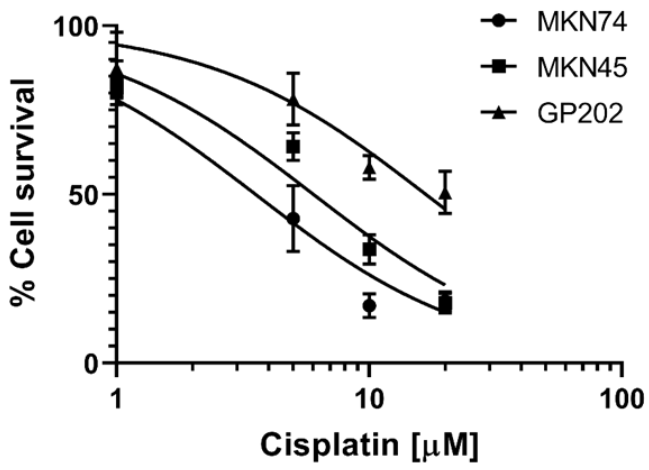

Figure S3. Determination of IC50 values in MKN74, MKN45 and GP202 cell lines. Cells were treated for 48 h with various cisplatin concentrations (1, 5, 10 and 20 μM) and cell survival was determined using a resazurin-based assay (PB). IC50 values were determined by non-linear regression analysis, as follows: MKN74 IC50 ~ 3.6 μM; MKN45 IC50 ~ 6 μM and; GP202 IC50 ~ 17 μM.

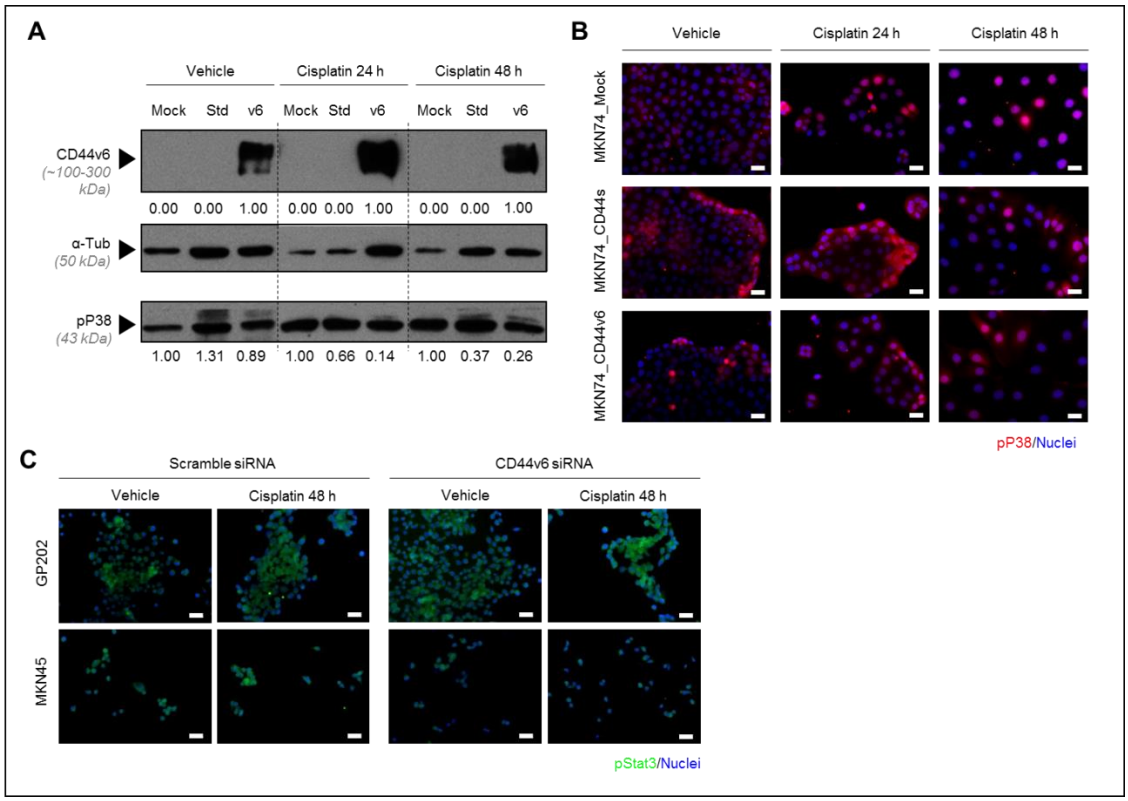

Figure S4: Expression of pP38 and pSTAT3 in MKN74 and GP202/MKN45 cells, respectively. **(A)** Western blotting of pP38 in MKN74 cell lines. CD44v6 and pP38 were run in the same gel as pSTAT3 (shown in Figure 4D) against the same tubulin; **(B)** Immunofluorescence of pP38 (seen in red) in untreated cell lines and upon treatment with cisplatin for 24 and 48 hours; **(C)** Immunofluorescence of pSTAT3 (seen in green) in vehicle and cisplatin treated GP202 and MKN45 cell lines (following a 24 h pre-incubation with scramble or CD44v6 siRNAs). Nuclei are stained with DAPI (seen in blue) and white scale bars represent a distance of 50 µm.

Table S1: Primers used in the characterization of v6 containing transcripts in the GP202 cells.

Orientation	In-text Primer Name	Binding Site	Primer Sequence (5' – 3')	Melting Temperature	Comment
Forward	A	Exon 5	CATCCCAGACGAAGACAGTCC	Tm = 66.0 °C	
	B	Exon v6	CCCATTCGACAACAGGGACA	Tm = 69.1 °C	
	C	Exon 5/ v3	GAATCCCTGCTACCAGTACG	Tm = 61.1 °C	
Reverse	D	Exon v6	TTGGCGATATCCCTCATGCC	Tm = 68.3 °C	
	E	Exon 16/ 17	GTGTCCATCTGATTCAGATCCA	Tm = 63.9 °C	
	F	Exon 17/ 18	TGATCAGCCATTCTGGAATTTG	Tm = 65.9 °C	
	G	Exon 19	GAATCTCTTCAACTTCTTCGAC	Tm = 58.6 °C	Amplifies specifically the short tailed isoform
	H	Exon 20	TCTTCATGTCCACATTCTGC	Tm = 61.4 °C	Amplifies the long and short tailed isoforms

CHAPTER III

A Fast Alternative to Soft-Lithography for the Fabrication of Organ-On-a-Chip Elastomeric-Based Devices and Microactuators

Published in Advanced Science, 2021, 8, 2003273

(https://doi.org/10.1002/advs.202003273)

A Fast Alternative to Soft-Lithography for the Fabrication of Organ-On-a-Chip Elastomeric-Based Devices and Microactuators

Daniel A. Ferreira[1,2,3], Mario Rothbauer[4,5], João P. Conde[6,7], Peter Ertl[8], Carla Oliveira,[1,9,10] Pedro L. Granja,[1,2,3]**

[1] i3S – Instituto de Investigação e Inovação em Saúde, Universidade do Porto, Rua Alfredo Allen, 208, 4200-135 Porto, Portugal

[2] INEB – Instituto de Engenharia Biomédica, Universidade do Porto, Rua Alfredo Allen, 208, 4200-135 Porto, Portugal

[3] ICBAS – Instituto de Ciências Biomédicas Abel Salazar, Universidade do Porto, Rua Jorge de Viterbo Ferreira, 228, 4050-313 Porto, Portugal

[4] Department of Orthopedics and Trauma Surgery, Karl Chiari Lab for Orthopedic Biology, Medical University of Vienna, Whäringer Gürtel 18-20, 1090 Vienna, Austria

[5] Institute of Applied Synthetic Chemistry, Vienna University of Technology (TUW), Getreidmarkt, 9/163, 1060 Vienna, Austria

[6] Department of Bioengineering, Instituto Superior Técnico, Universidade de Lisboa, Av. Rovisco Pais, 1, 1049-001 Lisboa, Portugal

[7] Instituto de Engenharia de Sistemas e Computadores – Microsistemas e Nanotecnologia (INESC MN), Rua Alves Redol, 9, 1000-029 Lisboa, Portugal

[8] Faculty of Technical Chemistry, Vienna University of Technology (TUW), Getreidemarkt 9, 1060 Vienna, Austria

[9] Ipatimup – Institute of Molecular Pathology and Immunology, Universidade do Porto, Rua Júlio Amaral de Carvalho 45, 4200-135 Porto, Portugal

[10] Department of Pathology, Faculty of Medicine, University of Porto, Alameda Prof. Hernâni Monteiro, 4200-319 Porto, Portugal

* Joint senior authorship

Keywords: microfluidics, fast prototyping, organ-on-a-chip, pdms, microactuators

ABSTRACT

Organ-on-a-chip technology promises to revolutionize how pre-clinical human trials are conducted. Engineering an *in-vitro* environment that mimics the functionality and architecture of human physiology is essential towards building better platforms for drug development and personalized medicine. However, the complex nature of these devices requires specialized, time consuming and expensive fabrication methodologies. Alternatives that reduce design-to-prototype time are needed, in order to fulfill the potential of these devices.

Here, a streamlined approach is proposed for the fabrication of organ-on-a-chip devices with incorporated microactuators, by using an adaptation of xurography. This method can generate multi-layered, membrane-integrated biochips in a matter of hours, using low-cost benchtop equipment. These devices are capable of withstanding considerable pressure without delamination. Furthermore, this method is suitable for the integration of flexible membranes, required for organ-on-a-chip applications, such as mechanical actuation or the establishment of biological barrier function. The devices are compatible with cell culture applications and present no cytotoxic effects or observable alterations on cellular homeostasis.

This fabrication method can rapidly generate organ-on-a-chip prototypes for a fraction of cost and time, in comparison to conventional soft lithography, constituting an interesting alternative to the current fabrication methods.

1. Introduction

Microfluidic devices are well established as experimental platforms in life sciences. Devices designed for cell sorting, DNA sequencing, electrophoresis, 3D cell culture are just a few examples of what can be achieved at the microscale.[1, 2] Miniaturization of biological procedures has many advantages. Not only does it reduce the bench footprint, it also requires minute quantities of reagents, solvents and biological samples. Moreover, these systems provide the ability to control aspects of the cell microenvironment at more relevant kinetic and spatial scales.[3] The design versatility and scalability of microfluidic platforms, through parallelization of devices in array-like designs[4-6], make them a powerful tool in any life sciences laboratory.

Recently, the concept of organ-on-a-chip devices was introduced.[7] These microfluidic systems are far more complex than cell-based lab-on-a-chip devices, as they aim to recreate the complex micro-physiological architecture and function of the organ they intend to emulate.[8-10] Importantly, the successful integration of microactuators within organ-on-a-chip devices, allowed the application of well-defined and cyclical strain on the cell culture substrate. The ability to control the intensity, duration and pattern of the mechanical forces within the system, make organ-on-a-chip platforms, a powerful tool to understand how mechanical transduction affects cellular response at the tissue level, thus modulating to a greater extent a key aspect of the *in vivo* native microenvironment, *i.e.,* the cellular response to biomechanical cues. Assessing the impact of mechanical forces at the cellular level and understanding how cells transduce these mechanical forces into biochemical signals, in a physiologically relevant context, is in fact one of the most innovative aspects of the organ on a chip technology, and of particular interest when emulating the *in-vivo* microenvironment of tissues exposed to strain.[11, 12] The relevance of mechanotransduction has been highlighted in several studies where microfluidic platforms were developed to simulate physiological levels of strain.[7, 13-15] Despite the obvious advantages of the technology, design of organ-on-a-chip microdevices is a complex procedure. Their three-dimensional (3D) layout and incorporation of several tissue-like features, such as a simplified stromal component and epithelial barrier architecture, is further complicated by the incorporation of embedded mechanical microactuators.[7, 11, 13, 14] Creating complex structures that correctly emulate the biological counterparts, usually implies fabricating multi-layered devices, with two or more chambers separated by porous membranes, as well as complex flexible mechanisms that serve as mechanical actuators. Also, replicating some organ functions requires the design of intricate microchannel geometries to house, in a

specific layout, the individual components of the organotypic unit being emulated[16, 17] or to manipulate diffusion distances.[5, 18] While geometry design, by itself, is not constrained by fabrication limitations, it is essential that they are amenable to correct cell culture maintenance and homeostasis.[19] Methods with a fast turnaround time from design to device, are key to reduce experimental costs at the early stages of organ-on-a-chip design. The challenge remains to develop a technology that allows the fast generation of workable prototypes, while retaining the characteristics of devices produced by soft lithography. Notably, the optical transparency of cured polydimethylsiloxane (PDMS), as well as its soft elastomeric nature, that is a key feature for organ-on-a-chip devices with embedded mechanical actuation.

The present study establishes an innovative method to fabricate complex multi-layered PDMS fluidic devices with integrated microactuators, suitable for organ-on-a-chip applications. The technique used is based on xurography[20] and relies in the machining of PDMS laminates using a benchtop cutting plotter as previously described.[21] The approach simplifies the entire fabrication procedure into 3 steps: design, machining and assembly. The devices produced with this method were characterized regarding the performance and biocompatibility of the materials and procedures, in view to establish a fast and efficient fabrication method for organ-on-a-chip applications. To this end, we thoroughly characterized the fabrication process regarding machining resolution, resistance to delamination and ability of these devices to sustain a long term epithelial gastric cell line (MKN74) culture. This was followed by the integration of microactuators within the chip and characterization of their reliability in reproducing biomechanical cues at physiological levels, as well as their ability to operate as in-line degassers to eliminate on-chip air bubbles.

The proposed method generates fully operational biochips, capable of sustaining long-term operation under cell culture conditions. Furthermore, they can be adapted to complex organ-on-a-chip designs, as shown by the successful integration of intercalating porous membranes, mechanical actuators and in-line degassers.

2. Results and discussion

2.1. Design and fabrication of a cost- and time-effective multi-layered organ-on-a-chip devices with built-in microactuators

In this study, we developed a fast and inexpensive method to fabricate complex multi-layered devices incorporating microactuators. Our approach is based on xurography, a technique that consists on the removal of material from thin film plates using a cutting plotter. Xurography was first developed as a technique to produce soft lithography molds.[20, 22] Given its versatility and speed of use, the technique was quickly adapted to directly fabricate chip elements.[21, 23, 24] Here, we used such an approach, by using a cutting plotter to directly machine thin, pre-cured laminated PDMS sheets. Each piece cut corresponds to one layer of the chip (**Figure 1 a-c**). A single plotter run, over a 9 x 20 cm area of PDMS laminate, can produce as much as 7 units of a double channel prototype. Machining time varies with the complexity of the structure being cut and the cutting route the blade performs, as determined by the user. Within a few seconds, all the PDMS layers required for a complete device can be produced. This obviates the most time-consuming step of soft lithography, namely the procedure of mold making and the casting and curing of the structural pieces, a process that, given the complexity of the tasks, can take up to two days for a double layered chip. Device assembly can then be performed following conventional soft lithography techniques, without any additional fabrication steps. Similarly to the soft lithographic process, bonding of the individual parts is dependent on the materials used, thus curing times will vary accordingly. The complete fabrication procedure is condensed in 3 steps: design, cutting and assembly (**Figure 1d**). Timewise, this is a major improvement on current fabrication methods of complex organ-on-a-chip devices with incorporated microactuators. Recent publications have also shown promising results regarding a novel adaptation of xurography, by using biocompatible adhesive tape as the building materials.[23, 24] Structures cut from adhesive tape, can be readily bonded, without requiring chemical treatment of the surface. Plotting of structures and complete chip assembly can be accomplished within minutes. Stallcop and colleagues,[23] have also demonstrated applicability of the technique for the fabrication of simple double layered open devices with successful integration of membranes, similar to a transwell configuration. From our experience however, although faster, the technique is not suited for the fabrication of microactuators. We found that PDMS membranes used as micro-diaphragms, bond well to adhesive tapes, but do not withstand continuous cyclical actuation (data not shown).

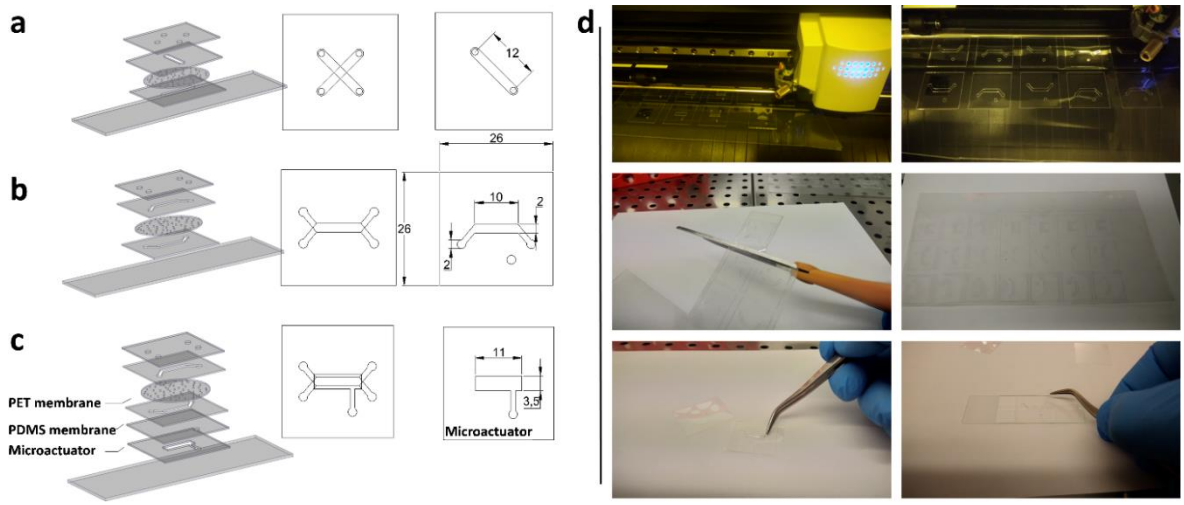

Figure 1. Exploded 3D view of (a) Device 1, (b) Device 2 and (c) Device 3, each depicted with a top-down view of the assembled structure to the right and corresponding measurements for the main fluidic and microactuator features. (values in millimeters). (d) Depiction of the fabrication method. Upon completion of the chip design using CAD software, a PDMS laminated sheet is fed into a cutting plotter. After the plotting process, each sheet holds several copies of a single chip, with each squared section corresponding to a level of the chip. Each layer is then manually cut from the laminated sheet and the offcuts are removed to reveal the microfluidic channels. The chip is then carefully mounted on top of a glass microscope slide.

2.2. Rapid prototyping by plotting allows adequate replication resolution of micropatterning

One important aspect to benchmark is the ability of this technology to reproduce with precision the computer assisted design (CAD) projected features, namely the original design sizing. This is required to ensure that the predicted pressure and shear stress are as close as possible to the simulated conditions. Here we characterized the lower limit of resolution by cutting in 250, 500 and 750 µm thick PDMS sheets, a series of rectangular shapes, ranging in width from 2000 µm, corresponding to original chip scaling, down to 200 µm (n=4). CAD theoretical dimensions were compared to real plotted dimensions across the range for all 3 PDMS thicknesses (**Figure 2a-c**). A width of 200 µm was the lowest achievable spacing with precision, below which, the blade starts rupturing the structure. This is similar to the results previously reported by Cosson and colleagues, for similar structures cut from thin PDMS sheets.[21] We observed lower variation to CAD design for larger structures, with deviations of 3.5, 2.0 and 0.6% for 250, 500, 750 µm thicknesses respectively (**Figure 2d**). Deviation to CAD theoretical dimension is conserved below 8% for 400 µm wide structures, on all thicknesses tested. Bellow 400 µm, cut accuracy starts to deteriorate, in particular for thicker PDMS sheets. Our results demonstrate that smaller structures, less than 400 µm wide can be reliably obtained using PDMS sheets with a

thickness of 500 µm or lower (**Figure2d**). To further characterize the method, we analyzed the impact of geometry on resolution. Using our chip design (**Figure 2e**), we measured the average size of the 3 most common geometric shapes, cut from 250, 500 and 750 µm thick PDMS sheets. We compared the width of linear and angular structures and the diameter of circular features, with the theoretical size from the CAD generated designs, namely 2000.00 µm for linear and circular features and 1285.58 µm for the angular access channels (**Figure 2e-h**). Deviation to CAD size was higher for angular structures, in particular for thicker substrates, namely 500 µm or higher. Nevertheless, variation was kept within acceptable levels, with a maximum of 9.5% variation for angular structures on 500 µm thick PDMS sheet (**Figure 2i**). The plotter copes better with linear and circular structures. For both geometries, variation was below 4%, irrespective of the thickness of the PDMS substrate, with the highest variation to CAD size registered for linear features cut from 250 µm thick PDMS sheets at 3.5% (**Figure 2i**).

Overall, our results show that precision of the machined structures cannot match that of photolithography and soft lithography, where the minimum feature size achievable ranges around 100 nm and lower.[25] The stronger point of the xurographic process resides rather in its low cost, speed of fabrication and flexibility of the process, as designs can be changed and tested quickly. Xurography limits are within the micrometric range which is nevertheless, well suited for cell culture based microfluidic applications. Structures of ca. 200 µm can be effectively cut, although for better resolution, sizes of 400 µm or higher should be used, especially when using thicker PDMS sheets. We did not observe major constrains to resolution regarding the geometries tested. For larger structures, between 1285 and 2000 µm, resolution was shown to vary within acceptable intervals, regardless of geometry or the thickness of the PDMS substrate.

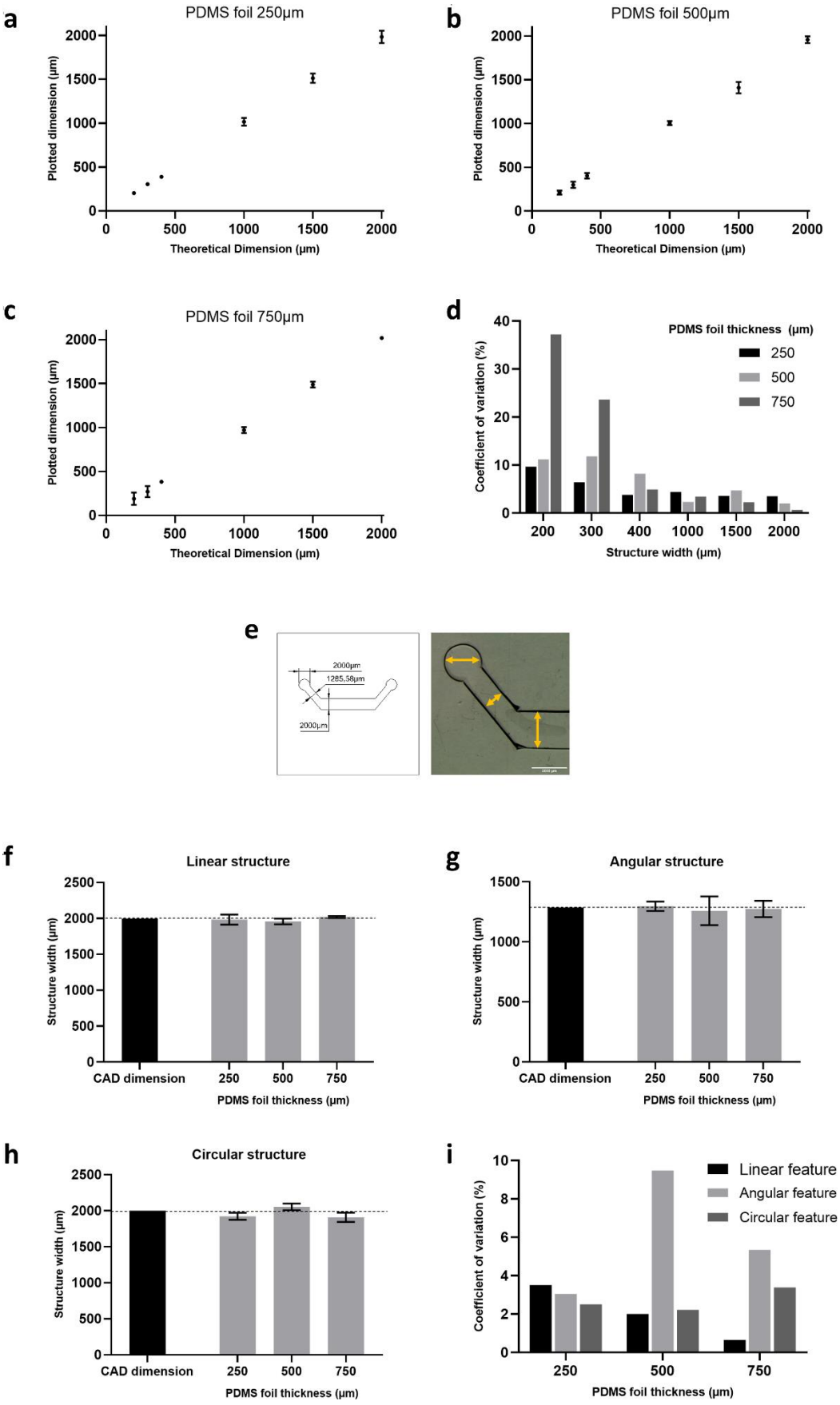

Figure 2. Assessment of resolution limits of the xurographic process. (a-c) CAD theoretical dimension was compared to plotted dimensions across a series of rectangular structures with defined size, cut from PDMS foil

sheets of 250, 500 and 750 µm thick. Results plotted as average dimension ± SD (n=4). Error bars not shown when the SD is smaller than the graphical symbol. (d) Variation to CAD size is represented as the coefficient of variation (%), for the conditions detailed in (a-c), as a function of structure width. (e) CAD design with theoretical dimensions and stereomicroscope image of a plotted structure. (f-h) Influence of geometry on resolution assessed by measuring linear, angular and circular features as shown on (e) and compared to theoretical CAD size (left most bar for each graph). Results were presented as average dimension ± SD (n=4). (i) Deviation to CAD size is represented as the coefficient of variation (%), for the conditions detailed in (f-h), as a function of PDMS sheet height.

2.3. Optimal layer bonding is achieved by a combination of O_2 plasma exposure and silanization

Devices entirely composed of laminated PET/PDMS plates require optimal bonding between all the layers. This promotes undisturbed fluid flow and ensures that cells are contained within their designated culture chamber, without unintended extravasation to the surrounding areas. Here, we have assessed the adhesion strength of both the PDMS-PDMS and the PET-PDMS bonds. For this purpose, we used Device 1, a two level, cross shaped PDMS device, with a PET membrane sandwiched between the two perfusion channels as described above (**Figure3a**). Bonding efficacy at room temperature and normal atmosphere was tested against a pressure range between 0 and 1000 mbar, in incremental 100 mbar steps. PDMS-PDMS bonding was performed by oxygen plasma oxidation.[26] The treatment replaces the methyl chemistry at the surface of polymerized PDMS with OH groups, thus establishing Si-OH bonds. These groups react with similar groups on the opposing plasma exposed surface, to form covalent Si-O-Si bonds, constituting a watertight, irreversible seal between two PDMS plates. The oxygen plasma treated surfaces, performed very well at standard operation pressure (between 10 and 50 mbar). No observable delamination on PDMS-PDMS contacts was observable, even at a high pressure of 300 mbar. Furthermore, pressure was ramped up to 1000 mbar, the maximum pressure achieved by the pressure controller in use, without delamination (**Figure 3b** – refer to blue overlay region on **Figure 3a** to identify PDMS-PDMS contacts).

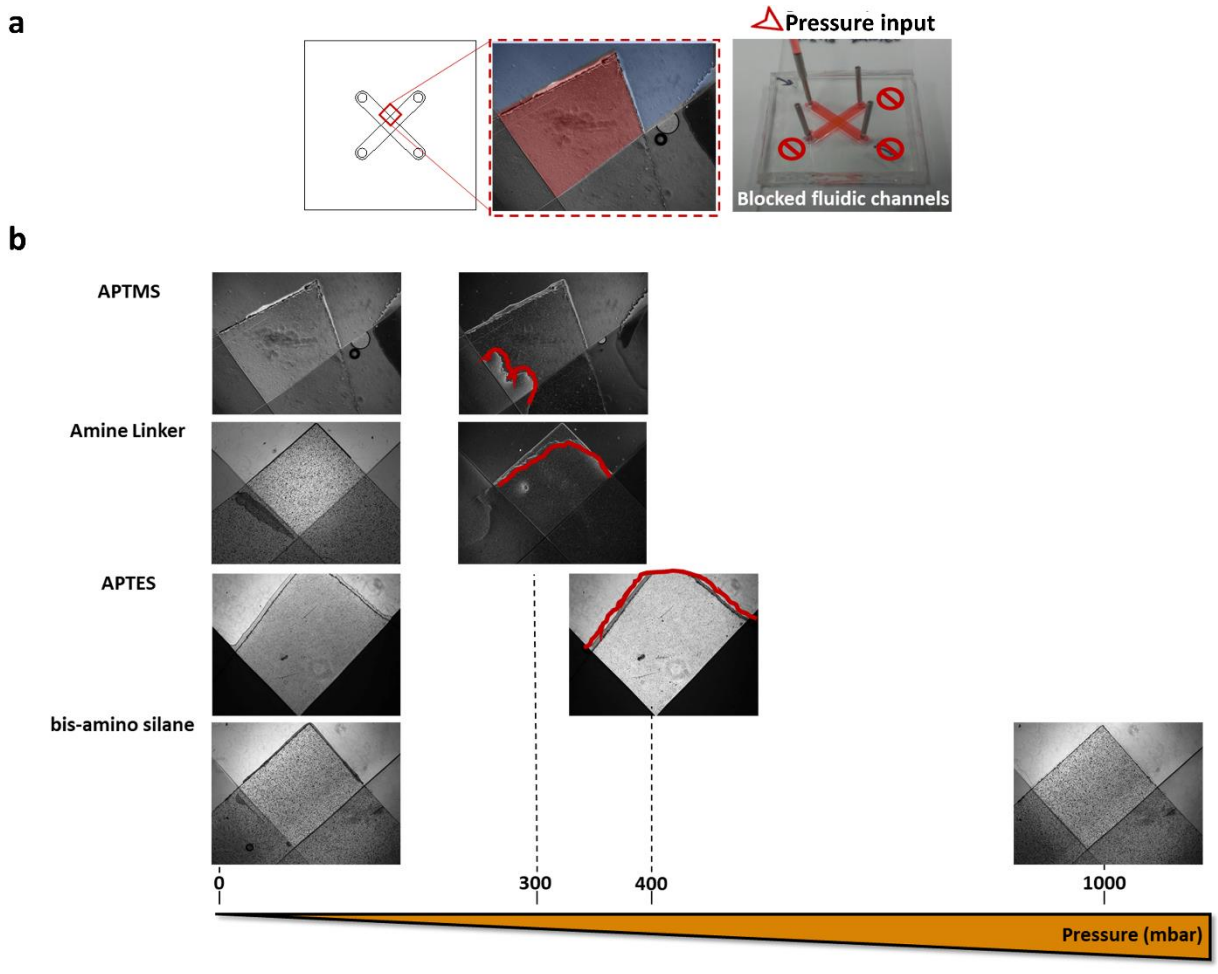

c

	Pressure (mbar)								
Surface treatment	0	...	200	300	400	500	600	...	1000
PDMS stamping		Critical delamination							
APTES				Critical delamination					
amine-PDMS linker				Partial delamination			Critical delamination		
APTMS				Partial delamination					Critical delamination
bis-amino silane	No delamination								

Figure 3. Pressure test for silanization bonding of PET membranes against PDMS laminates (a) Device 1 drawing, used to assess internal pressure resistance. The red square represents the photographed area to document the experiment (left). Magnification of the monitored zone, showing PDMS-PDMS contacts highlighted in blue and PET-PDMS contacts outlined in red (*center*). Experimental layout with chip filled with dyed double distilled H_2O. Three of the 4 outlets were blocked, and the system connected to a pressure generator (right). (b) Assessment of delamination over an increasing pressure range for the 4 silanes tested. Red outline depicts zones of delamination. (c) Table summarizing results of the delamination tests. Critical delamination was defined as complete detachment of the PET-PDMS contact area, while partial delamination was defined as only partial detachment of that contact region.

The PET-PDMS bond is a potentially critical weak spot in the structural integrity of the chip, as bonding two dissimilar materials may result in a weak or partial bond. Plasma oxidation proved to be insufficient for PET-PDMS adhesion at basal cell culture working conditions,

with delamination observed early on during the chip operation. Therefore, we evaluated the effectiveness of PDMS stamping and silane coupling as alternative methods to establish a pressure, temperature and humidity resistant PET-PDMS bond. PDMS stamping uses uncured PDMS as a mortar layer applied between PDMS plates, in order to promote the embedding of the plastic material within the PDMS polymeric structure.[27] This technique has the advantage of not requiring any chemical treatment of the PET membrane. Our results show that PDMS stamping produced a pressure resistant bond, as we were able to operate chips up to 200 mbar without delamination (**Figure 3c**). However, we observed that the PDMS-PDMS contact is compromised with the application of PDMS stamping. The PDMS mortar does not self-level during the stamping procedure and the PDMS mortar, when cured creates a rise on the surface. Furthermore, the PDMS mortar occasionally provokes the occlusion of the porous plastic membrane or the fluidic channel, yielding a low success rate during fabrication. Therefore, we did not further test this technique. Silane coupling is described as an effective method to permanently bond plastic membranes to PDMS. This method is compatible with oxygen plasma activation and well suited to bond polymers whose surface can be readily hydroxylated, such as PET membranes.[28, 29] Here, we tested a variety of trialkoxysilanes (APTMS and APTES) [28, 30], a dipodal silane (bis-amino silane) [31] and a linker incorporating an amine functionality at one terminal and a low molecular weight PDMS on the opposite terminal (amine-PDMS linker).[32] These silanes promote a chemical bond between PET and PDMS and were assayed regarding their ability to produce a stable bond under pressure and during cell culture operation. APTMS and APTES and bis-amino silane establish C-Si-O bonds with the oxygen activated PET surface, thus creating a chemistry that can be further hydroxylated to establish a Si-O-Si bond, thereby permanently binding the PET and PDMS surfaces. A notable particularity of the bis-amino silane, is the presence of 6 alkoxysilane reactive groups per silane molecule, resulting in the increase of its adhesive capacity. The amine-PDMS linker works as a single step reaction, not requiring previous hydroxylation of the plastic surface. Amine-PDMS linker forms an urethane linkage with the plastic surface, exposing a reactive PDMS group that can be bound directly to an opposite O_2 plasma-exposed PDMS surface. Our results indicate that surface amino functionalization with amine-PDMS linker, APTMS and bis-amino silane generated the strongest PET-PDMS bonds. These 3 silanes were the top performers, withstanding pressures up to 400 mbar with only partial or no delamination of the bond. In addition, bis-amino silane performed consistently and without delamination even at 1000 mbar (**Figure 3b** – refer to red overlay region on **Figure 3a** to identify PET-PDMS contacts). **Figure 3c** summarizes the conditions tested and results obtained for each of them.

To test the ability of the PET-PDMS bond to perform well at physiological conditions, which is essential for organ-on-a-chip operation, we assayed the bonding strength of APTMS, amine-PDMS linker and bis-amino silane, over long-term incubation under cell culture conditions. Membranes were bonded to a featureless PDMS square and completely immersed in cell culture medium over a period of 10 days. Under these conditions, structures treated with either APTMS or amine-PDMS linker, showed complete delamination after a period of 48 h (**Figure 4a**). Bis-amino silane was the top performer over long term incubation, forming a permanent bond between PET and PDMS after a 10-day period of incubation, without observable delamination. When membranes silanized with this method were pulled from PDMS, the PET-PDMS interface remained strong and the assembly teared at a random position (**Figure 4b**). This observation is a critical factor as biochips intended for cell culture applications are operated over an extended period, under high humidity and physiological temperatures.

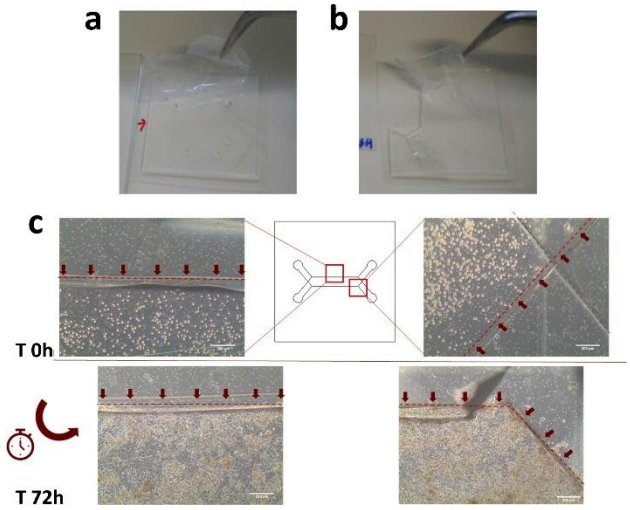

Figure 4. Silanization test under cell culture conditions. (a) Membrane silanized with APTMS, as compared to (b) a membrane silanized with bis-amino silane. The latter depicting full adhesion between both materials, with the PDMS tearing when the PET membrane is forcefully pulled. (c) Bond adhesiveness assessment at time of cell seeding (T0h) and T72h post-seeding with no observable cell extravasation. Red arrows indicate the outline of the cell culture chamber.

Therefore, for all further experimentation PET-PDMS bonding was performed by silane coupling with bis-amino silane. Bonding efficacy was further confirmed by monitoring cell loading and growth on Device 2 (**Figure 1b**), over a period of time. No extravasation to the lower compartment was noticeable during seeding and cells were kept for the entirety of the run within the confines of the cell culture chamber, without invasion of the PET-PDMS contact zone (**Figure 4c**). The success of the bonding procedure must rely not only in the

ability of the structure to withstand internal pressure, but also on its ability to maintain a stable bond over an extended period, in a humidified atmosphere. Surface passivation with bis-amino silane was the most reliable surface treatment regarding both aspects considered. The procedure selected combines O_2 plasma oxidation of the surfaces and silanization of PET materials with bis-amino silane, for long standing PDMS-PDMS and PET-PDMS bonding. Furthermore, we did not observe a correlation between delamination and geometry of the designs. Access portholes, fluid routing channels and cell culture chamber, all remained sealed throughout experimentation, regardless of geometry.

2.4. On-chip conditions and PET treatment do not affect cellular homeostasis

Fabrication methods intended for cell culture applications require consideration regarding the biocompatibility of all the materials and chemistries used. To assess these aspects, we used a human stomach adenocarcinoma epithelial cell line MKN74, as a biological model. These cells typically grow a confluent monolayer displaying selective paracellular permeability,[33] with fully functional cell-to-cell contacts and a typical cobblestone-like, epithelial geometry (**Figure 5a** – top plate). Experiments were performed on 24-well plates, under conditions identical to those found on-chip. This is important to better benchmark the performance of these cells compared to those growing under conventional cell culture conditions. When applicable, the surface of the 24-well PET plate was coated with bis-amino silane. We compared proliferation and doubling time of cells growing over a non-silanized surface, against cells growing over a silanized surface. Our observations showed no phenotypical differences between both groups (**Figure 5a**). Cells of both experimental groups were stained 48h post-seeding, against the proliferation marker Ki67. At this time-point, both were fully proliferative (**Figure 5b**). This was further evidenced by the observation that the doubling time was similar for both groups (**Figure 5c**). Finally, the metabolic activity was measured over a period of 8 days. Our results showed no difference between cells seeded on a silanized or a non-silanized surface (**Figure 5d**). Overall, our observations demonstrate that the surface treatment employed to permanently bond the PET membrane to PDMS, does not affect cellular homeostasis, nor does it induce cytotoxicity.

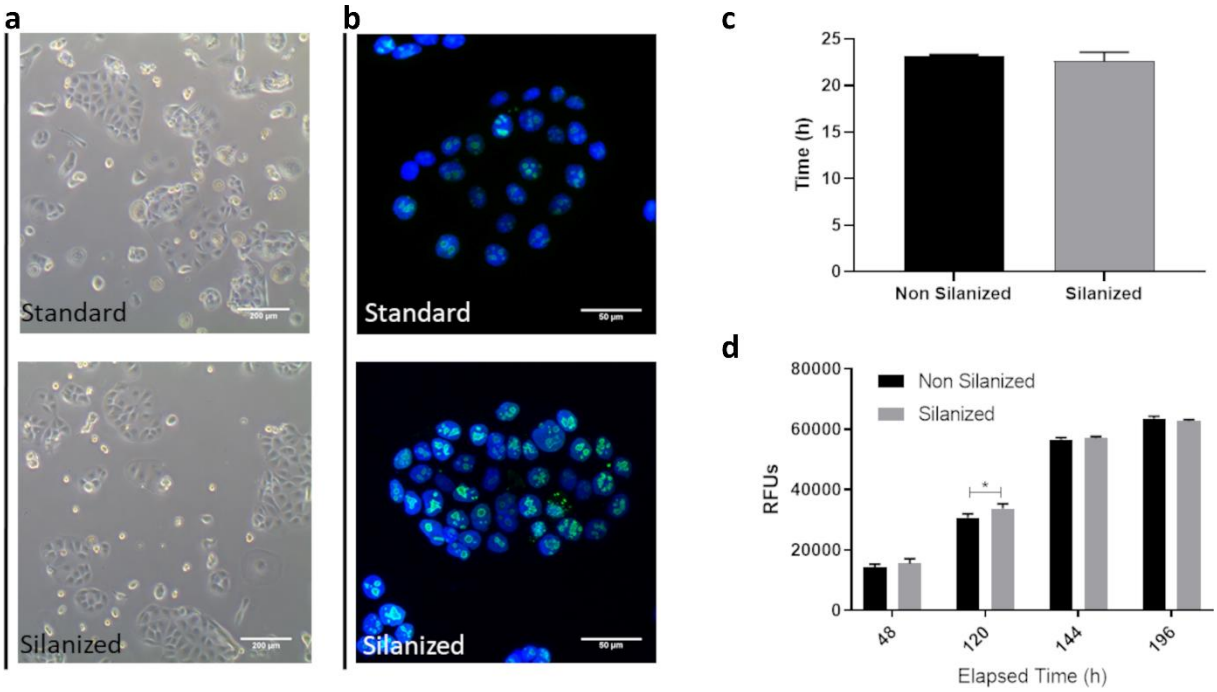

Figure 5. (a) Morphological study of phenotype of MKN74 cells growing under standard conditions with cells growing over silanized surfaces (scale bar 200 µm). (b) Ki67 staining of the same populations (scale bar 50 µm). (c) Population doubling time. (d) Comparative study of the metabolic activity of cells growing on a non-silanized vs. silanized surface. All graphical representations display average measurement ± SD (n=6).

We have established a fabrication procedure that generates stable, long-term operating devices under physiological conditions. Furthermore, silanization of the intercalating PET membranes does not adversely affect cellular maintenance, validating the procedure for cell culture applications.

2.5. Built-in microactuator allows mechanical stretching at physiological levels and impacts on-chip cellular organization and molecular signature

Mechanical stretching in living tissues is rarely of a single plane, linear nature. Hence, the microactuator was designed so that membrane displacement is applied from below the cell culture substrate (**Figure 1c**). By applying vacuum to the microactuator chamber, the flexible membrane above it is actuated in 3D, which in turn displaces the cell culture substrate above it (**Figure 6a**). Cell culture substrate stretching was assessed at 0, -50, -100, -150 and -200 mbar. At vacuum pressures below -200 mbar, within our 250 µm high actuator, we observed that the flexible PDMS membranes touched the bottom of the microactuator cavity. As a result, no measurements were recorded below this threshold since the stronger vacuum pressure did not reflect in further stretching of the membrane. In order to quantify the membrane stretching we photographed the porous membrane at

resting state and at actuated state and measured the interpore distance, to calculate the linear expansion effected. Surface expansion was then estimated numerically from the values obtained for the linear expansion and, in addition, we visually assessed the perimeter of expanding cells under actuation (**Figure 6b**). Within the pressure ranges tested we achieved surface expansion values between 5±2% at -50 mbar, up to 18±4% at -200 mbar (**Figure 6c**). These values are well within the surface expansion experienced by cells within living tissues of some of the most common organ-on-a-chip models, where cell stretching is an important physiological factor, namely gut [34], lung [35] and heart.[36] To further investigate the ability of the built-in microactuator, to induce physiological level alterations to the cell culture within the biochip, we performed a morphological and molecular characterization of a gastric epithelial population growing on-chip, under dynamic conditions. To emulate peristalsis-like motion similar to that experienced by gut cells *in vivo*, the stretching pattern was modelled as a sinusoidal wave of 0,15 Hz frequency, and maximum vacuum pressure of -100 mbar applied to the microactuator. These conditions generated a surface expansion around 10% as shown in **figure 6c** and promoted a range of physiological strain similar to that experienced by gut cells *in vivo*.[14, 34, 37] To emulate the gastric epithelium, we have used the MKN74 cell line. We have previously shown that these cells correctly express and localize adherens-junctions and tight-junctions partners when cultured in static conditions,[33] which promotes the establishment of a tightly knit epithelial barrier, once confluency is reached. Furthermore, our previous results show that once confluency is reached, transepithelial resistance rapidly increases, reaching a plateau above 150 $\Omega.cm^2$, at day 5 post-seeding and lasting at least 11 days.[33] Taking this in consideration, we have devised an experimental setup to assess the influence of dynamic conditions on a fully developed and selective epithelium. A confluent MKN74 population was cultured to confluency, taking on average 3 days, followed by 3 days under culture media flow alone or, in addition, with fluid flow and peristaltic actuation. This timescale provides an experimental window where the newly formed epithelium is properly packed and exhibiting selective permeability, similar to the normal gastric mucosa. A control population was also monitored, by growing for the same period of time MKN74 cells in transwell inserts under static conditions. We have observed that irrespective of the condition tested, cells reached confluency at around day 3 in culture when seeded at a density of $3,0x10^5$ cells/mL. Cells formed a compact layer which was undistinguishable on a phase contrast microscope (data not shown). Interestingly, once mechanical stretching was initiated, a marked difference was observable. MKN74 cells under mechanical actuation, seemed to develop a much thicker epithelial layer (**Figure 6d**). To further understand the parameters being effected by the mechanical stretching over the cell culture substrate, we marked cells with an antibody against the adherens-junction protein, E-cadherin and

assessed distribution of the F-actin cytoskeleton. Here, we observed that cells grown under static conditions displayed a flattened, undifferentiated appearance, identical to a squamous epithelium (**Figure 6e** – top plate). In contrast, cells under dynamic conditions, exhibit a markedly different phenotype. Flow alone, induced an increase in cell height and the formation of globular-like structures (**Figure 6e** – middle plate). The effect was even more striking on those cells under flow and peristaltic actuation. Furthermore, cells display an elongated shape, resembling a polarized state, with F-actin observable across the whole membrane, while E-cadherin was limited to the basolateral region of the cells. Interestingly, nuclear staining showed that nuclei are elongated and localized to the basal side of actuated cells, further evidencing differentiation traits that are not commonly found in gastric cells under static conditions (**Figure 6e** – bottom plate). We then compared average size of the engineered gastric epithelia. Our observations suggest that on-chip dynamic conditions are capable of eliciting a response at the cellular level, which is initiated with flow alone.

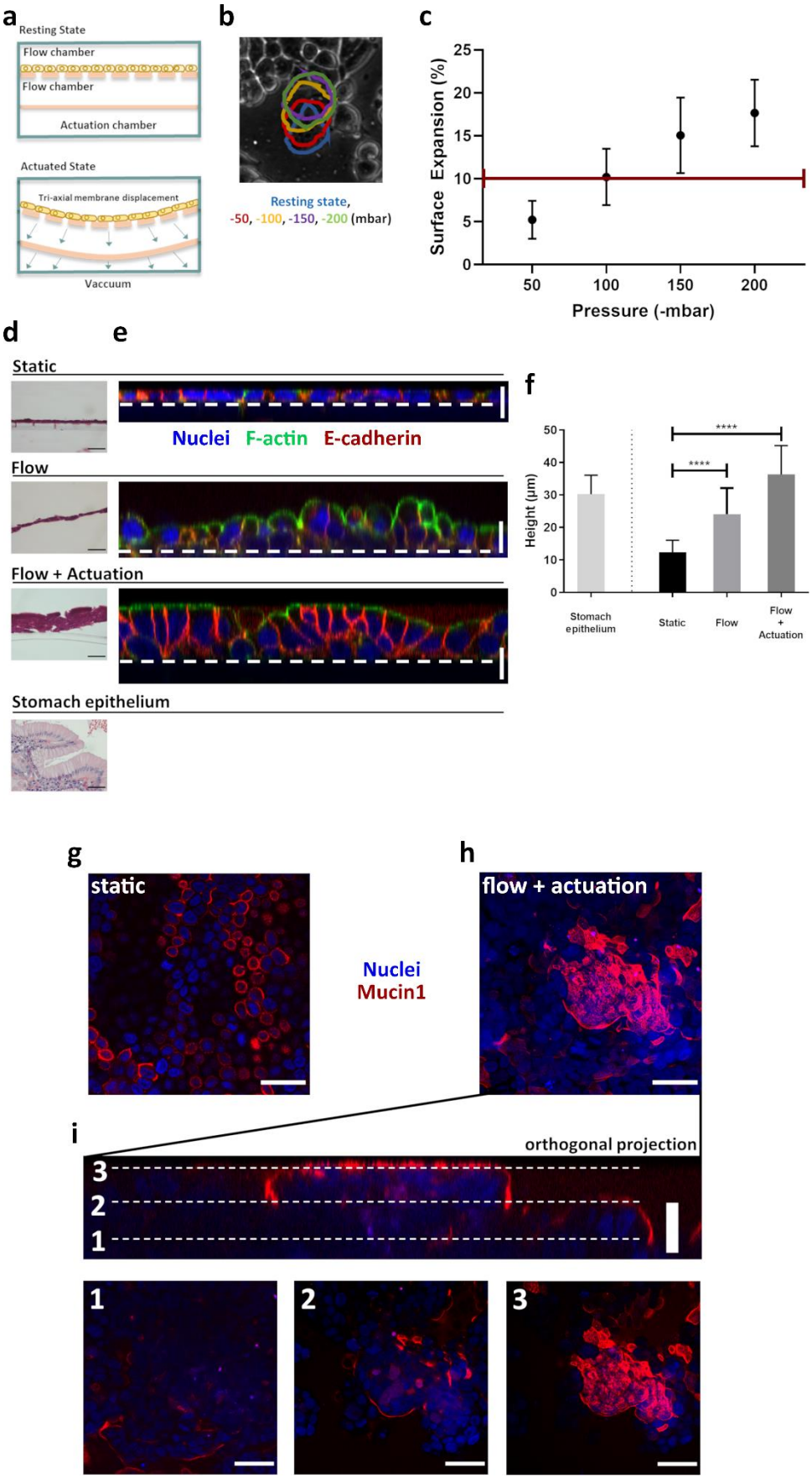

Figure 6. (a) Illustration of on-chip microactuator. (b) Vacuum pressure is applied at the actuation chamber, resulting in 3D cell surface expansion. *Color*-coded outlines exemplify cellular expansion for a single cell at

different actuation pressures. (c) Surface expansion as estimated from the linear expansion, at different pressure steps; red line represents average surface tension of *in vivo* gut cells.[34] (d) and (e) Qualitative comparison of epithelium height of MKN74 cells grown under static (transwell) vs dynamic conditions (flow or flow coupled with actuation). (d) stained with HE or (e) stained for F-actin (green) and E-cadherin (red); nuclear material stained with DAPI (blue). The white line highlights the PET membrane position. (f) Quantitative study of epithelium height of MKN74 cells grown under static vs dynamic conditions. Quantification was performed using orthogonal projections of z-stacks for each condition (z-step; 2 μm), except for normal stomach epithelium, which was quantified from HE stained specimens (n=3). Epithelium height was measured using image analysis software (Fiji). (g) and (h) Mucin-1 staining (red) of MKN74 cells grown under static or dynamic conditions (flow coupled with actuation), respectively (scale bar: 50 μm). Images represent a maximum intensity projection of a z-stack, post-processed using image analysis software (Fiji). Nuclear material stained with DAPI (blue). (i) Orthogonal projection of (h). Bottom plates represent the same microscopic field at 3 different z-heights. All graphical results presented as average measurements ± SD. Scale bar for orthogonal projections correspond to 20 μm and for HE images to 40 μm.

Average epithelium height increased 2-fold in cells under media flow alone, when compared to static conditions. The increase was even more striking when considering cells under flow coupled with mechanical actuation, with an almost 3-fold increase when compared to the epithelium height of cells under static conditions. Interestingly, the average height of the epithelium generated from actuated cells (approximately 36 μm), is similar to that observed in normal stomach epithelium (approximately 30 μm) (**Figure 6f**). Despite these findings, our observations suggest that the actuated epithelium resembles a pseudostratified columnar epithelium, rather than a simple columnar epithelium as found in normal gastric mucosa (**Figure 6d** – bottom plate). Finally, we studied expression of Mucin-1. In normal stomach mucosa, this protein is located at the apical surface of epithelial cells.[38] For cells under static conditions, expression of Mucin-1 was limited to single dispersed cells (**Figure 6g**). The mechanically actuated epithelium however, displayed zones of globular growth, where Mucin-1 was exclusively expressed at the apical surface (**Figure 6h**), closely resembling the expression of Mucin-1 in normal gastric mucosa. This is also in accordance with what has been previously demonstrated for 3D MKN74, gastric spheroids.[39, 40]

Overall, our data demonstrates that the proposed fabrication method can effectively be used to engineer biochips with fully integrated mechanical actuators without adding complexity to the fabrication procedure. The developed system reproduces mechanical strain at near physiological levels, suitable for a variety of organ-on-a-chip models, when substrate actuation is required. Furthermore, using a gastric epithelial model, we have demonstrated that the engineered microactuator is capable of eliciting a physiological response at the molecular level, by inducing differentiation and polarization traits,

characteristic of the normal gastric mucosa. Finally, our observations show that biochips fabricated with this method can be reliably used for long term experimentation, as no delamination of the microactuator components was observed over a period of 10 days under use (**Figure 7a**).

2.6. Built-in microactuator allows in-line degassing of air bubbles

A common complication observed during microfluidic operation is the formation of air bubbles.[41] Air bubbles can disrupt flow and the creation of an air-liquid interface may compromise cellular homeostasis and promote cellular death. Biochips that need to be operated at 37 °C, are particularly susceptible to this problem as the higher temperature leads to decreased gas solubility.[41] Under these circumstances, the volume of the air bubble will gradually expand over time. Taking advantage of the fact that the microactuator was entirely fabricated in PDMS, which is permeable to gas exchange, we tested its potential operation as an integrated bubble degasser using Device 3 (**Figure 1c**). As such, we monitored its ability to eliminate air bubbles from the flow path over time. We injected air in the main flow line and pushed the air bubbles up to the main culture chamber, at which point the chip was placed at 37 °C inside the cell culture incubator and a constant vacuum pressure of -50 mbar was applied, while monitoring air bubble area, every hour. Our results show that the vacuum actuator was able to effectively eliminate air bubbles over-time from the main culture chamber (**Figure 7b**). We observed that a -50 mbar constant vacuum pressure could effectively eliminate a bubble with an average area of 250.5 mm^2 over a period of 4 h (**Figure 7c**). This is an interesting observation, as it solves a common problem with standard microfluidic systems, without further complicating the architecture of the chip or increasing fabrication time. Taking in consideration these observations, we added a degassing step to our chip priming procedure. After sterilization and surface coating, but before cell seeding, the chip was allowed to equilibrate overnight at 37°C, while applying a constant vacuum pressure of -50 mbar. As the system was pressurized and fully contained throughout operation, this procedure was sufficient to prevent air bubble formation during experimental procedures.

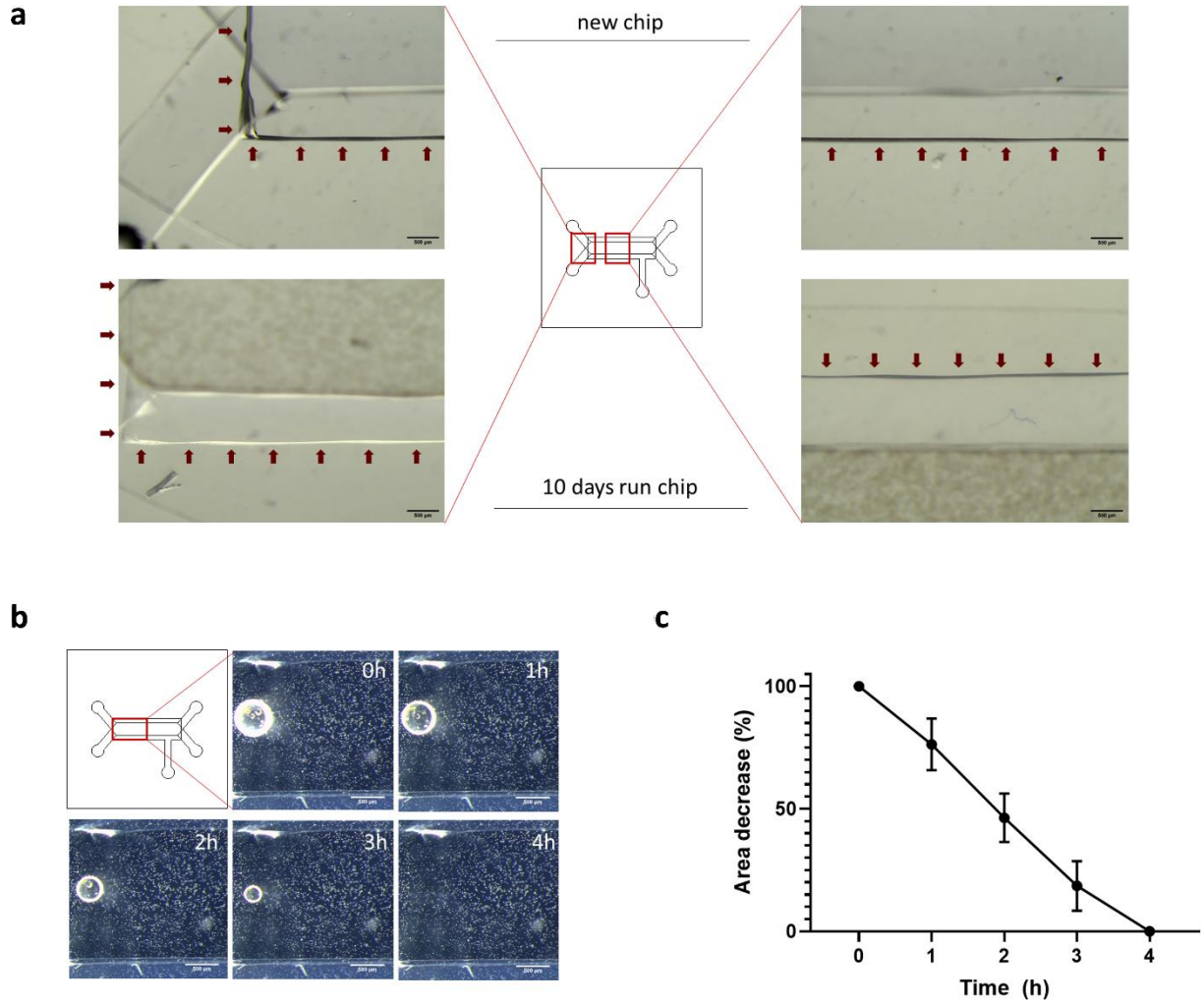

Figure 7. (a) Assessment of microactuator delamination over a period of 10 days. Top plates show a new chip prior to use. Red arrows point to the limits of the microactuator. Part of the flow channel network can be seen out of focus. The bottom plates show the detail of a chip that has been run for 10 days. No delamination of the microactuator was observed (red arrows). Fluidic channel with seeded MKN74 cells can be seen out of focus, above the microactuator (scale bars: 500 µm). (b) In-line air bubble degassing by application of a constant -50mbar vacuum pressure at the microactuator over a period of time. (c) Area of each bubble was measured using image analysis software (Fiji) and plotted as % of area decrease over-time. Results presented as average measurements ± SD.

3. Concluding remarks

Advances integrating microengineering and tissue engineering enabled the creation of organ-on-a-chip platforms, which aim is to recapitulate the micro-physiological and functional characteristics of human tissues. In particular, organ-on-a-chip devices excel in their ability to modulate the cellular response to mechanical cues, one aspect that is often underrepresented in conventional 2D culture models.[42] Modelling the complex tissue

response at a microscale, requires devices of complex architecture and functionality. Soft lithography is ideally suited for the fabrication of organ-on-a-chip platforms, given the biocompatibility, optical transparency and, importantly, the elastomeric nature of PDMS that enabled the development of mechanical actuators. However, soft lithography is a time-consuming procedure and requires specialized equipment and training.

In this work, we described a fully modular, rapid prototyping, alternative method for the fabrication of complex multi-layered microfluidic devices with integrated microactuators. Our approach reduces the complexity, number of steps, time and cost required to fabricate a functional microfluidic chip. We based our approach on xurography, a technique based on the removal of material from thin film plates using a cutting plotter.[20] Here we have explored a similar method to that described by Cosson and colleagues, by using a cutting plotter to directly machine thin laminated PDMS sheets.[21] In this work however, we have used commercially available thin PDMS laminates, thus eliminating the lengthy process of producing thin PDMS sheets, namely mixing/degassing PDMS, spin coating each individual PMDS sheet and fully curing them, reducing overall fabrication time. Structures fabricated were shown to have a similar resolution to those obtained by Cosson and colleagues. Good precision can be achieved in the micrometric range, with 200 µm structures at the lower end of resolution attainable. The described approach obviates the most time-consuming portion of the soft lithographic method, i.e. the fabrication of molds and the casting of individual parts. A full device can be plotted within seconds, from a strip of PDMS laminate. Despite this, each plotted PDMS layer and corresponding intercalating membranes, must still be assembled manually, using the same procedures employed in conventional soft lithography.

The full modularity of our fabrication method constitutes also a valuable characteristic for the early prototyping stages, as each aspect of the chip, i.e. chip robustness, cell culture maintenance and mechanical stretching, can be tested independently before new layers are added. Alterations to the design can thus be quickly implemented and tested. Importantly, we have demonstrated that our method permits the facile integration of microactuators without further complicating the design or fabrication process. Our prototype was able to stably sustain the effects of strain on the cell culture substrate at near physiological levels. Furthermore, we have demonstrated using a gastric model that microactuators fabricated with the proposed technique, are capable of eliciting a cellular and molecular response, inducing physiological level alterations to the cells growing within the chip. Devices were shown to be pressure resistant and performed well under cell culture conditions over a long period, as no delamination or leakage was observed. A combination of O_2 plasma exposure and chemical modification of membranes with a commonly used silane, namely bis-amino silane,[31] proved to be an effective process to produce leak-tight

devices, without affecting viability or cellular homeostasis. Furthermore, the versatility of the method was demonstrated by the successful adaptation of the microactuators as in-line degassers, eliminating air bubble formation during operation, which is one of the major challenges during biochip handling.

The described method can significantly contribute to the early stages of organ-on-a-chip development by reducing 3 of the main burdens facing a microfabrication laboratory, namely production time, cost and space requirement. It presents a fully modular, low cost and fast alternative to soft lithography, while retaining all the advantages of PDMS-based cell culture devices. Notably, the entire procedure is accomplished with portable benchtop equipment, reducing greatly the benchtop footprint. We are currently working on an advanced model of the stomach mucosa, using the technology described here. Our aim is to explore in a more physiologically relevant context, our previously described work of a 3D gastric mucosa model.[33, 43, 44]

4. Experimental Section

Preparation of chip-related materials: Prior to assembly, each plate design, was cut from PDMS foil (915 mm wide, Silex), using a desktop cutter (model CAMM-1 GS-24, Roland DG). The fluidic plates were cut from 500 µm high foil, whereas the plates forming the pneumatic portion of the device were cut from 250 µm high foil. Briefly, a section of PDMS foil of about 3 x 20 cm, was manually cut with scissors and one side of the protective backing plastic was removed. Finally, the laminate sheet was fed to the cutting plotter and the design transferred from the CAD software to a dedicated software, Roland Cut Studio (Roland DG). Cutting was performed with a carbide cemented blade (model ZEC-U5032, Roland DG). Blade pressure was set at 10 gram-force and speed at 20 $cm.s^{-1}$. After the machining process, the offcut material was removed with tweezers, to reveal the hollow fluidic and pneumatic features (**Figure 1d**).

The polyethylene terephthalate (PET) membrane (thickness 16 µm, pore size 8 µm, pore density $6e^4$ cm^2, it4ip), was cut manually from Ø25 mm discs, immersed in isopropanol (IPA), cleaned by ultrasound (5 min), dried with compressed air and stored in a dust-free container.

The top layer of each chip was fabricated by gravity casting PDMS on a circular petri dish. The PDMS base was mixed thoroughly with curing agent on a weight ratio of PDMS base to curing agent 10:1 (Sylgard 184, Dow Corning). The heavily aerated pre-polymer mix was degassed by centrifugation (5 min at 3166 g), carefully poured onto 90 mm petri dish and

cured at 70 °C for 1 h. The resulting PDMS plate was then cut in 26 mm square sections to match the machined PDMS layers.

Glass microscope slides were thoroughly cleaned by sequential incubation (5 min by ultrasound) in 2% (v/v) Helmanex III solution in double distilled water (Helma Analytics), followed by acetone and a final rinse in double distilled water. Clean slides were air dried with compressed air and stored in a dust-free container.

Microfluidic device design and assembly: To characterize the fabrication method, 3 microdevices were designed (**Figure 1**). Device 1 (**Figure 1a**) is a 5-layered fluidic system, with two fluidic linear channels measuring 12 mm in length, arrayed in a cross format and separated by a PET perforated membrane. Device 2 (**Figure 1b**) is built from 5 superimposed layers. It is composed by 3 alternating layers of 500 µm PDMS laminate foil and a cell culture treated PET membrane (**Figure 1b**). Fluidic features are rectangularly shaped, 2 mm (width) x 10 mm (length) x 0.5 mm (height), for a total cell culture area of 0.2 cm^2 and a total volume of 0.01 cm^3 (approximately 10 µL). Access to the cell culture area is made through an angular feature connecting to an access porthole of 2 mm in diameter. Fluid flow is applied unidirectionally, serving one porthole as an inlet and the other as an outlet for liquid ejection. Design for Device 3 (**Figure 1c**) was adapted from Device 2, by adding a lower portion, containing the pneumatic actuation system. The actuator is a two-piece assembly comprised of a 0.25 mm (height) flexible PDMS membrane and an actuation chamber with 35 mm (width) x 11 mm (length).

Assembly was performed from top to bottom. PDMS and glass structures were bonded permanently by exposure to O_2 plasma (1 min, 1 bar; Zepto Plasma Laboratory Unit, Diener) and bringing them into immediate conformal contact. This created a strong and irreversible bond between both layers.[26, 45] The microchannel outline was used as a guide to punch the inlet and outlet access channels through the top cast-on PDMS layer, followed by a thorough wash with IPA. Porous membranes were silanized as described below and sandwiched between two O_2 plasma exposed PDMS plates. Alignment of the fluidic and microactuator features was performed under a stereomicroscope (model SZX10, Olympus). When applicable, the microactuator was sealed below the fluidic assembly. Care was taken to ensure the correct alignment of the flow features with the pneumatic chamber. The process was finalized by sealing the chip assembly against a microscope glass slide.

Priming and operation: Fluid flow and pneumatic actuation were managed with a piezoelectric pressure controller (model OB1 Mk3, Elveflow). The equipment was tethered to a dedicated software (ESI, Microfluidic Software and SDK, Elveflow) and coupled to a flow sensor that allows control over the flow rates applied, up to a maximum of 80 µL/min. Mechanical actuation was achieved by application of vacuum pressure to the microactuator via poly(ether-ether-ketone) (PEEK) tubing (Idex).

Prior to operation, the microfluidic device was rinsed with ethanol 70% (v/v) and exposed to one UV cycle (20 min), after which, ethanol 70% was flushed through the fluidic features (15 min), followed by washing with phosphate buffered saline (PBS; 15min) solution. To promote cellular adhesion, the surface of the fluidic features was perfused with a fibronectin solution (50 µg/mL, Sigma) and incubated at room temperature for 2 h. Before connecting the biochip, the perfusion system was sterilized by flushing ethanol 70% (15 min), followed by rinsing with PBS (15 min). The perfusion system was then filled with cell culture medium and afterwards the microdevice was connected in-line and allowed to equilibrate overnight.

Cell culture: The human derived epithelial gastric cancer cell line, MKN74, was purchased from the Japanese Collection of Research Bioresources cell bank. Samples were stored in liquid nitrogen and tested negative for the presence of mycoplasma when thawed, and every month. Cells were routinely maintained in Roswell Park Memorial Institute (RPMI) 1640 medium with glutamax (Gibco), supplemented with 10% (v/v) fetal bovine serum (FBS, Biowest) and 1% (v/v) penicillin/streptomycin (pen/strep; Biowest) at 37°C, 5% CO_2 and in a high humidity atmosphere. Cells were reseeded every 3 days, or when confluency reached around 80%.

On-chip, cells were grown in CO_2-independent cell culture media (Gibco), supplemented with 4 mM of L-Glutamine (Gibco), 10% (v/v) FBS (Biowest) and 1% (v/v) pen/strep (Biowest). Prior to on-chip seeding cells were allowed to stabilize for 48h in CO2 independent cell culture media.. Cells were then detached by trypsinization and resuspended to a density of ca. $3.0x10^5$ cells/mL. The resulting suspension was loaded on the upper fluidic channel via a secondary port operated by a 4-way PEEK valve (Idex). Cells were allowed to sediment and attach for a period of 30 min, after which cell spread and density on the membrane was assessed under a phase contrast microscope. On-chip cells were cultured at 37 °C, in normal, high humidity atmosphere (without CO_2 buffering). Cell culture media was perfused at 0.5 µL/min for the duration of the experimental work.

Actuation protocol: Cells were seeded on-chip as detailed above and allowed to reach confluency. Mechanical stretching of the cell culture substrate was then effected by application of cyclic vacuum to the microactuator. In order to emulate peristalsis experienced by gut cells *in vivo*, the stretching pattern was modelled as a sinusoidal wave of 0,15 Hz frequency[14] and maximum vacuum pressure of -100 mbar.

Evaluation of machining precision: To assess the precision of the cutting plotter, CAD design dimensions were compared with those of machined pieces. For each condition tested, structures (n=4) were photographed under a stereomicroscope (model SZX10, Olympus) coupled with a camera (model EP50, Olympus) and length measurements were performed using image analysis software (Fiji).[46] Three key geometries (circular, angular and linear features) were measured in quadruplicate and results graphed as plotted dimensions against theoretical dimensions. Deviation to CAD size was plotted as coefficient of variation (%)

PET-PDMS bonding: Permanent bonding between PET membranes and PDMS laminates, requires surface treatment. A process of PDMS stamping was tested, as well as 4 different silanization protocols.

PDMS stamping was adapted from a previously described work.[27] Briefly, a batch of uncured PDMS pre-polymer was mixed in a ratio of PDMS base to curing agent of 10:1 and the borders of the PET membrane were immersed in this mixture. The surface of the PDMS laminate was also thinly coated with the uncured PDMS and both materials were pressed together and cured at 120 °C for 1 h.

Silanization of (3-aminopropyl)trimethoxysilane (APTMS) and (3-aminopropyl)triethoxysilane (APTES) was applied by vapor deposition. Briefly, clean membranes were exposed to a silane saturated atmosphere for 15 min, followed by a baking at 70 °C for 1 h. Membranes were then rinsed with IPA and both the membrane and the PDMS surface were exposed to O_2 plasma (1 min) and placed in contact. Pressure was applied overnight at room temperature.

Silane treatment with poly[dimethylsiloxane-co-(3-aminopropyl)methylsiloxane] (amine-PDMS linker) was performed by direct surface contact. The protocol was adapted from Wu J. *et al*.[32] Briefly, the PET membranes were covered with a droplet of amine-PDMS linker and exposed for 20 min to the amine-PDMS linker. To remove excess silane, membranes were immersed in IPA and sonicated for 1 min. PDMS and membranes were exposed to O_2

plasma (1 min) pressed together and baked at 80 °C for 1 h. Surface passivation with bis[3-(trimethoxysilyl)propyl]amine (bis-amino silane) was performed by securing the membranes vertically onto a PDMS support and exposing them to O_2 plasma (1 min). This procedure was followed by immediate incubation in 2% (v/v) bis-amino silane, 1% (v/v) double distilled water in IPA solution (20 min at 80 °C). Membranes were washed thoroughly with IPA and cured for 30 min at 70 °C. Prior to bonding, membranes were wetted for 30 min in ethanol 70% (v/v) and pressed against O_2 plasma exposed (1 min) PDMS laminates.

To test resistance to delamination of the PET-PDMS bond, Device 1 was used (**Figure 1a/3a**). Both perfusion channels were filled with H_2O, dyed with red food coloring and 3 of the outlets were plugged with 20Ga metal studs (**Figure 3a** – right plate). The remaining inlet was plugged to the pressure controller via polyethylene tubing (Instech). Pressure was applied in 100 mbar increments, up to 1000 mbar. The device was kept at each pressure step for 30 min after which the PET-PDMS interface was photographed under an inverted microscope (model IX71, Olympus).

Delamination under cell culture conditions was assessed by bonding a silanized PET membrane onto a featureless PDMS laminate and immersing the assembly in cell culture media. This assembly was then placed inside a cell culture incubator for 10 consecutive days, after which it was removed from the petri dish and the membrane was forcefully pulled from the PDMS with tweezers.

Metabolic activity and proliferation rate: Metabolic activity was assessed by the resazurin assay. Approximately 1000 cells/well were seeded in a 24-well plate and allowed to adhere for 24 h. Metabolic activity was assessed every 48 h for 15 days. For the measurement of metabolic activity, a stock solution of 0.1 mg/mL resazurin (Sigma) was diluted to 20% (v/v, resazurin/cell culture media). Culture media was replaced with 500 µL of this solution and incubated at 37 °C for 2 h. 200 µL of the resulting supernatant were transferred to an opaque 96-well plate with clear bottom (Greiner) and the fluorescence signal was measured (Ex 530 nm/Em 590 nm) in a fluorimeter (model Sinergy MX HM550, Biotek Instruments). Metabolic activity was expressed as average relative fluorescence units (RFUs) ± standard deviation (SD) (n=6).

The population doubling time, was estimated from the metabolic activity results registered between 0 and 48 h, at which point cells were non-confluent and growing at an optimal exponential rate.

Immunocytochemistry (IHC): IHC against Ki67, a marker of proliferation, was performed on a non-confluent population, 48 h post-seeding. IHC against F-actin, E-cadherin and Mucin-1, was performed on populations grown in transwell systems under static conditions or on populations grown on-chip, under dynamic conditions. Briefly, cells were washed in PBS with 0.05 mg/mL of $CaCl_2$ (3x 5 min), fixed with 4% (v/v) paraformaldehyde suspended in PBS (20 min at room temperature, Electron microscopy sciences). Fixation was followed by further washing with PBS (3x 5 min), followed by incubation in 50 mM NH_4Cl (10 min) and permeabilization with 0.2% (v/v) triton-X100 (5 min). Cells were rinsed with PBS (3x 5 min) and blocked in 5% (v/v) bovine serum albumin (BSA) in PBS (30 min). Primary antibody incubation was performed with rabbit anti-Ki67 (dilution 1:100 in 5% (v/v) BSA; Abcam), rabbit anti-E-Cadherin (24E10, dilution 1:100 in 5% (v/v) BSA, Cell Signaling), mouse anti-Mucin-1 (dilution 1:6, kindly gifted by Dr. Celso Reis – from i3S/Ipatimup, Portugal), overnight at 4 °C. Secondary reaction was done withanti-rabbit alexa fluor 594 antibody (dilution 1:500; Thermo Scientific) or anti-mouse alexa fluor 594 antibody (dilution 1:500; Thermo Scientific), for 2 h at room temperature. When applicable, secondary antibody was co-incubated with phalloidin (Biolegend) to stain the actin cytoskeleton. After rinsing with PBS (3x 5 min), cellular preparations were mounted in vectashield containing 2-(4-amidinophenyl)-1H-indole-6-carboxamidine (DAPI), for nuclei staining. Image acquisition was done in a SP5 confocal microscope (model SP5, Leica Microsystems).

For hematoxylin and eosin (HE) staining of membrane bound epithelial cells, sample membranes were removed from their supporting structure and fixed as described above. Samples were then embedded in optical cutting temperature (O.C.T.) compound, frozen, and then 3 µm sections were obtained using a cryostat. The sections were washed in double distilled water, stained 3 min in Gill's hematoxylin, incubated 6 min in running water, dehydrated, stained 1 min in eosin Y, cleared and mounted in entellan. Images were acquired with a multi-head optical microscope (Zeiss).

Epithelium characterization: The *in vitro* epithelium, was fixed and F-actin was stained with phalloidin and co-incubated with an antibody against E-cadherin as described above. Z-stacked fluorescence images were acquired with a 2 µm z-step value, on a SP5 confocal microscope (model SP5, Leica Microsystems). Z-stacks were post-processed and epithelium height measured using image analysis software (Fiji). Normal stomach mucosa height was measured from HE stained specimens. Non-cancerous/normal gastric mucosa samples were obtained and used with consent from the Tissue and Tumour Biobank of CHSJ/Ipatimup.[47]

Surface expansion: To assess surface expansion, a biochip (Device 3; **Figure 1c**), was filled with cell culture media and connected to the piezoelectric pressure controller using PEEK tubing. The magnitude of negative pressure applied was managed by the pressure controller, by creating a vacuum generated pull on the flexible PDMS membrane that, in turn, displaced the perforated cell culture membrane above it. By applying mechanical distension from below, the membrane is actuated three dimensionally by pulling and releasing in the x, y and z planes. Cell culture substrate stretching, was assessed at 0, -50, -100, -150 and -200 mbar. Still images were taken with an inverted microscope (model IX71, Olympus), at rest and actuated state and the average interpore distance (distance between two adjacent pores) in both states was measured using image analysis software (Fiji). Linear expansion was calculated as the amount of linear stretch sustained by the substrate according to the following equation:

$$\mathcal{E}_{lin}=(L_f-L_0)/L_0$$

where L_0 and L_f are the interpore length before and after actuation, respectively. Surface expansion was estimated from the linear expansion using the following formula:

$$\mathcal{E}_{SA}=(\mathcal{E}_{lin}+1)^2-1$$

$\mathcal{E}_{SA}$ is the surface area expansion and $\mathcal{E}_{lin}$ is the linear expansion. The results were plotted as percentage of $\mathcal{E}_{SA}$ ± SD relative to the rest state.

In-line degassing protocol: After priming, the chip was filled with PBS solution and allowed to equilibrate at 37 °C for at least 2 h. Air bubbles were injected through the system and pushed until they were inside the cell culture chamber. A constant vacuum pressure of -50mbar was applied on the microactuator and the air bubbles were photographed every hour under a stereomicroscope (Olympus SZX10) coupled with a camera (Olympus EP50), to monitor air bubble area variation.

Statistical analysis: Data was compiled and analyzed using the software Graphpad Prism (Graphpad Software). Data plotted in graphical format is presented as mean value ± SD, except deviation to CAD theoretical dimension, which was represented as coefficient of variation (%). Experimental determination of resolution limits tested with an n=4. Cell culture doubling time and metabolic rates (n=6) were compared using a two-way ANOVA statistical test. The latter were analyzed in conjunction with a Sidak's post hoc multiple comparison test. Epithelium height measurements (n=3) were compared using an unpaired t-test. Statistical significance was defined as $p<0.05$ (*), $p<0.01$ (**), $p< 0.0001$ (****).

Acknowledgements

This work was supported by Fundação para a Ciência e Tecnologia (FCT) and Doctoral Programme on Cellular and Molecular Biotechnology Applied to Health Sciences (BiotechHealth Programme; ref. PD/00016/2012), by Programa Operacional Potencial Humano (POPH), and SkinChip project (PTDC/BBB-BIO/1889/2014). The work has been also financed by: (1) Fundo Europeu de Desenvolvimento (FEDER) Regional funds through the COMPETE 2020 - Operacional Programme for Competitiveness and Internationalization (POCI), Portugal 2020, and by Portuguese funds through FCT/*Ministério da Ciência, Tecnologia e Inovação* in the framework of the projects "Institute for Research and Innovation in Health Sciences" (POCI-01-0145-FEDER-007274), 3DChroMe (POCI-01-0145-FEDER-30164); Norte Portugal Regional Programme (NORTE 2020), under the PORTUGAL 2020 Partnership Agreement, through the European Regional Development Fund (ERDF) for projects NORTE-01-0145-FEDER-000029 and DOCnet (NORTE-01-0145-FEDER-000003). DAF acknowledges FCT for his support through a FCT/BiotechHealth PhD Programme grant, ref. PD/BD/105976/2014. JPC acknowledges funding from the European Structural and Investment funds through the Compete Programme (Grant #: LISBOA-01-0145-FEDER-016405) and from National funds through FCT (SAICTPAC/0019/2015) via the research project POINT4PAC, and FCT funding through INESC MN (Unidade ID 5367).

The authors would also like to thank: Jorge Ferreira (Chromosome Instability Group, i3S/IBMC) for granting access to the plasma cleaner equipment and for the insightful scientific support; i3S Scientific Platform (Biointerfaces and Nanotechnology core facility, i3S/INEB), member of the national infrastructure PPBI - Portuguese Platform of Bioimaging (PPBI-POCI-01-0145-FEDER-022122), in particular Maria Lázaro for support and access to the SP5 confocal microscope; Aureliana Sousa (Biofabrication Group at i3S/INEB) for

scientific support and discussion; Dina Leitão (Centro Hospitalar e Universitário São João) for providing access to the normal gastric mucosa specimens; Celso Reis for kindly providing the antibody against Mucin-1.

Disclosures

Authors declare no conflict of interest.

References

[1] P. A. Auroux, D. Iossifidis, D. R. Reyes,A. Manz, Anal. Chem. **2002**, 74, 2637.
[2] S. K. Sia,G. M. Whitesides, Electrophoresis **2003**, 24, 3563.
[3] E. W. Young,D. J. Beebe, Chem. Soc. Rev. **2010**, 39, 1036.
[4] C. Moraes, M. Likhitpanichkul, C. J. Lam, B. M. Beca, Y. Sun,C. A. Simmons, Integrative Biology **2013**, 5, 673.
[5] P. J. Hung, P. J. Lee, P. Sabounchi, R. Lin,L. P. Lee, Biotechnol. Bioeng. **2005**, 89, 1.
[6] I. E. Araci,P. Brisk, Curr. Opin. Biotechnol. **2014**, 25, 60.
[7] D. Huh, B. D. Matthews, A. Mammoto, M. Montoya-Zavala, H. Y. Hsin,D. E. Ingber, Science **2010**, 328, 1662.
[8] C. Y. Chan, P.-H. Huang, F. Guo, X. Ding, V. Kapur, J. D. Mai, P. K. Yuen,T. J. Huang, Lab on a Chip **2013**, 13, 4697.
[9] D. Huh, Y.-s. Torisawa, G. A. Hamilton, H. J. Kim,D. E. Ingber, Lab on a Chip **2012**, 12, 2156.
[10] S. N. Bhatia,D. E. Ingber, Nat. Biotechnol. **2014**, 32, 760.
[11] O. T. Guenat,F. Berthiaume, Biomicrofluidics **2018**, 12,
[12] E. Ergir, B. Bachmann, H. Redl, G. Forte,P. Ertl, Front. Physiol. **2018**, 9, 1417.
[13] A. O. Stucki, J. D. Stucki, S. R. Hall, M. Felder, Y. Mermoud, R. A. Schmid, T. Geiser,O. T. Guenat, Lab Chip **2015**, 15, 1302.
[14] H. J. Kim, D. Huh, G. Hamilton,D. E. Ingber, Lab on a Chip **2012**, 12, 2165.
[15] A. Marsano, C. Conficconi, M. Lemme, P. Occhetta, E. Gaudiello, E. Votta, G. Cerino, A. Redaelli,M. Rasponi, Lab Chip **2016**, 16, 599.
[16] L. D. Ma, Y. T. Wang, J. R. Wang, J. L. Wu, X. S. Meng, P. Hu, X. Mu, Q. L. Liang,G. A. Luo, Lab Chip **2018**, 18, 2547.
[17] I. K. Zervantonakis, C. R. Kothapalli, S. Chung, R. Sudo,R. D. Kamm, Biomicrofluidics **2011**, 5, 13406.

[18] E. W. K. Young, Integrative Biology **2013**, 5, 1096.
[19] S. Varma,J. Voldman, Lab Chip **2018**, 18, 3333.
[20] D. A. Bartholomeusz, R. W. Boutte,J. D. Andrade, Journal of Microelectromechanical Systems **2005**, 14, 1364.
[21] S. Cosson, L. G. Aeberli, N. Brandenberg,M. P. Lutolf, Lab on a Chip **2015**, 15, 72.
[22] J. I. Martinez-Lopez, M. Mojica, C. A. Rodriguez,H. R. Siller, Sensors **2016**, 16,
[23] L. E. Stallcop, Y. R. Álvarez-García, A. M. Reyes-Ramos, K. P. Ramos-Cruz, M. M. Morgan, Y. Shi, L. Li, D. J. Beebe, M. Domenech,J. W. Warrick, Lab on a Chip **2018**, 18, 451.
[24] S. R. A. Kratz, C. Eilenberger, P. Schuller, B. Bachmann, S. Spitz, P. Ertl,M. Rothbauer, Sci. Rep. **2019**, 9, 9287.
[25] Y. N. Xia,G. M. Whitesides, Angewandte Chemie-International Edition **1998**, 37, 550.
[26] J. C. McDonald, D. C. Duffy, J. R. Anderson, D. T. Chiu, H. Wu, O. J. Schueller,G. M. Whitesides, Electrophoresis **2000**, 21, 27.
[27] B. H. Chueh, D. Huh, C. R. Kyrtsos, T. Houssin, N. Futai,S. Takayama, Anal. Chem. **2007**, 79, 3504.
[28] K. Aran, L. A. Sasso, N. Kamdar,J. D. Zahn, Lab Chip **2010**, 10, 548.
[29] L. Tang,N. Y. Lee, Lab on a Chip **2010**, 10, 1274.
[30] P. Fikar, G. Lissorgues, L. Rousseau, O. Francais, B. Le Pioufle, F. S. Hamdi, V. Georgiev,D. Georgiev, Microsystem Technologies-Micro-and Nanosystems-Information Storage and Processing Systems **2017**, 23, 3901.
[31] C. G. Sip,A. Folch, Biomicrofluidics **2014**, 8, 036504.
[32] J. Wu,N. Y. Lee, Lab on a Chip **2014**, 14, 1564.
[33] B. N. Lourenco, T. Dos Santos, C. Oliveira, C. C. Barrias,P. L. Granja, Acta Biomater. **2018**, 82, 68.
[34] M. D. Basson, Digestion **2003**, 68, 217.
[35] K. G. Birukov, J. R. Jacobson, A. A. Flores, S. Q. Ye, A. A. Birukova, A. D. Verin,J. G. Garcia, Am. J. Physiol. Lung Cell Mol. Physiol. **2003**, 285, L785.
[36] A. Mihic, J. Li, Y. Miyagi, M. Gagliardi, S. H. Li, J. Zu, R. D. Weisel, G. Keller,R. K. Li, Biomaterials **2014**, 35, 2798.
[37] C. P. Gayer,M. D. Basson, Cell. Signal. **2009**, 21, 1237.
[38] D. Boltin,Y. Niv, J Gastrointest Dig Syst **2013**, 3, 15519.
[39] S. Rocha, J. Carvalho, P. Oliveira, M. Voglstaetter, D. Schvartz, A. R. Thomsen, N. Walter, R. Khanduri, J. C. Sanchez, A. Keller, C. Oliveira,I. Nazarenko, Adv Sci (Weinh) **2019**, 6, 1800948.
[40] M. Balmana, S. Mereiter, F. Diniz, T. Feijao, C. C. Barrias,C. A. Reis, Molecules **2018**, 23,

[41] I. Pereiro, A. Fomitcheva Khartchenko, L. Petrini,G. V. Kaigala, Lab Chip **2019**, 19, 2296.
[42] K. Kaarj,J. Y. Yoon, Micromachines (Basel) **2019**, 10,
[43] T. d. Santos, B. N. Lourenço, J. Coentro,P. L. Granja, Concepts and Models for Drug Permeability Studies, (Eds: B. Sarmento), Woodhead Publishing, Chippenham, UK, 2016, Ch. 3.2.
[44] a) B. N. Lourenço, T. Dos Santos, J. Coentro, C. Barrias, C. Oliveira,P. L. Granja, in Proc. Frontiers in Bioengineering and Biotechnology, Montréal, **2016**; b) B. N. Lourenço, T. Dos Santos, J. Coentro, C. Barrias, C. Oliveira,P. L. Granja, presented at 10th World Biomaterials Congress, Montréal, May, **2016**.
[45] M. A. Eddings, M. A. Johnson,B. K. Gale, Journal of Micromechanics and Microengineering **2008**, 18,
[46] J. Schindelin, I. Arganda-Carreras, E. Frise, V. Kaynig, M. Longair, T. Pietzsch, S. Preibisch, C. Rueden, S. Saalfeld, B. Schmid, J. Y. Tinevez, D. J. White, V. Hartenstein, K. Eliceiri, P. Tomancak,A. Cardona, Nat. Methods **2012**, 9, 676.
[47] M. Rodrigues, I. Vito, R. Santos, J. Paiva, P. Pontes, P. Silva,F. Carneiro, Cell Tissue Bank **2009**, 10, 75.

CHAPTER IV

Bioinspired human stomach-on-a-chip with in-vivo like function and architecture

(In preparation)

Bioinspired human stomach-on-a-chip with in-vivo like function and architecture

*Daniel A. Ferreira[1,2,3], João P. Conde[4,5], Mario Rothbauer[6,7], Peter Ertl[8], * Pedro L. Granja,[1,2]*, Carla Oliveira,[1,9,10]*

[1] i3S – Instituto de Investigação e Inovação em Saúde, Universidade do Porto, Rua Alfredo Allen, 208, 4200-135 Porto, Portugal

[2] INEB – Instituto de Engenharia Biomédica, Universidade do Porto, Rua Alfredo Allen, 208, 4200-135 Porto, Portugal

[3] ICBAS – Instituto de Ciências Biomédicas Abel Salazar, Universidade do Porto, Rua Jorge de Viterbo Ferreira, 228, 4050-313 Porto, Portugal

[4] Department of Bioengineering, Instituto Superior Técnico, Universidade de Lisboa, Av. Rovisco Pais, 1, 1049-001 Lisboa, Portugal

[5] Instituto de Engenharia de Sistemas e Computadores – Microsistemas e Nanotecnologia (INESC MN), Rua Alves Redol, 9, 1000-029 Lisboa, Portugal

[6] Department of Orthopedics and Trauma Surgery, Karl Chiari Lab for Orthopedic Biology, Medical University of Vienna, Whäringer Gürtel 18-20, 1090 Vienna, Austria

[7] Institute of Applied Synthetic Chemistry, Vienna University of Technology (TUW), Getreidmarkt, 9/163, 1060 Vienna, Austria

[8] Faculty of Technical Chemistry, Vienna University of Technology (TUW), Getreidemarkt 9, 1060 Vienna, Austria

[9] Ipatimup – Institute of Molecular Pathology and Immunology, Universidade do Porto, Rua Júlio Amaral de Carvalho 45, 4200-135 Porto, Portugal

[10] Department of Pathology, Faculty of Medicine, University of Porto, Alameda Prof. Hernâni Monteiro, 4200-319 Porto, Portugal

* Joint senior authorship

Keywords: microfluidics, pdms, gastric mucosa, organ-on-a-chip, stomach-on-a-chip

ABSTRACT

Reproducing organotypic architecture and function is the hallmark of organ-on-a-chip technology. These biomimetic devices allow unprecedented control over the in vitro microenvironment, enabling the engineering of native tissue-like complex 3D architectures and the modulation of dynamic conditions, similar to those found in vivo. Herein, a bioinspired stomach-on-a-chip device supporting peristalsis-like motion and reconstituting organ-level epithelial architecture and function is described. The device simulates the upper epithelial interface, representing the three innermost layers of the gastric mucosa, namely the epithelial barrier, the basement membrane and the lamina propria. The dynamic environment imparted by mechanical actuation of the flexible on-chip cell culture substrate was shown to induce epithelial polarization and differentiation traits, characteristic of the native gastric mucosa. Furthermore, the stomach-on-a-chip was able to partially recapitulate gastric barrier function. The engineered platform highlights the importance of addressing the mechanical microenvironment of the native organ to potentiate an organ-level response of the artificial tissue. The proposed stomach-on-a-chip could be an alternative to current animal models, by providing a human-derived platform that can sustain a long-term biomimetic culture of the gastric mucosa.

1. Introduction

The stomach plays a central role in human physiology, and gastric dysfunction poses serious health risks with associated non-neglectable mortality and morbidity rates.[1-3] Gastric cancer, for instance, represented the fourth leading cause of estimated cancer related deaths in 2020.[4] The demand for better study models recapitulating accurately human gastric physiology is high, mainly to improve the way therapies for gastric-associated diseases are currently tested.

Two-dimensional (2D) cell culture models, lacking complexity of human tissue architecture and physiology, are commonly used for early stages of drug development but, as expected, their simplified nature has a very low predictive power in drug efficacy.[5, 6] Three dimensional (3D) models, engineered with bio-inspired matrices replicating the chemistry, assembly, multicellular nature and architecture of living organs, provide a better simulation of physiological conditions.[7, 8] Similarly, addition of primary cells and stem cells *in vitro*, was key to the development of increasingly complex *in vitro* gastric models.[9-12] Notwithstanding, these models were only developed for non-human cells. Recently, a long-lived, air-liquid interface gastric mucosoid culture model of human origin, was developed, closely resembling the phenotypical features of normal human gastric epithelium.[13] However, it represented the gastric epithelial layer only, limiting the evaluation of physiological responses. We previously reported a 3D two-layered model, mimicking the gastric mucosa and lamina propria.[14] The augmented 3D complexity reflected more closely the architecture of the native organ, while the fibroblastic components provided bioactive signaling to the epithelial layer. Despite notable progress, even the most advanced 3D culture models are limited and still lack the dynamic nature of the gastric mucosa, which is known to be extremely important for normal gastrointestinal physiology.[15, 16] *In vivo*, cells are continuously sensing their vicinity and mechanical cues can modulate, to a large extent, the cellular response at the biochemical level.[17, 18] The contribution of biomechanical forces is particularly relevant in tissues such as the gut, where cells are repeatedly exposed to strain.[19-22] Recent developments in soft-lithography, in particular in the fabrication of microactuators, enabled the creation of organ-on-a-chip devices, consisting in microfluidic platforms with capability to replicate a given functional sub-unit of a human organ.[21-25] This bioinspired technology enabled the application of precisely defined amounts of strain to cell culture substrates, thus allowing to understand, to a greater level of detail, the implications of mechanotransduction at the cellular and molecular level.[19, 26]

Recently, Lee and colleagues reported preliminary developments on a stomach-on-a-chip (SoC) model, where gut organoids were encased within a microfluidic device and were exposed to cyclic peristalsis-like stretching.[27] While presenting a promising model to address the effects of dynamic actuation on a differentiated gastric mucosa, the system used a Matrigel-derived supporting mesh that poorly recapitulated the human gastric extracellular matrix (ECM) composition and architecture. A more physiologically relevant environment, resembling the native gastric ECM, could be a critical asset when addressing system level response within these devices. Applications focusing on pathological ECM remodeling as is the case during tumor invasion, could particularly benefit from such a model, as these processes are largely mediated by alterations in ECM components.[28, 29]

In the current work, we propose a tissue engineered approach to design and fabricate a human-derived biomimetic SoC microdevice, experiencing peristalsis-like movement and intraluminal flow, with architecture and function emulating the native organ. The currently developed model was engineered to represent the three innermost layers of the gastric mucosa, namely the epithelial barrier, characterized by a tight cellular monolayer, the basement membrane, a layer mediating the adhesion and communication between the epithelial layer and the adjacent ECM, and an analogue of the lamina propria, consisting of a collagen type I mesh with embedded normal gastric fibroblasts, able to provide paracrine crosstalk between the lamina propria analogue and the epithelial layer. We then characterized the cellular and molecular alterations induced by the dynamic environment of the SoC, to assess its ability to promote functional and molecular traits characteristic of the native gastric mucosa.

The developed SoC represents a human-derived experimental *in vitro* asset for pre-clinical studies on host-pathogen interactions, drug-drug interactions, drug absorption or targeted delivery of compounds and nanoparticles among others.

2. Results and discussion

2.1. Design and fabrication of a multilayered stomach-on-a-chip device

The SoC was designed and fabricated using a rapid prototyping method we previously described.[25] This strategy was shown to be capable of rapidly generating multilayered polydimethylsiloxane (PDMS) microfluidic devices with integrated microactuators. Importantly, the technique was shown to be amenable to the fabrication of integrated microactuators, capable of eliciting physiological levels of mechanical stretching over cell culture substrates.

To represent the three innermost layers of the stomach wall (epithelial barrier, basement membrane and supporting lamina propria), the SoC was devised as 9-layered device (**Figure 1a**). The top layer was produced from thick PDMS, fabricated by gravity casting. The fluidic network was produced from 500 µm thick PDMS sheets and consisting of 3 fluid routing structures, intercalated by a 16 µm thick polyethylene terephthalate (PET) membrane (**Figure 1a-b**). The proposed 3-tiered fluidic structure was designed to enable the replication of an epithelial barrier architecture on the top chamber and importantly, to provide the efficient incorporation of a lamina propria analogue, in the middle culture chamber. This allowed ECM embedded fibroblasts to be adequately fed by flowing cell culture media above and underneath it. The microactuator was bonded directly below the fluidic network and is composed of a 2-part sub-assembly, namely a 250 µm thick PDMS membrane juxtaposed on a rectangular vacuum chamber of the same thickness (**Figure 1c**). The entire biochip was sealed against a microscope glass slide.

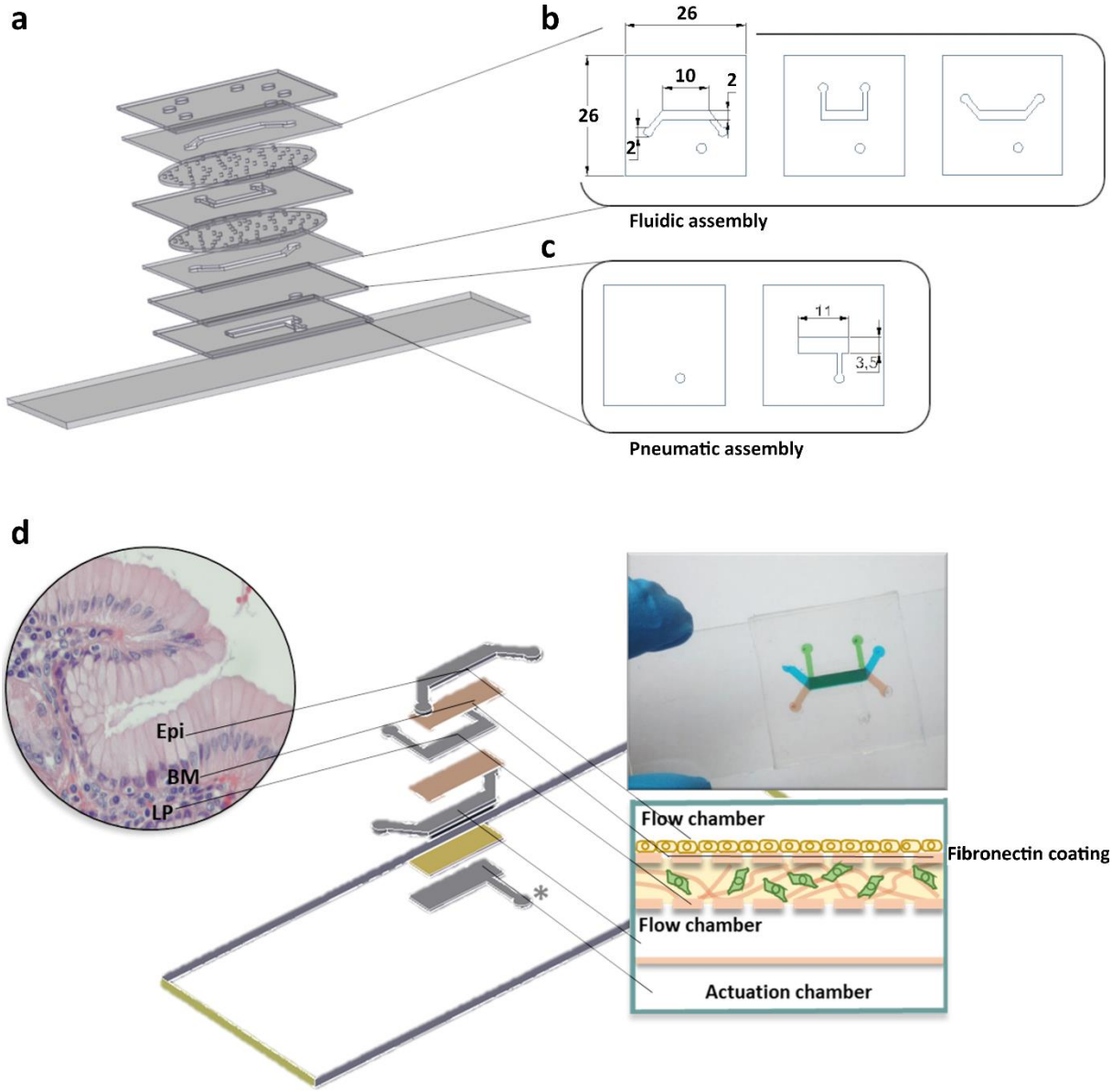

Figure 1. (a) Exploded view of the SoC depicting the 9 intercalating parts composing the fluidic and pneumatic assembly: the topmost layer corresponds to a thick PDMS layer produced by gravity casting to support tube attachment, while the bottommost layer corresponds to a microscope glass slide. (b) Top-down view of the fluidic structures composing the fluidic assembly. Each of the layers is intercalated by a PET membrane. (c) Top down view of the 2-part pneumatic assembly consisting of a thin 250 µm PDMS membrane (left) and a vacuum chamber placed underneath the membrane (right). (d) Schematic of the stomach-on-a-chip highlighting the engineered gastric mucosa with a schematic representation of the relevant gastric layers, and corresponding histological image representing the 3 innermost layers of the gastric wall, namely the epithelial barrier (Epi), the basement membrane (BM) and the lamina propria (LP).

2.2. On-chip emulation of stomach epithelium dynamics and architecture

To model the dynamic stomach microenvironment, peristalsis-like motion was imparted to the cell culture substrate by applying vacuum to the microactuator at cyclical intervals. The stretching pattern was modeled as a sinusoidal wave of 0.15 Hz frequency, which closely resembles the peristalsis pattern of the gut,[22, 30, 31] at a maximum vacuum pressure of -100 mbar. We have previously shown that under these conditions, the integrated microactuator could produce surface stretching of approximately 10%, which is within the physiological range of strain that *in vivo* gut cells experience.[25] Furthermore, as the microactuator was placed directly underneath the cell culture chamber, membrane flexing was effected from below, resulting in a tri-axial displacement of the cell culture membrane.

Cell culture media was perfused over the epithelial layer at a flow rate of 2 µL/min. As shear stress is not a dominant force on the stomach lumen, the fluidic routing structures were designed to keep shear stress at a low level. Taking in consideration a channel profile, 0.2 cm wide and 0.05 cm high, and a volumetric flow rate of $3.3x10^{-05}$ $cm^3.s^{-1}$, we estimated the shear stress over the epithelial cell culture to be about 0.003 $dyne.cm^{-2}$. This value is in line with the physiological shear stress experienced by gut cells *in vivo*, which ranges between 0.002 and 0.080 $dyne.cm^{-2}$.[22, 32]

Emulation of the stomach epithelium was achieved on the two upper fluidic channels. The top channel encased the basement membrane analogue, consisting of a thin 50 $µg.mL^{-1}$ fibronectin mesh coating the PET membrane, on top of which an epithelial monolayer was seeded (**Figure 1d**). To mimic the selective permeability of the gastric mucosa it is important that the epithelial layer forms a cohesive, tightly packed monolayer, expressing fully developed cell-to-cell contacts. Here, we used a monolayer culture of MKN74 epithelial gastric cells (**Table S1**). This cell line displays moderate differentiation, a typical epithelial cobblestone-like morphology and exhibits several characteristics of its epithelial origin, such as fully developed and correctly localized tight junctions, that mediate paracellular traffic across the epithelial barrier, as shown by staining of tight junction partners ZO-1 and occludin (**Figure S2a**), as well as functional E-cadherin mediated cell-to-cell contacts, via adherens-junctions, as observed by co-immunofluorescence against E-cadherin and adherens-junction partner α-catenin (**Figure S2b**). The adhesion complex mediates tight monolayer integrity by establishing cell-to-cell contacts and promotes an indirect link between the actin cytoskeleton of adjacent cells. The ability of cells to form an effective barrier was assessed by measuring the transepithelial resistance (TEER). Transwell

cultures of MKN74 cells, seeded at a cellular density of $3.0x10^5$ cells/mL, reached confluency on average within 3 days post-seeding. Interestingly, after day 2 the cell line already exhibited TEER values above 100 $\Omega.cm^2$, characteristic of a fully formed barrier, reaching an average of about 157 $\Omega.cm^2$ after 5 days in culture (**Figure S2c**). We have also previously reported that MKN74 cells grown in a 3D environment displayed further differentiation traits, namely a polarized phenotype and apical expression of mucins, characteristic of the normal gastric epithelium,[33] and that these traits were further enhanced when a 3D culture of MKN74 was grown under dynamic conditions, in a simplified microfluidic model of the stomach epithelium, featuring biomechanical stretching.[25] Taken together, these observations suggest that the MKN74 cell line was well suited to emulate the gastric barrier in the current SoC model.

To mimic the lamina propria, we used a 3 $mg.mL^{-1}$ collagen type I mesh since this matrix constituent is the most prevalent ECM protein in the human gastric lamina propria.[34] The collagen mesh was then embedded with normal gastric NST20 fibroblasts (**Table S1)**, thus providing biomimetic paracrine signaling to the epithelial culture, but also potentially introducing physiologically relevant ECM remodeling of the lamina propria analogue. The ECM was directly injected in the central fluidic channel, while the bottom perfusion channel acted as a direct feeding layer to the ECM embedded fibroblasts above it (**Figure 1d**).

2.3. On-chip conditions do not affect cellular homeostasis of the epithelial barrier

Despite PDMS based devices being permeable to air, it is unlikely that this exchange is sufficient to assure an efficient buffering capacity of the atmospheric 5% CO_2 used in conventional cell culture incubators. Particularly in pressurized perfusion systems, such as the one used here, the culture media vessel is isolated from the atmosphere of the cell culture incubator. We have thus opted to grow cells within the SoC in CO_2 independent medium. To ensure that cells growing under CO_2 depletion and cells growing under conventional cell culture atmosphere had the same basal readings, we compared their phenotype, proliferation, metabolic activity and doubling time, when fed with CO_2 independent culture medium in a CO_2-depleted atmosphere or with RPMI 1640 in the presence of CO_2. No phenotypic differences were registered between the two groups (**Figure 2a**). Furthermore, Ki67 staining at 48 h of growth showed fully proliferative

populations (**Figure 2b**) and both exhibited a comparable doubling rate (**Figure 2c**). Interestingly, we observed that cells growing under standard conditions, displayed a higher metabolic rate at early time points, than those grown in a CO_2 depleted atmosphere. However, this difference equalized after around 8 days in culture (**Figure 2d**). This observation could suggest that cells growing under CO_2 depleted conditions and fed with buffered medium, may need a longer period to attach and stabilize onto the substrate and start the replicative process until they reach a similar doubling rate than cells growing in standard conditions.

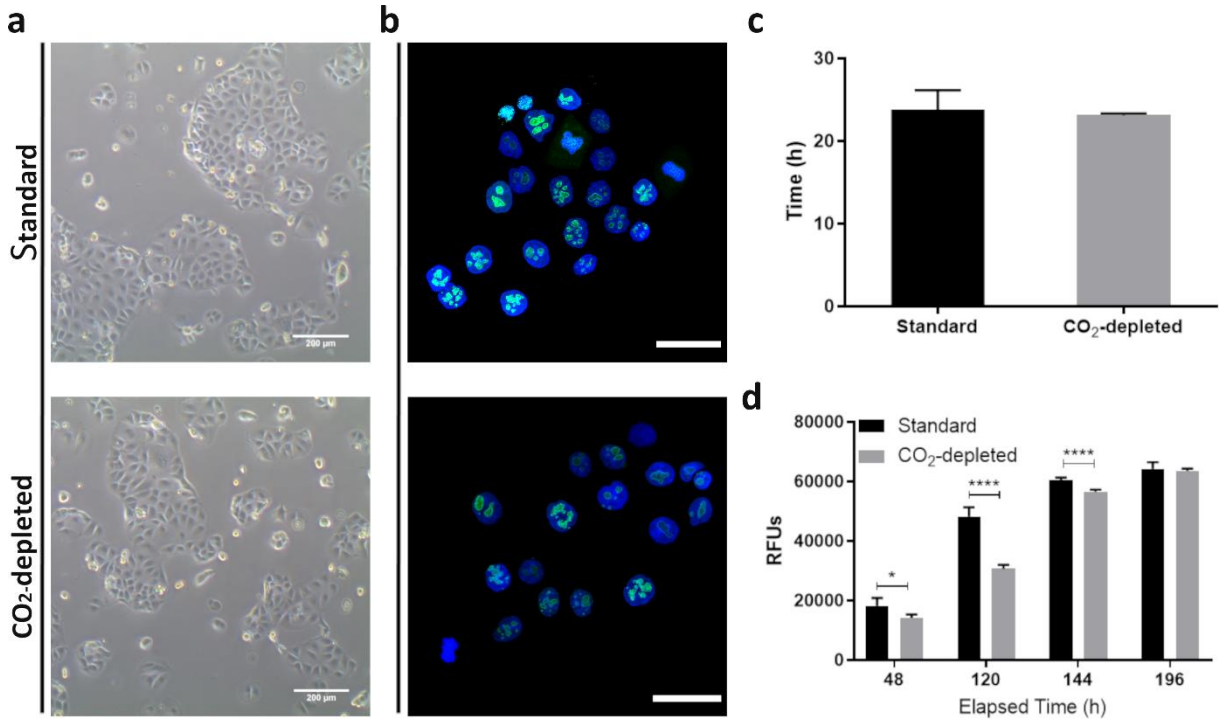

Figure 2. (a) Morphological study of MKN74 cells growing under standard conditions against cells growing under CO_2-depleted conditions (scale bar; 200 µm). (b) Ki67 staining of the same populations (scale bars; 50 µm). (c) Corresponding population doubling time. (d) Comparative study of the metabolic activity of cells growing under normal or CO_2-depleted conditions. All graphical representations display average measurement ± SD (n=6).

2.4. Impact of embedding stomach fibroblasts within a collagen type I mesh

To properly emulate the lamina propria of the stomach wall, it is important that the designed model replicates, at least in part, the cellular milieu of its native counterpart. Here, we used a normal stomach fibroblast cell line (NST-20) embedded in a collagen type I mesh, to

potentiate the paracrine crosstalk between the lamina propria and the epithelial barrier placed above it and to promote crucial native ECM remodeling. In this context, it was important to assess if ECM embedded fibroblasts are metabolically stable and growing in optimal conditions within the hydrogel mesh.

Initially we studied the off-chip behavior of gastric NST-20 fibroblasts seeded at an initial density of $2x10^5$ cells.mL^{-1} within a collagen type I mesh. Observations were carried out over an increasing range of collagen type I densities from 0.5 up to 3.0 mg.mL^{-1}. Metabolic activity of ECM embedded fibroblasts was assessed over a period of 17 days and quantified by resazurin assay. Our observations showed that the metabolic activity increased proportionally with increasing matrix density (**Figure 3a**). For 0.5 mg.mL^{-1} gels, metabolic activity peaked at day 5 and reached a stable plateau until the end of the experimental period. For any other mesh density, metabolic activity increased steadily, reaching a peak at day 11. The same conditions displayed a small reduction in metabolic activity after day 11, which stabilized around day 15-17 in culture. Our results suggest that fibroblasts growing in a 3.0 mg.mL^{-1} collagen mesh need a longer time to stabilize and start the replicative process (**Figure 3a**). This is most likely due to the stiffer environment in which cells were initially seeded. However, once cells stabilized and developed full anchoring, the stiffer conditions seemed more advantageous for cell metabolism. We also observed that by day 17, higher density hydrogels displayed lower overall cell count (data not shown). The higher metabolic rate registered for higher density hydrogels, despite the observable lower cell number per gel, suggests that cells seeded in stiffer hydrogels benefited from a higher metabolic activity. To address the hypothesis that the high metabolic rates observed for higher density gels, could result from cells growing selectively on the surface of the hydrogel, and thus not within a truly 3D environment, we performed a live-dead assay to assess the viability of the embedded fibroblasts and imaged the entire hydrogel volume by z-stack imaging. Our results showed that cells remained viable within the hydrogel, with no appreciable differences in viability from 1.0 up to 3.0 mg.mL^{-1}. The exception being the 0.5 mg.mL^{-1} mesh, where a higher number of dead cells could be observed in the core of the collagen disc (**Figure 3b**). We have observed that the lower density mesh potentiated very fast cell growth and migration and within 3 days the collagen mesh was completely occupied by the embedded fibroblasts. In turn, this could potentiate a higher density of cells in the core of the hydrogel mesh, which could ultimately lead to a nutrient-depleted region within the core of the gel. Calcein staining also allowed morphological characterization of the stomach fibroblasts within the 3D matrices. Cells displayed a typical elongated spindle shape, characteristic of a mesenchymal phenotype. Protrusions establishing contact between adjacent cells could also be observed, suggesting that cell-to-cell signaling was

being promoted within the collagen mesh (**Figure 3b**). Finally, evidence of ECM remodeling was also observed, as shown by immunocytochemistry against collagen type IV and fibronectin, both components of the native gastric lamina propria. *De novo* expression of collagen type-IV could be observed as early as 1 day post-seeding (data not shown), with extensive deposition of both collagen type-IV and fibronectin matrix proteins after 11 days in culture (**Figure 3c**). Taken together these observations suggest that NST-20 fibroblasts are not adversely affected by the embedding within the collagen type I matrix. Under these circumstances, they can reliably be used to mimic the environment of the gastric lamina propria. Furthermore, embedded NST-20 fibroblasts promote ECM remodeling, further enhancing the biomimetic nature of the lamina propria analogue.

It is well understood that fibroblasts anchored to a collagen substrate exert contractile forces that can reshape the collagen fibers into a higher density structure with concomitant loss of volume.[35, 36] However, integrating on-chip a fibroblast-laden collagen hydrogel, requires the hydrogel to withstand continued mechanical distension and retain as much as possible its shape, in order to fill-in the culture chamber completely, thus avoiding disruption of fluid flow. Therefore, we next conducted a gel contraction assay, using the same range of collagen mesh densities described above. We monitored fibroblast-laden hydrogel volume contraction every other day, for a period of 15 days. We observed a decrease of gel area proportional to decreasing hydrogel mesh density, with lower density meshes contracting significantly more. A 0.5 $mg.mL^{-1}$ mesh contracted on average down to 27% of its original size by day 15 in culture. In sharp contrast, a 3.0 $mg.mL^{-1}$ mesh retained 77% of its original size over the same period (**Figure 4a-b**).

Taking these observations into consideration, along with the fact that 3.0 $mg.mL^{-1}$ hydrogels can sustain mechanical actuation for extended periods of time without loss of integrity (data not shown), we decided to conduct further experimentation using a fibroblast laden 3.0 $mg.mL^{-1}$ collagen type I mesh.

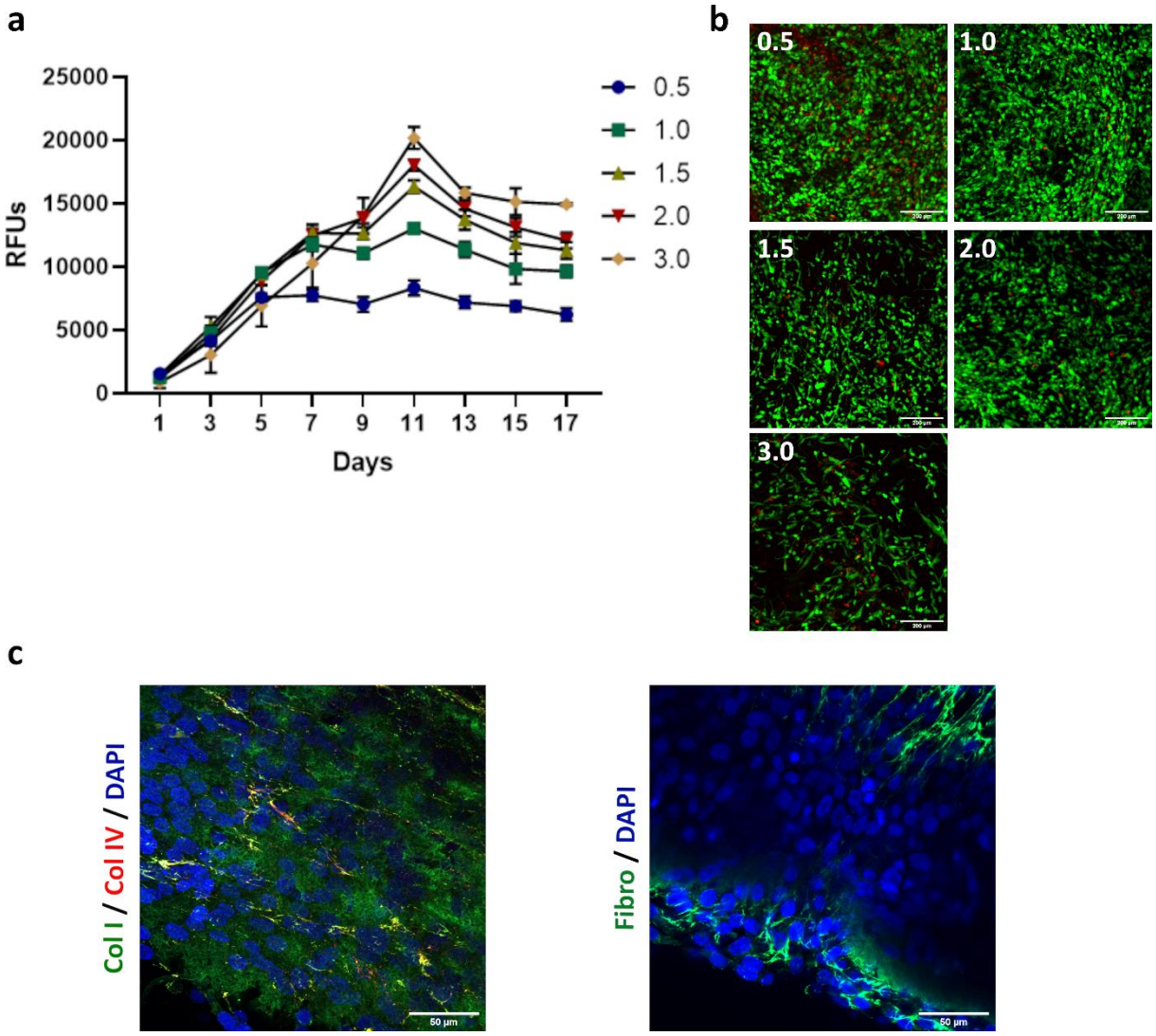

Figure 3. (a) Metabolic activity study of NST20 normal gastric fibroblasts embedded on a biomimetic collagen type I hydrogel mesh. Collagen type I was tested in a range of densities, namely 0.5, 1.0, 1.5, 2.0 and 3.0 mg.mL^{-1}, over a period of 17 days. (b) Live-dead assay performed for the aforementioned populations. Images represent a z-stack projection (z-step: 2 µm) across the entire thickness of the hydrogel. Live cells stained with calcein and depicted in green, whereas dead cells are stained with propidium iodide and seen in red (scale bars:200 µm). (c) Matrix remodeling as effected by the collagen type I embedded NST20 fibroblasts. Collagen type I staining of the supporting hydrogel can be observed in green (left panel). Collagen type IV stained in red (left panel) and fibronectin stained in green (right panel), show *de novo* deposition of ECM components by the fibroblastic population. Nuclei stained with DAPI (blue).

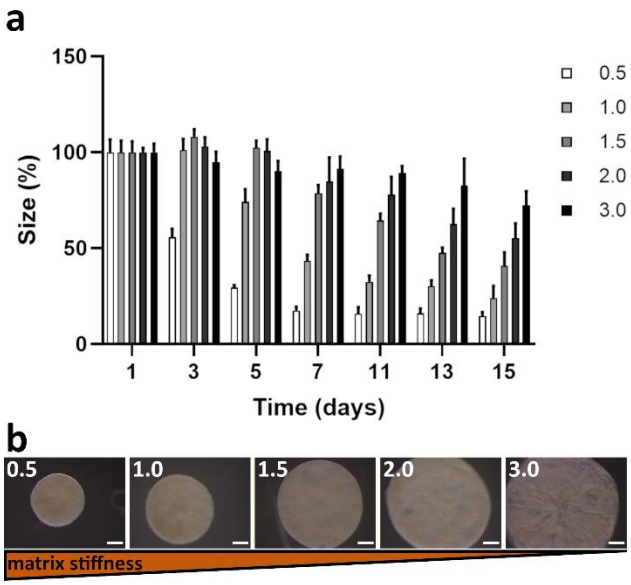

Figure 4. (a) ECM mesh contraction assay performed on fibroblast-laden hydrogels. Contraction tested on a range of collagen type I densities, namely 0.5, 1.0, 1.5, 2.0 and 3.0 mg.mL^{-1} over a period of 15 days. Results graphed as % of area reduction to original size (n=3). (b) Visual representation of the ECM mesh contraction assay. Images represent discs at day 15 post-seeding (scale bars: 500 µm).

2.5. A fibronectin thin mesh, mimics the basement membrane

The basement membrane is a highly organized sheet-like ECM that lines the basal side of the gastric epithelium. *In vivo*, the basement membrane anchors the epithelial layer, assisting in the maintenance of epithelial integrity and playing a crucial role in tissue compartmentalization.[37, 38] Given its preponderant role in tissue maintenance and disease,[39, 40] we aimed to reconstitute a biomimetic anchoring substrate for the epithelial barrier within the SoC to replicate the *in vivo* function of the basement membrane. Here, we tested on a single-channel microfluidic chip several coating formulations with collagen type IV (at 4mg/mL) and fibronectin (at 50 µg.mL^{-1}), namely a pure collagen type IV coating, mixtures of 4:1 and 1:4 mixture of collagen type IV and fibronectin and a pure fibronectin coating. Our results showed that MKN74 cells seeded over a thin coating of collagen type IV displayed an atypical phenotype, with a rounded shape. Over time, cells tended to remain isolated and exhibited cellular protrusions (**Figure 5a**, panel 1). This suggests that cells were attempting to establish typical epithelial cell-to-cell contacts but were unable to form a

sheet-like epithelial monolayer. In contrast, when a mixture of higher fibronectin concentration was used as surface coating, MKN74 cells started exhibiting the typical epithelial phenotype, with cells displaying a cobblestone-like appearance and occupying the entire culture chamber surface (**Figure 5a**, panel 2-3). This observation was more prominent when cells were seeded in a mesh of pure fibronectin (**Figure 5a**, panel 4), where cells displayed a normal phenotype, comparable to that of cells grown routinely in cell cultured-treated plastic vessels (**Figure 5a** – panel 5). Furthermore, it was evidenced by applying flow over the cell culture, that the anchoring substrate was essential for the rapid development of a confluent monolayer under fluid flow conditions. Cells started adhering to the basement membrane as early as 30 min post-seeding forming an 80% confluent monolayer within 24 h (**Figure 5b**), similarly to what was observed in transwell inserts. However, when seeded over uncoated PET membranes and left 24 h in culture, part of the cells detached from the membrane once a fluid-flow was applied. The created patchy seeding pattern took up to 5 days to reach confluency (data not shown). Taking these observations in consideration, we used a thin fibronectin mesh as a basement membrane analogue, thus providing an anchoring substrate capable of providing relevant biomechanical cues.

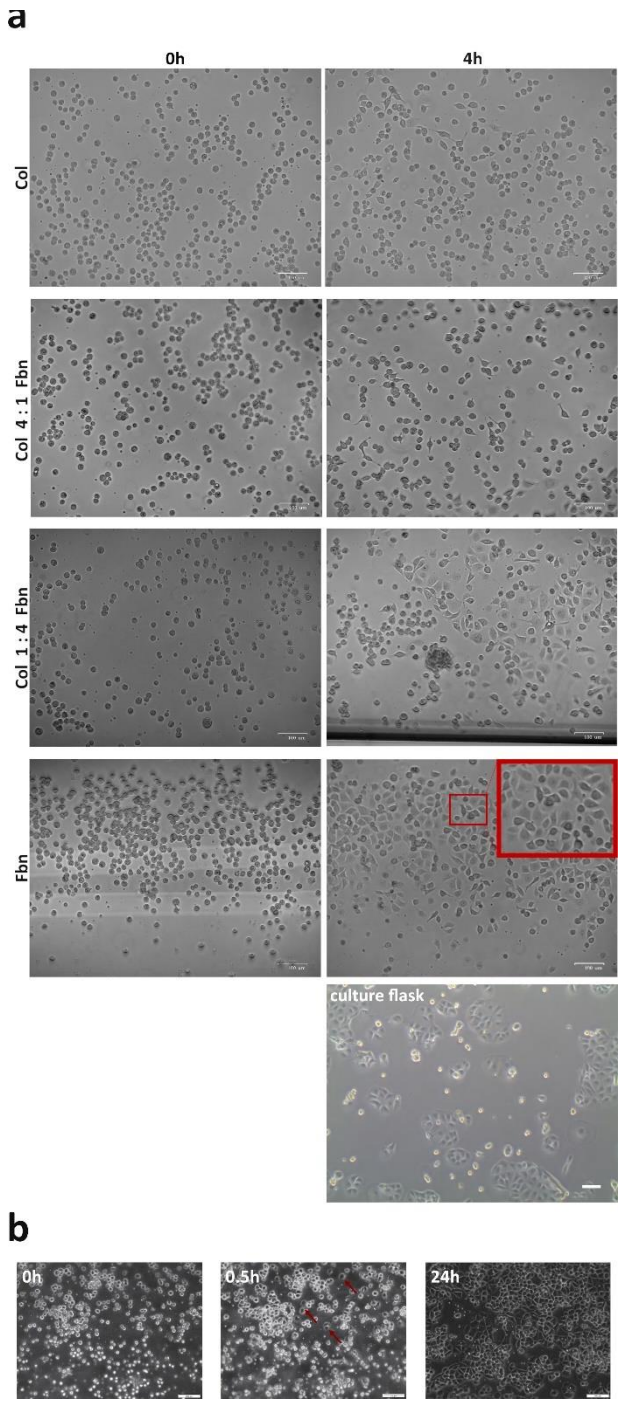

Figure 5. (a)Testing of different coating formulations to mimic the basement membrane. Substrate adhesion was assessed on pure collagen (Col) type IV, a mixture at different ratios of collagen type IV and fibronectin (Fbn), as well as a pure fibronectin coating. The red rectangle on the lower panel depicts a zoomed-in area highlighting the typical cobblestone-like pattern of MKN74 epithelial cells when seeded over a thin fibronectin mesh (scale bar:100 µm). For comparative purposes, the lower right panel shows the typical MKN74 phenotype displayed by cells growing under conventional cell culture conditions on plastic tissue culture treated flasks (scale bar:100 µm). (b) MKN74 cells seeded on-chip, over a fibronectin coating at time 0, 0.5 and 24 h post-seeding (scale bars: 100 µm). MKN74 cells quickly developed stable anchoring when seeded over a fibronectin mesh, with cells attaching as fast as 30 min post-seeding (central panel). Red arrows highlight adherent cells.

2.6. Stomach-on-a-chip device replicates the gastric epithelial barrier

The engineered stomach epithelium was housed within the upper portion of the biochip structure. The perforated membrane allowed communication between the adjacent fluidic structures, while ensuring that cells were kept within their designated confines, as was observed by staining the epithelial cells and the fibroblasts with cell tracker (**Figure 6a**). Importantly, barrier function did not appear to be affected by on-chip culture, as we observed that on-chip MKN74 cells correctly expressed and localized at the cell membrane, adherens-junctions partner E-cadherin and tight-junctions partner ZO-1 (**Figure 6b**). To understand the contribution of the dynamic conditions, towards the establishment of *in vitro* gastric function, we quantified pepsin activity at day 7 in culture under static and dynamic conditions (n=3). Comparison with the transwell static system (S), showed that a regimen of flow alone (F), was not sufficient to induce an increase in pepsin activity (**Figure 6c**). We have observed previously that fluid flow alone, initiated differentiation with concurrent development of a pseudocolumnar epithelium. However, fluid flow alone did not induce a sufficiently strong stimulus for gastric cells to acquire a fully differentiated phenotype.[25] On the other hand, when fluid flow was coupled with biomechanical actuation (F+MA) an increase in pepsin activity was observable (**Figure 6c**). Here, we showed that mechanical stretching of the epithelial population induced a significant increase in pepsin activity, suggesting that mechanical actuation might be promoting cytodifferentiation similar to that observed in the native organ. Finally, as the fibroblast-laden hydrogel is at the inner core of the chip, we also assessed the viability of the fibroblastic population growing on-chip by the live-dead assay. No major deviation was observed compared to our previous results obtained on off-chip collagen discs, with most of the fibroblastic population being viable within the hydrogel (**Figure 6d**). This confirmed the efficiency of the lower perfusion compartment in providing correct feeding to the embedded fibroblasts.

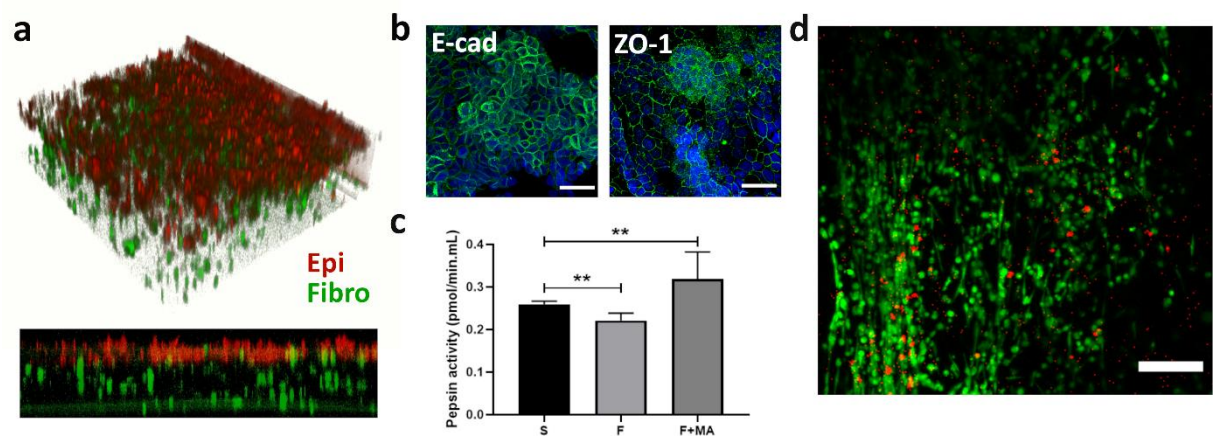

Figure 6. (a) 3D projection of the stomach-on-a-chip biological barrier. On-chip long-term operation generated a fully developed epithelial barrier (stained with cell tracker in red). Below the epithelial layer, fibroblasts could be seen (stained with cell tracker in green) interspersed on a collagen type I matrix. (b) Epithelial barrier function was confirmed on-chip by staining MKN74 cells against adherens junction protein E-cadherin and tight junction protein ZO-1, evidencing fully functional cell-to-cell contacts and paracellular selectivity (scale bars: 50 µm). Nuclei stained with DAPI (blue). (c) Pepsin activity study on static vs dynamic conditions. Results reflected the conversion of the inactive precursor pepsinogen, to the active form, pepsin, by autocleavage under acidic conditions. Graph represents mean values ± SD (n=3). (d) Live-dead assay of on-chip NST20 fibroblasts, with live cells stained in green and dead cells stained in red. On-chip viability was within acceptable levels and similar to that registered off-chip using fibroblast-laden collagen discs, evidencing the efficiency of the chip design in providing correct feeding to the cells within its core (scale bar: 200 µm). All images taken after 6 days of culture on-chip.

2.7. Stomach-on-a-chip replicates gastric epithelial barrier-function and selective permeability

Selective permeability to small molecules and drugs is a characteristic of epithelial interfaces, such as that of the human stomach. Therefore, we compared transport of a small 40 kDa molecule, namely fluorescein isothiocyanate (FITC)-labelled dextran, across the artificial epithelium to assess the impact of dynamic conditions, as well as of the engineered 3D architecture on paracellular transport across the epithelial barrier. Experimental conditions were measured on-chip for epithelial cells with culture media flow only (F), flow and mechanical actuation (F+MA), or the fully assembled SoC containing the epithelial and the fibroblastic populations and subjected to flow and mechanical actuation (SoC+F+MA). All of these conditions were compared to cells growing in static transwell conditions (S).With

this setup, we aimed to assess independently the contribution of each factor, namely the effect of flow, mechanical actuation and the on-chip emulation of the lamina propria, towards the establishment of organ level function within the chip. Here, a solution of FITC-labelled dextran was either added to the apical side of the epithelium in the transwell static condition or perfused over the apical side of the SoC at a flow rate of 2 µL/min. Samples were collected from the basal side chamber every 30 min, for a total period of 180 min. The transwell inserts were slowly stirred for 5 s after each sample collection, to counteract the static nature of the transwell system and to avoid the saturation of the epithelial barrier surface with FITC-labelled dextran molecules, which could limit diffusion across the barrier. Our observations showed a marked difference in paracellular permeability for cells growing under static conditions compared to dynamic conditions, with a significant difference already observable already at 30 min (**Figure 7**). Flow alone (F) was sufficient to induce a marked decrease in the permeability of the gastric epithelium, in agreement to what we have previously reported, as flow alone was sufficient to induce alterations in the phenotype and molecular signature of these cells on a simplified microfluidic model of the gastric epithelium.[25] A similar permeability profile was observed for MKN74 cells under flow and mechanical actuation (F+MA), as well as for the fully assembled SoC (SoC+F+MA). Overall, our results suggest that dynamic conditions play a significant role in the establishment of a tightly knit epithelium, displaying highly selective permeability across the epithelial barrier, when compared to a static model. This is a relevant observation, as conventional gastric static layouts, used as diffusion models across the epithelial barrier, may be underestimating the contribution of paracellular selectivity across the barrier.

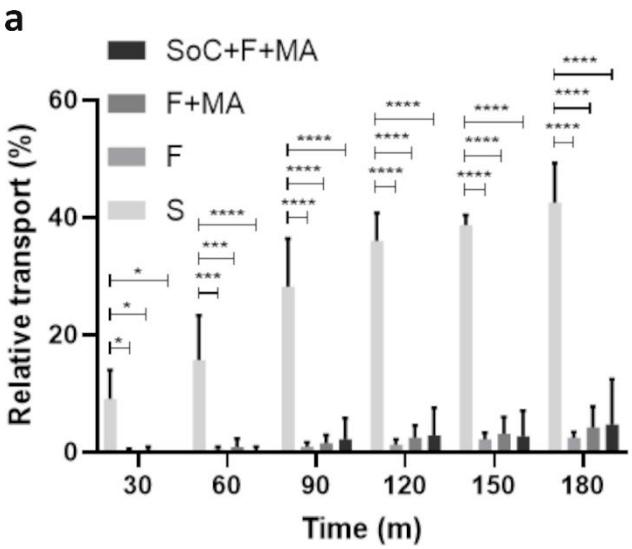

Figure 7. Gastric permeability study by assessing the capability of a small molecule (FITC-dextran) to cross the epithelial barrier. MKN74 epithelial cells grown without the fibroblastic population, either in transwell inserts under static conditions (S), or on-chip under flow (F) or flow coupled with mechanical actuation (F+MA). The condition SoC+F+MA refers to the fully assembled stomach-on-a-chip (SoC). Results shown as relative transport (%) over time. Graph represents mean values ± SD (n=3).

In a previous work, we have shown that imparting mechanical actuation on a simplified microfluidic model of the gastric epithelium exerted a profound effect on cell morphology and its molecular signature. A MKN74 epithelial monolayer cultured under dynamic conditions, *i.e.,* flow and mechanical distension, displayed differentiation traits, such as a polarized epithelium and increased cell height, characteristic of the normal gastric epithelium. Furthermore, mucin-1 expression could be observed in the apical surface of zones of globular growth, resembling mucin-1 expression in normal gastric tissue.[25]

Here, we aimed to characterize the phenotypic and molecular traits developed by the SoC gastric epithelium under dynamic conditions. As reported above, MKN74 cells formed a selective barrier after 2 days in culture when seeded at a density of $3.0x10^5$ cells/mL. Taking this in consideration, the MKN74 cell population was seeded on-chip and allowed to reach confluency over a period of 3 days, followed by 3 days under flow regime and mechanical stretching of the cell culture substrate. Upon application of mechanical stretching and fluid flow, the SoC epithelium thickened considerably, reaching an average thickness of 38.5 µm and globular-like structures developed across its surface (**Figure 8a**). This is in sharp contrast to what was observed in static MKN74 cultures grown in transwell inserts, where cells formed a flattened monolayer similar to a squamous epithelium (**Figure 8b**). Accordingly, the bioengineered SoC epithelium acquired a polarized state, with cells

displaying a columnar shape with elongated nuclei located at the basal side and E-cadherin expression exclusively across the basolateral region. This phenotype closely resembled a pseudostratified columnar epithelium, similar in many aspects to its *in vivo* counterpart (**Figure 8a**). Concurrently, expression of mucin-1 could be observed across the apical surface of the globular structures (**Figure 8c**). This is in accordance to what can be observed in the native stomach [41] and as previously reported for other MKN74 3D gastric models.[25, 33, 42] Overall, our observations show that the engineered device, closely mimics the gastric architecture and microenvironment, by reproducing the 3 innermost-layers of the gastric epithelium. Furthermore, the peristalsis-like actuation and intra-luminal flow simulation seemed capable of producing physiologically relevant stimuli, inducing the MKN74 cell line, an otherwise moderately differentiated cell line that typically forms a squamous-like epithelium, to undergo further differentiation and acquire phenotypical characteristics typical of the normal gastric epithelium. The engineered SoC was not only capable of replicating the gastric mucosa architecture, by displaying a degree of differentiation and polarization characteristic of the native organ, but it also allowed the partial reproduction of gastric function, as shown by enhanced barrier function. Importantly, the modularity of the SoC has been shown to be amenable to study different aspects of gastric physiology and disease. Here we chose to replicate the mesenchymal signaling between the fibroblastic population, typically found within the gastric lamina propria and essential for tissue homeostasis. However, the lamina propria's, cellular and molecular milieu is diverse and other aspects could be easily studied. Components of the immune system could be added to study response to induced inflammation or response to tumor initiation. Likewise, an endothelial interface could be established on the lower perfusion channel, thus increasing the complexity of the system to represent the vasculature of the lamina propria, a model that would be well suited to study tumor invasion and intravasation.

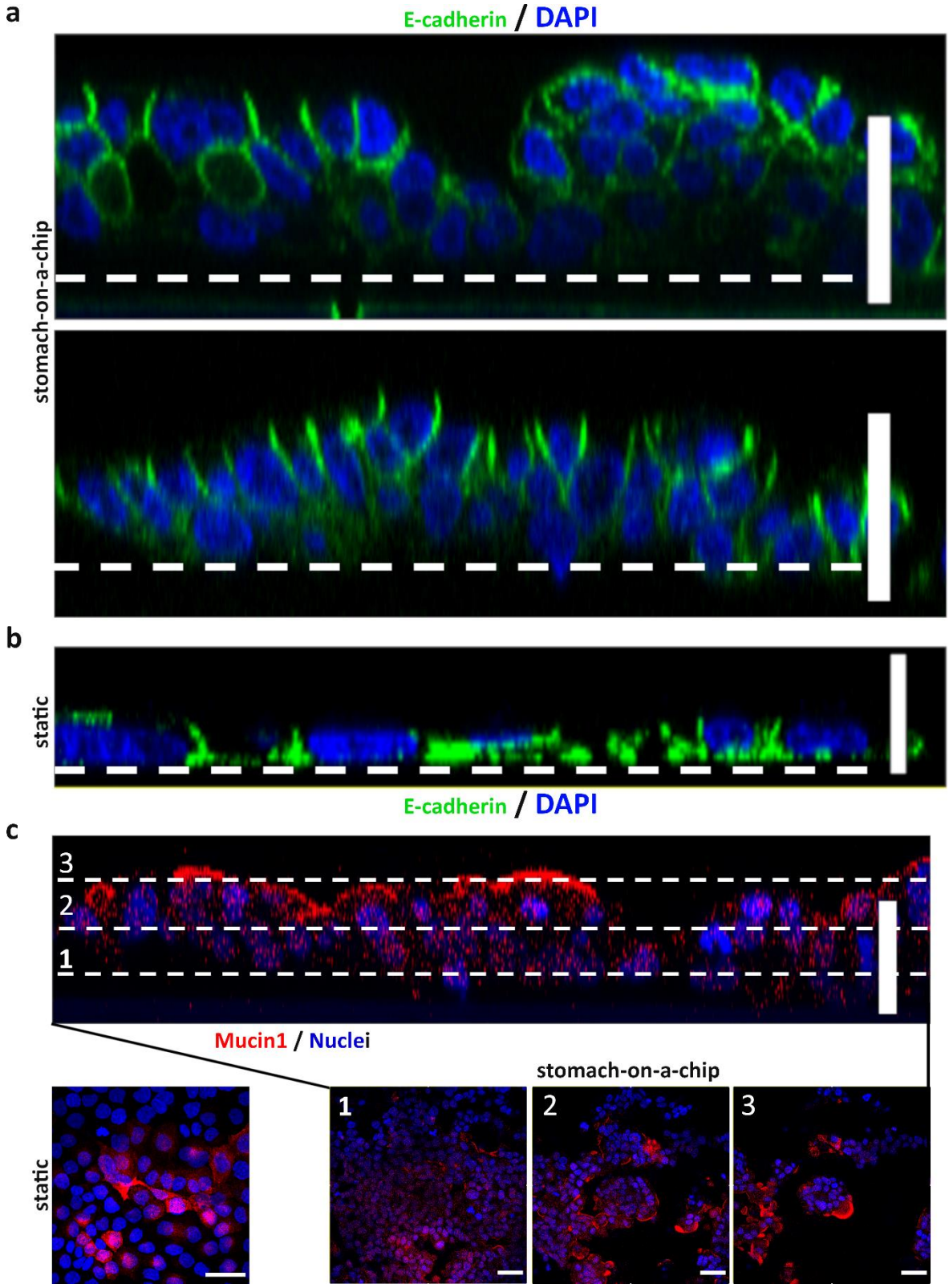

Figure 8. Comparison study of gastric epithelium under static conditions vs. SoC. Cells analyzed after 6 days, either in static or dynamic conditions. Mechanical actuation was only applied on the last 3 days of the 6-day period. (a) SoC grown epithelium developed globular-like structures over-time (upper panel) and cells acquire an elongated, polarized epithelium with e-cadherin (green) expression exclusively on the basolateral side and nuclei in the basal position, resembling a pseudostratified epithelium (lower panel) (scale bars: 50 µm). (b) MKN74 cells grown in transwell inserts under static conditions displayed a flattened, undifferentiated

appearance, similar to a squamous epithelium (top panel; scale bar: 20 µm). (c) Mucin-1 staining of SoC grown epithelium. Orthogonal projection of an on-chip epithelium grown under dynamic conditions (scale bar: 50 µm). Lower panels represent the same microscopic section captured at 3 different z-heights (scale bars: 100 µm), displaying predominant apical expression of mucin-1. Lower left panel shows a MKN74 population grown under static conditions and stained for mucin-1 (scale bar: 50 µm) displaying random cytoplasmatic expression. Nuclei stained with DAPI (blue).

3. Concluding remarks

Organ-on-a-chip devices enable a faithful replication of the tissue microenvironment, reproducing both architecture and *in vivo* dynamic conditions in one single device, to potentiate the development of organotypic function. In this work, we designed and fabricated a SoC replicating both architectural and functional traits of the native organ. Our model could sustain a long-term 3D co-culture of epithelial and mesenchymal cells, without deleterious effects on cell homeostasis and viability. Importantly, we have demonstrated its capability for eliciting organ-level response, where cells developed phenotypic molecular and functional traits characteristic of the normal gastric mucosa, that are usually not observable in 2D cultures. These observations outline the relevance of faithfully replicating *in vitro* the microenvironment of the gastric mucosa and, in particular, the importance of mimicking the dynamic nature of the native organ in order to engineer a biomimetic analogue. Unlike the organoid-on-a-chip gastric system, previously reported by Lee and colleagues, our stratified design allows easy access to both the apical and the basal side of the gastric epithelium, presenting a versatile model that can be used to study/simulate both luminal and systemic infection of the gastric mucosa. A further advantage of the currently proposed system is the use of a biomimetic supporting ECM as a lamina propria analogue.

The presently reported SoC constitutes a valuable tool to study gastric absorption dynamics, as well as host-pathogen interplay and directed-targeting therapies. Another interesting prospect, given the epithelial nature of gastric cancer, is the use of this device to elucidate several aspects of gastric cancer initiation and progression. In the past, our group identified the presence in early-stage gastric cancer of a particular subset of CD44 isoforms containing variable exon v6 (CD44v6). *De novo* expression of CD44v6 isoforms seemed to be associated with disease progression through ECM remodeling and increased resistance to cisplatin-based chemotherapy.[43-46] The currently developed SoC could be a

suitable model to study the role of CD44v6 expression in gastric cancer. Furthermore, our previous observations suggest that CD44v6 could be an early onset marker for disease progression.[43] We are currently undergoing preliminary experimentation regarding the use of the SoC as a platform to study site-directed targeting of CD44v6 expressing cells using nanoparticle-based homing systems.[47, 48]

In summary, the low cost of the fabrication method, coupled with the robust physiological response that the system elicits, makes the present SoC device a functional microfluidic platform to model the dynamic gastric microenvironment.

4. Experimental section

Design: The conceived SoC consisted of 9 intercalated parts (**Figure 1a**). From top to bottom, the top 6 layers formed the fluidic portion of the biochip. Layer 7 and 8 composed the microactuator and the bottom layer was a microscope slide. The PDMS microchannels were designed with a 10 mm (length) x 2 mm (width) main rectangular chamber and access holes measuring 2 mm in diameter (**Figure 1b**). Each fluidic layer was separated by a 16 µm thick perforated PET membrane (pore size 8 µm, pore density $6x10^4$ cm^2; it4ip). The microactuator was a two-part assembly, composed of a 250 µm flexible PDMS membrane on top of a vacuum chamber. The vacuum chamber was 250 µm-thick and 11 mm (length) x 3.5 mm (width). The vacuum chamber is larger than the fluidic channels, thus ensuring proper actuation of the entire cell culture surface (**Figure 1c**). The whole structure was assembled on top of a microscope glass slide and, for that reason, each structure was centered on a 26 mm square PDMS laminate, to fit flush with the width of the microscope slide.

Fabrication: The SoC microdevice was fabricated from pre-cured PDMS laminated sheets and PET porous membranes using a method previously developed by our group.[25] Briefly, the device was designed using computer aided design (CAD) software, exported to a cutting plotter (model CAMM-1 GS-24; Roland DG) and machined onto pre-cured PDMS sheets (915 mm wide; MVQ silicones). The top layer was fabricated by gravity casting. Prior to assembly, every material was thoroughly cleaned. Machined PDMS plates were washed with isopropanol (IPA) and air dried with compressed air. PET membranes were immersed

in IPA, incubated in an ultra-sound bath for 15 min, and dried with pressurized air. Microscope slides were incubated sequentially (5 min by ultrasound) in 2% (v/v) helmanex III (Helma Analytics) solution in double distilled water, followed by acetone and a final rinse in double distilled water. Clean slides were dried with compressed air and clean materials were either used immediately or stored in a dust-free environment.

Assembly of the chip was performed sequentially, from top to bottom (**Figure 1a**). PDMS plates and glass slides were bonded by exposure to O_2 plasma for 1 min (Zepto Plasma Laboratory Unit, Diener). Structures were then brought into conformal contact, placed between two glass slides and pressure was applied overnight. The outline of the microchannels in each layer was used as a guide to puncture access inlet and outlet holes through the top layer, with a 20 ga luer stub (Instech). To integrate the PET membranes, silanization of the PET surface was required. Following the cleaning procedure, both sides of the membrane were exposed to O_2 plasma and immersed in 2% (v/v) bis-amino silane, 1% (v/v) double distilled water in IPA solution (20 min at 80 °C), followed by thorough cleaning with IPA and cured for 30 min at 70 °C. Membranes were then immersed for 30 min in 70% ethanol (v/v). Prior to bonding, both sides of the PDMS structures were exposed to O_2 plasma and the wetted membrane was immediately sandwiched between them. This sub-assembly was further cured for 1 h at 70 °C.

Calculation of transient shear stress: Transient shear stress imparted by the perfusion regimen, was determined by the following equation:

$$T = 6.\mu.Q/h^2.w$$ [49]

where μ is the dynamic viscosity of the culture medium (mPa.s), Q is the volumetric flow rate ($cm^3.s^{-1}$) and *h* and *w* are the height and width, respectively, of the microchannel (cm). The average dynamic viscosity of the CO_2 independent cell culture medium was determined by rheometry and averaged at 0.77±0.07 mPa.s (**Figure S1**).

Cell culture: The human-derived gastric cancer cell lines AGS and MKN74 were available at i3S/Ipatimup's cell line repository. For the SoC, the human-derived adenocarcinoma epithelial cell line, MKN74 was used. The human stomach normal fibroblast cell line NST20 was a kind gift of Dr. Luis Filipe Santos Silva (I3S/Ipatimup, Portugal).

Cell lines were routinely maintained at 37 °C and 5% CO_2, under a humidified atmosphere and fed with Roswell park memorial institute (RPMI) 1640 (Gibco), supplemented with 10%

(v/v) fetal bovine serum (FBS; Biowest) and 1% (v/v) penicillin/streptomycin (pen/strep; Biowest). Cells were reseeded when confluency reached about 80% and tested for the presence of mycoplasma when thawed and every month when in culture.

Before on-chip seeding, MKN74 and NST20 cells were conditioned for at least 48 h in CO_2 independent cell culture medium (Gibco), supplemented with 4 mM of L-glutamine (Gibco), 10% (v/v) FBS (Biowest) and 1% (v/v) pen/strep (Biowest) in a humidified normal atmosphere (i.e., without CO_2 buffering) at 37 °C.

Chip priming was started by sterilization with UV radiation (20 min), followed by flushing with 70% ethanol (20 min). Finally, the devices were rinsed with phosphate buffered saline (PBS; 3x 15 min, Fisher BioReagents). Following sterilization, the fluidic portion was incubated with a 50 $\mu g.mL^{-1}$ fibronectin solution (Sigma) for 2 h at room temperature.

NST20 fibroblasts were embedded in a collagen type I matrix. Cells were harvested by trypsinization and suspended in an ECM solution of 3 $mg.mL^{-1}$ collagen type I to a final density of 200,000 $cells.mL^{-1}$. The resulting suspension was carefully injected into the middle-tier microchannel and incubated for 30 min at 37 °C to allow gelification. The device was then coupled to a piezoelectric controller via poly(ether-ether-ketone) (PEEK) tubing (Idex), and CO_2 independent culture medium was perfused at a flow rate of 2 $\mu L.min^{-1}$. The system was allowed to equilibrate overnight, with the microactuator set to -50 mbar constant vacuum pressure to allow degassing of potential microbubbles present in the culture.[25]

To replicate the epithelial barrier, MKN74 cells were collected by trypsinization and resuspended to a density of $3.0x10^5$ cells/mL. This suspension was then injected via a 4-way PEEK valve (Idex) onto the upper fluidic channel. Cell seeding density was controlled under a phase contrast microscope and culture media flow was reinstated in both top and bottom fluidic channels at a flow rate of 2 $\mu L.min^{-1}$, 1 h after cell seeding. Cells were allowed a 72 h growth and stabilization period after which mechanical stretching was effected by application of cyclic vacuum. To emulate peristalsis motion experienced by gut cells *in vivo*, the stretching pattern was modelled as a sinusoidal wave of 0.15 Hz frequency and maximum vacuum pressure at -100 mbar.

Cell tracker staining: To monitor cell loading and compartmentalization on the SoC, MKN74 epithelial cells and NST20 fibroblasts were stained with CellTracker™ Green CMFDA and CellTracker™ Red CMPTX dyes, respectively. Staining was performed according to the manufacturer's instructions. Briefly, cells were harvested and suspended in CellTracker staining solution (1:1000 dilution) for 30 min at 37 ºC. Staining solution was then removed

and cell seeding and/or embedding was performed as described above. Epithelial layer was grown to confluency after which the chip was imaged under a confocal microscope (model SP5; Leica Microsystems).

Morphological characterization: For immunofluorescence imaging, cells were washed in PBS with 0.05 mg/mL of $CaCl_2$ (3x5 min), fixed with 4% (v/v) paraformaldehyde suspended in PBS (20 min at room temperature) and thoroughly washed with PBS (3x 5 min). Cells were further incubated in 50 mM NH_4Cl (10 min), followed by permeabilization of cellular membranes with 0,2% (v/v) Triton X-100 in PBS (5 min). Blocking was achieved with 5% (v/v) bovine serum albumin (BSA; Sigma) solution in PBS. Primary antibodies used were rabbit anti-E-cadherin (24E10, dilution 1:100; Cell Signaling), rabbit anti-ZO1 (dilution 1:200; ThermoFisher Scientific), rabbit anti-ocludin (dilution 1:50; Santa Cruz), rabbit anti-collagen I (dilution 1:100; Rockland), mouse anti-collagen IV (dilution 1:100; Dako), and rabbit anti-fibronectin (dilution 1:150; Sigma). Primary antibodies were diluted in 5% (v/v) BSA diluted in PBS and incubated at 4 ºC overnight. Secondary antibodies were diluted in 5% (v/v) BSA diluted in PBS and incubation was performed in the dark for 2 h at room temperature. Antibodies used were anti-rabbit alexa fluor 488 antibody and/or anti-mouse alexa fluor 594 antibody (dilution 1:500; Thermo Scientific). Cellular preparations were mounted in vectashield containing 2-(4-amidinophenyl)-1H-indole-6-carboxamidine (DAPI) for nuclei counter staining. Image acquisition was performed with a confocal microscope as before.

Characterization of a lamina propria analogue and analysis of ECM deposition: To emulate the lamina propria, a collagen type I (5 $mg.mL^{-1}$; Ibidi) hydrogel embedded with normal stomach fibroblasts (NST20 cell line) was used. A range of collagen type I densities was tested, namely, 0.5, 1.0, 1.5, 2.0 and 3.0 $mg.mL^{-1}$. Cell embedding and gelification of hydrogels was performed according to the manufacturer's recommendations. Briefly, NST20 cells were trypsinized and resuspended to a final cellular density of $2x10^5$ $cells.mL^{-1}$ per hydrogel. After combining the fibroblasts with the collagen type I, 30 µL per gel of the resulting suspension were plated on the bottom of a flat-faced well of a 24-well plate well (Corning). To trigger gelification and ensure cell viability, fibroblast embedded hydrogels were incubated for 30 min at 37 ºC under a humidified, normal (without CO_2 control) atmosphere. After gelification, 1 mL of CO_2 independent medium (supplemented as described above), was added to each well and gel contraction was monitored for 15 days. Discs were photographed every other day under a stereomicroscope (Olympus SZX10) coupled with a camera (Olympus EP50) and disc perimeter was measured using image

analysis software (Fiji). The results were plotted as average % size difference over time, normalized to day 0 disc size.

ECM remodeling was studied by immunofluorescence. Fibroblast-embedded discs were collected at day 11 post-seeding and stained with primary antibodies against collagen type I, collagen type IV or fibronectin. Image acquisition was done in a confocal microscope as before.

Metabolic activity of collagen-embedded fibroblasts: Metabolic activity was assessed by the resazurin assay. NST-20 cells were embedded in collagen type I discs as described above. Metabolic activity was assessed after the first 24 h in culture and every 48h for 15 days, for which a stock solution of 0.1 mg/mL resazurin (Sigma) was diluted to 20% (v/v; resazurin/cell culture media). Culture media was replaced with 500 µL of this solution and incubated at 37 °C for 2 h. 200 µL of the resulting supernatant were transferred to an opaque 96-well plate with clear bottom (Greiner) and the fluorescence signal was measured (excitation 530 nm/emission 590 nm) in a multiwell plate reader (model Sinergy MX HM550; Biotek Instruments). Metabolic activity was expressed as average relative fluorescence units (RFUs) ± standard deviation (SD).

Cell viability assay: To assess viability of the NST20 fibroblasts embedded on a collagen type I mesh, a live dead assay was performed. Briefly, a staining solution containing 2 µg/mL of calcein and 2.5 µg/mL of propidium iodide was prepared. Cells were washed thrice with unsupplemented culture medium, followed by a 20 min incubation at 37 ºC with staining solution. Finally, cells were washed twice with unsupplemented culture medium and immediately imaged under a confocal microscope as before. Z-stacks were acquired with a 2 µm z-step and post-processed using image analysis software (Fiji).[50]

Epithelium characterization: The on-chip formed epithelium was fixed and stained with an antibody against E-cadherin as described above. Z-stacked fluorescence images were acquired with a 2 µm z-step value, using a confocal microscope as before. Z-stacks were post-processed and epithelium height measured using image analysis software (Fiji). For 3D rendering of the stomach epithelium, z-stacks were processed using Fiji's 3D viewer plugin.

Paracellular permeability: To measure the paracellular permeability, the transport of fluorescein isothiocyanate (FITC)-labelled dextran (40 kDa; Sigma) across the epithelium was assessed over time. For on-chip measurements, cells were grown to confluency and cultured under cell culture media flow (2 $\mu L.min^{-1}$) with or without exposure to cyclic mechanical actuation for 3 days at a 0.15 Hz frequency. FITC-dextran solution (1 $mg.mL^{-1}$) was perfused through the top channel and 30 µL samples were collected at the lower channel outlet every 30 min, for a period of 3 h. Samples were analyzed in a multiwell plate reader (model Sinergy MX HM550; Biotek Instruments) at 488 nm excitation and 520 nm emission. Static conditions were studied using transwell inserts (Corning), coated with fibronectin (50 $\mu g.mL^{-1}$). Cells were allowed to reach confluency and grown for 3 additional days. Permeability was assessed by adding 200 µL of 1 $mg.mL^{-1}$ FITC-dextran solution to the apical side of the transwell and collecting 50 µL samples from the basal side, while replenishing the same volume with fresh medium. Samples were collected up to 3 h and analyzed in a multiwell plate reader as before at 488nm excitation and 520 nm emission.

In both dynamic and static conditions, permeability was assessed as the relative transport of small molecules across the epithelial barrier and expressed as the fluorescence value collected at the basal channel, normalized to the fluorescence signal of the solution added to the apical side. Results were plotted as average percentage of FITC-dextran release, against elapsed time (n=3).

Pepsin/pepsinogen activity: Gastric epithelial function was measured by quantifying the specific activity of pepsin/pepsinogen. A pepsin/pepsinogen activity assay kit (Biovision) was used. The procedure was performed according to the manufacturer's instructions. Briefly, cells were grown for 3 days post-confluency, either in transwell inserts (static conditions) or on-chip, with culture media flow and in the presence or absence of cyclic mechanical stretching (0.15 Hz frequency and -100 mbar vacuum pressure). Samples (100 µL) were collected from the basal side and 20 µL were added to 80 µL of pepsin assay buffer. A pepsin substrate working solution (pepsin substrate stock solution and pepsin assay buffer at a ratio of 1:10 (v/v)), was then added to the previous mix to start the reaction. Fluorescence was measured in a multiwell plate reader as before at 328 nm excitation and 418 nm emission in kinetic mode for 1 h at 37 ºC. Sample pepsin activity was calculated according to the following equation:

$$\text{Sample pepsin activity} = B/(\Delta T \times P)$$

where B is the amount of peptide substrate cleaved, calculated from the standard curve, ΔT, is the linear phase reaction time t_2-t_1 (min) and P is the amount of sample (mL). Results are expressed as $pmol.min^{-1}.mL^{-1}$.

Statistical analysis: Data was compiled and analyzed using the software Graphpad Prism (Graphpad Software). Data was plotted in graphical format presented as mean value ± SD. Cell culture doubling time and metabolic rates (n=6) were compared using a two-way ANOVA statistical test. The latter were analyzed in conjunction with a Sidak's post hoc multiple comparison test. Relative transport across the paracellular route, was analyzed using a two way ANOVA, in conjunction with Tukey's multiple comparison test. Pepsin activity mean values were compared using a non-parametric Mann-Whitney U test (n=3). Statistical significance was defined as $p<0.05$ (*), $p<0.01$ (**), $p< 0.0001$ (****).

Acknowledgements

This work was supported by Fundação para a Ciência e Tecnologia (FCT) and BiotechHealth Programme (Doctoral Programme on Cellular and Molecular Biotechnology Applied to Health Sciences; ref. PD/00016/2012), by Programa Operacional Potencial Humano (POPH), and SkinChip project (PTDC/BBB-BIO/1889/2014). The work has been also financed by: (1) Fundo Europeu de Desenvolvimento (FEDER) Regional funds through the COMPETE 2020 - Operacional Programme for Competitiveness and Internationalization (POCI), Portugal 2020, and by Portuguese funds through FCT/*Ministério da Ciência, Tecnologia e Inovação* in the framework of the projects (1.1) "Institute for Research and Innovation in Health Sciences" (POCI-01-0145-FEDER-007274), (1.2) 3DChroMe (POCI-01-0145-FEDER-30164); (2) Norte Portugal Regional Programme (NORTE 2020), under the PORTUGAL 2020 Partnership Agreement, through the European Regional Development Fund (ERDF) for projects (2.1) NORTE-01-0145-FEDER-000029 and (2.2) DOCnet (NORTE-01-0145-FEDER-000003). DF acknowledges FCT for his support through a FCT/BiotechHealth PhD programme grant, ref. PD/BD/105976/2014. JPC acknowledges funding from the European Structural and Investment funds through the Compete programme (Grant #: LISBOA-01-0145-FEDER-

016405) and from National funds through FCT (SAICTPAC/0019/2015) via the research project POINT4PAC, and FCT funding through INESC MN (Unidade ID 5367).

The authors would also like to thank: Jorge Ferreira (Chromosome Instability Group, i3S/IBMC) for granting access to the plasma cleaner equipment and for the insightful scientific support; Maria Lázaro (Biointerfaces and Nanotechnology core facility, i3S/INEB) for support and access to the XP5 confocal microscope; Filipa Sousa (Biofabrication Group at i3S/INEB) for scientific support and discussion.

Disclosures

Authors declare no conflict of interest.

References

[1] R. H. Hunt, M. Camilleri, S. E. Crowe, E. M. El-Omar, J. G. Fox, E. J. Kuipers, P. Malfertheiner, K. E. McColl, D. M. Pritchard, M. Rugge, A. Sonnenberg, K. Sugano,J. Tack, Gut **2015**, 64, 1650.

[2] M. H. Ross,W. Pawlina, Histology : a text and atlas, Lippincott Williams & Wilkins, Philadelphia, Pa. ; London, **2011.**

[3] P. J. Kumar,M. L. Clark, Kumar & Clark's clinical medicine, Saunders Elsevier, Edinburgh, **2009.**

[4] H. Sung, J. Ferlay, R. L. Siegel, M. Laversanne, I. Soerjomataram, A. Jemal,F. Bray, CA Cancer J. Clin. **2021**, 71, 209.

[5] S. A. Langhans, Front. Pharmacol. **2018**, 9, 6.

[6] J. Arrowsmith,P. Miller, Nat. Rev. Drug Discov. **2013**, 12, 569.

[7] F. Pampaloni, E. G. Reynaud,E. H. Stelzer, Nat. Rev. Mol. Cell Biol. **2007**, 8, 839.

[8] R. Edmondson, J. J. Broglie, A. F. Adcock,L. J. Yang, Assay Drug Dev. Technol. **2014**, 12, 207.

[9] N. Barker, M. Huch, P. Kujala, M. van de Wetering, H. J. Snippert, J. H. van Es, T. Sato, D. E. Stange, H. Begthel, M. van den Born, E. Danenberg, S. van den Brink, J. Korving, A. Abo, P. J. Peters, N. Wright, R. Poulsom,H. Clevers, Cell Stem Cell **2010**, 6, 25.

[10] T. Grikscheit, A. Srinivasan,J. P. Vacanti, J. Pediatr. Surg. **2003**, 38, 1305.

[11] T. Sato, R. G. Vries, H. J. Snippert, M. van de Wetering, N. Barker, D. E. Stange, J. H. van Es, A. Abo, P. Kujala, P. J. Peters,H. Clevers, Nature **2009**, 459, 262.

[12] A. L. Speer, F. G. Sala, J. A. Matthews,T. C. Grikscheit, J. Surg. Res. **2011**, 171, 6.

[13] F. Boccellato, S. Woelffling, A. Imai-Matsushima, G. Sanchez, C. Goosmann, M. Schmid, H. Berger, P. Morey, C. Denecke, J. Ordemann,T. F. Meyer, Gut **2019**, 68, 400.

[14] B. N. Lourenco, T. Dos Santos, C. Oliveira, C. C. Barrias,P. L. Granja, Acta Biomater. **2018**, 82, 68.

[15] M. Bashashati,R. A. Hejazi, Dig. Dis. Sci. **2018**, 63, 3164.

[16] I. R. Sanderson, Am. J. Clin. Nutr. **1999**, 69, 1028S.

[17] T. Mammoto, A. Mammoto,D. E. Ingber, Annu. Rev. Cell Dev. Biol. **2013**, 29, 27.

[18] C. T. Lim, A. Bershadsky,M. P. Sheetz, Journal of the Royal Society Interface **2010**, 7, S291.

[19] O. T. Guenat,F. Berthiaume, Biomicrofluidics **2018**, 12,

[20] C. Moraes, M. Likhitpanichkul, C. J. Lam, B. M. Beca, Y. Sun,C. A. Simmons, Integrative Biology **2013**, 5, 673.

[21] D. Huh, B. D. Matthews, A. Mammoto, M. Montoya-Zavala, H. Y. Hsin,D. E. Ingber, Science **2010**, 328, 1662.

[22] H. J. Kim, D. Huh, G. Hamilton,D. E. Ingber, Lab on a Chip **2012**, 12, 2165.

[23] A. O. Stucki, J. D. Stucki, S. R. Hall, M. Felder, Y. Mermoud, R. A. Schmid, T. Geiser,O. T. Guenat, Lab Chip **2015**, 15, 1302.

[24] M. Wufuer, G. Lee, W. Hur, B. Jeon, B. J. Kim, T. H. Choi,S. Lee, Sci. Rep. **2016**, 6,

[25] D. A. Ferreira, M. Rothbauer, J. P. Conde, P. Ertl, C. Oliveira,P. L. Granja, Adv Sci (Weinh) **2021**, 8, 2003273.

[26] E. Ergir, B. Bachmann, H. Redl, G. Forte,P. Ertl, Front. Physiol. **2018**, 9, 1417.

[27] K. K. Lee, H. A. McCauley, T. R. Broda, M. J. Kofron, J. M. Wells,C. I. Hong, Lab Chip **2018**, 18, 3079.

[28] X. He, B. Lee,Y. Jiang, Adv. Exp. Med. Biol. **2016**, 936, 73.

[29] W. P. Daley, S. B. Peters,M. Larsen, J. Cell Sci. **2008**, 121, 255.

[30] C. P. Gayer,M. D. Basson, Cell. Signal. **2009**, 21, 1237.

[31] M. D. Basson, Digestion **2003**, 68, 217.

[32] T. Ishikawa, T. Sato, G. Mohit, Y. Imai,T. Yamaguchi, J. Theor. Biol. **2011**, 279, 63.

[33] S. Rocha, J. Carvalho, P. Oliveira, M. Voglstaetter, D. Schvartz, A. R. Thomsen, N. Walter, R. Khanduri, J. C. Sanchez, A. Keller, C. Oliveira,I. Nazarenko, Adv Sci (Weinh) **2019**, 6, 1800948.

[34] A. Gillessen, B. Voss, J. Rauterberg,W. Domschke, Scand. J. Gastroenterol. **1993**, 28, 688.

[35] E. Bell, B. Ivarsson,C. Merrill, Proc. Natl. Acad. Sci. U. S. A. **1979**, 76, 1274.

[36] T. Zhang, J. H. Day, X. Su, A. G. Guadarrama, N. K. Sandbo, S. Esnault, L. C. Denlinger, E. Berthier,A. B. Theberge, Front Bioeng Biotechnol **2019**, 7, 196.

[37] A. Pozzi, P. D. Yurchenco,R. V. Iozzo, Matrix Biol. **2017**, 57-58, 1.

[38] T. Rozario,D. W. DeSimone, Dev. Biol. **2010**, 341, 126.

[39] R. Sekiguchi,K. M. Yamada, Curr. Top. Dev. Biol. **2018**, 130, 143.

[40] A. M. Moreira, J. Pereira, S. Melo, M. S. Fernandes, P. Carneiro, R. Seruca,J. Figueiredo, Cells **2020**, 9,

[41] D. Boltin,Y. Niv, J Gastrointest Dig Syst **2013**, 3, 15519.

[42] M. Balmana, S. Mereiter, F. Diniz, T. Feijao, C. C. Barrias,C. A. Reis, Molecules **2018**, 23,

[43] C. B. da Cunha, C. Oliveira, X. Wen, B. Gomes, S. Sousa, G. Suriano, M. Grellier, D. G. Huntsman, F. Carneiro, P. L. Granja,R. Seruca, Lab. Invest. **2010**, 90, 1604.

[44] C. Pereira, D. Ferreira, N. Mendes, P. L. Granja, G. M. Almeida,C. Oliveira, Cancers (Basel) **2020**, 12, 858.

[45] B. N. Lourenco, N. L. Springer, D. Ferreira, C. Oliveira, P. L. Granja,C. Fischbach, Integr. Biol. (Camb.) **2018**, 10, 145.

[46] C. Branco da Cunha, D. D. Klumpers, S. T. Koshy, J. C. Weaver, O. Chaudhuri, R. Seruca, F. Carneiro, P. L. Granja,D. J. Mooney, Biomaterials **2016**, 98, 152.

[47] P. J. Kennedy, F. Sousa, D. Ferreira, C. Pereira, M. Nestor, C. Oliveira, P. L. Granja,B. Sarmento, Acta Biomater. **2018**,

[48] P. J. Kennedy, I. Perreira, D. Ferreira, M. Nestor, C. Oliveira, P. L. Granja,B. Sarmento, Eur. J. Pharm. Biopharm. **2018**, 127, 366.

[49] Y. Wan, J. Yang, J. Yang, J. Bei,S. Wang, Biomaterials **2003**, 24, 3757.

[50] J. Schindelin, I. Arganda-Carreras, E. Frise, V. Kaynig, M. Longair, T. Pietzsch, S. Preibisch, C. Rueden, S. Saalfeld, B. Schmid, J. Y. Tinevez, D. J. White, V. Hartenstein, K. Eliceiri, P. Tomancak,A. Cardona, Nat. Methods **2012**, 9, 676.

Supporting Information

(This section includes supporting materials for the original paper 3 - Bioinspired human stomach-on-a-chip with in-vivo like function and architecture)

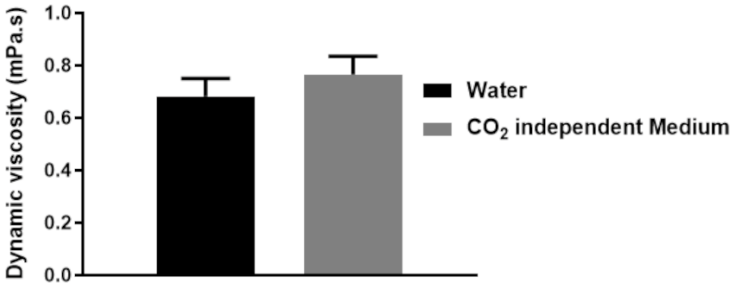

Figure S1. Average dynamic viscosity of CO_2 independent medium used as a buffering system for the stomach-on-a-chip operation. The average dynamic viscosity of the culture medium was determined to calculate the transient shear stress over the cell culture substrate. Graph represents average measurements ± SD (n=4).

	STRs															
Cell Lines	D3S1358	TH01	D21S11	D18S51	Penta E	D5S818	D13S137	D7S820	D16S539	CSF1PO	Penta D	Amel	VWA	D8S1179	TPO	FGA
MKN74	16	6	33.2	12	11-14	11	11	9	9-11	12	9	X	16-20	11-16	8-11	23
AGS	16	6-7	29	13	13-16	9-12	12	10-11	11-13	11-12	9-10	X	16-17	13	11-12	23-24
NST-20	14-15	6	27-31.2	13-16	12-18	10-12	11	8-10	11-12	10-12 (+11)	9-11	XY	16-17	11-13	9	19-20

Table S1. Genetic profiling of gastric cell lines, MKN74, AGS and NST-20. Autosomal STR profile for all the cell lines used was obtained by co-amplification of 15 STRs and amelogenin. In some cases, allelic imbalance was identified. The allele exhibiting lower intensity (less than 50% of the major allele) is identified with (-). Low intensity signal, below 20% of the major allele (but above 10%), are marked with (+). A signal below 10% was not called.

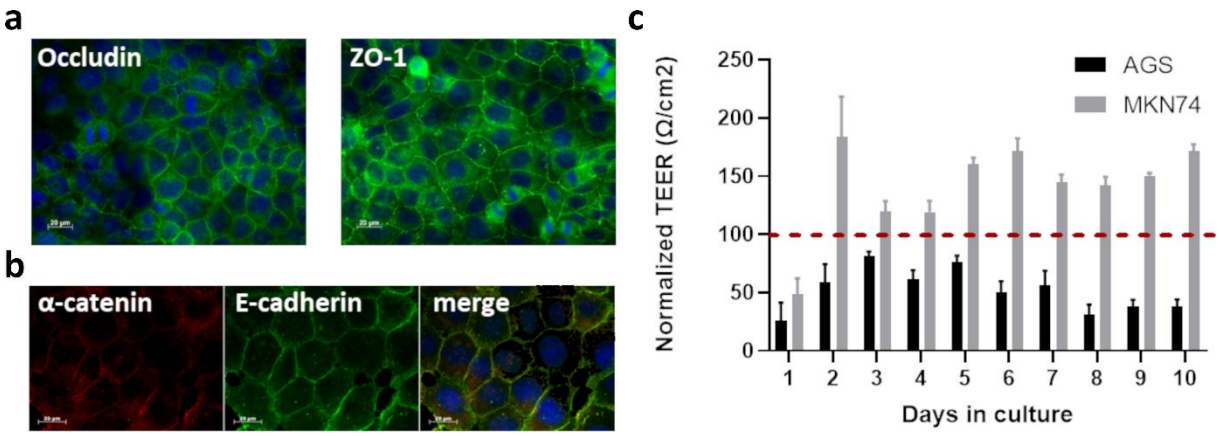

Figure S2. (a) Immunocytochemistry of tight-junction partners, occludin and ZO-1 on MKN74 cells. The proper expression and localization of these two molecules at the cell membrane denotes the correct assembly of the tight-junction complex. (b) MKN74 immunocytochemistry of MKN74 cells against adherens-junction partners e-cadherin and α-catenin, evidencing proper assembly of the adherens-junction complex that mediates cell-to-cell contact and adhesion. Immunocytochemistry images acquired on an inverted fluorescence microscope at 63x objective magnification (model: Zeiss axiovert). Scale bars: 20 µm. (c) Transepithelial resistance (TEER) of MKN74 cell line measured over a course of 10 days. The AGS gastric cell line was used as a negative control. The red line denotes the threshold normalized TEER value that indicates a fully formed barrier.

Experimental section (supplementary information):

Barrier integrity for gastric cell lines: Transepithelial electric resistance (TEER) was monitored to assess the ability of MKN74 cells to establish a fully functional epithelial barrier. AGS and MKN74 cells were seeded at a density of $0.5x10^5$ cells.mL^{-1} to ensure an even distribution of cells, and approximately 60% confluency, 24 h post-seeding. Cells were seeded on the apical side of a 24-well transwell insert (PET membrane, 8 µm pore size, 0.33 cm^2 surface area; Corning) and allowed to equilibrate for 24 h under normal cell culture conditions. TEER was measured using an EVOM2 voltohmeter (World Precision Instruments) every day up to 10 days and cell culture media was refreshed every other day. Results were plotted as normalized TEER (Ω.cm^{-2}). Barrier integrity was considered effective for measurements above 100 Ω.cm^{-2}.

CHAPTER IV

DISCUSSION AND CONCLUDING REMARKS

Chapters II through **IV** describe the main outputs of this thesis. Each chapter provides a detailed analysis and discussion of the results. Therefore, in this section we opted to present an overarching discussion, integrating all the concepts and results previously detailed.

GC is a complex and heterogeneous disease with a difficult diagnosis and poor prognosis. Understanding GC onset and progression, requires a deep knowledge over the cellular and molecular alterations leading to the disease. Only by understanding the core fundamental basics of the disease, can the most prominent challenges of developing new diagnostic and patient management tools be tackled. Identifying new biomarkers capable of predicting disease onset or severity, biomarkers suitable for functional stratification of patients or potential candidates for targeted therapy is of paramount importance. One such candidate is the adhesion molecule CD44v6. While the canonical form CD44 is ubiquitously expressed in the human body, the alternatively spliced CD44v6, is recurrently altered throughout all stages of gastric cancer development. The first chapter of the experimental section was dedicated to exploring the role and clinical implication, of the adhesion molecule CD44v6 in the context of GC (**Chapter II**). Expression of the CD44v6 isoform is regularly associated with GC, however, it is still unclear if this molecule plays any significant role as a driver of the transformative process, if it has a significant role in therapy response or if its expression is a simple bystander effect resulting from the malignant transformation. To study this, we generated two isogenic gastric cancer cell lines stably expressing *de novo* CD44v6 or the canonical CD44s isoforms. These cell lines were tested against several cancer cell hallmarks. Our observations did not show a differential response among CD44v6 and CD44s cells and potential for invasion, motility, cell adhesion or tumorigenic potential, suggesting that CD44v6 is not a driver of the transformative process. These observations are not unexpected as it has been shown previously that CD44v6 is already observed in premalignant gastric lesions.[1] Despite our evidence not indicating a clear association of CD44v6 expression as a driver effect in the malignant transformative process, it is also important to understand if the expression of CD44v6 modulates in any capacity the response of tumor cells to chemotherapy, potentially modulating resistance to current treatment regimens. Thus, the same cell lines were also tested against the chemotherapeutic agent cisplatin to elucidate the role played by CD44v6 in response to therapy. A correlation was established between CD44v6 expression and increased resistance to cisplatin-mediated apoptosis. Concomitantly, downregulating CD44v6 in cells endogenously expressing CD44v6 led to increased sensitivity to cisplatin. Uncovering the molecular mechanism behind this response to cisplatin, indicated STAT3 and P38 as likely candidates modulating the process. In fact both Stat3 and P38 signaling pathways have

been associated with cisplatin-mediated survival. [2, 3] Interestingly, our work pertaining co-cultures of CD44v6+ and CD44v6- cells, showed a selective advantage of CD44v6 cells in a heterogeneous tumor environment in response to cisplatin therapy. The selective resistance and overgrowth of CD44v6+ cells after therapy is suggestive of a mechanism through which relapsed tumors are enriched in CD44v6+ cells, a plausible effect, as CD44s and CD44v have been described as CSC markers in several tumors, including GC.[4, 5]

Tackling the multitude of cellular and molecular aspects of a disease, requires specialized tools that can accurately predict the *in vivo* response in an artificial environment. Traditionally, *in vitro* cellular, and acellular models have been employed to dissect some of the molecular aspects of GC. These systems are inexpensive, easy to use and in the case of cell line models, retain many of the characteristics of the tissue of origin. However, they lack any systemic type of response and thus are of limited usefulness to predict organ-level human physiology. *In vivo* models on the other hand, do offer an additional level of complexity, as they modulate much more than chemical or cellular interactions. In fact, the cornerstone for comparative medicine, is based on the broad concept that animal models share many behavioral and physiological traits with humans. Despite the undisputed relevance and contribution of animal models for basic and clinical research, their use also entails some pitfalls. Firstly, one must consider the ethical burden of using experimental animal models. Secondly, despite their higher relevance to study tissue- and systemic-level responses, animal models ultimately fail in replicating human physiology. In fact, only a small percentage of animal tested drugs approved for human experimentation, reach phase I clinical trials.[6] The latter part of this thesis, concerning **chapters III** and **IV**, was dedicated to the creation of a biomimetic and dynamic 3D model of the gastric mucosa, replicating both architecture and function of the native organ. Tissue engineering principles have helped shape the way towards the development of bioinspired and biomimetic models to study human physiology. One such model is the conceptual organ-on-a-chip, a microfluidic platform capable of sustaining *in vitro* a biomimetic, functional sub-unit analogue of a living organ. Developing a highly complex system, such as the stomach-on-a-chip, is an extremely complex endeavor that requires troubleshooting through several iterations of similar devices, to optimize efficient fluid flow, adequate cell culture maintenance and biomimetic performance of the microactuator. Although a fast and relatively simple method, conventional soft lithography takes a few days to produce a fully functional device and implies high costs, as it requires access to a clean room facility and specialized training. We soon realized that going through the testing of several stomach-on-a-chip prototypes, required a fast turn-around, that soft-lithography was not providing. We therefore set out to

develop a novel fabrication method inspired in xurography to develop complex, multilayered and mechanically actuated organ-on-a-chip prototypes. **Chapter III** outlines the principles of a new microfabrication method for elastomeric organ-on-a-chip devices and microactuators. The described methodology was based in xurography, a technique that uses a cutting plotter to rapidly generate microfluidic structures (Figure 1). Devices fabricated with this technology were shown to be amenable to the maintenance of a long-term cell culture and capable of withstanding conventional microfluidic and cell culture conditions, namely, low cytotoxicity, resistance to delamination under pressurized conditions and a humidified atmosphere. Importantly, the designed integrated microactuator was shown to perform efficiently in two crucial aspects. First, the application of a biorelevant mechanical stimulus, to the cell culture substrate, replicating a quantifiable surface stretching of the cells similar to that experienced by gut cells *in vivo*, as well as application of a biomimetic pattern of mechanical actuation emulating the gut peristalsis, effectively validating the device and fabrication method for organ-on-a-chip applications. Secondly, we tackled the potential of the microactuator to solve a perennial problem with microfluidic devices operating under standard cell culture conditions, that is the expansion of air bubbles that are trapped within the cell culture chamber or that find their way there, during perfusion. We took advantage of the fact that the microactuator was placed directly underneath the cell culture area and that the assembly was entirely fabricated in the gas permeable silicone, PDMS, to promote air bubble elimination inside the cell culture chamber. Our results demonstrated that the inclusion of a degassing step, at the beginning of each chip run, effectively eliminated air bubbles present within the fluidic routing system and was a key factor in increasing the rate of success during the experimental run.

The developed method proved to be a crucial asset during the development of the stomach-on-a-chip device. We have shown that fabrication of a complex multilayered device could be accomplished in a few hours and at low cost, using only benchtop equipment. This represents a significant reduction in fabrication cost and time and space requirement, three of the main burdens constraining a biofabrication lab.

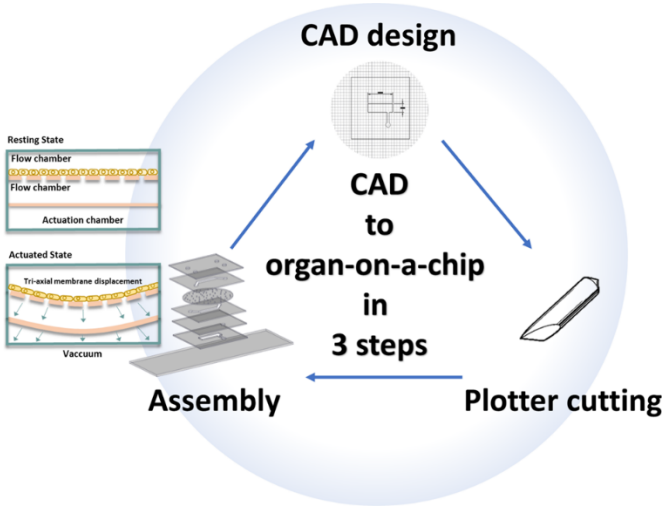

Figure 1 Graphical abstract for original paper 2, described in Chapter II. Schematic detail of the xurography-based, 3-step system developed to fabricate organ-on-a-chip devices.

In the later part of **chapter III** and in **chapter IV** the fabrication methodology was applied to engineer a proof-of-principle human derived stomach-on-a-chip device. The design incorporated several aspects of the gastric mucosa microarchitecture, namely a reproduction of the gastric columnar epithelium and the associated basement membrane, serving as an anchoring substrate, the fibroblast-rich lamina propria and also the ability to reproduce intra-luminal flow and peristaltic-like movement (Figure 2). By replicating this tightly controlled niche *in vitro*, we demonstrated that the gastric mucosa analogue within the device, was able to recapitulate key aspects of the native stomach that are normally not observed in conventional 2D cell culture. The stomach-on-a-chip recapitulated enhanced gastric function, namely by displaying increased selectivity to paracellular trafficking of small molecules and increased pepsin activity. Interestingly, application of a dynamic environment within the chip, reflected phenotypic and molecular changes characteristic of a well differentiated gastric epithelium, such as the acquisition of a polarized epithelium phenotype, exclusive expression of adhesion molecules at the basolateral side of the cell membrane and spatially restricted mucin expression. Our observations demonstrated the importance of faithfully replicating the tissue-microenvironment as well as considering the implementation of biomechanical cues when studying in an *in vitro* context, the physiology of organs that are exposed to strain.

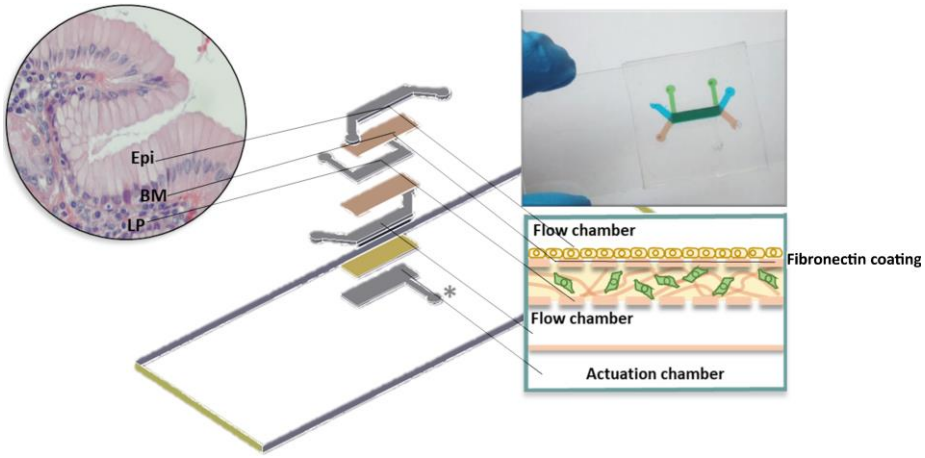

Figure 2 Graphical abstract for original paper 3. Schematic exploded view of the engineered stomach-on-a-chip platform. The device reproduces the 3 inner layers of the gastric mucosa, the epithelial layer, the basement membrane and the lamina propria. Flow chambers above and below the biological model ensure cell feeding and replicate intraluminal flow. The actuation chamber below the assembly effects peristaltic-like mechanical stretching of the cell culture substrate at physiological levels.

Composite biological systems such as the stomach-on-a-chip developed, could be the much-needed middle-ground between conventional 2D cell culture models and *in vivo* animal models. They represent a human derived biological platform that is capable of mimicking both the native organ architecture as well as replicate key functional traits of the organ or functional sub-unit represented. Fabrication methods such as the one developed in this work, could be the stepping-stone towards a cost-effective scaling-up of the technology that could see it translated to the pharmaceutical industry as testing platforms for cytotoxicity and pharmacokinetics assay in pre-clinical trials. Furthermore, harnessing the power of patient-derived primary cells or iPSCs within these devices, could potentially pave the way for a new era of personalized therapy.

In summary, we presented a multidisciplinary approach to engineer two *in vitro* models of the gastric environment that could be a significant contribution to improve the understanding over the processes mediating the transformative process leading to GC. On a first approach we established a simpler but highly relevant cell culture model expressing *de novo* CD44v6, a putative GC biomarker. Despite its simplicity, the model proved to be a robust tool to address the role played by CD44v6 in resistance to cisplatin therapy in GC. A second approach, based on tissue-engineering and microfluidics principles, was used to develop a

fabrication method for organ-on-a-chip devices that resulted in a biomimetic stomach-on-a-chip prototype device. Complex 3D cell culture models such as these, have the potential to be powerful tools to study GC in a physiologically relevant context. The accurate depiction of 3 layers of the gastric mucosa, means that the stomach-on-a-chip is particularly suited to unraveling the mechanisms of GC initiation and progression as this disease often develops at the epithelial layer and invades the adjacent tissue towards the lamina propria and the inner strata of the gastric wall. Furthermore, by combining the two technologies developed in this work, *i.e.*, the stomach-on-a-chip platform, seeded with a co-culture of the generated CD44v6+ and CD44s isogenic cell lines, an interesting tool could be created to study site-directed targeting of CD44v6 expressing cells, using a nanoparticle based homing system previously developed by our group.[7-9]

Finally, transitioning the stomach-on-a-chip model from an immortalized cell line system to gastric primary cells or gastric iPSCs, would be a significant contribution towards using the microdevice as a personalized medicine tool and potentially reaching the market as a point-of-diagnosis or point-of-treatment device.

References

[1] D. G. Hackam,D. A. Redelmeier, JAMA **2006**, 296, 1731.

[2] C. B. da Cunha, C. Oliveira, X. Wen, B. Gomes, S. Sousa, G. Suriano, M. Grellier, D. G. Huntsman, F. Carneiro, P. L. Granja,R. Seruca, Lab. Invest. **2010**, 90, 1604.

[3] C. Y. Sun, J. Nie, J. P. Huang, G. J. Zheng,B. Feng, Biomed. Pharmacother. **2019**, 117, 109135.

[4] I. W. Achkar, N. Abdulrahman, H. Al-Sulaiti, J. M. Joseph, S. Uddin,F. Mraiche, J. Transl. Med. **2018**, 16, 96.

[5] M. Zoller, Nat. Rev. Cancer **2011**, 11, 254.

[6] H. Kodama, S. Murata, M. Ishida, H. Yamamoto, T. Yamaguchi, S. Kaida, T. Miyake, K. Takebayashi, R. Kushima,M. Tani, Br. J. Cancer **2017**, 116, 186.

[7] P. J. Kennedy, F. Sousa, D. Ferreira, C. Pereira, M. Nestor, C. Oliveira, P. L. Granja,B. Sarmento, Acta Biomater. **2018**,

[8] P. J. Kennedy, I. Perreira, D. Ferreira, M. Nestor, C. Oliveira, P. L. Granja,B. Sarmento, Eur. J. Pharm. Biopharm. **2018**, 127, 366.

[9] B. N. Lourenco, R. F. Pereira, C. C. Barrias, C. Fischbach, C. Oliveira,P. L. Granja, Nanomaterials (Basel) **2021**, 11,

APPENDIX

European Patent Application no. 20201000039961 (application submitted)

FABRICATION OF MICROACTUATOR AND IN-LINE DEGASSER IN ORGAN-ON-CHIPS, DEVICES AND METHODS THEREOF

Daniel A. Ferreira[1,2,3], Peter Ertl[4], Carla Oliveira[1,5,6], Pedro L. Granja,[1,2,3]

[1] i3S – Instituto de Investigação e Inovação em Saúde, Universidade do Porto, Rua Alfredo Allen, 208, 4200-135 Porto, Portugal

[2] INEB – Instituto de Engenharia Biomédica, Universidade do Porto, Rua Alfredo Allen, 208, 4200-135 Porto, Portugal

[3] ICBAS – Instituto de Ciências Biomédicas Abel Salazar, Universidade do Porto, Rua Jorge de Viterbo Ferreira, 228, 4050-313 Porto, Portugal

[4] Faculty of Technical Chemistry, Vienna University of Technology (TUW), Getreidemarkt 9, 1060 Vienna, Austria

[5] Ipatimup – Institute of Molecular Pathology and Immunology, Universidade do Porto, Rua Júlio Amaral de Carvalho 45, 4200-135 Porto, Portugal

[6] Department of Pathology, Faculty of Medicine, University of Porto, Alameda Prof. Hernâni Monteiro, 4200-319 Porto, Portugal

Title

FABRICATION OF MICROACTUATOR AND IN-LINE DEGASSER IN ORGAN-ON-CHIPS, DEVICES AND METHODS THEREOF

SUMMARY

The present invention refers to a method for the fabrication of complex organ-on-a-chip devices with incorporated mechanical microactuator and bubble degasser.

The method herein described is based on the micro-structuring of polydimethylsiloxane (PDMS) laminates, using a cutting plotter to generate multi-layered, membrane integrated biochips in a matter of hours, using low-cost benchtop equipment. Furthermore, a material permeable to gas exchange placed directly underneath the flow chamber and a degassing step allows to operate an integrated bubble degasser.

The present invention also describes examples of a device for cell culture of gastric fibroblasts and an epithelial gastric cell line with no cytotoxic effects or impact on cellular homeostasis, stepping towards an advanced model of the stomach mucosa.

The devices and methods herein described can be advantageously used in the early stages of organ-on-a-chip development by reducing three of the main burdens facing a microfabrication laboratory, namely production time, cost and space requirement. Fabricated devices retain several desirable qualities such as transparency, flexibility for mechanical actuation, biocompatibility and capability of gaseous exchanges with the exterior environment, allowing elimination of air bubbles formed during operation, which is one of the major challenges during biochip handling.

DESCRIPTION

FABRICATION OF MICROACTUATOR AND IN-LINE DEGASSER IN ORGAN-ON-CHIPS, DEVICES AND METHODS THEREOF

Technical field of the invention

The present invention relates to the technical field of supports for cultivation of cell lines and tissues characterized by topography and properties.

State of the art

Microfluidic devices are well established as experimental platforms in life sciences (1, 2). These systems provide the ability to control aspects of the cell microenvironment at more relevant kinetic and spatial scales (3). The design versatility and scalability of microfluidic platforms, through parallelization of devices in array-like designs (4-6), make them a powerful tool. Development of this technology was aided by the advent of soft lithography (7), a term that refers to a subset of fabrication techniques using the flexible silicon elastomer, polydimethylsiloxane (PDMS), as the primary building material. The combination of photolithography (8) with the ability of PDMS to faithfully replicate the molded structures at nano level resolution, means that high fidelity, fully customizable devices can be produced in a matter of days, at a relatively low cost (7). Despite the obvious advantages, soft lithography also has its drawbacks. It requires access to a clean room facility and casting molds produced by photolithography suffer quick wear and tear. Not surprisingly, efforts have been made towards the development of fabrication techniques relying in simpler and space-saving techniques (9). Alternative methods include milling, laser engraving and paper-based microfluidics (10-12). This is particularly important in an academic or pre-industrial context, where prototype design must go through several iterations and plastic injection molding is not a viable financial option. 3D printing of thermoplastics has also been explored as it can generate one-piece, enclosed devices, which are of particular interest for cell culture applications (13, 14). Importantly, the consequences these procedures have for biological applications, particularly at the cellular level, remain largely unknown. In fact, culturing cells within these devices requires extensive optimization, despite their many advantages over conventional cell culture (15). The substantially lower culture chamber volume, the shear stress imparted by the flow of culture media over the cell culture surface, and their relatively low permeability to atmospheric gases, require a careful optimization to ensure an efficient oxygen and nutrient supply and

a stable pH throughout the experimental run. This is particularly important when developing organ-on-chip devices. Organ-on-a-chip devices are more complex than cell-based lab-on-a-chip devices, as they aim to recreate the complex micro-physiological architecture and function of the organ they intend to emulate (16-18). Harnessing the cellular microenvironment at the tissue level also requires tackling the impact of mechanical forces at the cellular level and understanding how cells transduce these mechanical forces into biochemical signals, in a physiologically relevant context (19-24). The successful integration of microactuators within organ-on-a-chip devices allowed the application of well-defined and cyclical strain on the cell culture substrate. The ability to control the intensity, duration and pattern of the mechanical forces within the system, make organ-on-a-chip platforms a powerful tool to understand how mechanical transduction affects cellular response at the tissue level, thus modulating to a greater extent a key aspect of the in-vivo native microenvironment. Although ideally suited for the aforementioned tasks, design of organ-on-chip microdevices is a complex procedure. Their three-dimensional (3D) layout and incorporation of several tissue-like features, such as a simplified stromal component and epithelial barrier architecture, is further complicated by the incorporation of embedded mechanical microactuators (19-22). Creating complex structures that correctly emulate the biological counterparts, usually implies fabricating multi-layered devices, with two or more chambers separated by porous membranes, as well as complex flexible mechanisms that serve as mechanical actuators. Also, replicating some organ functions requires the design of intricate microchannel geometries to house, in a specific layout, the individual components of the organotypic unit being emulated (25, 26) or to manipulate diffusion distances (5, 27). While geometry design, by itself, is not constrained by fabrication limitations, it is essential that they are amenable to correct cell culture maintenance and homeostasis (28). Methods with a fast turnaround time, from design to device, are key to reduce experimental costs at the early stages of organ-on-a-chip design. Additionally, a common complication observed during microfluidic operation is the formation of air bubbles (29). Biochips that need to be operated at 37°C, are particularly susceptible to this problem as the higher temperature leads to decreased gas solubility (29). Under these circumstances, the volume of the air bubble will gradually expand over time and air bubbles can disrupt flow and the creation of an air-liquid interface may compromise cellular homeostasis and promote cellular death.

Detailed description of the Invention

The invention discloses a facile fabrication method that is time saving and permits the fabrication of the described devices at a fraction of the time and cost, when compared to current state of the art technology. Said devices allow application of differential patterns of mechanical actuation on cell culture substrates and can be irreversibly or reversibly bonded to the cell culture fluidic chamber for added versatility. The same cell culture substrate can be subjected to different strain patterns by application of distinct actuator chambers beneath it. Furthermore, a material permeable to gas exchange placed directly underneath the flow chamber and a degassing step allows to operate an integrated bubble degasser.

For microfluidic device layout, the device is designed using the CAD software, Autocad (2014 Version), and made to fit a 26x26mm plate, suitable for bonding squared to a standard microscope glass slide (Figure 1). Fluidic features are rectangular shaped, 2mm (width) x 10mm (length) channels, for a total cell culture area of 0.2cm2. Access to the cell culture area is made through a linear feature connecting to an access porthole (Figure 1a -c). The actuation and degassing chamber (Figure 1e) is 3,5mm (width) x 11mm (length), topped by a flexible Polydimethylsiloxane (PDMS) membrane (Figure 1d). In one embodiment, a full device consists of 9 superimposed layers (Figure 2). A fluidic upper portion, where liquid and cell handling is performed, contains a top layer of cast-on PDMS, (Sylgard, Dow Corning, Midland, MI; mixed on a weight ratio of 10:1 PDMS base to curing agent respectively), where access portholes are punched with a 20Ga puncher. This is followed by 5 alternating layers of 500µm PDMS laminate (Silex, Hampshire, UK) and a cell culture treated polyethylene terephtalate (PET) perforated membrane (thickness 16µm, pore size 8µm, pore density $6e^4cm^2$). The bottom part of the device contains the pneumatic actuation and/or the degassing system, consisting of 2, 250µm PDMS laminate layers (Silex, Hampshire, UK) placed on top of a glass slide.

For preparation of chip-related materials, prior to assembly, each plate design, is cut from PDMS foil (915 mm wide; Silex), using a desktop cutter (model CAMM-1 GS-24; Roland DG). The fluidic plates are cut from 500 µm high foil. The plates forming the pneumatic portion of the device are cut from 250 µm high foil. In one embodiment, a section of PDMS foil of about 3 x 20 cm, is manually cut with scissors and one side of the protective backing plastic is removed. Finally, the laminate sheet is fed to the cutting plotter and the design transferred from the computer assisted design (CAD) software to a dedicated software, Roland Cut Studio (Roland DG). After the machining process, the offcut material is removed with tweezers, to reveal the hollow fluidic and pneumatic features. In one embodiment, a

PET membrane (thickness 16 µm, pore size 8 µm, pore density 6e4 cm2; it4ip), is cut manually from Ø25 mm discs, immersed in isopropanol (IPA), cleaned by ultrasound (5 min), dried with compressed air and stored in a dust-free container. In one embodiment, the top layer of each chip is fabricated by gravity casting PDMS on a circular petri dish. The PDMS base is mixed thoroughly with curing agent on a weight ratio of PDMS base to curing agent 10:1 (Sylgard 184, Dow Corning). The heavily aerated pre-polymer mix is degassed by centrifugation (5 min at 4000 rpm), poured carefully onto 90 mm petri dish and cured at 70 °C for 1 h. The resulting PDMS plate is then cut in 26 mm square sections to match the machined PDMS layers. Glass microscope slides are thoroughly cleaned by sequential incubation (5 min by ultrasound) in 2% (v/v) Helmanex III solution in ddH2O (Helma Analytics), followed by acetone and a final rinse in double distilled H2O. Clean slides are air dried with compressed air and stored in a dust-free container.

For assembly (Figure 2), each laminate plate is cut individually, with a Desktop Cutter, CAMM-1 GS-24 (Roland DG, Japan) and thoroughly cleaned with isopropanol (IPA) followed by a drying step with compressed air at 1,5bar in a dust free environment. PET membranes are cut manually and cleaned in the same manner. PET membranes must first be silanized prior to bonding to ensure long term adhesion during incubation at 37°C. Briefly, membranes are exposed to O_2 plasma (Zepto Plasma Laboratory Unit, Diener, Ebhausen, Germany), for 1 minute. These are then heated 20 minutes in 2% Bis [3-(trimethoxysilyl)propyl]amine, 1% ddH2O in isopropanol (IPA) at 80°C, followed by a rinse with IPA and cured for 30 minutes at 70°C. Membranes are then wetted for 30 minutes in 70% ethanol and brought immediately into conformal contact with the PDMS plates previously exposed to O2 plasma. Final structure is obtained by repeating the previous steps, bringing into contact each PDMS plate and PET membrane as needed for each microdevice design (two, three, four, etc, layered devices). The bottom structure of the device is a glass slide, bonded permanently to the PDMS assembly, by exposure to O_2 plasma. The whole structure is further baked at 70°C for 1 hour.

Microdevice is then primed before cell seeding. Device is initially sterilized by exposure to UV light for 20 minutes, followed by perfusion of a 70% ethanol solution for another twenty minutes. The device is then rinsed 3 times with Phosphate Buffered Saline (PBS) and coated with a fibronectin solution (50µg/mL, Sigma) for 2 hours.

The priming step further includes an in-line air bubble degassing (Figure 3). For this purpose, the chip is filled with PBS solution and allowed to equilibrate at 37°C for at least 2h. To operate a bubble degasser, PDMS, which is permeable to gas exchange, is placed directly underneath the flow chamber, spanning its surface, and a constant vacuum pressure of -50mbar is applied over a period of 4h - 16h, with the system was pressurized and fully contained throughout operation. This is able to effectively eliminate air bubbles over-time from the main culture chamber (Figure 3A). A -50mbar constant vacuum pressure can effectively eliminate a bubble with an average area of 250.5 mm^2 over a period of 4 h (Figure 3B). and this solves a common problem with standard microfluidic systems.

For device seeding, cells maintained in CO_2 independent medium (Gibco), supplemented with 10% FBS (Lonza), 1% Penicilin/streptomycin (Gibco) and 4mM L-Glutamine (Gibco). Are employed. In one embodiment, gastric fibroblasts are seeded at a density of 200000 cells/mL, on the middle perfusion channel, embedded in a collagen type I matrix (3,0mg/mL, IBIDI, Germany). Collagen type I is allowed to gel for 30 minutes at 37°C after which the device is coupled to a piezoelectric perfusion control system, OB1 (Elveflow, France). In one embodiment, gastric cells, such as the MKN-74 cell line, are seeded on the top channel at a density of $1,0x10^5$ 258 cells/mL and allowed to adhere for 30 minutes before re-initiating perfusion of cell culture media (Figure 4).

For mechanical actuation, after confluency of the epithelial monolayer, mechanical actuation is started by application of vaccum on the actuation chamber. Vaccum controlled actuation is managed by the Elveflow system, applied at a frequency of 0,15Hz for a varying period of days, ranging from 3 days to 8 days of actuation (Figure 5a-d).

Device perfusion under operation is conducted at 37°C, under high humidity and normal atmosphere. Cell culture media perfusion is done at a rate of 2µL/min.

Thus, the present invention refers to a method for fabrication of microactuator and in-line air bubble degasser system for organ-on-a-chip devices characterized by comprising the steps of:

a) Rendering a device comprising 2 or more sheets designed to create 1 or more chambers;

b) Cutting-out the generated sheet designs of laminated Polydimethylsiloxane (PDMS) with a thickness of 500-250µm, most preferably 250µm;

c) Mounting each plotted layer on top of the preceding layer and bonding together through plasma activation of the surface;

d) Bonding the assembly to a glass slide;

e) Priming the surface, seeding cells and perfusing the fluidic portions of the sheets;

f) Degassing air bubbles in-line by applying a constant vacuum pressure to the chamber, most preferably of -50 mbar;

g) Cell stretching by vacuum-controlled actuation on the chamber.

In another embodiment, the said seeding of cells is performed by perfusing a fibroblasts embedded in collagen type I and an epithelial cell suspension, such as the human derived epithelial gastric cancer cell line MKN74, (which can be purchased from the Japanese Collection of Research Bioresources cell bank).

In another embodiment, the said seeding of cells is performed by flipping the device over and perfusing endothelial cells, creating an epithelial – endothelial barrier interface.

In one embodiment, the said seeding of cells is performed by bonding PET membranes in between the flow chambers, serving as the cell culture surface, creating cell to cell interactions.

By developing the above-mentioned method, a microactuator and in-line air bubble degasser system for organ-on-a-chip devices can be fabricated.

Thus, the present invention also refers to a microactuator and in-line air bubble degasser system for organ-on-a-chip devices characterized by comprising 2 or more sheets designed to create 1 or more chambers.

In another embodiment, the said sheets are characterized by comprising laminated Polydimethylsiloxane (PDMS) with a preferable thickness of 500-250µm.

In another embodiment, the said sheets are characterized by further comprising a glass slide.

In another embodiment, the said sheets is characterized by also comprising seeded cells.

In one embodiment, the said seeded cells are characterized by comprising fibroblasts, epithelial cells such as the human derived epithelial gastric cancer cell line MKN74, endothelial cells and combinations thereof.

In another embodiment, the said microactuator and in-line degasser chamber is characterized by comprising a coupling to vacuum to apply a constant pressure, most preferably of -50 mbar.

In another embodiment, the said microactuator and in-line degasser chamber is characterized by comprising coupling to vacuum to control mechanical stretching of cells.

In other embodiments, the said microactuator and in-line degasser chamber comprise 2 or more independent chambers.

In conclusion, the disclosed method generates a system capable of sustaining long term operation under cell culture conditions. Furthermore, it can be adapted to complex organ-on-a-chip designs, by intercalating porous membranes, mechanical actuators and in-line degassers. The present invention establishes the steps of an innovative method to fabricate

complex multi-layered polydimethylsiloxane (PDMS) fluidic devices with integrated microactuators and air bubble degasser that relies in the machining of PDMS laminates using a benchtop cutting plotter. The technique simplifies the entire fabrication procedure. The fabrication process demonstrates the ability to sustain a long-term culture of an epithelial gastric cell line (MKN74), with integration of microactuator within the chip, reproducing biomechanical cues at physiological levels, as well as ability to operate as in-line degassers to eliminate on-chip air bubbles.

Other examples

To characterize the fabrication method, 3 microdevices were designed (Figure 6). Device 1 is a 5-layered fluidic system, with two fluidic linear channels measuring 12 mm in length, arrayed in a cross format and separated by a PET perforated membrane (Figure 6A). Device 2 is built from 5 superimposed layers. It is composed by three alternating layers of 500 µm PDMS laminate foil nd a cell culture treated PET membrane (Figure 6B). Fluidic features are rectangularly shaped, 2 mm (width) x 10 mm (length) x 0.5 mm (height), for a total cell culture area of 0.2 cm2 273 and a total volume of 0.01 cm3 274 (approximately 10 µL). Access to the cell culture area is made through a linear feature connecting to an access porthole of 2 mm in diameter (FIG. 1B). Fluid flow is applied unidirectionally, serving one porthole as an inlet and the other as an outlet for liquid ejection. Device 3 was adapted from Device 2, by adding a lower portion, containing the pneumatic actuation system. The actuator is a two-piece assembly comprised of a 0.25 mm(height) flexible PDMS membrane and an actuation chamber with 35 mm (width) x 11 mm (length) (Figure 6C).

Brief Description of the Figures

Figure 1: CAD drawing of each PDMS laminate layer composing the biochip. Parts a), b) and c) represent the top, middle and bottom portion of the fluidic assembly respectively, cut from 500µm PDMS laminate. Parts d) and e) constitute the pneumatic actuator, cut from 250µm PDMS laminate. All measurements are plotted in mm.

Figure 2: Exploded view of the biochip assembly. From top to bottom, each PDMS layer (grey) constituting the fluidic portion of the chip is separated by a perforated PET membrane (pink). The actuation chamber (*), is topped by a 250µm PDMS membrane (yellow). The

entire assembly is mounted on a microscope glass slide (transparent layer). (Note: The cast-on PDMS layer on top.

Figure 3: In-line air bubble degassing. After priming, the chip was filled with PBS solution and allowed to equilibrate at 37°C for at least 2h. Air bubbles were injected through the system and pushed until they were inside the cell culture chamber. A constant vacuum pressure of -50mbar was applied on the microactuator and the air bubbles were photographed every hour under a stereomicroscope (Olympus SZX10) coupled with a camera (Olympus EP50), in order to monitor air bubble area variation. A) In-line air bubble degassing by application of a constant -50mbar vacuum pressure at the microactuator over a period of time. (B) Area of each bubble was measured using Fiji software and plotted as % of area decrease over-time. Results presented as average measurements ± SD.

Figure 4: Phenotype of MKN74 cells. Metabolic activity was assessed by the resazurin assay. Approximately 1000 cells/well were seeded in a 24-well plate and allowed to adhere for 24 h. Metabolic activity was assessed every 48h for 15 days. For the measurement of metabolic activity, a stock solution of 0.1 mg/ml resazurin (Sigma) was diluted to 20% (v/v, resazurin/cell culture media). Culture media was replaced with 500 µL of this solution and incubated at 37 °C for 2 h. 200 µL of the resulting supernatant were transferred to an opaque 96-well plate with clear bottom (Greiner) and the fluorescence signal was measured (Ex 530 nm/Em 590 nm) in a fluorimeter (model Sinergy MX HM550; Biotek Instruments). Metabolic activity was expressed as average relative fluorescence units (RFUs) ± standard deviation (SD). The population doubling time, was estimated from the metabolic activity results registered between 0 and 48 h, at which point cells were non confluent and growing at an optimal exponential rate. Immunohistochemistry against Ki67, a marker of proliferation, was performed on a non-confluent population, 48 h post seeding. Briefly, cells were washed with PBS (3x 5 min) and fixed with 4% (v/v) paraformaldehyde suspended in PBS (20 min at room temperature). Fixation was followed by further washing with PBS (3x 5 min), followed by incubation in 50 mM NH_4Cl (10 min) and permeabilization with 0.2% (v/v) triton-X100 (5 min). Cells were rinsed with PBS (3x 5 min) and blocked in 5% (v/v) bovine serum albumin (BSA) in PBS (30 min). Primary antibody incubation was performed with rabbit anti-Ki67 (dilution 1:100 in 5% (v/v) BSA; Abcam) overnight at 4 °C. Secondary reaction was done with an anti-rabbit alexa fluor antibody (dilution 1:500; Thermo Scientific) for 2 h at room temperature. After rinsing with PBS (3x 5 min), cellular preparations were mounted in Vectashield containing 2-(4-Amidinophenyl)-1H-indole444 6-carboxamidine

(DAPI), for nuclei staining. Image acquisition was done in a SP5 confocal microscope (model SP5; Leica Microsystems).

(A) Comparison study of phenotype of MKN74 cells growing under standard conditions with cells growing over silanized surfaces or under CO2 depleted conditions. (B) Ki67 staining of the same populations. (C) and (E) show population doubling time. (D) Comparative study of the metabolic activity of cells growing on a non-silanized vs. silanized surface and (F) cells growing under normal or CO_2 depleted conditions. All graphical representations display average measurement ± SD.

Figure 5: **On-chip microactuator.** To assess surface expansion, a biochip (Device 3), was filled with cell culture media and connected to the piezoelectric pressure controller using PEEK tubing. The magnitude of negative pressure applied was managed by the pressure controller, by creating a vacuum generated pull on the flexible PDMS membrane that, in turn, displaced the perforated cell culture membrane above it. By applying mechanical distension from below, the membrane is actuated three dimensionally, by pulling and releasing in the x, y and z planes. Cell culture substrate stretching, was assessed at 0, -50, -100, -150 and -200 mbar. Still images were taken with an inverted microscope (Olympus IX71), at rest and actuated state and the average interpore distance (distance between two adjacent pores) in both states was measured using image analysis software (Fiji). Linear expansion was calculated as the amount of linear stretch sustained by the substrate according to the following equation: Ɛlin=(Lf-L0)/L0, where L0 and Lf are the interpore length before and after actuation, respectively. Surface expansion was estimated from the linear expansion using the following formula: ƐSA=(Ɛlin+1)2-1 ƐSA is the surface expansion and Ɛlin is the linear expansion. The results were plotted as percentage of ƐSA ± SD relative to the rest state.

(A) Illustration of On-chip microactuator. (B) Vacuum pressure is applied at the actuation chamber, resulting in 3D cell surface expansion. Colour-coded outlines exemplify cellular expansion for a single cell at different actuation pressures. (C) Surface expansion as estimated from the linear expansion, at different pressure steps. Red line represents average surface tension of in-vivo gut cells. (D) Assessment of microactuator delamination over a period of 10 days. Top plates show a new chip prior to use. Red arrows point to the limits of the microactuator. Part of the flow channel network can be seen out of focus. The bottom plates show the detail of a chip that has been run for 10 days. No delamination of

the microactuator is observed (red arrows). Fluidic channel with seeded MKN74 cells can be seen out of focus, above the microactuator.

Figure 6: Other devices: Exploded 3D view of (A) Device 1, (B) Device 2 and (C) Device 3, each depicted with a top-down view of the assembled structure to the right and corresponding measurements for the main fluidic and microactuator features. Values are in millimetres.

References

1. Auroux PA, Iossifidis D, Reyes DR, Manz A. Micro total analysis systems. 2. Analytical standard operations and applications. Analytical chemistry. 2002;74(12):2637-52.

2. Sia SK, Whitesides GM. Microfluidic devices fabricated in poly(dimethylsiloxane) for biological studies. Electrophoresis. 2003;24(21):3563-76.

3. Young EW, Beebe DJ. Fundamentals of microfluidic cell culture in controlled microenvironments. Chem Soc Rev. 2010;39(3):1036-48.

4. Moraes C, Likhitpanichkul M, Lam CJ, Beca BM, Sun Y, Simmons CA. Microdevice array886 based identification of distinct mechanobiological response profiles in layer-specific valve interstitial cells. Integrative Biology. 2013;5(4):673-80.

5. Hung PJ, Lee PJ, Sabounchi P, Lin R, Lee LP. Continuous perfusion microfluidic cell culture array for high-throughput cell-based assays. Biotechnol Bioeng. 2005;89(1):1-8.

6. Araci IE, Brisk P. Recent developments in microfluidic large scale integration. Curr Opin Biotechnol. 2014;25:60-8.

7. Folch A, Ayon A, Hurtado O, Schmidt MA, Toner M. Molding of deep polydimethylsiloxane microstructures for microfluidics and biological applications. J Biomech Eng. 1999;121(1):28-34.

8. Zaouk R, Park BY, Madou MJ. Introduction to microfabrication techniques. Methods Mol Biol. 2006;321:5-15.

9. Gale B, Jafek A, Lambert C, Goenner B, Moghimifam H, Nze U, et al. A Review of Current Methods in Microfluidic Device Fabrication and Future Commercialization Prospects. Inventions. 2018;3:60.

10. Wlodarczyk KL, Carter RM, Jahanbakhsh A, Lopes AA, Mackenzie MD, Maier RRJ, et al. Rapid Laser Manufacturing of Microfluidic Devices from Glass Substrates. Micromachines (Basel). 2018;9(8).

11. Guckenberger DJ, de Groot TE, Wan AM, Beebe DJ, Young EW. Micromilling: a method for ultra-rapid prototyping of plastic microfluidic devices. Lab Chip. 2015;15(11):2364-78.

12. Akyazi T, Basabe-Desmonts L, Benito-Lopez F. Review on microfluidic paper-based analytical devices towards commercialisation. Anal Chim Acta. 2018;1001:1-17.

13. Dragone V, Sans V, Rosnes MH, Kitson PJ, Cronin L. 3D-printed devices for continuous908 flow organic chemistry. Beilstein J Org Chem. 2013;9:951-9.

14. Costa PF, Hutmacher DW, Theodoropoulos C, Gomes ME, Reis RL, Vaquette C. Additively Manufactured Device for Dynamic Culture of Large Arrays of 3D Tissue Engineered Constructs. Adv Healthc Mater. 2015;4(6):864-73.

15. Halldorsson S, Lucumi E, Gómez-Sjöberg R, Fleming RMT. Advantages and challenges of microfluidic cell culture in polydimethylsiloxane devices. Biosensors and Bioelectronics.

2015;63:218-31.

16. Chan CY, Huang P-H, Guo F, Ding X, Kapur V, Mai JD, et al. Accelerating drug discovery

via organs-on-chips. Lab on a Chip. 2013;13(24):4697-710.

17. Huh D, Torisawa Y-s, Hamilton GA, Kim HJ, Ingber DE. Microengineered physiological biomimicry: Organs-on-Chips. Lab on a Chip. 2012;12(12):2156-64.

18. Bhatia SN, Ingber DE. Microfluidic organs-on-chips. Nat Biotechnol. 2014;32(8):760-72.

19. Huh D, Matthews BD, Mammoto A, Montoya-Zavala M, Hsin HY, Ingber DE. Reconstituting organ-level lung functions on a chip. Science. 2010;328(5986):1662-8.

20. Stucki AO, Stucki JD, Hall SR, Felder M, Mermoud Y, Schmid RA, et al. A lung-on-a-chip array with an integrated bio-inspired respiration mechanism. Lab Chip. 2015;15(5):1302-10.

21. Guenat OT, Berthiaume F. Incorporating mechanical strain in organs-on-a-chip: Lung and skin. Biomicrofluidics. 2018;12(4). 22. Kim HJ, Huh D, Hamilton G, Ingber DE. Human gut-on-a-chip inhabited by microbial flora that experiences intestinal peristalsis-like motions and flow. Lab on a Chip. 2012;12(12):2165-74.

23. Marsano A, Conficconi C, Lemme M, Occhetta P, Gaudiello E, Votta E, et al. Beating heart on a chip: a novel microfluidic platform to generate functional 3D cardiac microtissues. Lab Chip. 2016;16(3):599-610.

24. Ergir E, Bachmann B, Redl H, Forte G, Ertl P. Small Force, Big Impact: Next Generation Organ-on-a-Chip Systems Incorporating Biomechanical Cues. Front Physiol. 2018;9:1417.

25. Ma LD, Wang YT, Wang JR, Wu JL, Meng XS, Hu P, et al. Design and fabrication of a liver935 on-a-chip platform for convenient, highly efficient, and safe in situ perfusion culture of 3D hepatic spheroids. Lab Chip. 2018;18(17):2547-62.

26. Zervantonakis IK, Kothapalli CR, Chung S, Sudo R, Kamm RD. Microfluidic devices for studying heterotypic cell-cell interactions and tissue specimen cultures under controlled microenvironments. Biomicrofluidics. 2011;5(1):13406.

27. Young EWK. Cells, tissues, and organs on chips: challenges and opportunities for the cancer tumor microenvironment. Integrative Biology. 2013;5(9):1096-109.

28. Varma S, Voldman J. Caring for cells in microsystems: principles and practices of cell-safe device design and operation. Lab Chip. 2018;18(22):3333-52.

29 Pereiro I, Fomitcheva Khartchenko A, Petrini L, Kaigala GV. Nip the bubble in the bud: a 982 guide to avoid gas nucleation in microfluidics. Lab Chip. 2019;19(14):2296-314.

Claims

1. Method for fabrication of microactuator and in-line degasser system for organ-on-a-chip devices characterized by comprising the steps of:

a) Rendering a device comprising 2 or more sheets designed to create 1 or more chambers;
b) Cutting-out the generated sheet designs of laminated Polydimethylsiloxane (PDMS) with a thickness of 500-250µm, most preferably 250µm;
c) Mounting each plotted layer on top of the preceding layer and bonding together through plasma activation of the surface;
d) Bonding the assembly to a glass slide;
e) Priming the surface, seeding cells and perfusing the fluidic portions of the sheets;
f) Degassing air bubbles in-line by applying a constant vacuum pressure to the chamber, most preferably of -50 mbar;
g) Cell stretching by vacuum-controlled mechanical actuation on the chamber.

2. Method according to claim 1, in which the said seeding of cells in step e) is performed by perfusing fibroblasts embedded in collagen type I and an epithelial cell suspension, such as the human derived epithelial gastric cancer cell line MKN74.

3. Method according to claim 1, in which the said seeding of cells in step e) is performed by flipping the device over and perfusing endothelial cells, creating an epithelial – endothelial barrier interface.

4. Method according to claim 1, in which the said seeding of cells in step e) is performed by bonding polyethylene terephtalate (PET) membranes in between the flow chambers, serving as the cell culture surface, creating cell to cell interactions.

5. System for organ-on-a-chip devices characterized by comprising 2 or more sheets designed to create 1 or more chambers.

6. System according to claim 5 in which the said sheets are characterized by, comprising laminated Polydimethylsiloxane (PDMS) with a preferable thickness of 500-250µm.

7. System according to claims 5-6 in which the said sheets are characterized by further comprising a glass slide.

8. System according to claims 5-7 in which the said sheets are characterized by further comprising seeded cells.

9. System according to claims 5-8 in which the said seeded cells are characterized by comprising fibroblasts, epithelial cells such as the human derived epithelial gastric cancer cell line MKN74, endothelial cells and combinations thereof.

10. System according to claims 5-9 in which the said in-line degasser chamber is characterized by comprising a coupling to vacuum to apply a constant pressure, most preferably of -50 mbar.

11. System according to claims 5-10 in which the said microactuator and in-line degasser chamber is characterized by comprising coupling to vacuum to control mechanical stretching of cells.

12. System according to claims 5-11, in which the said microactuator and in-line degasser chamber comprise 2 or more independent chambers.

Figures

Fig. 1

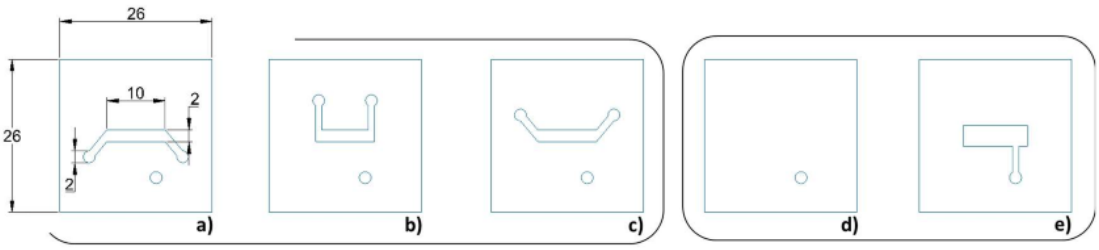

Fig. 2

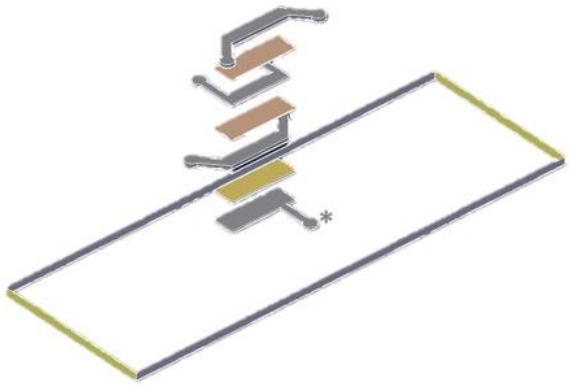

Fig. 3

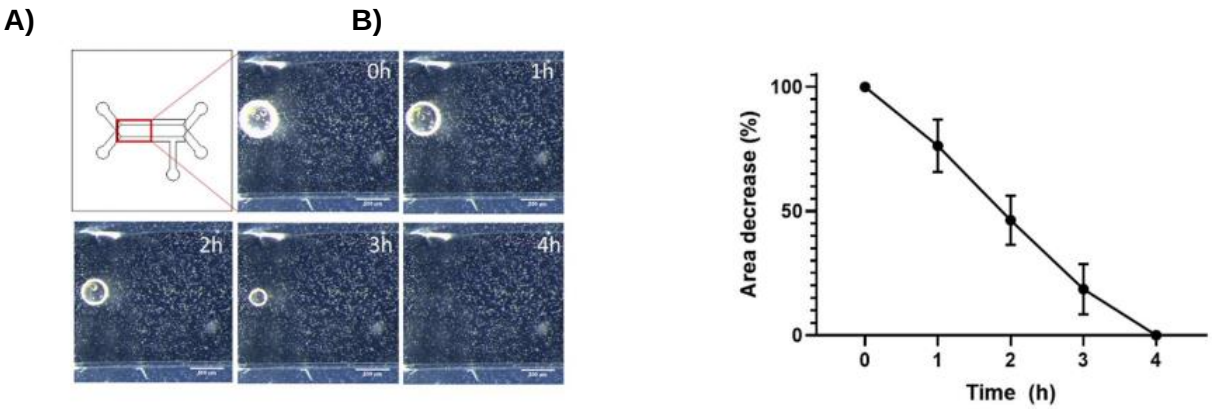

Fig. 4

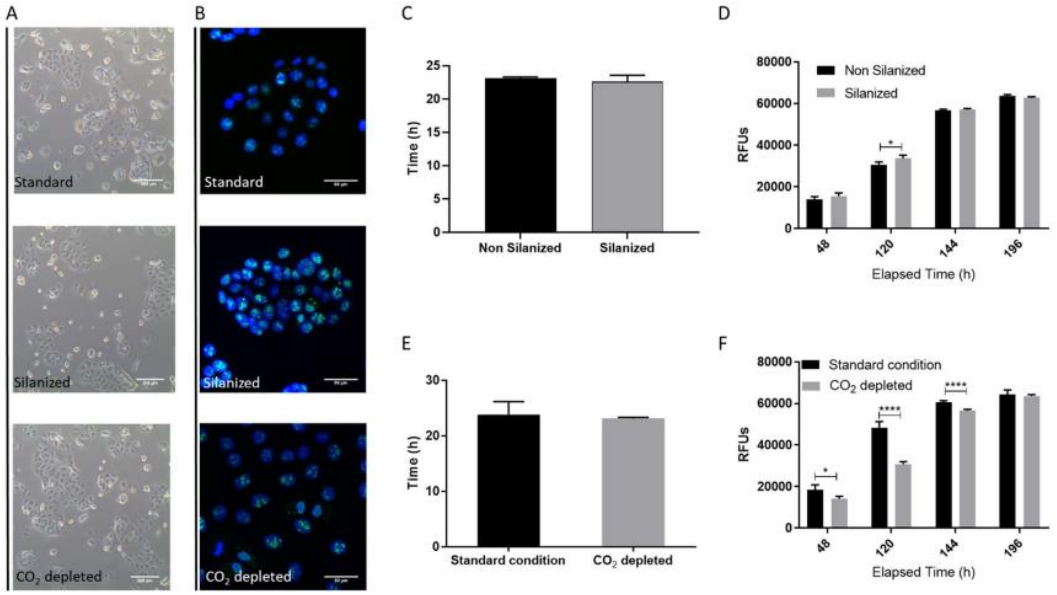
A
B
C
D
Standard
Standard
Silanized
Silanized
CO2 depleted
CO2 depleted
Time (h)
Non Silanized
Silanized
RFUs
Non Silanized
Silanized
Elapsed Time (h)
E
F
Time (h)
Standard condition
CO2 depleted
RFUs
Standard condition
CO2 depleted
Elapsed Time (h)

Fig. 5

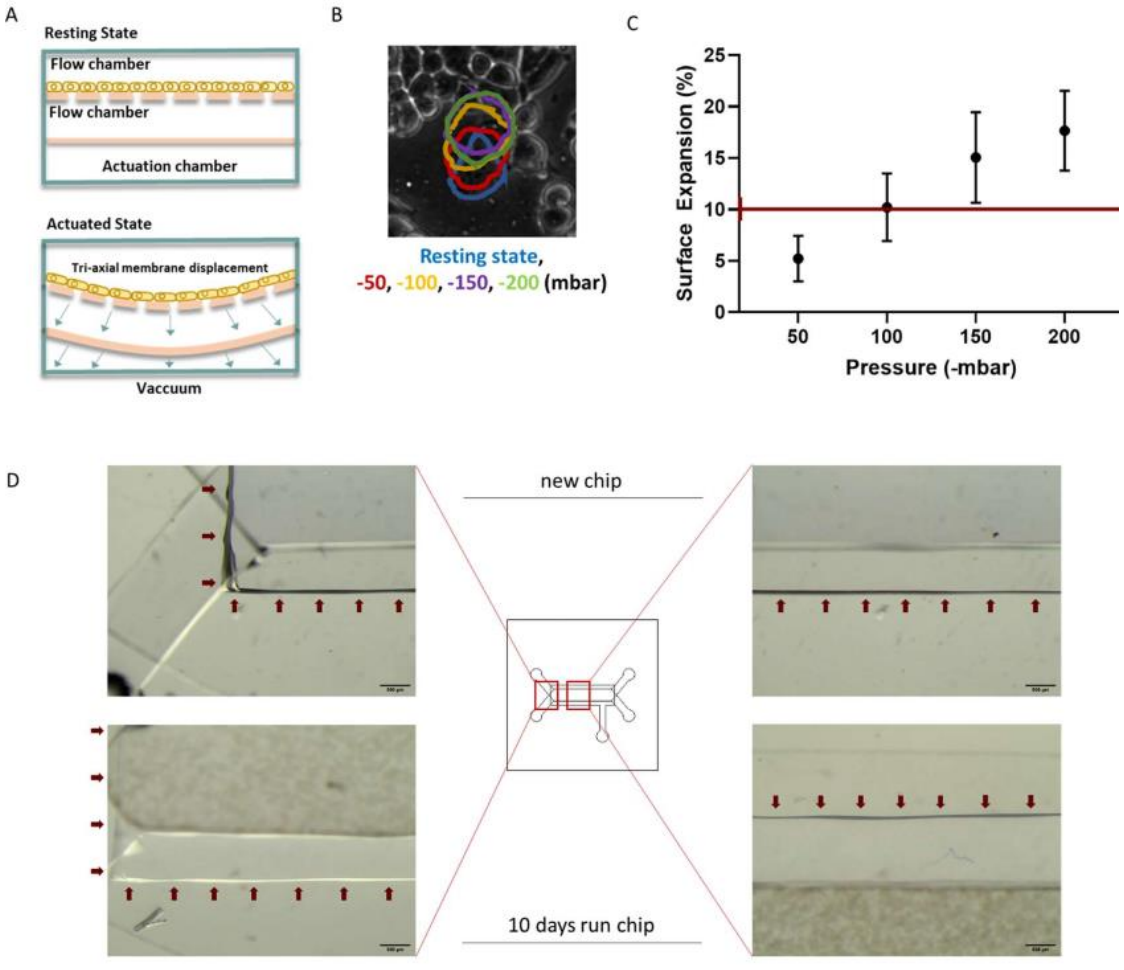
A
Resting State
Flow chamber
Flow chamber
Actuation chamber
Actuated State
Tri-axial membrane displacement
Vaccuum
B
Resting state,
-50, -100, -150, -200 (mbar)
C
Surface Expansion (%)
Pressure (-mbar)
D
new chip
10 days run chip

Fig. 6

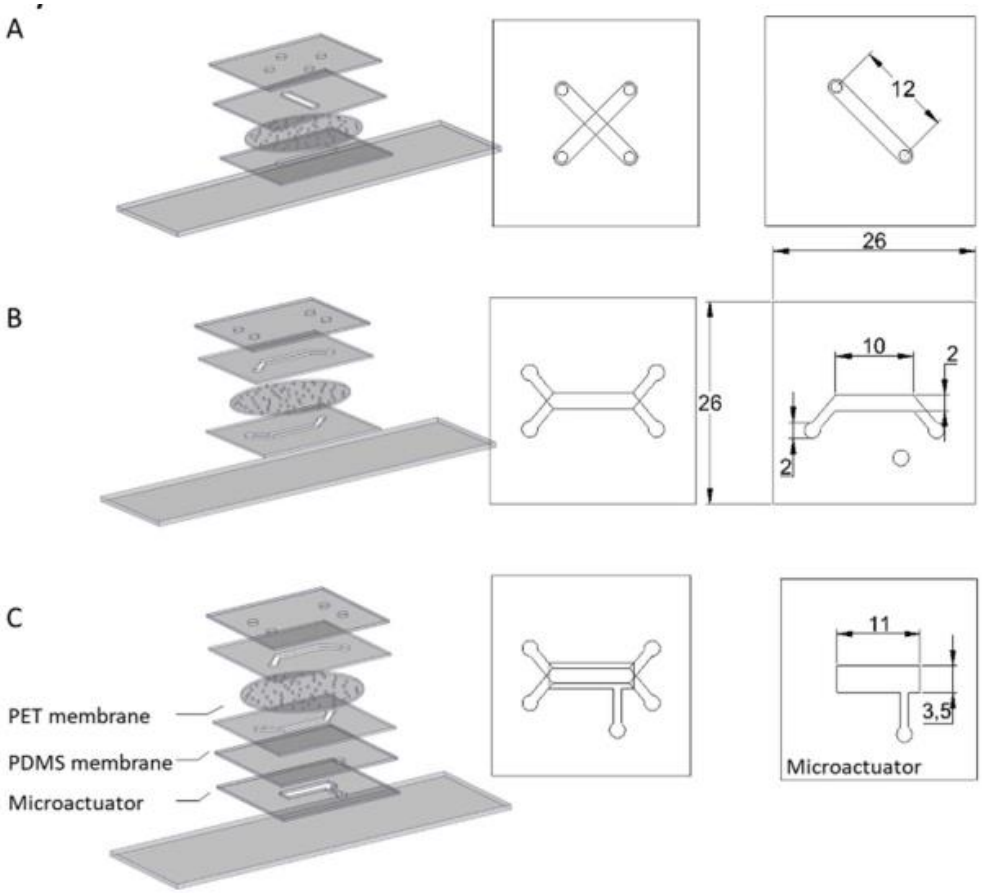
A
12
26
B
26
10
2
2
C
PET membrane
PDMS membrane
Microactuator
11
3,5
Microactuator